INVESTIGATION OF HORIZONTAL CO-CURRENT TWO-PHASE SLUG FLOW PHENOMENA

by

Marcus Naraidoo

A dissertation submitted to the University of Bristol in support of an application for the degree of Doctor of Philosophy in the Department of Mathematics of the Faculty of Science.

October, 1989

ABSTRACT

In the following, horizontal co-current two-phase slug flow is studied. Inception of slug flow from wavy-stratified flow has previously been treated as a Kelvin-Helmholtz type instability of an incompressible stratified gas over an incompressible liquid. The effect of a compressible gas is studied, and this is seen to destabilise the linear theory. Subsequent experimental analysis of slug flows suggest that the initial stages of the transition from wavy-stratified flow may be treated as a wave motion. By modeling the gas as a quasi-steady, one-dimensional flow over an unsteady, two-dimensional liquid a Cauchy theorem boundary-integral technique is used to calculate the movement of the interface. In this fashion the effects of the relative gas Mach number and the pressure within the gas may be studied. It is found that for a given entry pressure of the gas the interface does not exhibit slug like behaviour for gas Mach numbers below a particular value, but that slug like behaviour is observed to occur for small changes in the Mach number above this value. This method is also used to study high pressure steam-water like flows by using the equation of state for steam to modify the interfacial pressure distribution. It is found that steam behaves in an anomalous fashion. Relatively low pressure steam (100 atm.) slugs more quickly than higher pressure steam (180 atm.). Careful analysis of the experimental results suggests that some slug flows are flows of fast moving regions of entrained droplets. The effect of a region of entrained droplets on an unsteady one-dimensional gas flow is studied. The form and magnitude of the resulting pressure pulses are found to vary with the droplet radius, the droplet void fraction, the gas Mach number and the pressure. The results suggest that droplet entrainment plays an important rôle, and that the experimentally observed pressure pulses are influenced by this.

ACKNOWLEDGEMENTS

In preparing the work for this thesis I would like to acknowledge the kind help and guidance given to me by my supervisor Professor D. Howell Peregrine who has always encouraged me with his ideas and enthusiasm. And Dr. David Pearce, my industrial supervisor at the Central Electricity Generating Board's research laboratories, for his assistance and encouragement, and his constant enthusiasm for a better understanding in the field of two-phase flow.

I would especially like to thank Dr. Ian Stewart for his constant help and advice in computational matters - "like trying to teach an amoeba how to use an abacus" - and for the odd pint when things were not going so well.

The financial support of the Science and Engineering Research Council, and of Cooperative Awards in Science and Engineering through the Central Electricity Generating Board is gratefully acknowledged.

Finally, none of this work would have been possible without the constant encouragement and care shown to me by Lynne Freeman.

Thank you, all of you.

To Lynne

MEMORANDUM

The work in this dissertation is the independent and original work of the author except where explicit reference to the contrary has been made. It has not been submitted for any other degree or award to this or any other university.

M. Naraidoo.

Marcus Naraidoo

October, 1989

CONTENTS

1. INTRODUCTION

The importance of multiphase flows to us all may, at first, be hard to appreciate, but in fact we may see such flows around us from day to day. For example, when a temperature inversion causes fog, or water condenses into clouds, or we boil water for a cup of tea or even pour beer from a bottle we are in fact experiencing multiphase flows. Of more importance, perhaps, are the multiphase flows that allow our industries to function. When oil is brought onshore via submarine pipeline, or electricity is produced by boiling water with fossil or nuclear fuels, or when chemical reactions proceed in fluidized beds, or sewage is treated, multiphase flows are in evidence.

Multiphase flows, then, are flows in which the motions of the phases are coupled to one another. Flows such as solid-liquid, solid-gas and gas-liquid flows form a two-phase subset of all the possible multiphase flows. The following study considers only gas-liquid two-phase flows in horizontal pipes.

Most work on multiphase flows, and two-phase flows in particular, is empirical. Engineering processes need fast answers to problems that they encounter, and as two-phase flows are common in industry a means is required by which engineers can predict what type of flow they would get for a particular arrangement of plant and with specific flow rates of the phases. Flow régime maps provide a convenient means for doing this. For example, maps such as the Baker flow régime map (later modified by Bell, Fig. 3.2 of Chapter 3) and the Mandhane flow régime map (Fig. 3.3 of Chapter 3) allow the engineer to predict how the phases would behave, and hence design the plant, provided that the plant arrangement and two-phase compounds are admissible to that particular map.

Flow régime maps are produced by conducting experiments either on a laboratory scale, or more rarely on existing plant when there is no danger to the plant, to determine the type of flow that arises for a particular combination of mass fluxes or superficial velocities (these are velocities which are averaged over the entire tube cross-section). For example, if one is interested in two-phase air-water flow down horizontal pipes one may arrange a laboratory experiment of air-water flow down a horizontal pipe and observe the flow types that arise for various air and water mass fluxes. If the variation of the régimes with these fluxes is plotted on a diagram we obtain a flow régime map for the air and water. If we ever need to know anything about such air-water flows we then only need to consult our tailor-made flow régime map to obtain the answer. However, problems may arise if the laboratory experiment is a small scale representation of a much larger arrangement of plant. In this case, the flow régime maps may no longer be representative of what happens on the larger scale as the régime boundaries are often affected by scale changes. In addition to problems with extrapolating small scale experiments to larger scales other problems may arise. For instance, if an air-water flow régime map is used to predict the flow transitions within a steam-water system we may expect some discrepancies. While flow régime maps provide a quick and easy means of predicting the flow type of a specific combination of fluids under certain conditions they cannot be relied upon for a whole class of fluids in a variety of conditions. In order to describe an oil-water flow at 5 atm. and at 8°C one may obtain a flow régime map, but this map is almost useless for the same fluids in the same tube at 100°C. Thus, while flow régime maps are very useful once they are obtained they tend to be very specific in nature, and very costly to obtain.

Early mathematical modelling of two-phase flows was by means of experimental correlations such as the Lockhart-Martinelli correlations to obtain mathematical expressions to describe two-phase flows (see Lockhart & Martinelli (1949)). While there was some success in this approach, more fundamental mathematical modelling of two-phase flows (and hence, greater physical understanding of the flows) was sought.

Gas-liquid two-phase flows are generally considered to fall into two easily defined categories. These classes are vertical two-phase flows and horizontal two-phase flows. Fig. 1.1 shows the various régimes of vertical two-phase flow, while Fig. 1.2 shows the régimes for horizontal two-phase flow.

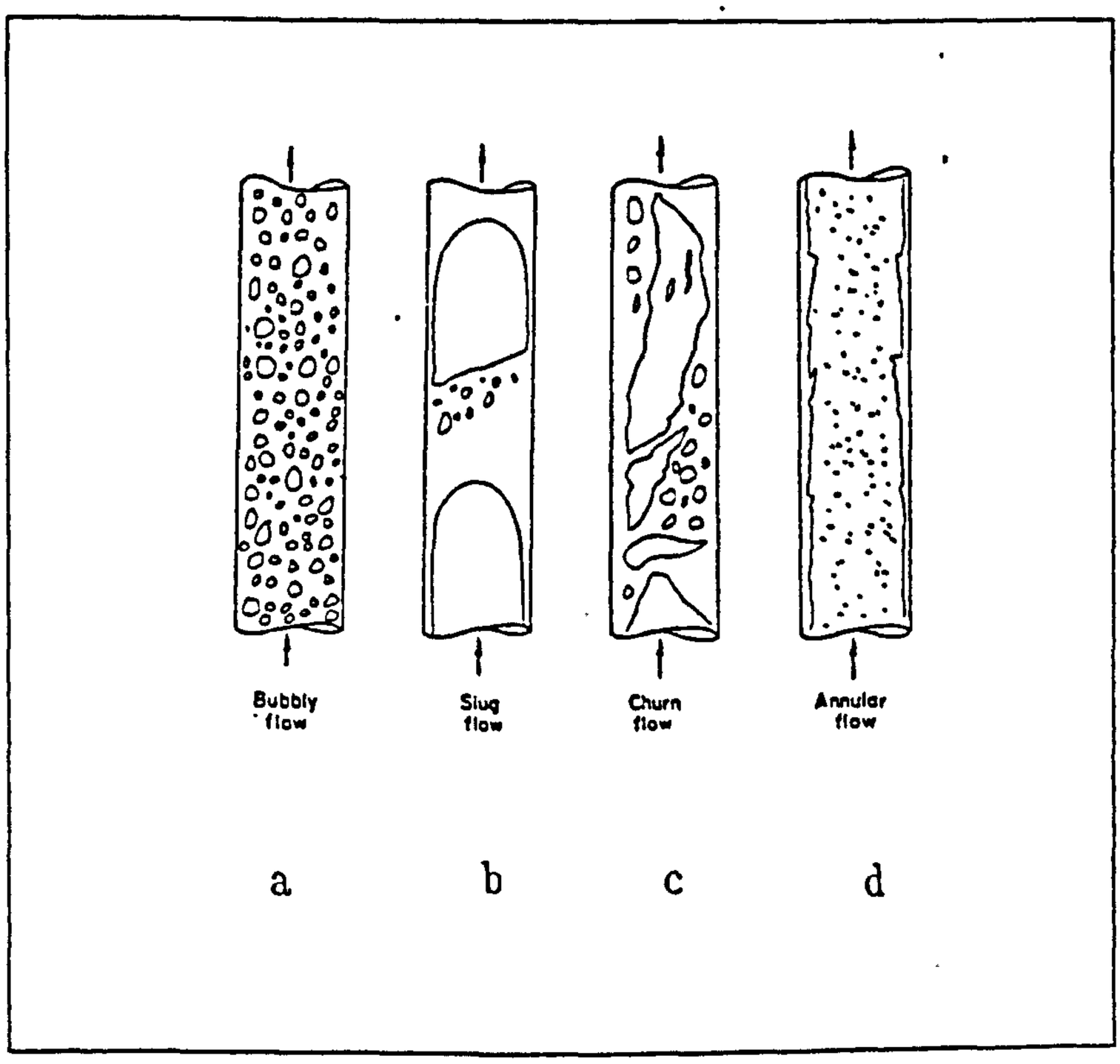

Fig. 1.1

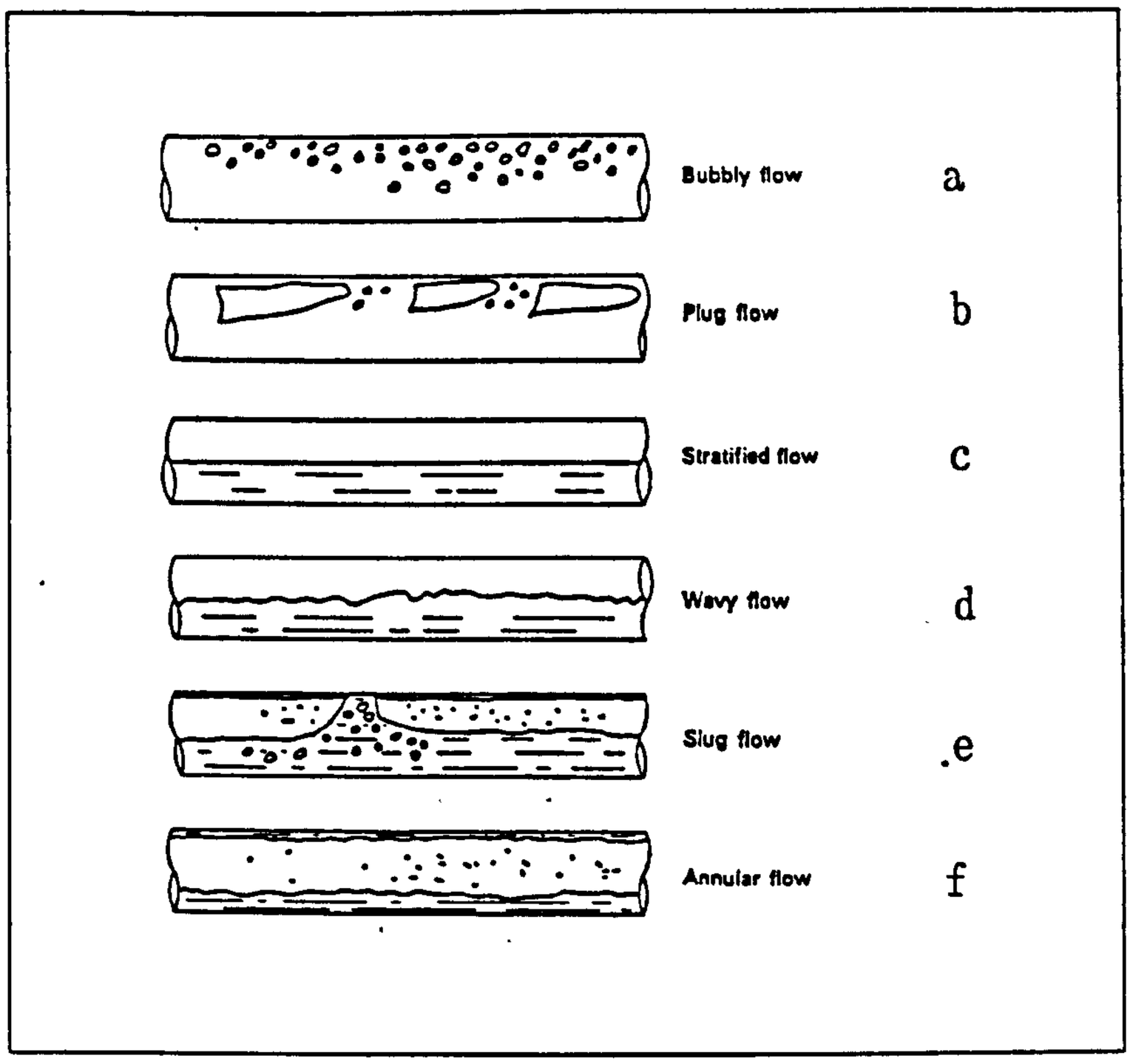

Fig. 1.2

The flows are then again generally subdivided into two further classes each. These are co-current flow (in which both phases travel in the same direction) and counter-current flow (where they are in opposite directions). Of these two main classes of two-phase flow, vertical two-phase flow has been studied more extensively in the past, while advances in modeling horizontal two-phase flow have been achieved more recently.

Vertical two-phase flows are more easily modeled since these flows often possess symmetry and this then simplifies the mathematical aspect of the problem, while most horizontal flows (with the exception of an idealised annular flow) possess no such symmetry. A discussion of the basic differences between vertical and horizontal two-phase flows can be found in Wallis (1969), Hewitt & Hall-Taylor (1970), Pai (1977) and Bergles et al. (1981).

The Central Electricity Generating Board (hereafter CEGB) and many petrochemical companies have recently become particularly interested in some aspects of horizontal two-phase flow, although the particular régimes in which there is interest vary (as the desired applications vary). The oil companies are interested in the transition from wavy-stratified flow to slug flow (Fig. 1.2d to 1.2e). Oil and air may flow safely in stratified layers for great distances, but if a slug is formed the results can be disastrous. A slug travels much faster than the stratified oil and on arriving at the onshore separator may have sufficient momentum to cause considerable damage. The CEGB are interested primarily in annular flows (Fig. 1.2f). For cooling purposes it is advantageous to maintain a wetted layer around the entire circumference of the cooling pipes as this aids heat transfer. If a pipe ruptures, however, a situation may arise in which the tube is not constantly wetted. This may cause further hot spots to develop on the pipe leading to a further loss of the coolant and this may have disastrous effects. In this situation it is desirable to maintain a slug flow. This allows an intermittent wetting of the pipe circumference which may prevent further hot spots from developing and thus avert an accident. These applications of horizontal two-phase slug flow provided the motivation for the following work. In particular we consider two-phase co-current slug flow, and the transition to this flow type from wavy-stratified flow.

At this point a brief discussion of the nomenclature used to describe these flows is appropriate. In much of the literature on two-phase flows, and in particular in literature originating from within the CEGB, the term "surge" is used to describe the type of flow shown in Fig. 1.2e . In fact Coney (1974) uses the term "slug" flow to describe the flow as shown in Fig. 1.2e and "surge" flow to describe a very

similar flow, but for which the entire tube diameter is never totally blocked by continuous liquid. Thus the term "surge" is often misused, since it is not the flow of Fig. 1.2e but something quite similar. It is, in fact, a particular type of slug flow. New terms to describe other subsets of slug flow are also used, such as the "pseudo-slug" of Lin & Hanratty (1987) (for which the flow "looks" like slug flow, but the pressure variation differs). Since many authors tend to avoid using the term "surge" or "pseudo-slug", we shall avoid confusion and use the term "slug" to describe the flow of Fig. 1.2e, and all slug-like flows.

Extensive simple modelling (some semi-empirical) of slug flow has been performed by many authors. When observations of the gas-liquid interface in two-phase flow experiments are made, for particular flow conditions surface waves may be seen to grow into fast moving slugs (Kordyban & Ranov (1970)). This rapid growth of these waves has led to the treatment of the slug growth problem as a Kelvin-Helmholtz type of instability (Drazin & Reid (1985) p.14). This approach assumes that long wavelength waves (small wave number) are primarily responsible for slug growth. While this assumption makes the problem mathematically tractable, observations of slug flows suggest that perhaps the smaller wavelength waves are the more unstable. Furthermore, experiments suggest that the theoretical value of the critical velocity for the Kelvin-Helmholtz instability to occur is a factor of two too small for predicting slug flows in a closed channel (Wallis & Dobson (1973) for example). In an attempt to reconcile this, Kordyban & Ranov (1970) considered waves of finite amplitude but their stability condition was rather difficult to use. An improvement came in the parer by Taitel & Dukler (1976), but they still required qualitative arguments to obtain the coefficients of their expressions. This was finally reconciled in the fine paper by Mishima & Ishii (1980) who obtain the stability

criterion of Taitel & Dukler from purely theoretical considerations.

While such considerations may provide information about the stability of wavy-stratified flow, or whether the flow becomes slug flow, they provide no information about the evolving profile of the interface, just whether slug flow occurs or not.

Often the analysis of single phase flows is aided by parameters which characterise the flow. However, two-phase flows are much more difficult to characterise than single phase flows, so while a non-turbulent single phase flow may be well described by specifying the flow Reynolds number and the Mach number (these give the reader a "feel" for the flow - how important viscosity and the effects of compressibility are to the flow) this is not sufficient for two-phase flows.

The choice of parameters to describe a two-phase flow very much depend upon what aspect of the flow is of interest. If one is more interested in the liquid dynamics then perhaps one scales lengths relative to the undisturbed depth of the liquid and velocity through a $\sqrt{gh_B}$ type term (h_B is the liquid depth and g the acceleration due to gravity). However, if one is interested in the gas dynamics then a more natural choice of velocity for scaling is the gas sound speed. By scaling in this fashion we may study the effects of compressibility, and so investigate whether compressibility is of importance to slug flows. This illustrates the difficulties in scaling two-phase flow problems. By choosing the liquid scaling, fast information in the gas dynamics is lost, whilst the gas scaling treats the liquid as being almost stationary.

To try to overcome this problem there are, in addition to the above flow parameters for each phase, a multitude of parameters that describe the interaction between the phases. The density ratio, $\frac{\rho_G}{\rho_L}$ and the viscosity ratio, $\frac{\mu_G}{\mu_L}$ are frequently used. The gas and liquid superficial velocities are often used to characterise the flow velocities. These are velocities of the phases obtained from the respective phase mass flux and density, and averaged over the entire tube cross-section. The superficial velocity of a gas, U_{GS} corresponding to a gas mass flux Q_G and density ρ_G is

$$U_{GS} = \frac{Q_G}{\rho_G A}$$

where A is the total cross-sectional area. Another term called the vapour quality is often used. The vapour quality, often denoted x in the literature, is defined as the ratio of the vapour flow rate to the total flow rate

$$x = \frac{Q_G}{Q_G + Q_L}$$

Another parameter that is sometimes used is the Lockhart-Martinelli parameter X. This is the ratio of the frictional pressure gradients that the gas and liquid would experience if they were flowing alone in the tube:

$$X = \sqrt{\frac{(dp/dx)_L}{(dp/dx)_G}}$$

where x is the spatial co-ordinate along the pipe.

Whilst these and other numbers are sometimes used to parameterise two-phase flows we shall avoid using such numbers and only use numbers which seem to physically describe the flows under consideration. For example, to gauge the importance of the pressure forces within the gas to those within the liquid which give rise to the asymmetry of some of the results of Chapter 4 we shall use

$$\mathcal{P} = \frac{\frac{1}{2}\rho_G u_G^2}{\rho_L g a}$$

where u_G is the actual gas velocity and a is the wave amplitude at the crest, in analogy with the gravity current scaling of Wallis & Dobson (1973).

Another problem with two-phase flow studies is the large parameter space of variables that affect the flow. We shall see in Chapter 4, where we look at the liquid dynamics, that parameters such as the initial amplitude of the wave, the equilibrium depth of liquid in the tube, the total tube diameter, the gas Mach number and the gas entry pressure all affect the results. In fact, the number of parameters is so large that we cannot hope to study all of the various combinations, and in Chapter 4 we only consider variations in the gas Mach number and gas entry pressure.

Experiments have suggested that there is a whole wealth of detail in the growth of a slug. Dukler & Hubbard (1975) consider that a slug is formed when the liquid layer completely bridges the entire tube cross-section, and indeed, Markovich (1983a and 1983b) observes such a blockage in his slug flow experiments. However, Coney (1974) noticed that for air-water flows in the CEGB horizontal test facility (25 mm diameter perspex pipe) with gas and liquid superficial velocities in the

ranges $8\ m\ s^{-1} \lesssim U_{GS} \lesssim 20\ m\ s^{-1}$ and $0.3\ m\ s^{-1} \lesssim U_{LS} \lesssim 1.5\ m\ s^{-1}$ respectively (and even for some lower gas and liquid superficial velocities) the liquid layer never completely bridged the entire tube cross-section. For such flows the bridging model of Dukler & Hubbard is inappropriate. .

To gain a deeper understanding of the mode of the growth of a slug the experimental work of Chapter 3 was performed. At this point, perhaps a discussion about the term used to describe the gas-liquid interfacial profile is in order. In the light of the Kelvin-Helmholtz type work, perhaps the obvious term to describe the form of the interface would be "instability". After all, the Kelvin-Helmholtz approach seeks a stability criterion and so perhaps describing the surface profile in terms of "surface instability" is fine. However, the surface is invariably strongly disturbed and such stability criteria may not be relevant and so "surface instability" may not be appropriate. Likewise, "surface disturbance" may not be sufficient as it is unclear which part of the disturbance grows. Likewise, "wavelet" may seem logical. However, strictly speaking "wavelet" means part of a wave (as in the Huygens' construction in optics). In the light of the experimental work of Chapter 3, for the parameter space under consideration, the term "wave" best describes the surface profile. A wave motion, whether arising from the growth of a Kelvin-Helmholtz type instability or from some entry phenomenon, say, is clearly seen to propagate and sometimes grow, although it may not always grow into a slug.

In both Chapters 4 and 5 the gas is treated as compressible as Chapter 2 suggests that compressibility has a destabilising effect on the linear one-dimensional Kelvin-Helmholtz instability type flow.

The observation of wave propagation and growth suggests one method by which the early stages of slug flow may be modeled. Slug inception may, perhaps, be regarded as a shallow water-like phenomenon. In Chapter 4 the treatment of slug growth in terms of water wave considerations for which the interfacial pressure distribution is modified by the gas, is considered. This approach treats the liquid as being inviscid, two-dimensional and unsteady, and the gas as compressible, one-dimensional and quasi-steady. Whilst most of the established literature ignores the effect of compressibility within the gas the work in Chapter 2 suggests compressibility destabilises the linear Kelvin-Helmholtz theory, and so compressibility is retained in Chapter 4. With this approach the evolution of an initial wave form, such as a solitary wave or a wave train of some type, can be studied. This is achieved by solving Laplace's equation within the liquid by performing a boundary integral calculation (Dold (1990 - to appear), Dold & Peregrine (1986)). This scheme has been used previously for a variety of water flow problems, such as waves up beaches or over submerged structures. A discussion of the efficiency and accuracy of the scheme can be found in Tanaka, Dold, Lewy & Peregrine (1987). This scheme is applied to air-water flows with entry pressures of up to 5 atm. so that comparison with the results of Chapter 3 may be made, and for steam-water like flows by using the equation of state for steam (Keenan et al. (1978)) for steam at pressures of 100, 140 and 180 atm. and saturation temperatures.

In addition to observing the propagation and growth of surface waves, the experimental work suggests that for some flow conditions a fully formed slug does not consist of a region of continuous liquid which largely fills the entire tube cross-section. While we may expect slugs to consist of such regions when the fractional depth of liquid

(the ratio of the liquid depth to the tube diameter) is large, we may not expect this to be the case when the fractional depth is small. When the fractional depth is small, as in the experimental work of Chapter 3, we find that slugs appear to be regions of densely entrained droplets. Chapter 5 investigates the effect of regions of entrainment of various droplet densities on the gas dynamics of an interacting gas in a two-dimensional pipe of constant cross-section. This work suggests that, as a result of the coupling between the momenta of the two phases, pressure pulses of large magnitude travel rapidly throughout the gas, and that the magnitude and sharpness of these pulses is greatly affected by the droplet radius (in agreement with Comfort III & Crowe (1980) and Martin & Padmanabhan (1979)). The conservation equations for the gas-liquid system are those obtained from volume averaging considerations by Soo (1976) (and reviewed by Drew (1983)). Whilst such an approach appears mathematically rigorous in translating microscale quantities into macroscale ones, criticisms leveled at this approach concentrate on inaccuracies introduced into the momentum interaction modelling through the constitutive relations that are used to obtain the terms of the interaction (see Chapter 5). Nevertheless, this approach is adopted in preference to methods which rely upon semi-empirical modelling. The system is then solved numerically by a Roe type characteristic following, shock capturing scheme (Roe (1986b)).

Two-phase flows are, largely, not "nice" in the same sense as turbulent flows are not nice, nor are meteorological flows. The borders between flow régimes are not very sharp but are somewhat fuzzy (Wallis (1969) p.8). The boundaries are affected by a whole manner of things, such as tube diameter (Harrison (1975) and Lin & Hanratty (1987)), the effect of tube roughness (Taitel (1977)), the choice of two-phase mixer (see Fig. 3.5 for an example), the surface

tension of the liquid and the effects of draining films on the tube walls, to name but a few. To model all of these aspects and the rôles played by stresses, thermodynamic non-equilibria, bubble and droplet entrainment, droplet fragmentation, bubble coalescence and flow through various geometries is very difficult. Thus, because of the complexities of two-phase flows, global modelling for the entire range of flow types is impractical. Specific régimes and some transitions may be modeled, but then usually after simplifying assumptions have been made. Any analytic solutions are often solutions to an over-simplified case bearing little resemblance to real two-phase flow found in industry where pipes are not two-dimensional, smooth and perfectly horizontal. Increasingly, two-phase flow modelling is following in the footsteps of turbulence or geophysical fluid dynamics modelling or the statistical modelling of liquids, where modelling the problem numerically is necessary in order to make further advancements.

Despite this trend toward numerical modelling of two-phase flows there is still much fine theoretical modelling, such as that concerning the modes of droplet breakup by Azzopardi (1983) or about local volume averaging for the equations of two-phase flow by Gray (1983), to name but two. Ultimately this improved modelling can only be appreciated, in many cases, through the numerical solution of the new description of the two-phase system.

2. PRELIMINARY WORK - COMPRESSIBLE KELVIN-HELMHOLTZ INSTABILITY

2.1 Introduction

It is important to predict the onset of slug flow within a gas-liquid two-phase flow for a variety of reasons. If there is slug flow within an off-shore oil pipeline the slug can have disastrous effects when it reaches the separator. Similarly, slug flows can have beneficial consequences. If there is a loss of coolant accident within a nuclear reactor, slug flow is preferred to stratified flow if annular flow has ceased.

The purpose of this chapter is to summarise the most popular analytic methods used for predicting slug flow, and then discuss why compressibility effects of the gas may be important to such models. It is not the purpose of the chapter to develop a two-layer compressible long wave small amplitude model which is as accurate as some of the existing empirical models. It is merely to show that compressibility effects within the gas destabilise the linear long wave Kelvin-Helmholtz theory.

When gas flows over a wavy surface, to a first approximation, a component of the pressure in phase with the wave profile and a component in phase with the wave slope are produced, Miles (1962). Kordyban & Ranov (1970) noted that below a critical value of pressure "only the component in phase with the wave slope contributes energy to the wave. If this exceeds the energy dissipated by the wave the wave will grow".

A Kelvin-Helmholtz instability occurs when a gas-liquid interface is perturbed, and when the gas velocity is sufficiently high. The gas flow

over the crests and troughs of the perturbation gives rise to a lower pressure component in phase with the wave slope over the crests than over the troughs (Bernoulli's principle). When the pressure drop becomes sufficiently large to overcome the stabilising effect of gravity we have a Kelvin-Helmholtz instability (Fig. 2.1).

Diagrammatic representation of a Kelvin-Helmholtz instability

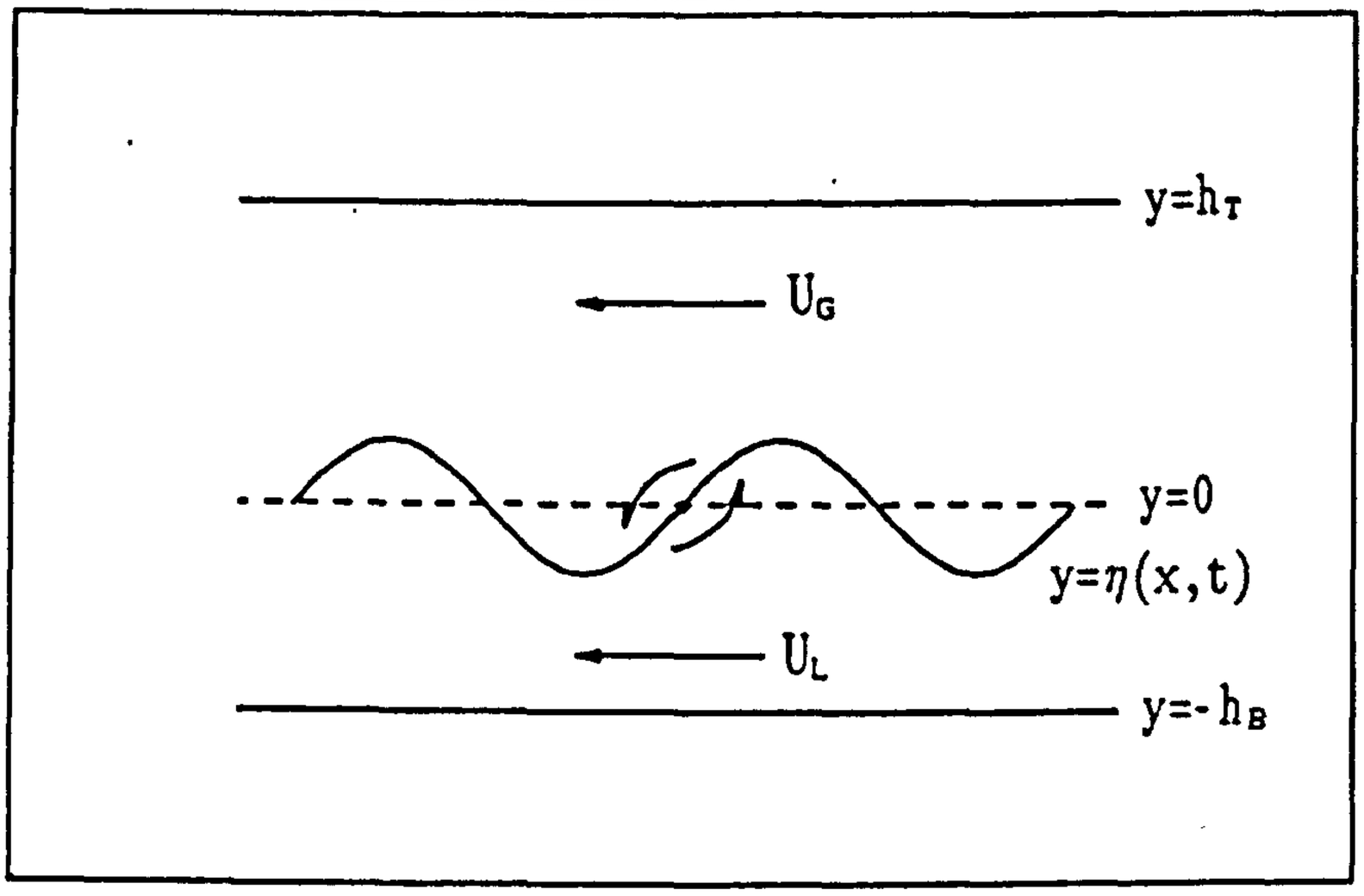

Fig. 2.1

With reference to Fig. 2.1 the classical criterion for a Kelvin-Helmholtz instability growth in a two-dimensional channel when the flow is irrotational and the fluids are incompressible with $\rho_G \ll \rho_L$ (where ρ_i is the density of the gas or liquid) and U_G and U_L are the free stream velocities of the gas and liquid respectively, is

$$U_G - U_L = \sqrt{\left[\frac{\rho_L - \rho_G}{\rho_G}\right] g h_T} \qquad (2.1.1)$$

(Helmholtz (1868), Kelvin (1871), Milne-Thomson (1950)). However, Mishima & Ishii (1980) pointed out in their fine review of two-phase modelling, this over predicts the gas-liquid relative velocity by a factor of two which Wallis & Dobson (1973) noted from experimental observations of flow in a horizontal rectangular channel.

Kordyban & Ranov (1970) noted the following two points:

" (a) The slugs occur when a wavy interface already exists and the slugs represent an extension of growth of a particular wave, considerably beyond the range of wave steepness when simple harmonic waves can be expected;

(b) The pressure distribution over the wave is modified by the proximity of the upper wall."

Kordyban & Ranov did not restrict their analysis for the criterion of slug formation to long waves and they obtain the following result for slug formation in a closed rectangular channel:

$$(U_G - U_L)^2 \geq \frac{\rho_L g}{\rho_G k} \frac{1}{\coth(kh_T - 0.9) + 0.45 \coth^2(kh_T - 0.9)} \qquad (2.1.2)$$

where k is the wave number. They obtain this criterion by considering waves of limiting amplitude. The implicit equation for the wave profile is:

$$\eta = B\sinh[k(\eta+h_B)]\cos(kx)$$

(where B is a constant) and they say that the waves of limiting amplitude occur when there is a cusp in the wave peak, and analysis of the above equation shows that this occurs when:

$$k\eta\coth[k(\eta+h_B)] \longrightarrow 1$$

They use this relationship to derive equation (2.1.2). With equation (2.1.2) they obtain reasonable agreement with experiment. The drawback of this criterion is that it is necessary to know the depth of gas in the tube, h_T, and the wavelength of the waves, and these values are not easily determined. However, if disturbances with all possible values of k are considered to be present, then there is not much difficulty in obtaining the wavelength if the fastest growing wave is selected.

Other formulations have considered the geometry of the problem, such as whether the flow is within a pipe of circular cross-section. Taitel & Dukler (1976) obtain the following expressions for slug formation between horizontal parallel plates:

$$U_G - U_L \geq K_1 \sqrt{\left[\frac{\rho_L - \rho_G}{\rho_G}\right] g h_T} \qquad (2.1.3)$$

where

$$K_1 = \sqrt{\frac{2}{\frac{h_T}{h_C}\left[\frac{h_T}{h_C} + 1\right]}} \qquad (2.1.4)$$

and h_C is the distance from the wave peak to the top of the tube or channel, or for a horizontal or near horizontal pipe:

$$U_G - U_L \geq K_2 \sqrt{\frac{1}{\frac{dA_L}{dh_B}}\left[\frac{\rho_L - \rho_G}{\rho_G}\right] A_G \, g\cos\beta} \qquad (2.1.5)$$

where

$$K_2 = \frac{A_{GC}}{A_G} \qquad (2.1.6)$$

where A_i (i=G or L) is the cross-sectional area occupied by the respective phases, A_{GC} is the area admissible to the gas over the crest, A is the total cross-sectional area, β is the angle of inclination of the pipe to the horizontal and $\frac{dA_L}{dh_B}$ is the variation of the liquid area with the bottom topography. In practice, K_1 and K_2 were obtained from empirical arguments.

Mishima & Ishii (1980) attempt to obtain the K's from a theoretical approach. They use the concept of the "most dangerous wave", the wave with maximum growth rate. They argue that slugs form in the following fashion. When a surface perturbation occurs a particular wave will continue to grow until it reaches a "limiting" amplitude after which it

cannot be considered to be infinitesimal. This wave has the wavelength of the "most dangerous wave". They obtain, for flow between parallel plates, the following expression from purely theoretical considerations:

$$U_G - U_L \geq 0.487 \sqrt{\left[\frac{\rho_L - \rho_G}{\rho_G}\right] g h_T} \qquad (2.1.7)$$

for the case when $\rho_G \ll \rho_L$. This expression is in good agreement with experiments (see Mishima & Ishii (1980)).

Lin & Hanratty (1986) also observed that the Kelvin-Helmholtz small amplitude, long wavelength theory over predicted the gas-liquid relative velocity for the initiation of slug flow. Andritsos & Hanratty (1987) observed that this is because the inviscid theory underestimates the destabilising effects of the gas on the inertia of the liquid. They conclude that the Kelvin-Helmholtz approach is a good first approximation for the relative gas velocity required to initiate irregular finite amplitude waves on the gas liquid interface. Suppose U_{Gfa} is the gas velocity when there are finite amplitude waves on the gas-liquid interface (as opposed to free stream gas velocity U_G, or the superficial gas velocity U_{GS}) then they obtain the following expression:

$$(U_{Gfa} - U_L)^2 \geq \left[\frac{k\sigma}{\rho_G} + \frac{\rho_L g}{\rho_G k}\right] \tanh(kh_T) \qquad (2.1.8)$$

where σ is the surface tension, for the condition that irregular finite amplitude waves are formed on the interface. Inviscid Kelvin-Helmholtz theory predicts that the minimum value of U_{Gfa}-U_L is obtained for waves with wave number;

$$k_{min} = \sqrt{\frac{\rho_L g}{\sigma}} \qquad (2.1.9)$$

Equation (2.1.8), together with (2.1.9) forms only a first approximation

for the criterion for slug flow to occur. They go on to say that after taking into account the small effects of liquid height and the liquid viscosity, the following semi-empirical equation for gas-liquid flow is obtained:

$$U_{GS} = U_{Gfa} \frac{1}{1-\alpha} \left[\frac{\theta_w}{\theta}\right]^{0.025} \left[\frac{1}{\tanh(k_{min} h_B/10)}\right]^{0.1} \qquad (2.1.10)$$

where U_{GS} is the superficial gas velocity and θ is a dimensionless group (defined by Taylor (1963)) which takes the liquid viscosity into account:

$$\theta = \frac{\rho_L \sigma^2}{\rho_G \mu_L^2 U_G^2} \qquad (2.1.11)$$

and μ_L is the liquid viscosity. The term θ_w is the value of this group for water which parameterises the equation. The term α is the liquid void fraction, the fraction of the tube cross-section that the liquid flows through, so $(1-\alpha)$ is the gas void fraction. Andritsos & Hanratty (1987) conclude that equations (2.1.8) and (2.1.10) are in good agreement with experimental observations.

It is interesting to note, however, that all of these attempts to predict the onset of slug flow treat the gaseous phase as incompressible. Whilst it is plausible that the gas flow over a stratified liquid may be treated as incompressible during the initial stages of the flow (when the surface perturbations are small), perhaps this is not the case when the liquid level rises. Consider a gas with a Mach number of 0.05 flowing through an area A. If the gas then flows through a constriction of $\frac{1}{10}$A the Mach number becomes 0.5 for an ideal gas with ratio of specific heats 1.4. So changes in the cross-section may give rise to Mach numbers for which compressibility is important. In the light of this the following analysis was performed.

2.2 Compressible Kelvin-Helmholtz theory

Consider a gas and liquid flowing co-currently between two horizontal planes as shown in Fig. 2.2:

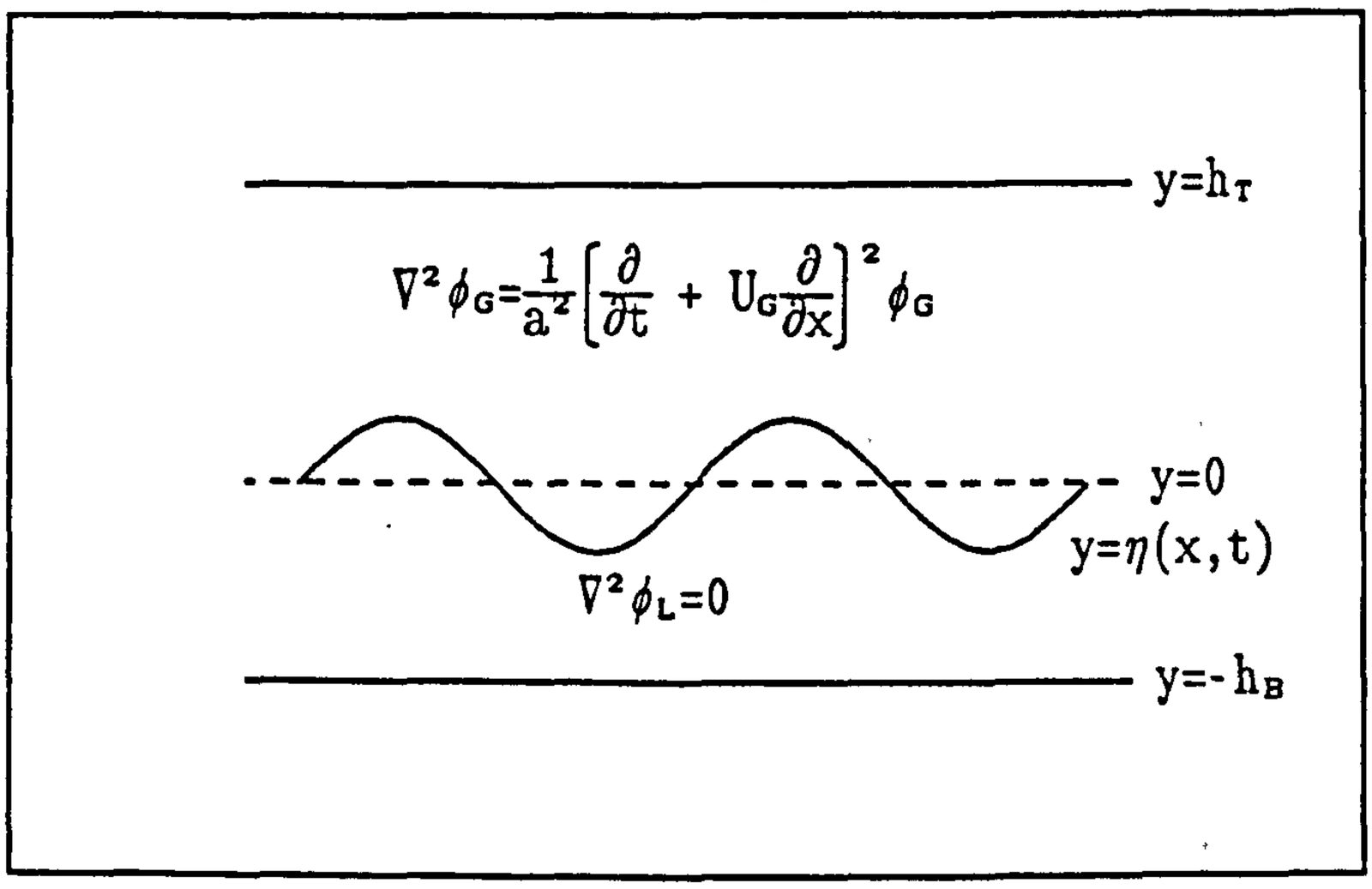

Fig. 2.2

and that the free stream gas and liquid velocities may be denoted U_G and U_L respectively. If we define the superficial velocity of phase i by:

$$U_{is} = \frac{Q_i}{\rho_i A}$$

then we may define the Froude number of that phase by:

$$Fr_i = \frac{U_{is}^2}{gH}$$

and the Reynolds number of phase i by:

$$Re_i = \frac{\rho_i H U_{is}}{\mu_i}$$

where H is the tube diameter or channel depth, and Q_i is the mass flux of phase i. For the flows under consideration we have the gas Mach

number, defined by $M_G = \frac{U_{GS}}{a}$ of the order 0.01. For an air-water flow in a 50 mm pipe the liquid Reynolds number is of the order $1x10^4$, and the gas Reynolds number is of the order $1x10^5$, so we treat the liquid and the gas as inviscid. The Froude numbers for the liquid and gas flow are of the order 0.1 and 20 respectively.

When Kelvin analysed what is now known as the Kelvin-Helmholtz instability, he assumed that the initial perturbation to the stratified flow was irrotational, Drazin & Reid (1985) p.16. Since the flow is considered to be inviscid, then the flow always remains irrotational (Kelvin circulation theorem). Drazin & Reid remind us that by assuming irrotationality we may prove instability but not stability. However, they go on to show that "rotational disturbances are no more unstable, and so Kelvin did find a necessary as well as sufficient condition for instability".

So, if we consider our initial state to be a perturbed irrotational stratified flow, then we have irrotational flow always. Thus, we may define velocity potentials, ϕ_G and ϕ_L for the gas and liquid respectively. To model the transition we make the following simplifying assumptions:

1. The density of the gas is constant in section

$$\rho_G = \rho_G(x,t) \qquad (2.2.1)$$

2. The interface has gentle slopes.

3. The liquid density is constant.

4. The gas is isentropic defined by

$$p_o = p_o(\rho_G) \quad , \quad \frac{dp_o}{d\rho_G} = a^2 \qquad (2.2.2)$$

where p_o is the pressure distribution along the top of the tube and a is the sound speed in the gas.

Further progress may be made by either assuming that the long wave limit is the important type of wave for initiating slug flow (i.e. that long waves are the most unstable), or that shorter wavelength waves are the most important, and that these are the most unstable. The former avenue considers linearisation with respect to the perturbation quantities of the shallow water wave equations for channel flow (Appendix A), to obtain the long wave stability criterion.

However, if we assume that the long wave limit is not the most important, from a stability point of view, and we look for a stability criterion for waves whose wave number, k, is not much less than unity, then we can always return to the long wave limit if that is desired.

It is doubtful that long waves are necessarily the most unstable. For the flow of stratified liquids they are not, and in most instances when the surface tension is zero the shortest waves are most unstable (see Drazin & Reid (1985) Chapter 6). Perhaps, also, long waves arise by some means other than an instability of the Kelvin-Helmholtz type; entry conditions for instance. So, to find a stability criterion we consider a velocity potential within the gas of the form:

$$\phi_G = G(y)e^{i(kx-\omega t)} \qquad (2.2.3)$$

where k is the wave number and ω the frequency. Then substituting this into the wave equation for a wave motion within a medium moving with velocity U_G (Whitham (1974) p.255):

$$\nabla^2\phi_G = \frac{1}{a^2}\left[\frac{\partial}{\partial t} + U_G\frac{\partial}{\partial x}\right]^2\phi_G \qquad (2.2.4)$$

where a is the sound speed in the gas, and solving the resulting

equation for the form of the function G(y) with boundary condition:

$$\hat{v}_G = \frac{\partial \phi_G}{\partial y} = 0 \quad . \qquad \text{on } y = h_T$$

gives: $$G(y) = A^* \cosh \kappa(y - h_T) \qquad (2.2.5)$$

where A^* is a constant and $\kappa^2 = k^2 - \frac{1}{a^2}(\omega - kU_G)^2 > 0$ for the disturbance wave speed c $(= \frac{\omega}{k})$ to be less than $a + U_G$.

When the kinematic boundary condition on $y = \eta(x,t)$

$$\frac{D\eta}{Dt} = v \qquad (2.2.6)$$

where D/Dt is the convective derivative, is linearised about $y = 0$ we get the following linearised kinematic boundary condition:

$$\frac{\partial \eta}{\partial t} = \frac{\partial \phi_G}{\partial y} - U_G \frac{\partial \eta}{\partial x} \qquad (2.2.7)$$

and similarly linearising the dynamic boundary condition gives:

$$\left[\frac{\partial}{\partial t} + U\frac{\partial}{\partial x}\right]\phi = -g\eta - \frac{p}{\rho} \qquad (2.2.8)$$

We consider the surface perturbation to be in phase with the velocity perturbation ($\eta^* \in \mathbb{R}$) (in analogy with Kordyban (1963) and others) and to have the following form:

$$\eta(x,t) = \eta^* \, e^{i(kx - \omega t)} \qquad (2.2.9)$$

then substituting (2.2.3) with G(y) as given in (2.2.5) and (2.2.9) into

(2.2.7) we obtain:

$$A^* = i(U_G - c)\frac{k\eta^*}{\kappa \sinh \kappa h_T}$$

and thus the disturbance velocity potential within the gas is:

$$\phi_G = -i(U_G - c)\frac{k \cosh \kappa(y - h_T)}{\kappa \sinh \kappa h_T}\eta^* e^{i(kx-\omega t)} \qquad (2.2.10)$$

A similar analysis for the incompressible liquid (subject to potential flow, $\nabla^2\phi_L = 0$) yields the liquid disturbance velocity potential to be:

$$\phi_L = i(U_L - c)\frac{\cosh k(y + h_B)}{\sinh \kappa h_B}\eta^* e^{i(kx-\omega t)} \qquad (2.2.11)$$

If surface tension is neglected, then we need to satisfy the condition that the pressure at the interface is continuous, so:

$$p_G - \rho_G g\eta^* e^{i(kx-\omega t)} = p_L - \rho_L g\eta^* e^{i(kx-\omega t)} \qquad (2.2.12)$$

on $y = 0$, where p_G is the pressure within the undisturbed gas, p_L that within the undisturbed liquid and g the acceleration due to gravity. The conservation of momentum within the gas may be written as:

$$\frac{\partial}{\partial t}(U_G + \hat{u}_G) + (U_G + \hat{u}_G)\frac{\partial}{\partial x}(U_G + \hat{u}_G) + \hat{v}_G\frac{\partial}{\partial y}(U_G + \hat{u}_G) = -\frac{1}{\rho_G}\frac{\partial p_G}{\partial x}$$

where we have written:

$$u_G = U_G + \hat{u}_G$$

$$u_L = U_L + \hat{u}_L$$

where $\hat{u}_i$ is the perturbation velocity, and U_i the free stream velocity of the phases (i = G or L). If this is linearised with respect to the

perturbation, neglecting terms that are second order in the small quantity and assuming that the free stream velocity is steady, then:

$$\frac{\partial \hat{u}_G}{\partial t} + U_G\frac{\partial \hat{u}_G}{\partial x} + \hat{v}_G\frac{\partial U_G}{\partial y} = -\frac{1}{\rho_G}\frac{\partial p_G}{\partial x}$$

If we also take the free stream velocity to be uniform in section, then:

$$\frac{\partial \hat{u}_G}{\partial t} + U_G\frac{\partial \hat{u}_G}{\partial x} = -\frac{1}{\rho_G}\frac{\partial p_G}{\partial x} \qquad (2.2.13)$$

We obtain a similar expression for the liquid. Substituting (2.2.10) into (2.2.13), and similarly (2.2.11), then:

$$i(U_G - c)^2 \frac{k^3 \cosh \kappa(y - h_T)}{\kappa \sinh \kappa h_T}\eta^* e^{i(kx-\omega t)} = -\frac{1}{\rho_G}\frac{\partial p_G}{\partial x} \qquad (2.2.14)$$

$$-i(U_L - c)^2 \frac{k^2 \cosh k(y + h_B)}{\sinh kh_B}\eta^* e^{i(kx-\omega t)} = -\frac{1}{\rho_L}\frac{\partial p_L}{\partial x} \qquad (2.2.15)$$

Differentiating (2.2.12) with respect to x (and remembering that the gas is compressible so that we may write $\frac{\partial \rho_G}{\partial x} = \frac{1}{a^2}\frac{\partial p_G}{\partial x}$) then:

$$\frac{\partial p_G}{\partial x}\left[1 - \frac{1}{a^2}g\eta^* e^{i(kx-\omega t)}\right] - \rho_G gik\eta^* e^{i(kx-\omega t)} = \frac{\partial p_L}{\partial x} - \rho_L gik\eta^* e^{i(kx-\omega t)} \qquad (2.2.16)$$

at y = 0. Then substituting (2.2.14) and (2.2.15) into (2.2.16) gives:

$$\left\{\rho_G(U_G - c)^2 \frac{k^2 \cosh \kappa(y - h_T)}{\kappa \sinh \kappa h_T}\left[1 - \frac{1}{a^2}g\eta^* e^{i(kx-\omega t)}\right] + \rho_G g\right\}\eta^* e^{i(kx-\omega t)}$$

$$= \left\{\rho_L g - \rho_L(U_L - c)^2 \frac{k \cosh k(y + h_B)}{\sinh kh_B}\right\}\eta^* e^{i(kx-\omega t)}$$

and evaluating this on y = 0 and neglecting the products of small quantities gives:

$$(U_L - c)^2 + \frac{\rho_G}{\rho_L}(U_G - c)^2 \frac{k \tanh kh_B}{\kappa \tanh \kappa h_T} = \left[1 - \frac{\rho_G}{\rho_L}\right] \frac{g}{k} \tanh kh_B \qquad (2.2.17)$$

Recall that $\kappa^2 = k^2 - \frac{1}{a^2}(\omega - kU_G)^2 = k^2\left[1 - \frac{(c - U_G)^2}{a^2}\right]$, then (2.2.17) becomes:

$$(U_L - c)^2 + \frac{\rho_G}{\rho_L}(U_G - c)^2 \frac{\tanh kh_B}{\sqrt{1 - \frac{(c-U_G)^2}{a^2}} \tanh\left[\sqrt{1 - \frac{(c-U_G)^2}{a^2}}\, kh_T\right]}$$

$$= \left[1 - \frac{\rho_G}{\rho_L}\right] \frac{g}{k} \tanh kh_B \qquad (2.2.18)$$

Considering the limit when k is small, but retaining $0(k^2)$ terms and above, then:

$$(U_L - c)^2 + \left[\frac{\rho_G}{\rho_L}(U_G - c)^2 \frac{1}{1 - \frac{(c-U_G)^2}{a^2}} \frac{h_B}{h_T} - \left[1 - \frac{\rho_G}{\rho_L}\right] gh_B\right] + \left[\left[1 - \frac{\rho_G}{\rho_L}\right] gh_B^3 + \frac{\rho_G}{\rho_L} \frac{(U_G - c)^2}{1 - \frac{(c-U_G)^2}{a^2}} \frac{h_B}{h_T}\left\{\left[1 - \frac{c^2}{a^2}\right] h_T^2 - h_B^2\right\}\right] \frac{k^2}{3} = 0 \qquad (2.2.19)$$

To simplify (2.2.19) we may consider the flow from a reference frame moving with the gas velocity U_G. Then we define a liquid velocity relative to the moving frame, U_{LG}, the velocity of the liquid relative to the gas. Equation (2.2.19) then becomes, after neglecting terms $0(k^2)$ and above:

$$(U_{LG} - c)^2 + \frac{\rho_G h_B}{\rho_L h_T} \frac{c^2}{1 - \frac{c^2}{a^2}} - \left[1 - \frac{\rho_G}{\rho_L}\right] gh_B = 0$$

or, more simply:

$$\left[1 - \frac{\rho_G}{\rho_L}\right] gh_B - (U_{LG} - c)^2 = fn(c) \qquad (2.2.20)$$

where fn(c) is the function of perturbation velocity. To see what effect compressibility has on the criterion for slug flow consider the situation shown in Figs. 2.3 and 2.4 . We can see that in general the above equation will have two roots (Fig. 2.3), $c=U_1$ and $c=U_2$. If $U_{LG} > \sqrt{(g'h_B)}$ where g′ is the reduced gravity

$$\left[1 - \frac{\rho_G}{\rho_L}\right]g$$

then perhaps there exists a critical value of fn(c) such that there is only one root of the above equation (Fig. 2.4). Now, as c increases fn(c) increases, and there are no real roots to the equation. The imaginary part of the complex roots causes an exponential growth.

Fig. 2.3

Diagrammatic representation of 2.2.20 showing two possible solutions

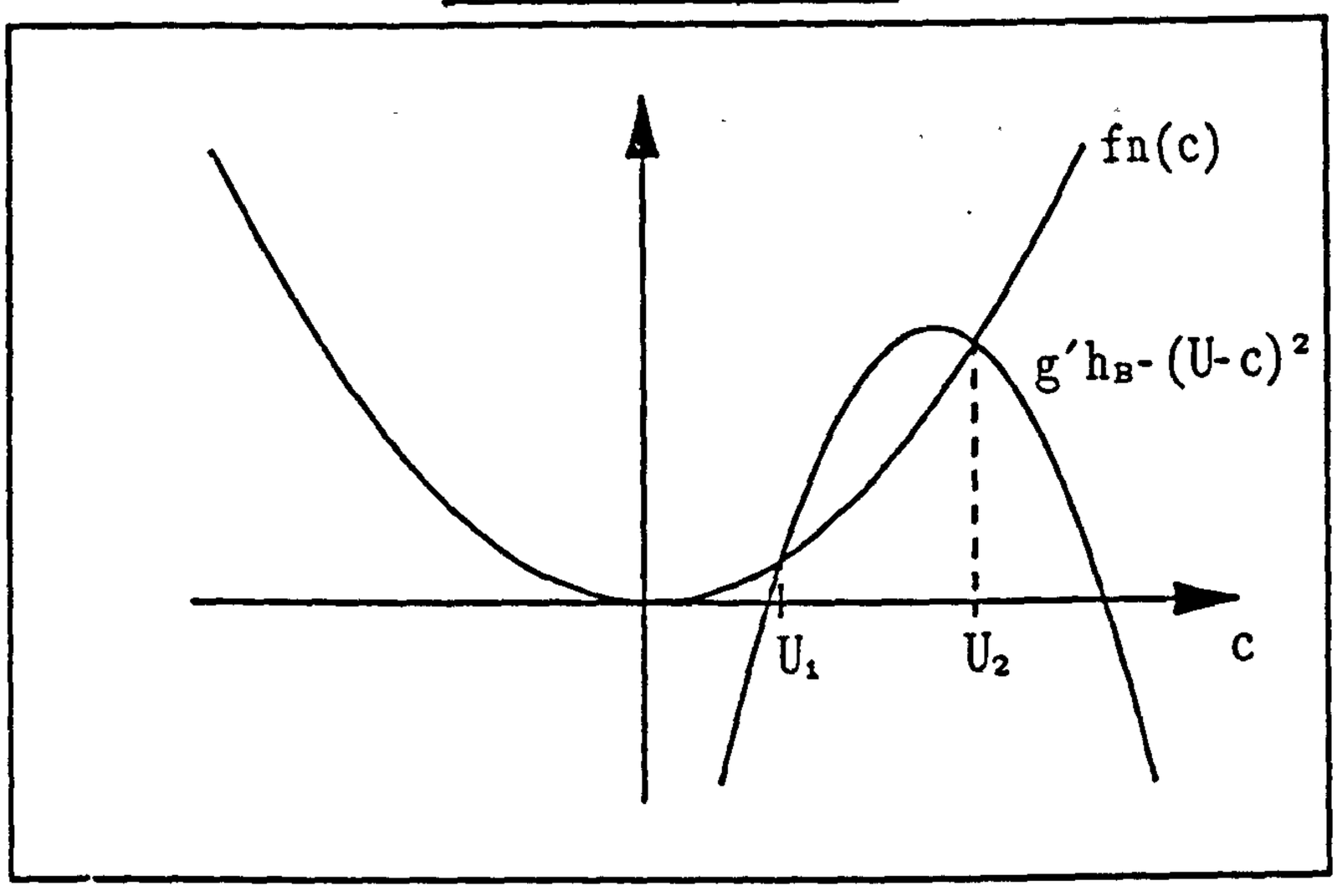

Fig. 2.4

Diagrammatic representation of 2.2.20 showing a possible critical solution

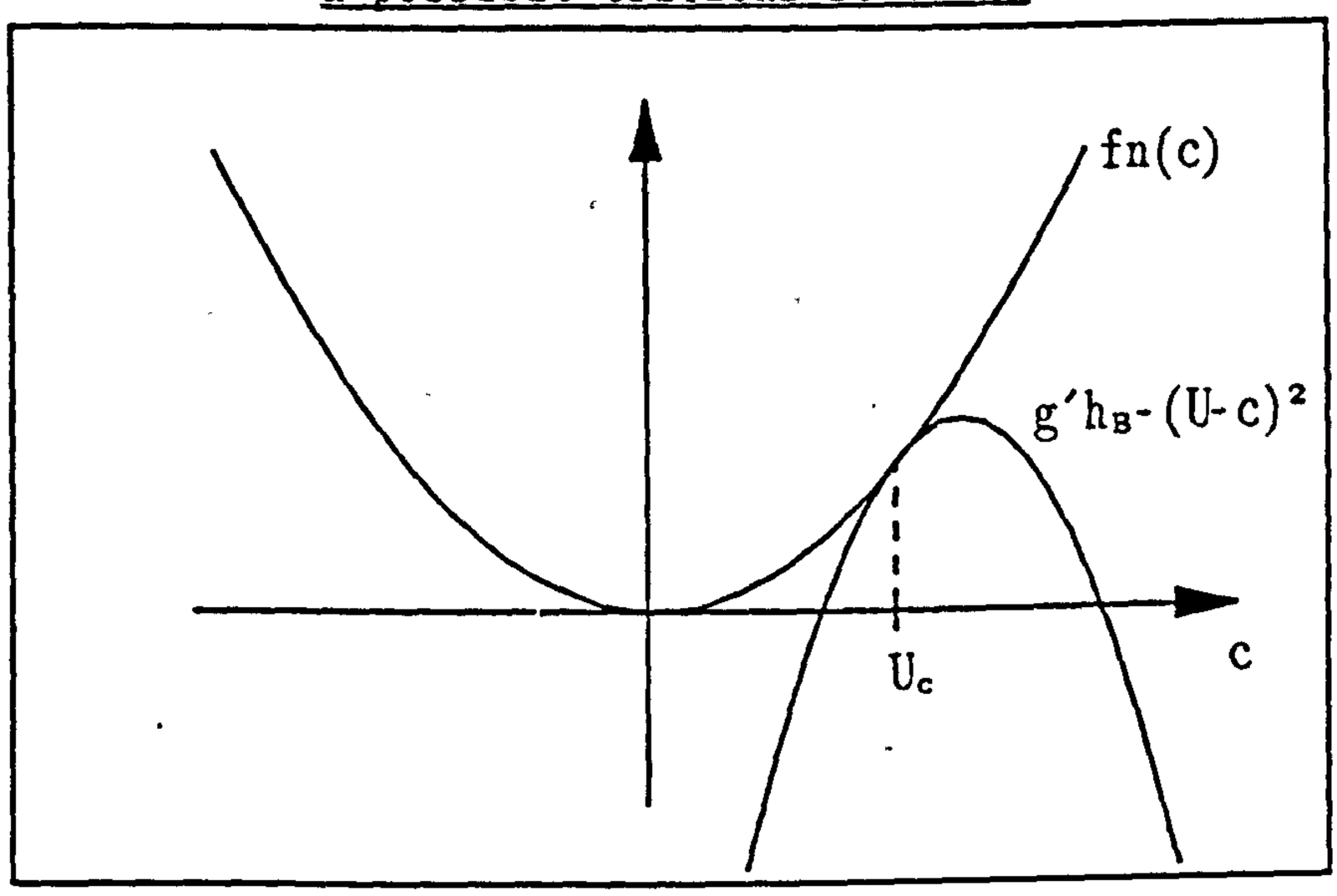

Whilst Figs. 2.3 and 2.4 show qualitatively the effects of compressibility, we seek a more quantitative solution to (2.2.19).

The instabilities will grow (exponentially) if the imaginary part of their wave speed is non-zero positive. We again formulate the expression in terms of the liquid velocity relative to the gas. For values of the Mach number less than unity, to determine whether the complex part is non-zero we look for the solutions of:

$$-\left[1 + \frac{\rho_G}{\rho_L}h_B h_T \frac{k^2}{3}\right]\frac{c^4}{a^2} + 2\left[U_G + U_L + 2\frac{\rho_G}{\rho_L}h_B h_T \frac{k^2}{3} U_G\right]\frac{c^3}{a^2}$$

$$+ \left[1 + \frac{\rho_G h_B}{\rho_L h_T} + \frac{g' h_B}{a^2} - \frac{U_G^2}{a^2} - 4\frac{U_L U_G}{a^2} - \frac{U_L^2}{a^2} - \right.$$

$$\left.\left\{\frac{\rho_G h_T}{\rho_L h_B}(h_B^2 - h_T^2) + \frac{g' h_B^3}{a^3} + 6\frac{\rho_G h_B}{\rho_L h_T}h_T^2\frac{U_G^2}{a^2}\right\}\frac{k^2}{3}\right]c^2$$

$$- \left[2U_L + 2\frac{\rho_G h_B}{\rho_L h_T}U_G + 2\frac{g' h_B}{a^2}U_G - 2\frac{U_G^2 U_L}{a^2} - 2\frac{U_L^2 U_G}{a^2} - \right.$$

$$\left.\left\{2\frac{\rho_G h_B}{\rho_L h_T}(h_B^2 - h_T^2)U_G + 2g' h_B^3\frac{U_G}{a^2} + 4\frac{\rho_G h_B}{\rho_L h_T}h_T^2\frac{U_G^3}{a^2}\right\}\frac{k^3}{3}\right]c$$

$$+ \left[U_L^2 + \frac{\rho_G h_B}{\rho_L h_T}U_G^2 + \frac{g' h_B}{a^2}U_G^2 - g' h_B - \frac{U_G^2 U_L^2}{a^2} - \right.$$

$$\left.\left\{\frac{\rho_G h_B}{\rho_L h_T}(h_B^2 - h_T^2)U_G^2 + g' h_B\frac{U_G^2}{a^2} - g' h_B^3 + \frac{\rho_G h_B}{\rho_L h_T}h_T^2\frac{U_G^4}{a^2}\right\}\frac{k^2}{3}\right] = 0 \quad (2.2.21)$$

If we consider a flow in which the Mach number of the unperturbed gas flow is low, and the perturbation wavelength is very long, then the above equation reduces to the classical Kelvin-Helmholtz form. For a gas-liquid flow in which the liquid density is much greater than the gas density, we obtain the classical criterion for slug flow:

$$U_{LG}^2 = (U_G - U_L)^2 \geq \left[\frac{\rho_L - \rho_G}{\rho_G}\right]g h_T \quad .$$

However, this is of no interest to us. The result was inevitable once the effect of compressibility of the gas, the Mach number, was removed. To say something about the effect of compressibility it is necessary to retain the Mach number in the equation. Equation (2.2.21)

is analytically unmanageable. So, we are forced to consider only very long waves such that terms in k^2 are negligible.

Consider a gas-liquid flow for which $\frac{\rho_G}{\rho_L} \ll 1$ and the gas Mach number, M_G, is in the range 0.01 to 0.1 with a liquid velocity $U_L \sim \frac{1}{10} U_G$. By using this and neglecting terms $O(k^2)$ in (2.2.21) may be reduced to a quadratic in c, the disturbance velocity. For unstable behaviour we require that there is a non-zero imaginary component in c, and so:

$$\left[\frac{\rho_G h_B}{\rho_L h_T}a^2 + g'h_B\right]U_G^4 + 2U_L\left[\frac{\rho_G h_B}{\rho_L h_T}a^2 + g'h_B - U_L^2\right]U_G^3 - a^2\left[\frac{\rho_G h_B}{\rho_L h_T}a^2 + 2g'h_B\right]U_G^2$$

$$+ 2a^2U_L\left[\frac{\rho_G h_B}{\rho_L h_T}a^2 + g'h_Ba^2 + U_L^2\right]U_G + \left[U_L^4 - \frac{\rho_G h_B}{\rho_L h_T}U_L^2a^2 - \left[1 + \frac{\rho_G h_B}{\rho_L h_T}\right]g'h_Ba^2\right.$$

$$\left. - g'h_BU_L^2 + g'^2h_B^2 - g'h_BU_L^2\right]a^2 \leq 0 \qquad (2.2.22)$$

Again, this is a rather complicated expression, and rather than try to push the analysis further, it is better to resort to computational means to study this stability criterion for various flows.

2.3 Results

Equation (2.2.21) may be solved numerically to give $(U_G - U_L)^2$ for the entire range of gas void fractions, $(1-\alpha)$. This can be done for all α $(= \frac{h_B}{H}$, where H is the distance between the parallel planes in the two dimensional case) provided the fluid densities and sound speed in the gas are specified.

Consider air-water flow with $\rho_G = 1.225$ kg m^{-3}, $\rho_L = 1000$ kg m^{-3} at a temperature of 15°C. The speed of sound in dry air is then 340.6 m s^{-1}. If the distance between the planes is 51.67 mm (2 inches) then we obtain Fig. 2.5 for the marginal stability curve. Also shown are the classical Kelvin-Helmholtz incompressible gas stability curve and the finite amplitude solution of Mishima & Ishii (1980) given in equation (2.1.7).

Fig. 2.5

Comparison of the classical Kelvin-Helmholtz stability criterion with compressible Kelvin-Helmholtz type and the Mishima & Ishii finite amplitude solution

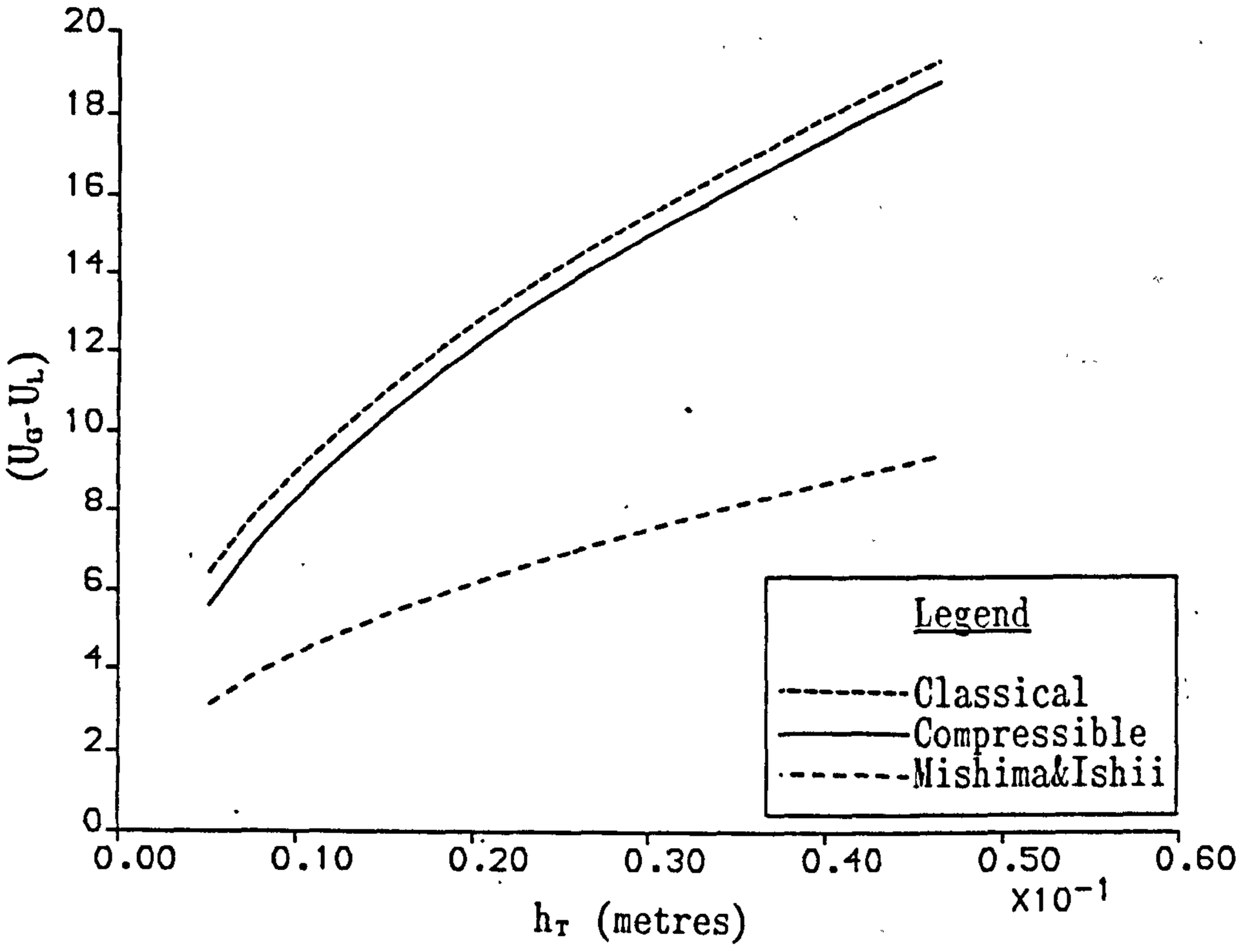

Fig. 2.6

Comparison of the compressible Kelvin-Helmholtz type stability criterion for dry air with a disperse fog

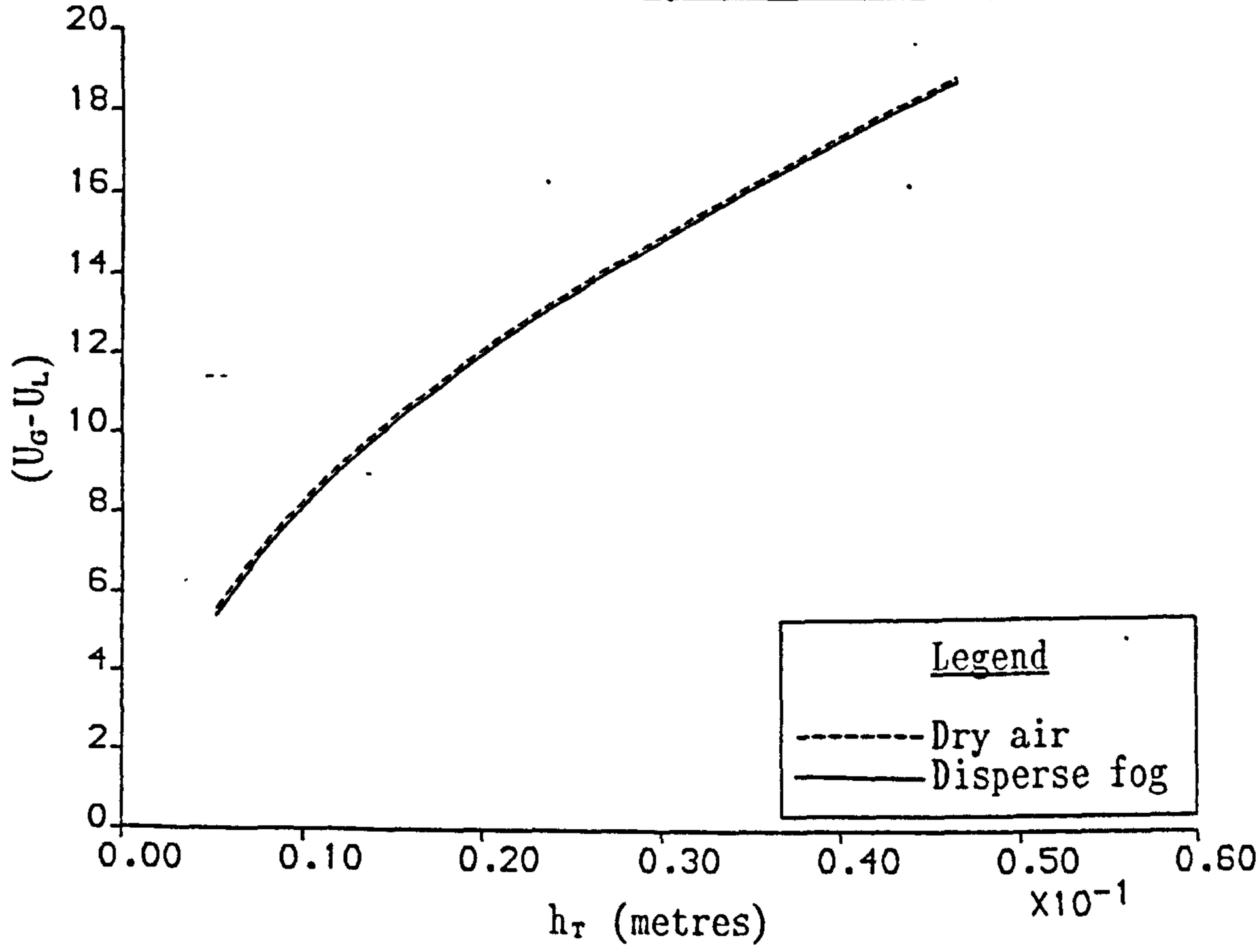

Clearly, the compressible flow solution is a considerably poorer predictor of the slug flow transition than the Mishima & Ishii solution (which agrees reasonably well with experiment). However, the object of this exercise was to see whether compressibility effects are of importance. Clearly, a small amplitude long wave approach cannot produce a criterion for the transition, as well as that produced by a finite amplitude approach. However, compressibility is seen to destabilise the flow predicted by the classical Kelvin-Helmholtz theory. The following is the approximate criterion for the air-water flow discussed:

$$(U_G - U_L) \geq 0.898\sqrt{\left[\frac{\rho_L - \rho_G}{\rho_G}\right] g h_T} \qquad (2.3.1)$$

This result has been calculated using the sound speed in dry air at 15°C. If instead we consider water vapour to be present within the air so that instead of dry air we have moist air, then Davidson (1975) and Wei & Wu (1981) point out that the sound speed is attenuated.

To study the effect of the attenuation of the speed of sound on the stability condition let us consider what would happen if the attenuated sound speed were 300 m s^{-1} (which is not unreasonable). Then Fig. 2.6 shows that there is a further destabilisation of the stability criterion, albeit only slightly.

2.4 Conclusion

Clearly, modelling the gaseous phase as a compressible fluid does not reconcile the difference between the small-amplitude long-wave theories and experiment. Indeed, including the compressibility effects does not produce a stability criterion as accurate as that obtained from a finite amplitude approach. Perhaps this is indicative that the shorter wavelength waves are more unstable than the long wavelength waves. But perhaps this was to be expected. However, by modelling the gas as compressible an interesting result has been obtained. It can be seen that the compressibility effects destabilise the small amplitude long wave linear theory. While this destabilisation is small (circa 10%) it shows that compressibility is influencing even the linear theory small amplitude waves.

This suggests that perhaps it could be interesting to include the effects of the compressibility of the gas when modelling the gas dynamics within two-phase flows.

Having arrived at this conclusion there were two possible avenues for further research.

One possibility was to incorporate the effect of a compressible gas in a finite amplitude model for predicting the onset of slug flow. This approach may improve the correlation with experimental observations, but provides no information about the surface profile of the growing slug, or the subsequent evolution of the large amplitude wave. This avenue of study was not pursued.

The second possibility was to concentrate on a sub-domain of the slug flow régime. In order to formulate a good model for a specific type of transition to slug flow, some experiments were performed to gain a deeper understanding of the transition. The experiments were to provide the basis for a theoretical model which would allow the surface profile and the evolution of the slug to be predicted. Hopefully, this model could then be extended to more complicated two-phase flows, such as steam-water flow, or perhaps even flows with fluids near to their thermodynamic critical point.

With this in mind, the following experimental work was conducted.

3. EXPERIMENTAL OBSERVATIONS OF HORIZONTAL TWO-PHASE FLOWS

3.1 Introduction

This study is concerned with co-current, horizontal two-phase flow in a pipe, and in particular with the initiation of slug flow.

This work is motivated by the thought that the effects of compressibility within the gaseous phase may be important, especially when the gap over the crest of the water wave is small. Indeed, some researchers have noticed that the proximity of the upper wall in two-phase flows is responsible for causing an earlier transition to slug flow than is predicted by many models. The following experimental work was performed to gain better qualitative understanding of the transition to slug flow within a particular sub-domain of the slug flow régime. As a prelude to this experimental work we first review previous work in this field.

In an attempt to understand the mechanism for the transition to slug flow, Dukler & Hubbard (1975) suggested the following model.

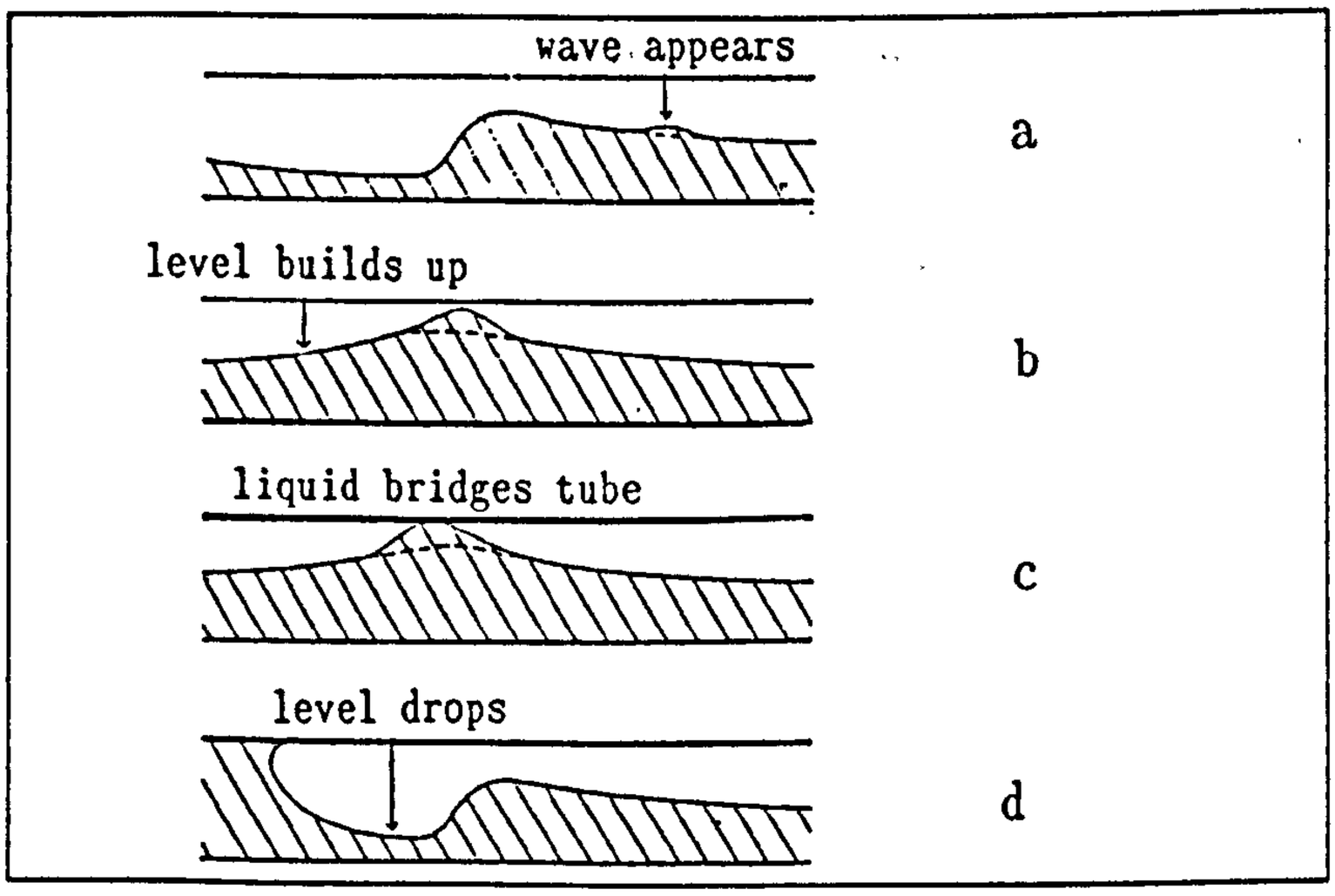

Figs. 3.1(a) to 3.1(d)

Briefly, they postulated, with reference to experiment, that after the gas and liquid enter the tube the liquid slows down (perhaps due to entry phenomena or wall friction), and as a result the level rises. Waves appear on the interface and travel along it (Fig. 3.1(a)). This results in further building up the level of liquid within the tube (Fig. 3.1(b)) until the liquid finally bridges the entire tube cross-section (Fig. 3.1(c)). Liquid at the bridge is then swept down the tube at the gas velocity, scooping up liquid in front and shedding liquid at the rear until the slug length stabilizes (Fig. 3.1(d)). The liquid level to the rear of the fast moving slug is now low, and the process is repeated.

Note, that whilst they suggest a model for the transition to slug flow the domain of validity for which this model holds is unclear from their 1975 paper.

Dukler & Hubbard (1975) performed experiments using ciné film and photography in order to obtain a qualitative understanding for the mode of transition to slug flow in a 1.5 inch diameter 65 feet long tube. As a result they suggest the formation of a "mixing vortex" at the front of the slug which causes gas to become entrained within the liquid region, until ultimately the gas aerates the bridge completely, and the slug can no longer be thought of as bridging the entire tube cross-section.

For the purposes of any theoretical modelling, this aeration phenomenon is generally ignored. If we just consider the slug flow régime for a moment, with reference to the Baker flow régime map as modified by Bell et al. (1970) (Fig. 3.2), or with reference to the Mandhane et al. (1974) map (Fig. 3.3)

Baker flow régime map as modified by Bell et al. (1970)

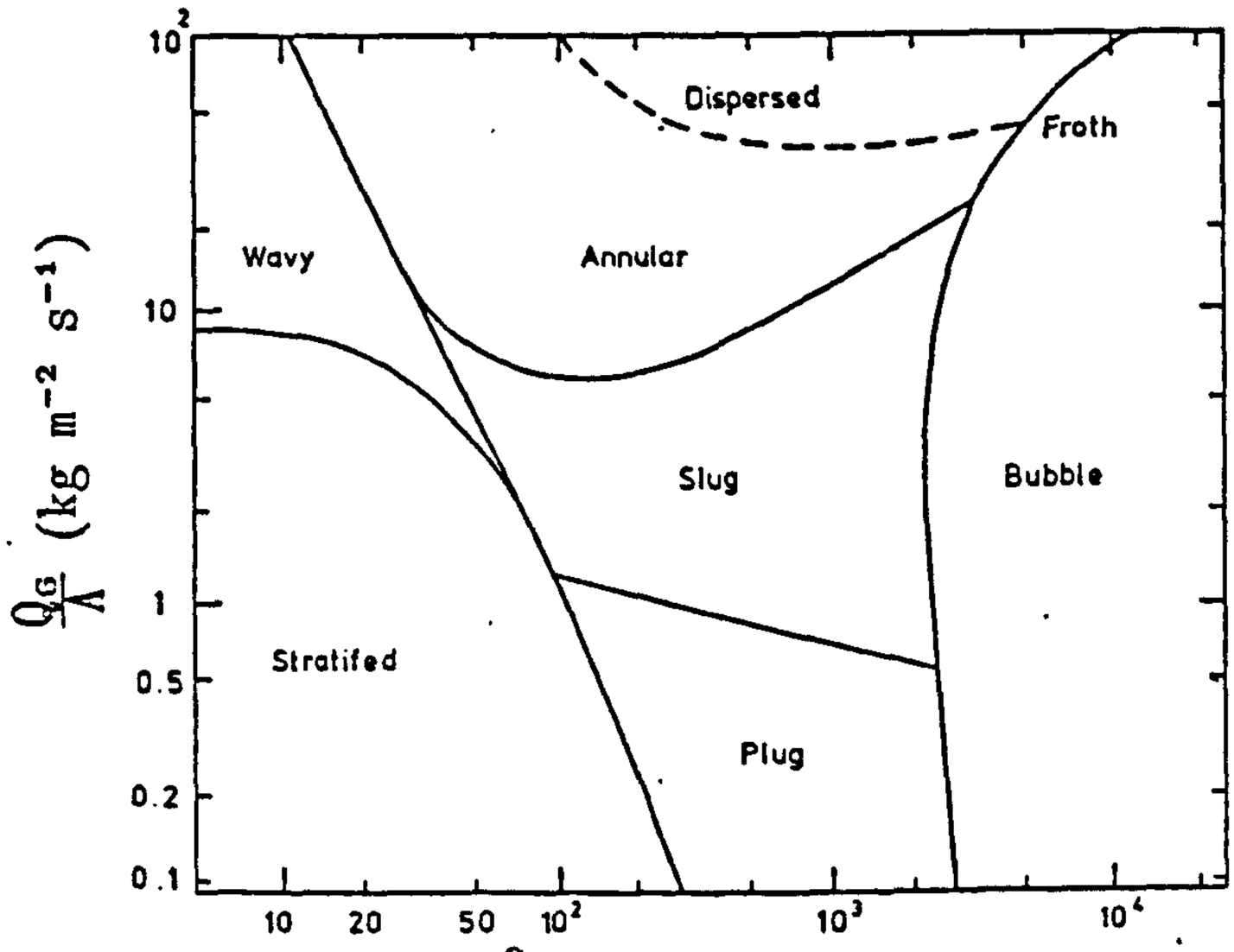

Fig. 3.2

where the Q_i (i=G or L) are the mass fluxes of the respective phases, and A is the cross-sectional area of the tube.

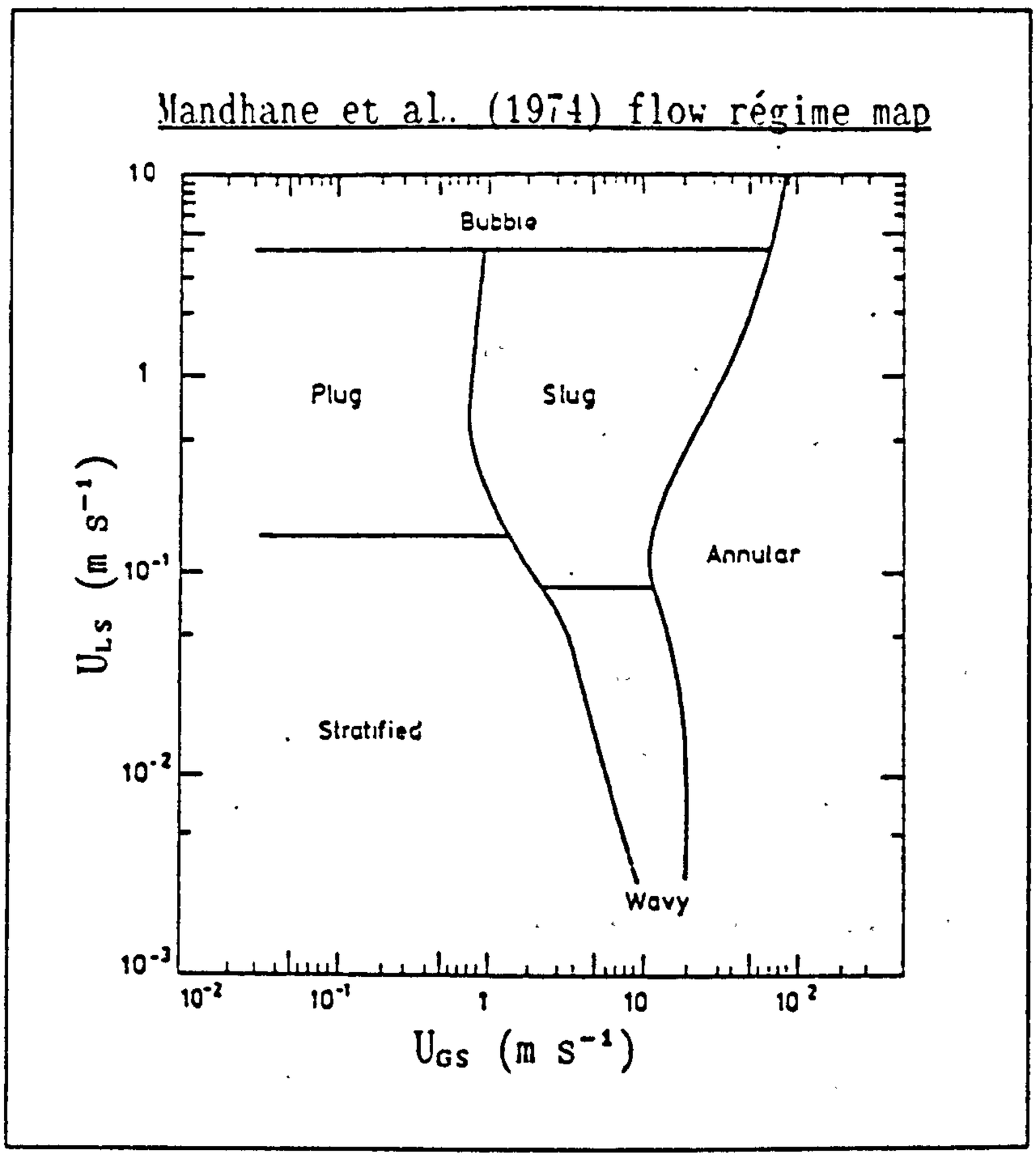

Fig. 3.3

In Fig. 3.3 the U_{is} are the superficial velocities of the phases defined by:

$$U_{is} = \frac{Q_i}{\rho_i A}$$

It would seem reasonable to assume that the nature of the slug flow differs qualitatively depending on whether we are near the bubble flow régime, or are near the stratified flow régime.

Therefore, it seems counter-intuitive to assume that a model as simple as that suggested by Dukler & Hubbard (1975) can be valid within the entire slug flow régime. Nevertheless, other researchers still use the bridging of the pipe phenomenon as their criterion for slug flow to occur. Taitel & Dukler (1977) use this criterion when theoretically modelling the slug frequency. Whilst this mode of transition undoubtedly exists (Markovich (1983a & 1983b)) great care should be

taken to ensure that it is used within the correct subset of flow parameters within the slug flow régime, and not generally, as is the wont of some researchers.

Other models have been suggested for slug flow, such as that of Wallis & Dobson (1973) who clearly describe the two (main) modes of slug flow; the first adopted by Dukler & Hubbard (1975), and the second, a more intermittent "blocking" in which liquid contact with the tube roof is not maintained continuously. They mention the similarities of the former mode with plug flow (see Fig. 1.2b). The experimental work of Wallis & Dobson (1973) is of exceptional quality since they actually report what they see, as opposed to what they think they see (Wallis & Dobson (1973) §6.2 & §6.3). However, when they suggest a theoretical model for the slug flow, they again consider the bridging case with, as suggested by Kordyban (1961), the slug "skating" over the underlying liquid in the form of an "inverse" Benjamin bubble (see Benjamin (1968)). Their theory gives reasonable agreement with experiments for the type of slug flow that the model is valid for.

Other researchers have employed different methods by which they model slug flow, for instance as loss-less waves for which the transition to slug flow is based on a minimum wave energy transfer hypothesis (Gardner (1978)).

Also, the effect on the system of changes in geometry have been investigated by Harrison (1975), Yu (1973), Lin & Hanratty (1987) and Taitel & Dukler (1987) to name but a few.

3.2 Experimental arrangement

In order to gain better understanding of the qualitative nature of co-current gas-liquid flow within a certain parameter domain, some experimental work was performed. It was hoped that this work would provide some experimental data for the interfacial growth rate, surface slopes and entrainment for this type of horizontal two-phase air-water flow.

These experiments were conducted at the Central Electricity Generating Board's research station, the Central Electricity Research Laboratories, hereafter CERL, where there are extensive two-phase flow facilities. A part of these facilities is a two-phase flow rig (Fig. 3.4 - next page) and the experimental work described here was performed on that rig. During the construction of the rig the position of vertical risers, the lengths of the test sections and how horizontal they are, the exits of the test sections to the two-phase separator and how these affect two-phase flows within the test sections were all considered with reference to experimental recommendations by other experimenters.

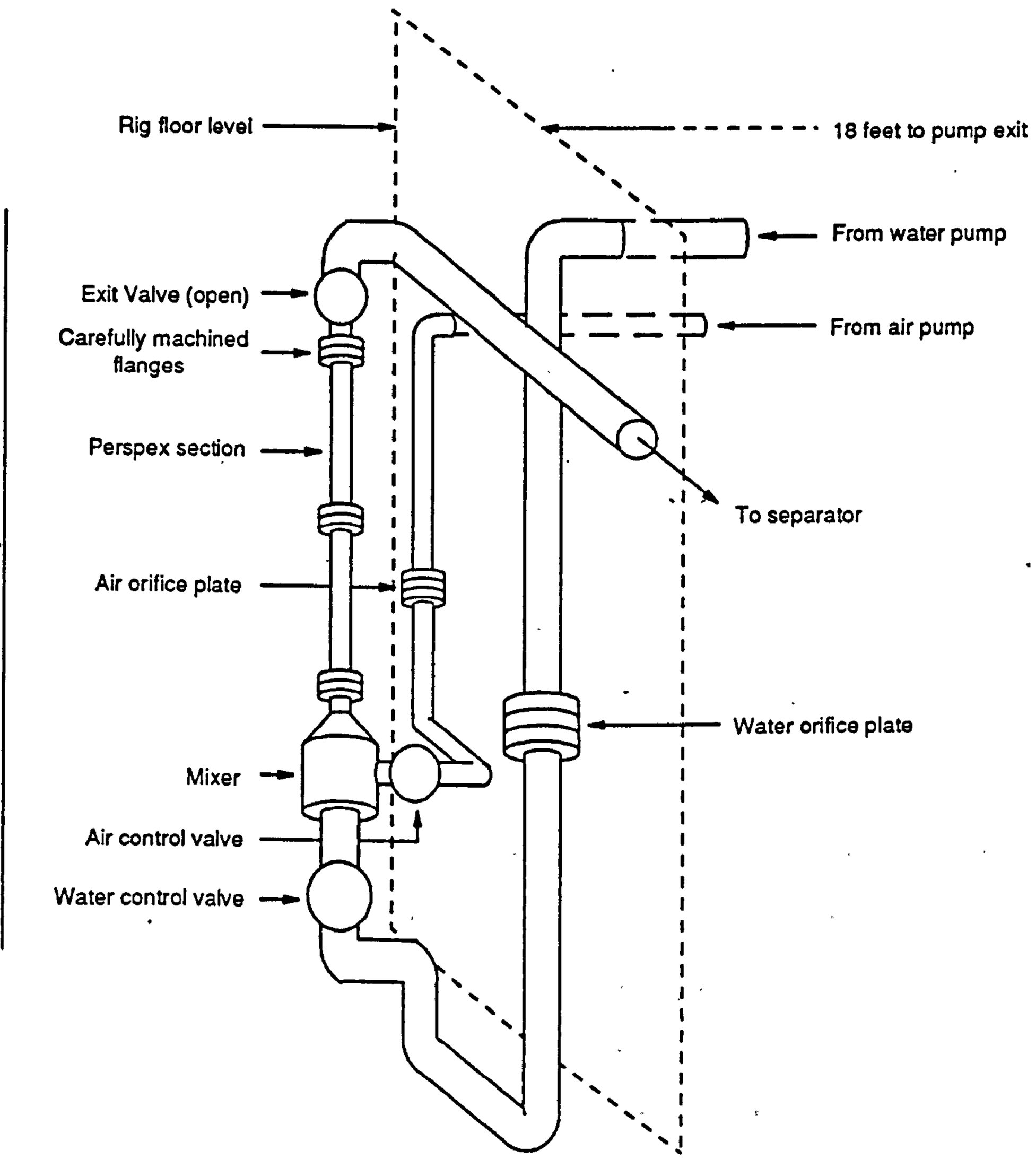

Fig. 3.4 Schematic of Test Section 6 of the two-phase flow rig facility at the Central Electricity Research Laboratories

The experimental facility of Section 6 consists of a 51.67 mm internal diameter circular cross-section horizontal perspex pipe, in two sections, of total length 4.03 m. (i.e. 78 diameters long) from the exit of the mixer to the exit pipe to the separator. The connections between pipes, and pipe and mixer, were machined so that there were no irregularities for the fluids to encounter. The mixer was of the perforated pot type (Fig. 3.5, schematic).

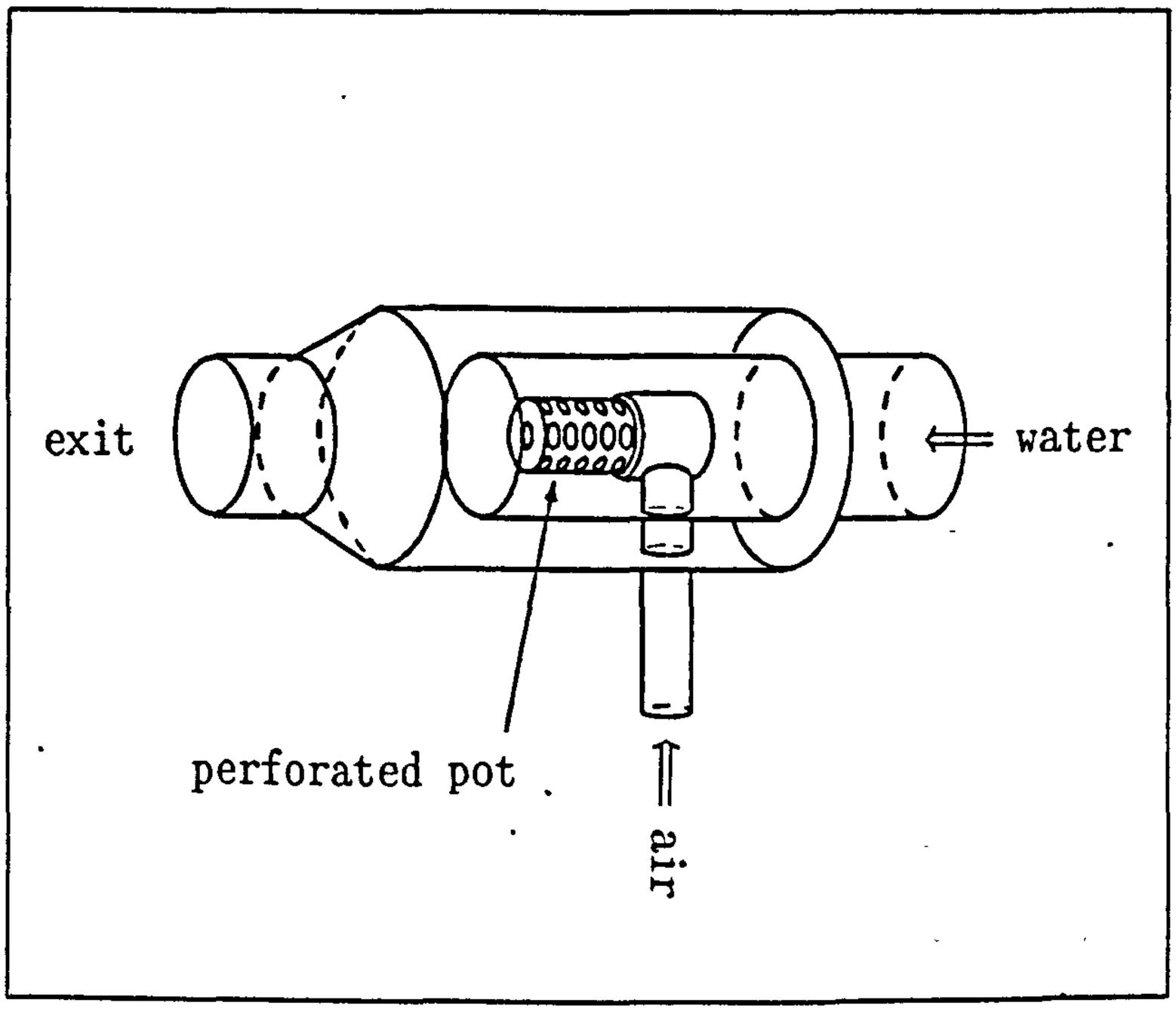

Fig. 3.5

This type of mixer was recommended by the CEGB technicians as the best to use for the flow régime under consideration because the design of the perforated pot minimised "blow-back" of the impelling water. Another advantage of this mixer was that the air and water were thought to be well mixed within it, so possible biases in the flow due to conditions upstream of the mixer are thought to be minimised. However, an extensive study of the flow within the mixer., and comparisons with other types of mixer was not performed. Extensive checks were made to verify that the flow rates of air and water through the mixer were as predicted from orifice plate measurements.

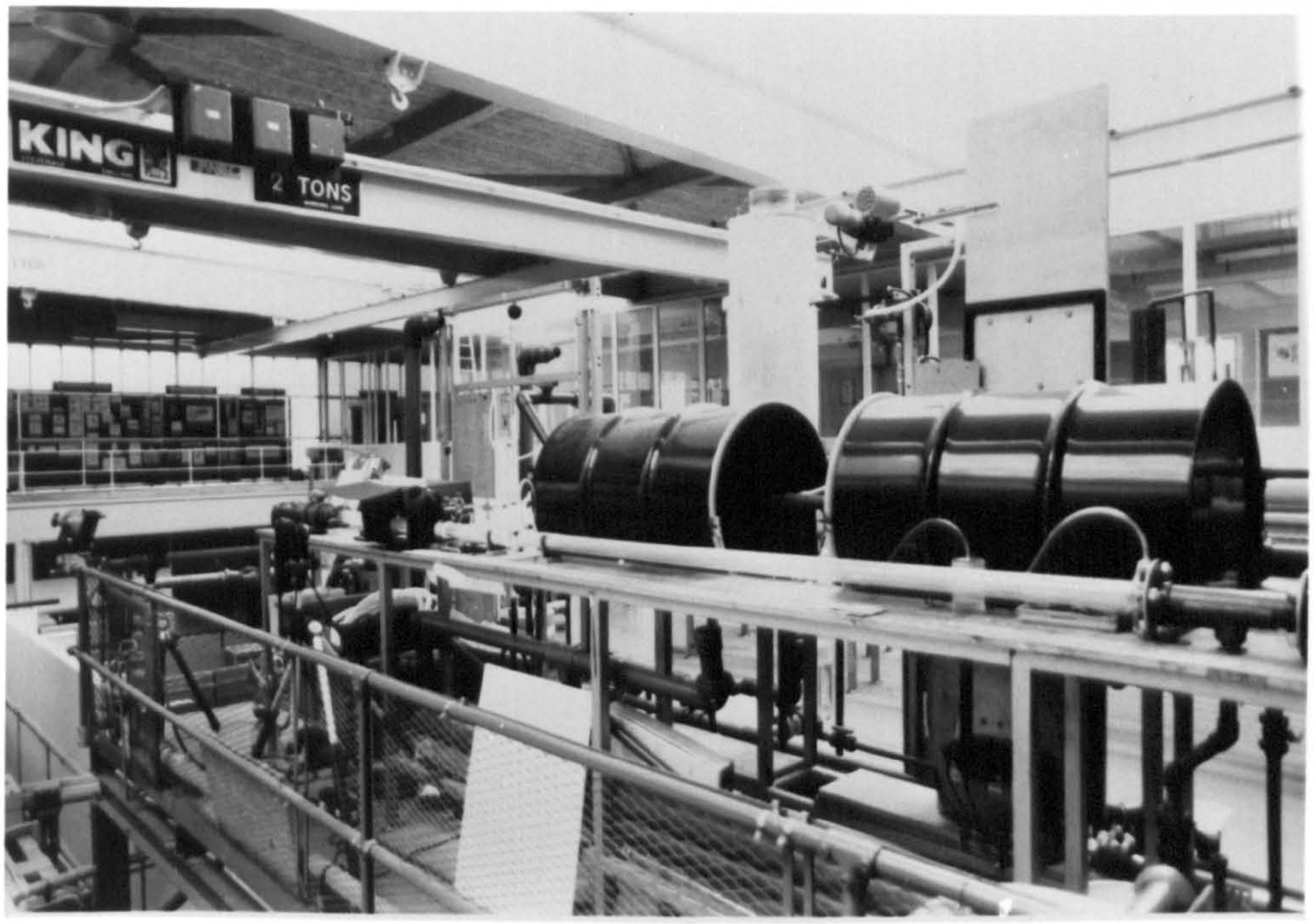

The above plate shows the perspex section of the two phase rig facility at CERL in the foreground of the photograph. The mixer is located off to the right. Towards the left the tripod mounted Nikon F301 can be seen in front of the hide surrounding the tube and the front silvered mirror. This hide was necessary to eliminate reflections from the sky-light and from the strip lighting. To the far left the inclined manometer can just be seen. The flash gun(s) are located behind the hide. All of the other equipment in the photograph was used on other sections of the test facility.

The experimental work was in three parts, all of which were photographic. The field of view for all this work was centred 2.7 m. downstream of the mixer outlet, and the flow of both gas and liquid is from right to left in the photographs and diagrams.

Mass fluxes for the liquid (water) before entry to the mixer were obtained by measuring the pressure differential indicated by a Flutic® (specific gravity 15.8) manometer across a calibrated orifice plate and

then the expression:

$$Q_L = k_L \sqrt{\frac{\Delta h_{Fluitic}}{15.8}} \quad . \qquad (3.2.1)$$

is used to calculate the liquid mass flux Q_L, and where k_L is the orifice plate constant, either 0.1617 or 0.0538 depending on the plate used.

Similarly, gas (air) mass fluxes before entry to the mixer were calculated using the pressure difference given by a water manometer across a calibrated orifice plate and the expression:

$$Q_G = k_G \sqrt{\frac{273.15\ P\ \Delta h_{water}}{14.7(T + 273.15)}} \qquad (3.2.2)$$

is used to calculate the gas mass flux Q_G, and again k_G is the gas orifice plate constant of either 0.02861 or 0.001529 depending on the plate used, and where P and T are the gas pressure and temperature given by a pressure transducer and a thermocouple prior to crossing the orifice plate. In both cases the Δh refers to the difference in the levels of the relevant liquid in the vertical limbs of the manometers.

3.3 Photographic

Initially various flows were photographed using a Nikon FM still camera with a 50 mm. f1.4 lens. This was later changed to a 105 mm f4 lens, with the camera placed further from the tube. This change permitted the insertion of a front silvered mirror at 45° to the horizontal above the tube lying along the axis of the tube (Fig. 3.6) to obtain a top view of the flows.

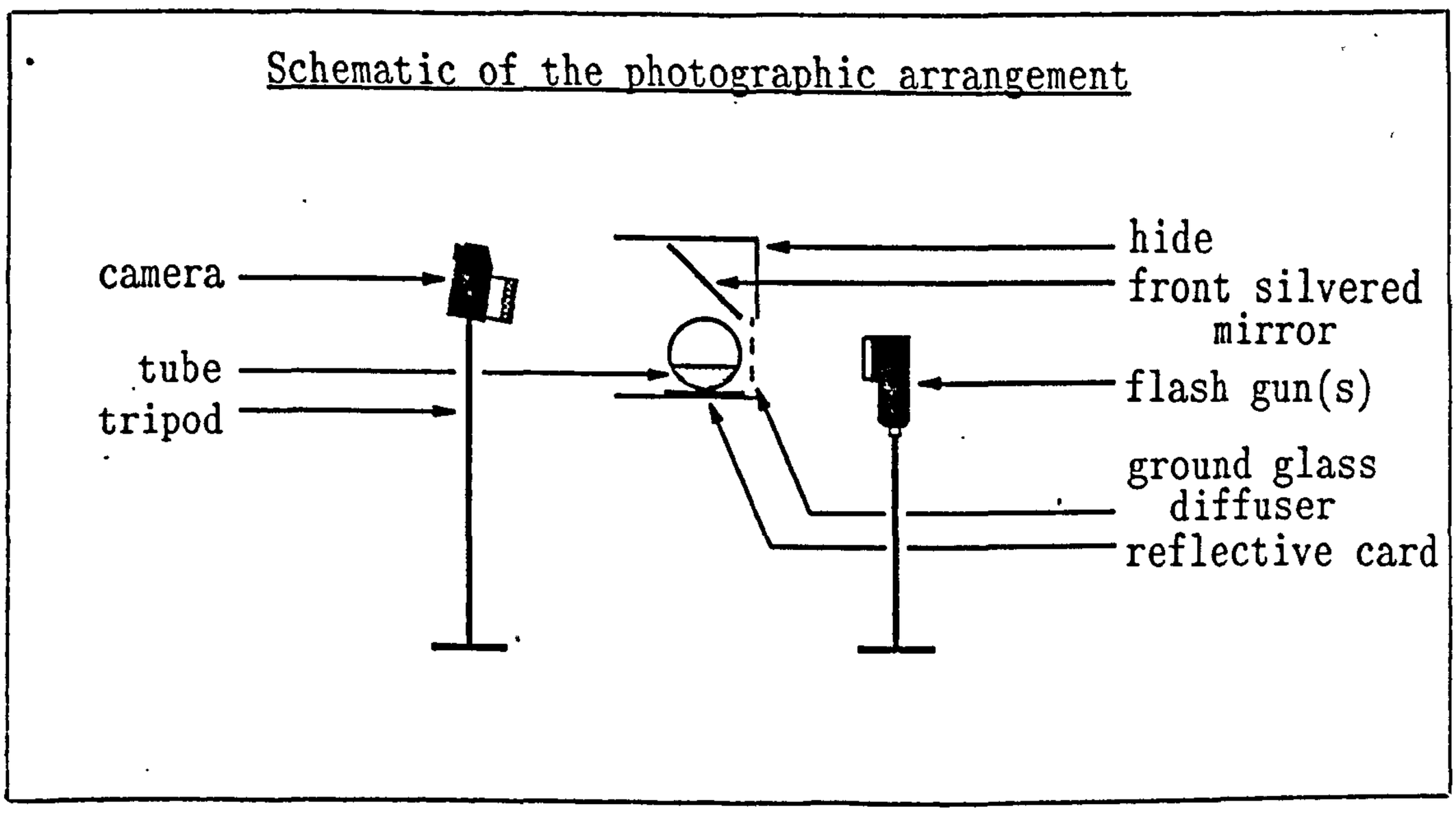

Fig. 3.6

This arrangement, although potentially informative, posed the problem that neither image, side nor top, could be kept simultaneously in focus as the depth of field of the lens was not sufficient at the speed and aperture that the flow and lighting dictated. Illumination for the still photography was by means of a mercury vapour flash discharge tube, with an intervening diffuser, synchronized to the camera shutter speed of 1/250 s. Despite the inability to focus both images really sharply, the final result was more than adequate in that one or other image was only just out of focus.

The photographic studies concentrated on the slug flow régime and the initial growth of a slug with little or no attempt to photograph other flow transitions, and we concentrate on the stages of the growth.

Since the nature of the flow resulted in many fully developed slugs propagating down the tube, and it was not desired to photograph all of these, the camera was triggered manually ensuring that slugs in various stages of development were observed. This was not an easy task, and the mass fluxes of the air and water had to be adjusted (initially) by trial and error in order that the slugs could be produced predictably, and with reasonable frequency, within the limited field of view of the camera. Once the appropriate range of mass fluxes had been determined it was only necessary to change the gas and liquid fluxes by small amounts so that all the stages of the transition to slug flow could be photographed.

3.4 Fast ciné photography

In order to obtain more information about growth rates, speed, entrainment etc. of individual slugs a fast ciné camera, Milliken model DBM 5AM 11 mm., working at 250 frames per second (accurate to one frame in 250), with film for up to 16 seconds was used. It filmed action within the same field of view as that of the still camera. Illumination for the fast ciné was by means of eight 1kW halogen lamps via a ground glass diffuser.

Despite this amount of light, however, the reflected image on the front silvered mirror was never sufficiently illuminated to be recorded. A further problem was the heat generated by the lamps. The heat close to the perspex tubing was sufficient to cause the perspex to sag! As a result of this, the lamps could only ever be used briefly during the duration of the filming.

It was not desired that the large number of fully formed slugs should always be filmed, so triggering was again done manually. To capture as many waves as possible growing within the camera's field of view, and because once fired the camera had to use the entire reel of film, the mass flux parameter space was slightly altered from that used for the still photography.

As with the still photographs no attempt was made to investigate any other flow transitions.

3.5 Twin-flash photographs

Finally, because of the wasteful nature of the fast ciné (sometimes no slugs were filmed within the 16 seconds of flow) a technique was developed by the author which would enable some data about growth rates and droplet and interface movement to be obtained from high quality still photographs.

In order to obtain such information a Nikon F301 camera with 50 mm f1.8 lens was mounted in the previous position. The author designed and made some TTL circuitry (Appendix D) which from one input signal could fire the camera with a shutter speed of 1/250 s. and two Metablitz flash guns; one synchronized with the shutter opening and the other to fire at some adjustable time later whilst the camera shutter is still open. In this way, and by using colour filters on the flash guns, two coloured images of the same slug at different measurable times could be recorded on the same still photograph. Subsequent analysis of the colour photographs by viewing through suitable filters and under suitable illumination allowed measurements to be taken from these cheaper still photographs.

Although much information concerning velocities, growth rates of the disturbance and droplet movement were potentially available from such experiments it would have been helpful to have obtained some measurements of the pressure within the gas due to the motion of the slug. Unfortunately, CERL could provide no fast pressure transducers and it was decided, after a trial, that an inclined water manometer, which was the only available equipment, could yield no useful results.

The three distinct methods of obtaining data the results are presented in three sections. All of these results pertain to data from within the intersection of the parameter spaces indicated on the Baker flow régime map as modified by Bell et al. (1970) (Fig. 3.7) or on the Mandhane et al. (1974) flow map (Fig. 3.8).

Baker flow régime map as modified by Bell et al. (1970) showing the regions of experimental work

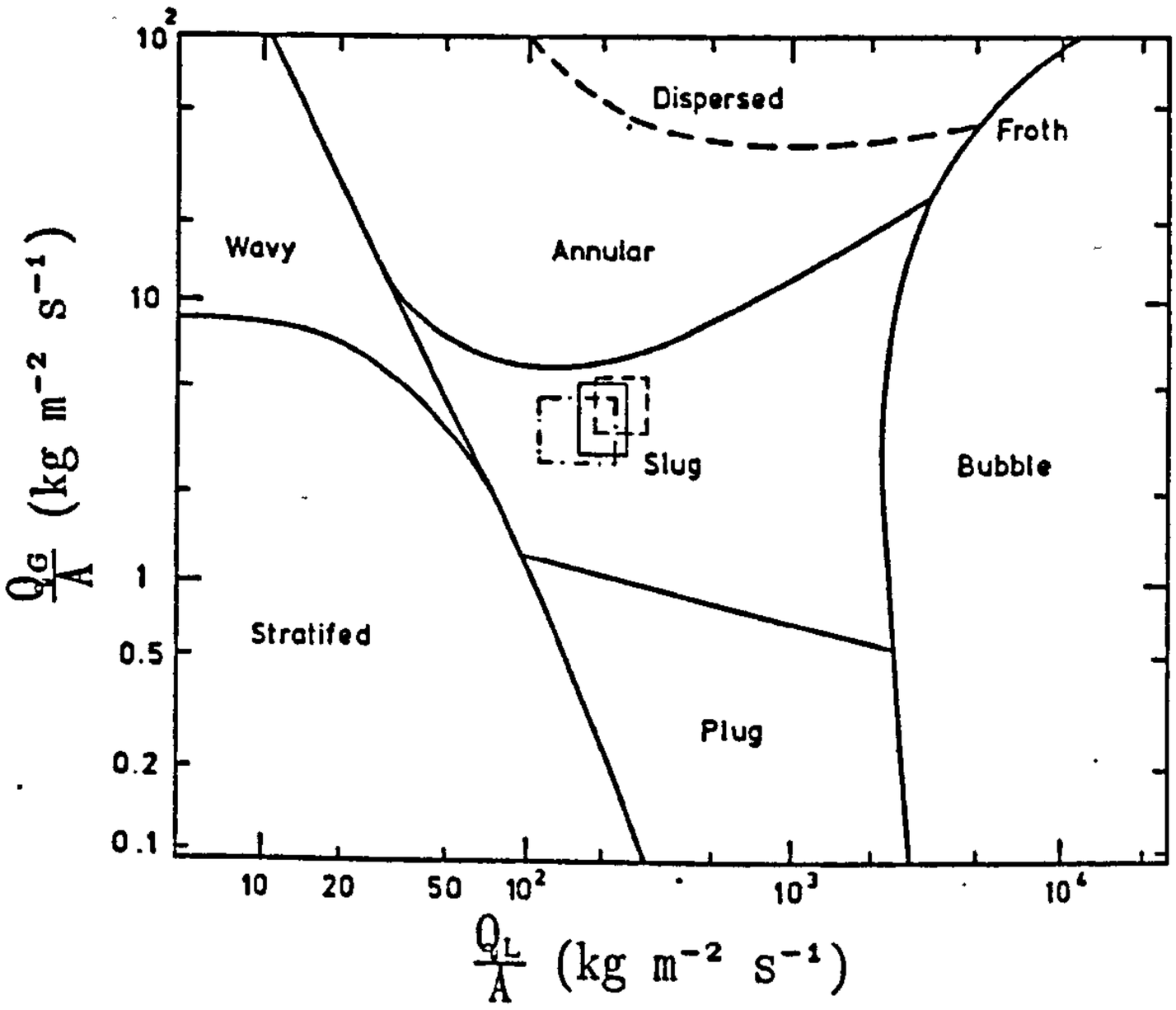

Fig. 3.7

Legend

——— B&W still
–·–·– Colour still
– – – – Fast ciné

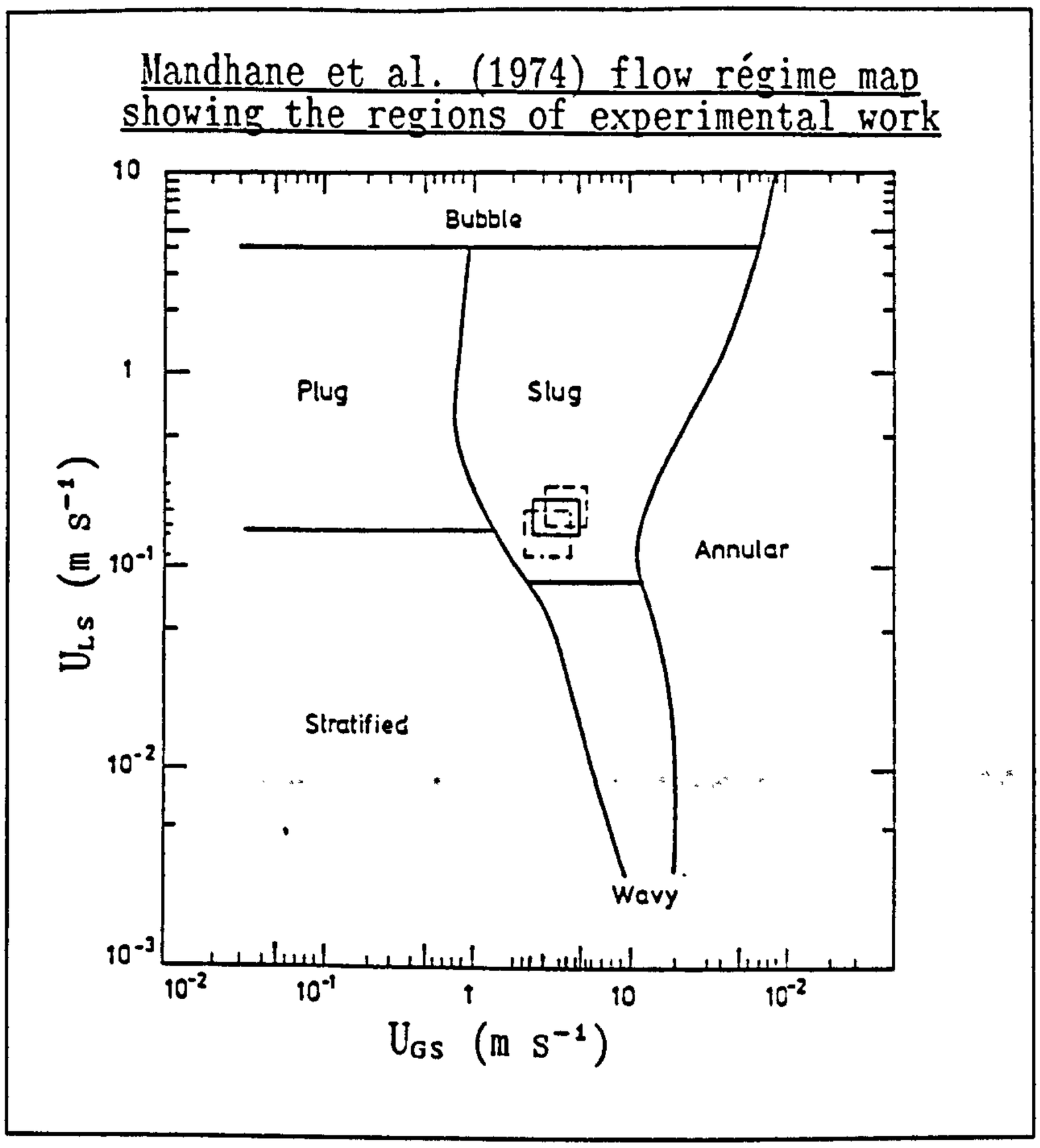
Mandhane et al. (1974) flow régime map
showing the regions of experimental work
10
1
10^{-1}
10^{-2}
10^{-3}
Bubble
Plug
Slug
Annular
Stratified
Wavy
U_{LS} (m S^{-1})
10^{-2}
10^{-1}
1
10
10^{-2}
U_{GS} (m S^{-1})

Fig. 3.8

3.6 Results from still photography

The following photographs (the data concerning these can be found in Appendix B) were obtained in the first part of the study. The order of the following plates is intended to show the stages in the evolution of a slug, from a small wave to a fully formed slug. Naturally, therefore, there is some subjectivity in the choice and order of the plates. However, after studying a great number of plates, and with the benefit of the fast ciné it is hoped that the subjectivity has been minimised.

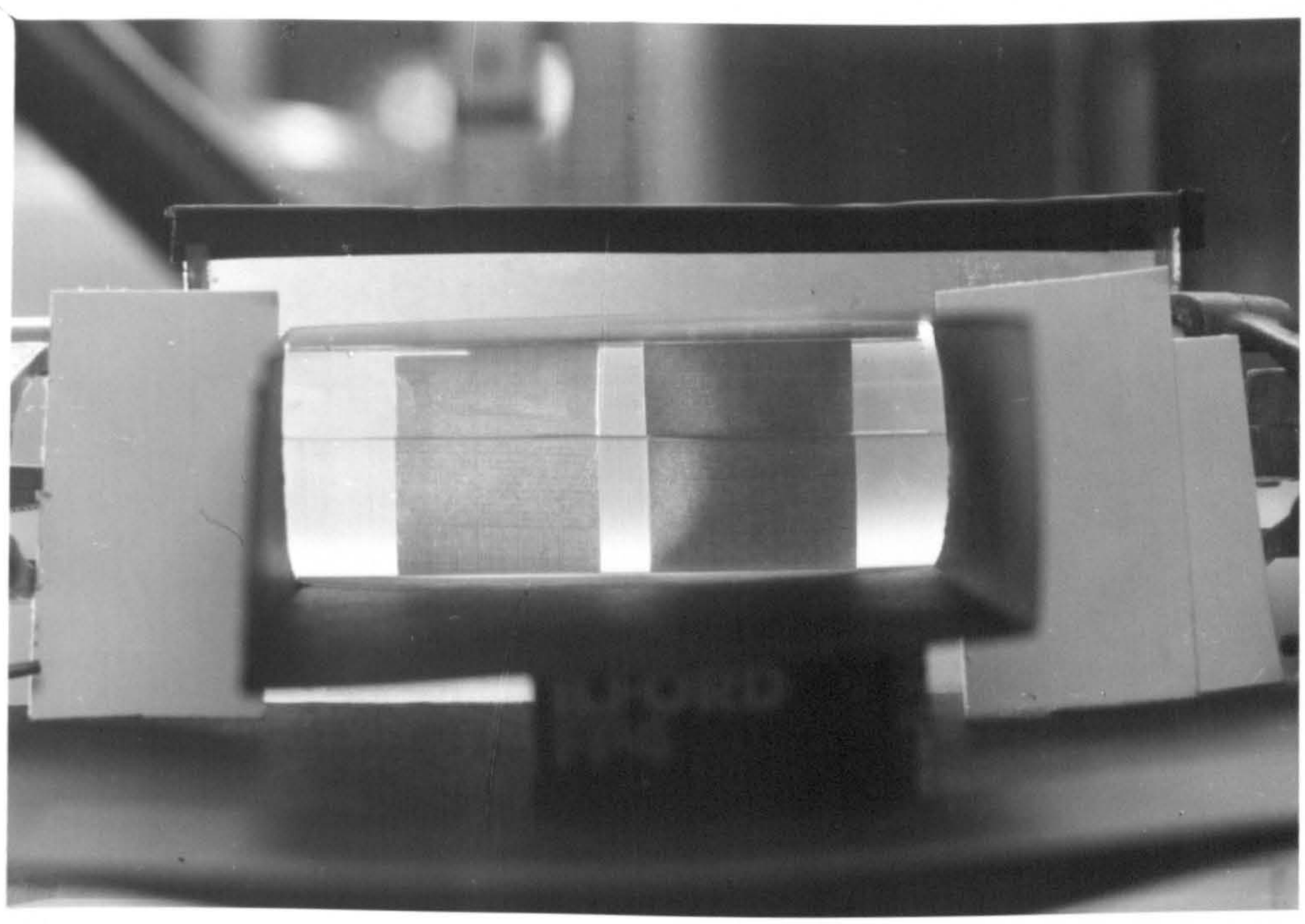

Plate 1

Since the perspex pipe was of circular cross-section, there may be some concern that the photography produced distorted images. The distortion should be least near the centre of the tube, and greatest near the top and bottom of the tube This was investigated in Appendix B and shown on plate 1. By looking at the graph paper within the tube, semi-covered with water, the right piece across the diameter, the left around the rear semi-circumference, we can see little distortion of the small squares on the graph paper. It must be pointed out, however, that

this photograph is taken with front lighting, while the remainder are illuminated from the rear. This should not affect the observed distortion.

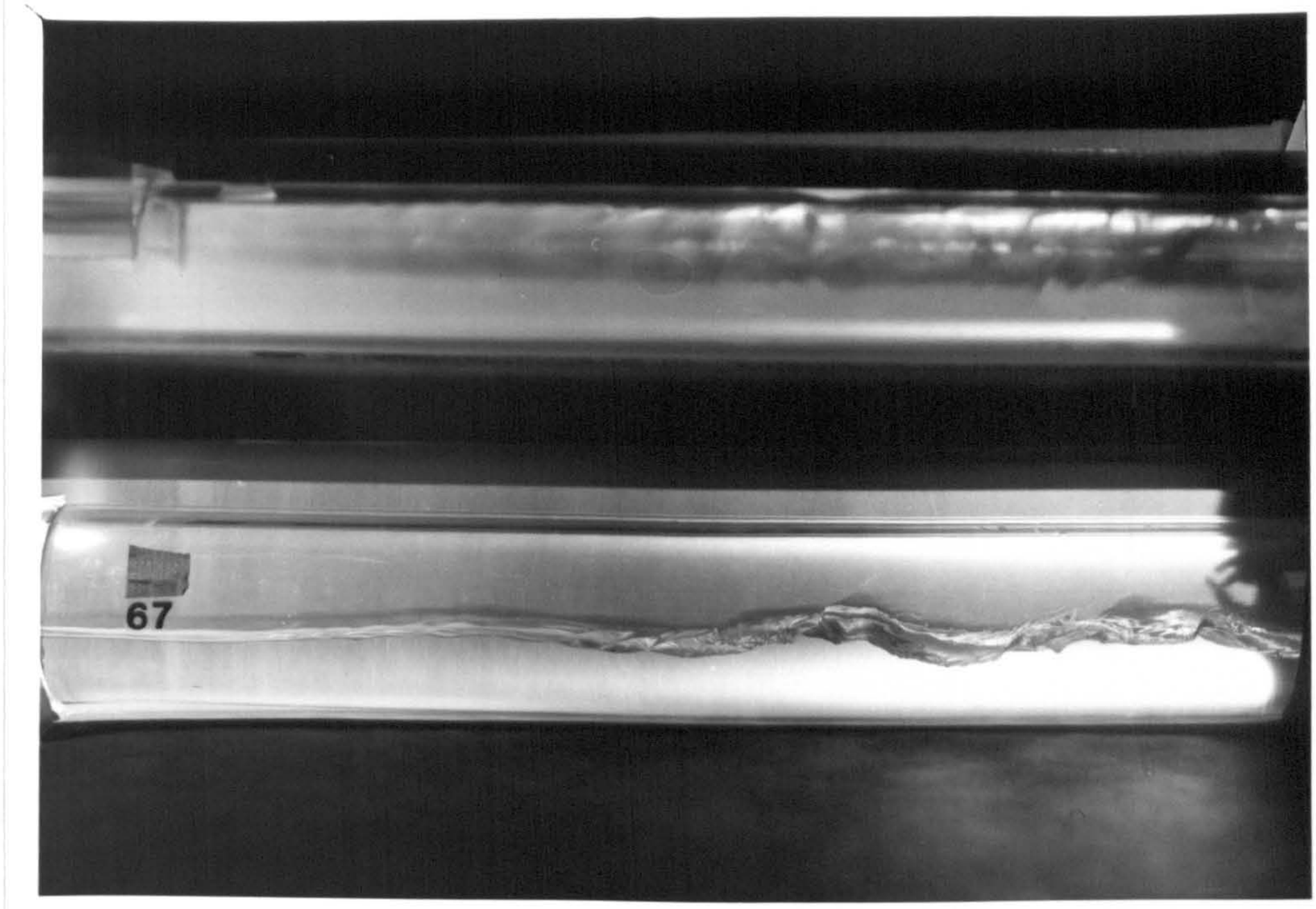

Plate 2

Plate 2 shows the form of the interface before a wave, such as that off-centre-right, begins to grow rapidly and form a slug. The interface in this form may be termed wavy-stratified (see Fig. 1.2d). Subsequent measurements taken from photographs such as this enable us to obtain the range of parameters for the initial conditions, such as undisturbed depth of water to tube diameter ratio and some tentative guesses at the upper bounds of the initial wave amplitude to undisturbed water depth ratio for the disturbance, which we use in theoretical calculations.

Further careful inspection of plate 2 reveals tiny capillary waves on the liquid-gas interface and on the sides of the perspex tube in the region of the main wave.

Little, if any, information can be obtained from the reflected image.

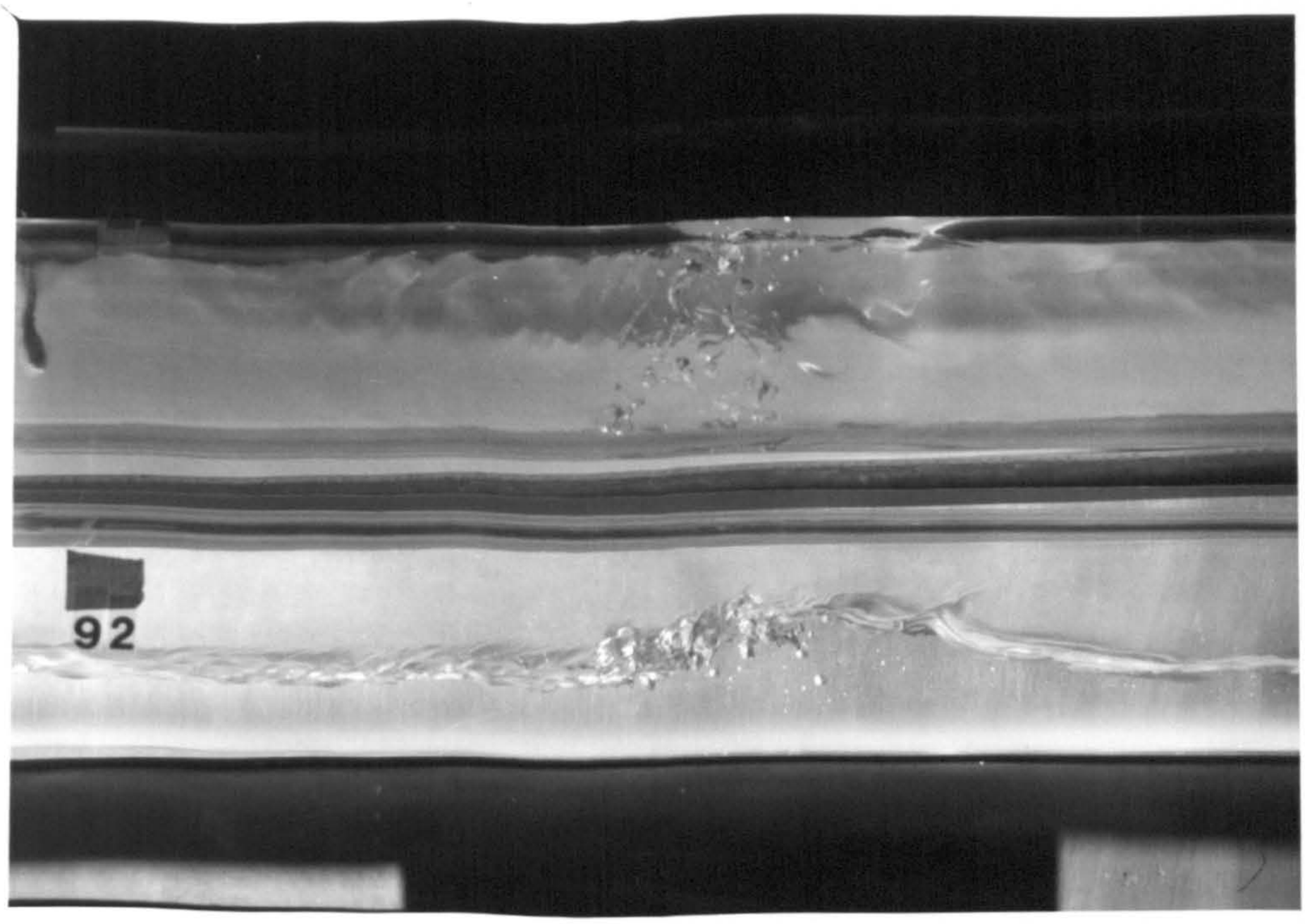

Plate 3

Plate 3 shows the growth of a wave like the one shown on plate 2. All the capillary waves can be seen more clearly now, and we can already see a little entrained air within the liquid to the front of the wave. The front of the wave appears rather rough, yet the overhead shot shows us that these "splashes" are in fact quite dispersed. To the rear of the wave in this case there appears to be a secondary crest. The rear surface of the wave is smooth.

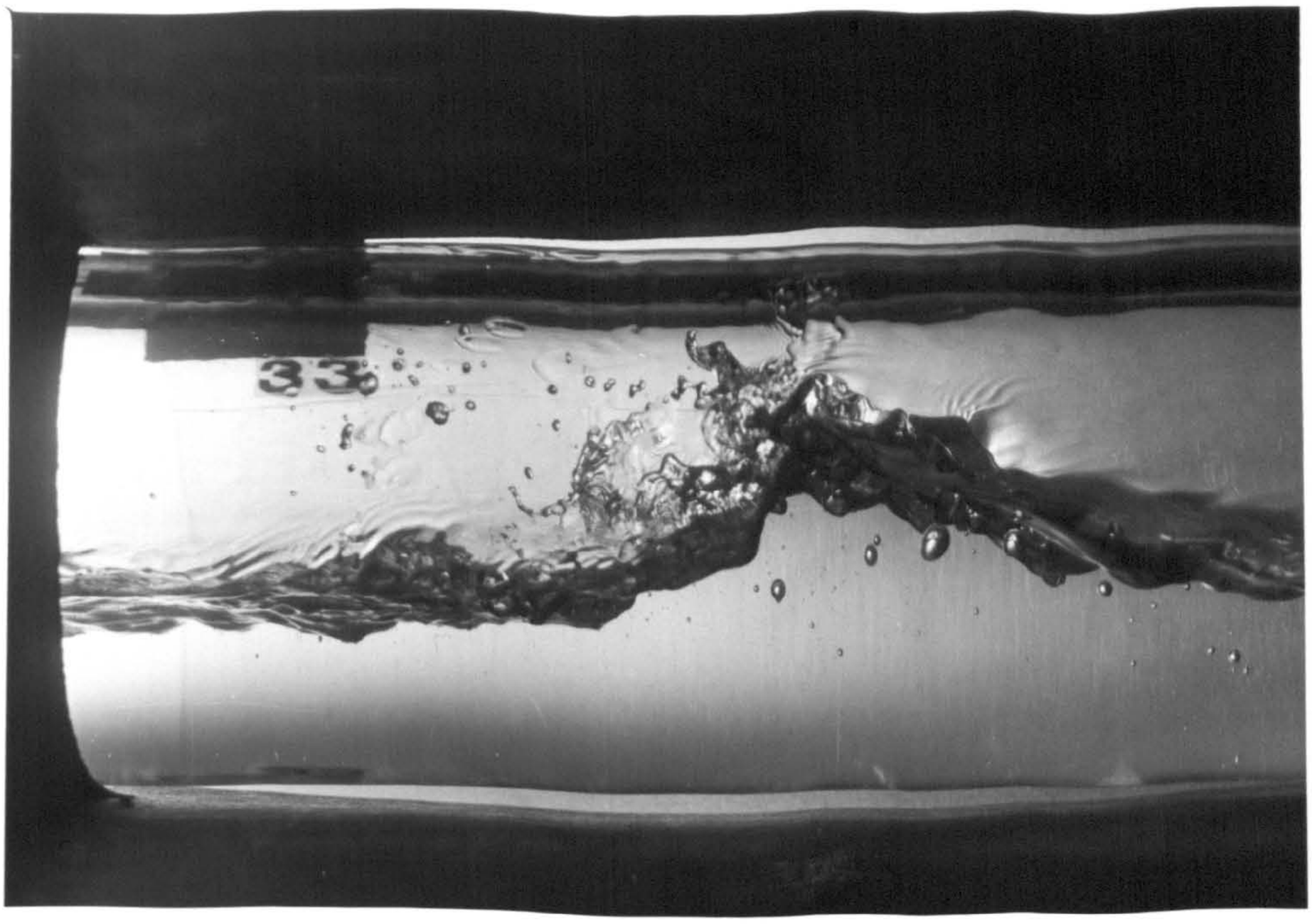

Plate 4

Plate 4 shows a close up of a more developed wave. This close up shows very clearly capillary waves on the thin film covering the tube walls to the front and rear of the wave. These appear to be on a draining liquid film.

There is again some entrained air, but there is now a significant amount of liquid being entrained into the gas flow to the front of the wave. The droplets appear to be travelling approximately horizontally, and slightly upward at this time This can be deduced by looking at the angle of the wakes of the droplets that impact upon the sides of the tube. The majority of entrained droplets seem to be drawn from the crest of the wave or from the rear surface of the wave immediately behind the crest region at this time. Again, the rear surface remains very smooth. Both the front and the rear surfaces are rather steep - greater than 25° from the horizontal.

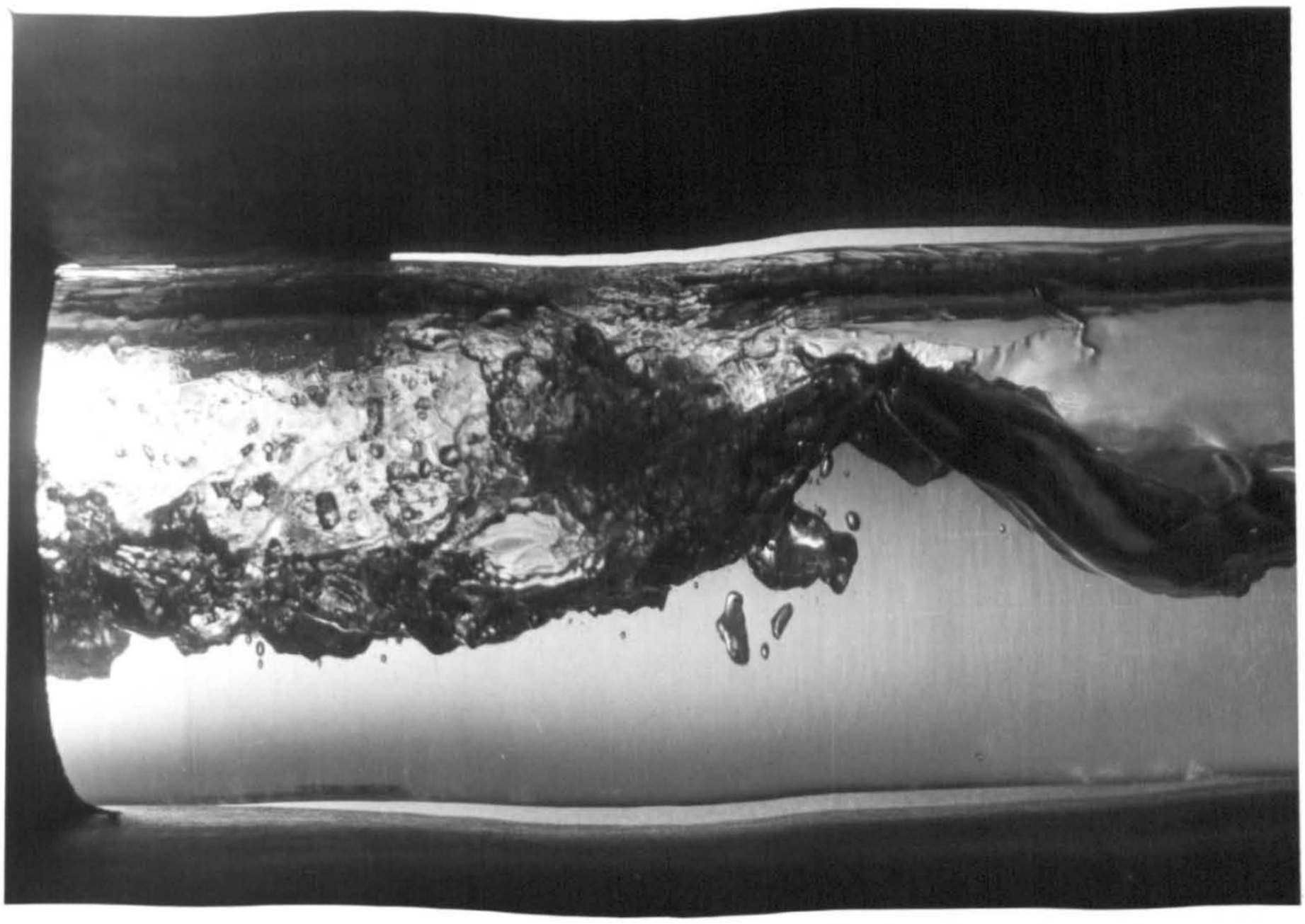

Plate 5

Plate 5 is taken at a slightly more developed stage in the transition to slug flow. Both the front and the rear surfaces are somewhat steeper - between 30° and 45° - and parts of the rear surface are steeper than the front surface. The peak of the wave is now approximately two-thirds of the way up from the bottom of the tube. While there is a little entrained air the amount of entrained liquid has increased greatly. The dense entrainment to the front of the wave is of a very frothy nature. It no longer appears to be drawn from the rear surface of the wave, but rather from the crest or the front surface suggesting either a locally low pressure region, or the action of a vortex or eddy in that region. Much of the froth seems to be drawn toward the top of the tube where there appears to be some wetting of the tube. To the front of this densely entrained region there are again more dispersed droplets - some rather large in size. In contrast with the relatively smooth rear surface of the wave, the liquid at the front of the wave is choppy and disturbed.

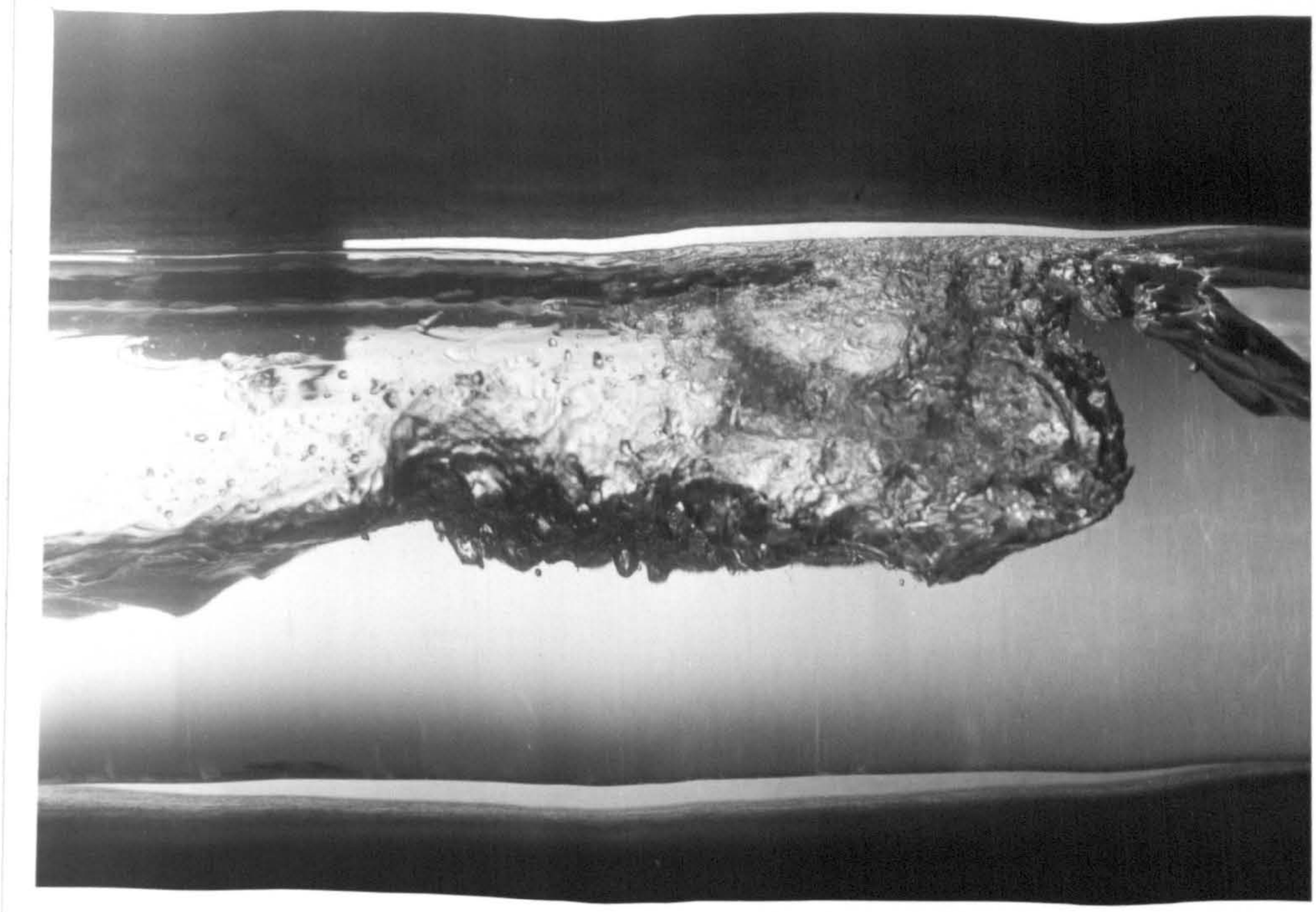

Plate 6

Plate 6 is of a wave which appears to be at an interesting and "critical" stage. In comparison to the previous plate, a wave fills nearly the entire tube. The wave of this form is clearly a breaking wave. To the front of the wave there is again a region of very densely entrained liquid. This wave has entrained no gas. The crest of this wave appears to be contributing much liquid to the entrained flow. In front of the densely entrained region there is again a region of more disperse droplets, some again rather large, and we can again tell from the wakes of these droplets on the walls of the tube that they are travelling horizontally now. Again it must be noted that the rear face of this very steep wave is still smooth whilst the front is even more choppy and disturbed. This photograph appears to suggest that the (continuous) liquid region (i.e. not the entrained liquid) completely spans the entire tube cross-section. However, an overhead view is required to confirm such a conclusion. Closer inspection of this plate suggests that there may be an eddy or vortex immediately in front of the wave. Liquid is being entrained into the gas flow in this region perhaps by interfacial shear stresses caused by this vortex or eddy.

Further in front of the wave a small hump (off-centre left) can be seen. This can also be seen in other photographs when the flow is at a similar stage. Perhaps this is also due to an eddy or vortex in the region in front of the wave. Finally, it should be noted that the rear of this breaking wave is considerably steeper than is found for breaking waves on the oceans or at beaches.

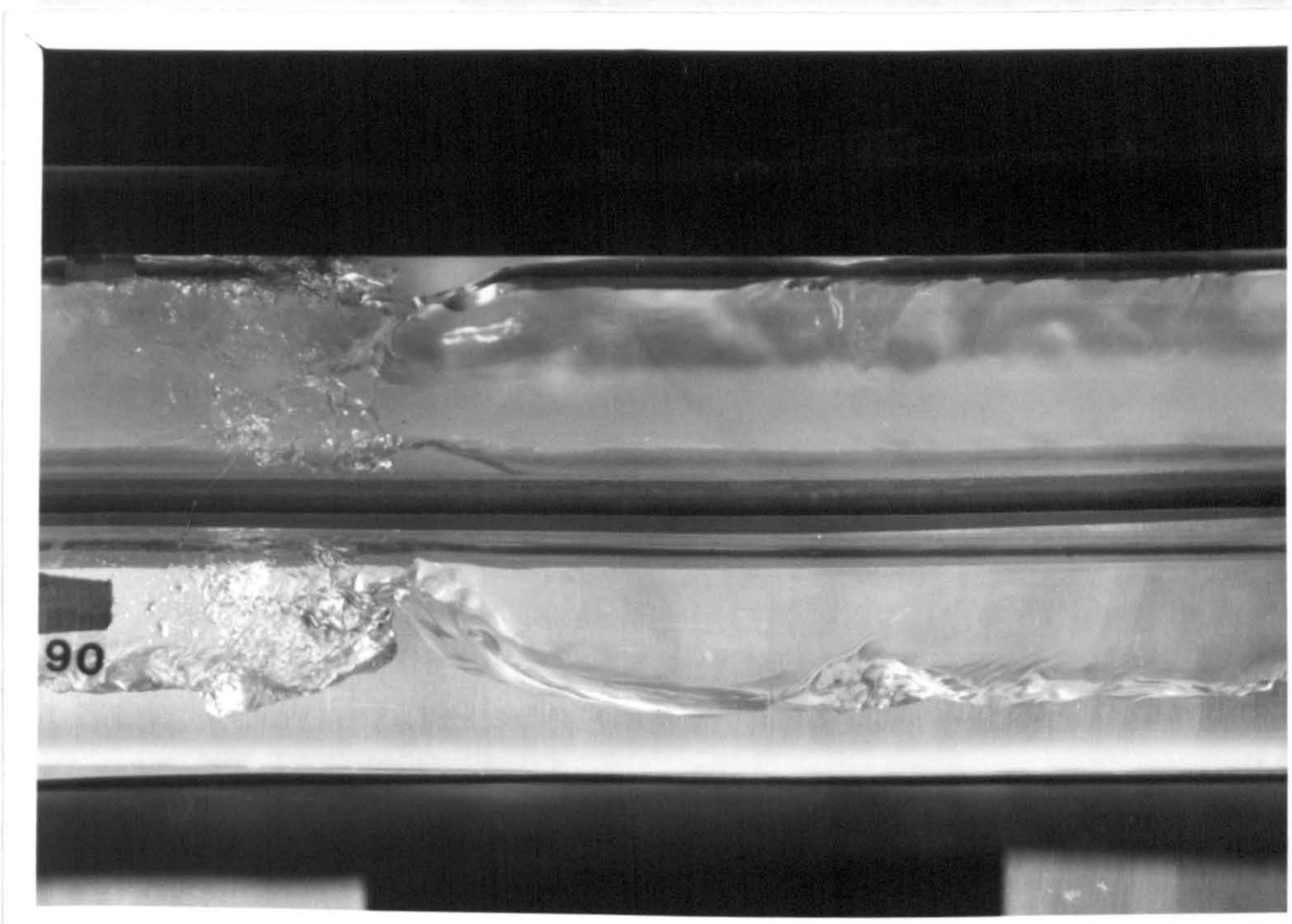

Plate 7

Plate 7 and 8 correspond very nearly to plate 6; plate 7 taken earlier and plate 8 later (but only slightly). Neither show the instability at the "critical" stage shown on plate 6, however with these plates we can reaffirm what has already been said. The wave surfaces are very steep with the rear surface smooth and the front very disturbed. There are two distinct regions of entrainment, a dense region close to the wave, and a sparse region further away. Much liquid appears to be entrained from the crest. In addition the top shots impart further information, showing the gap over the crest of the wave available for the gas to flow through.

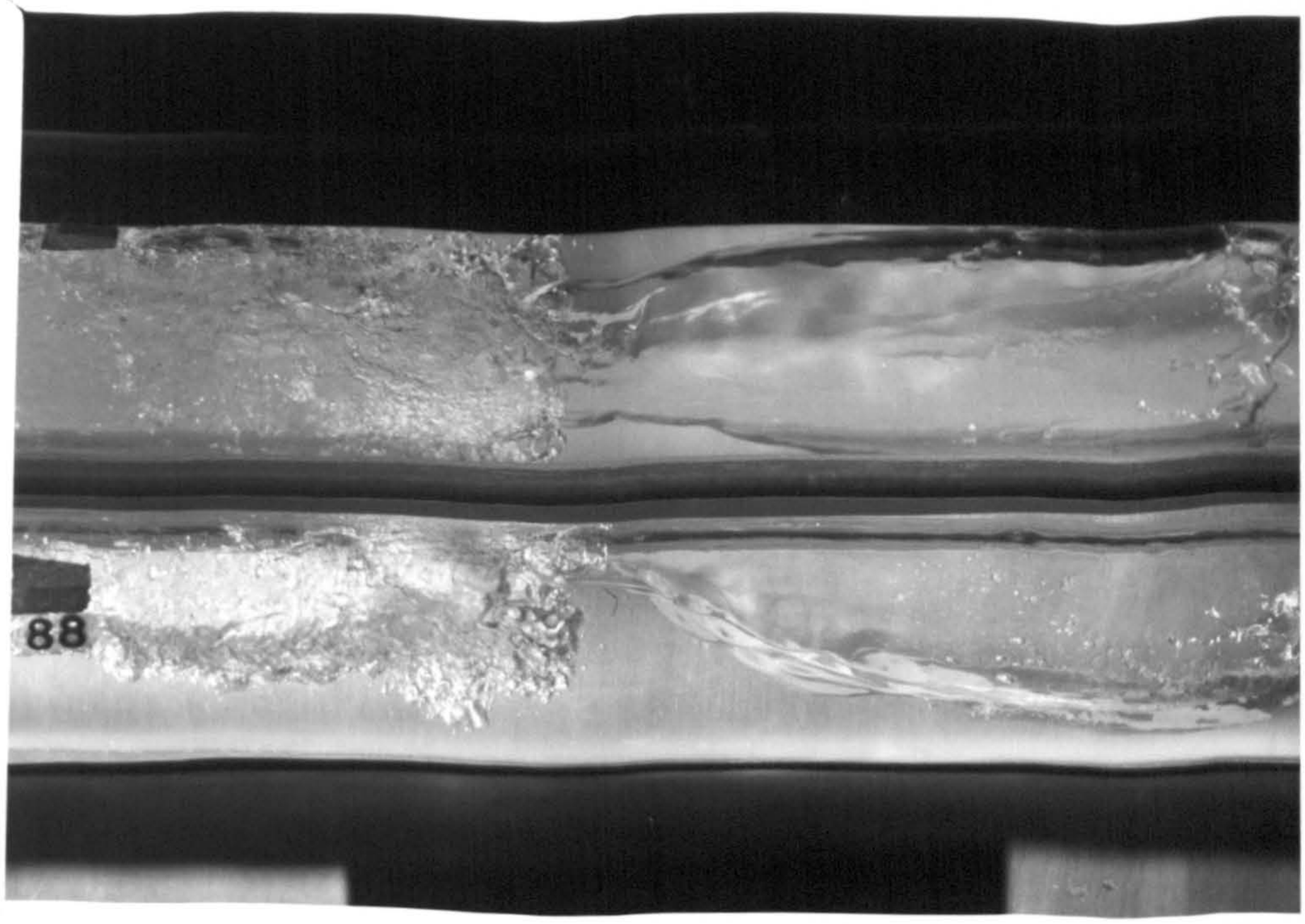

Plate 8

Plate 8 shows that the rear surface is smooth right up to the crest of the wave. Both plates show that there is a clear path through which the gas may flow over the liquid until the entrained region is encountered. The liquid surface across the top of the wave appears horizontal. Plate 8 (being later than plate 6) shows that as the slug forms there is a distinct gap in the cross-section occupied by the liquid, before the entrained region through which the gas may flow. Careful inspection of the photographs suggests that the liquid entrainment seems more pronounced near the sides of the tube, although this may be due to the curvature of the tube. There has been no entire bridging of the tube cross-section.

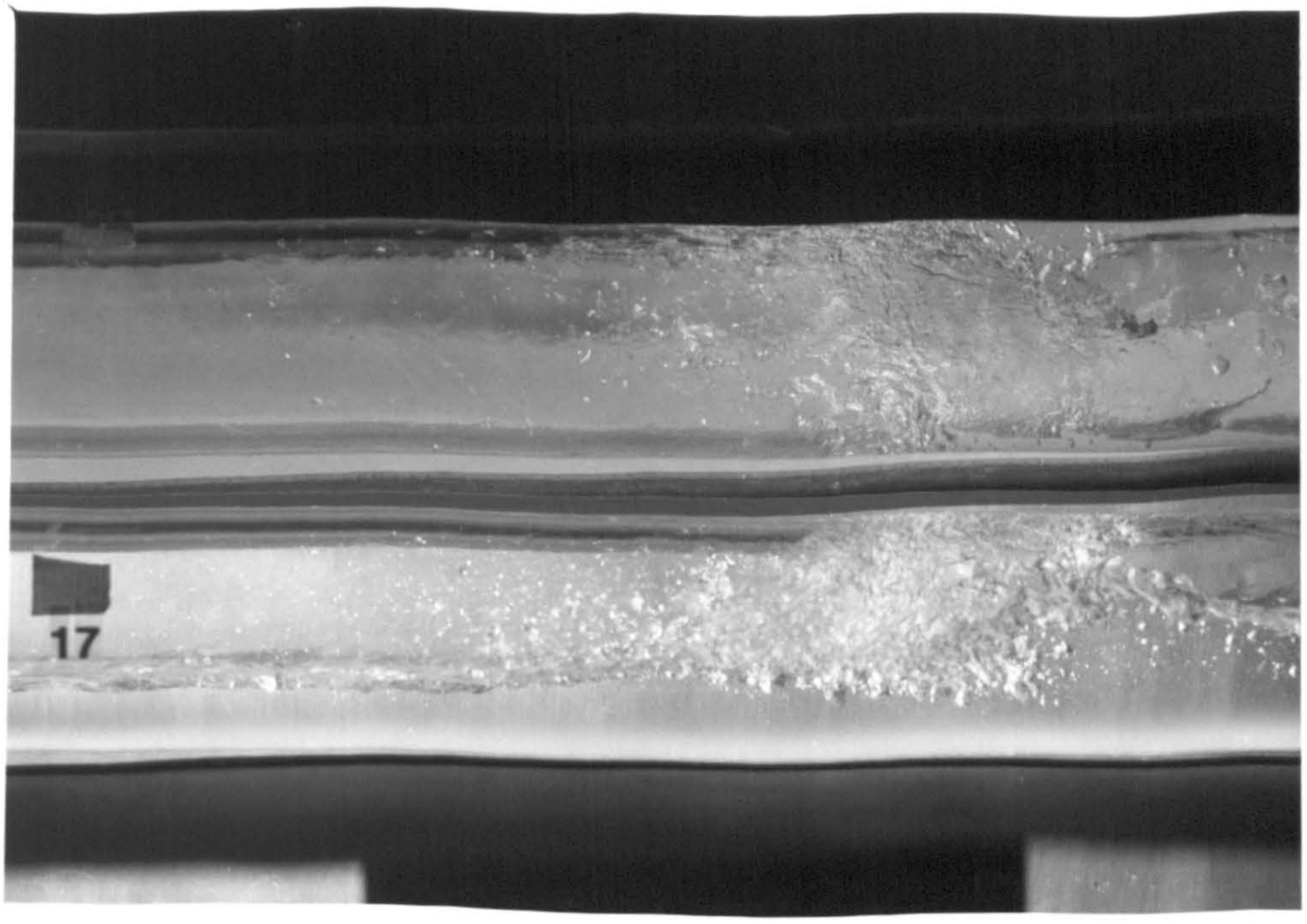

Plate 9

Plate 9 shows the situation slightly later than plate 8. The densely entrained region is growing, apparently at the expense of the liquid ahead of the wave and with liquid drawn from the crest of the wave itself. Nevertheless, there still remains a clear channel at the top of the tube through which the gas may flow.

Plate 10

Plate 10 shows how the densely entrained region grows still further. To the far left of the plate one can see where the densely entrained region meets the sparsely entrained region, and the entrainment appears to be largely at the expense of the liquid in the body of the wave (right of centre) which now appears smaller than before. Yet again the liquid does not completely block the tube.

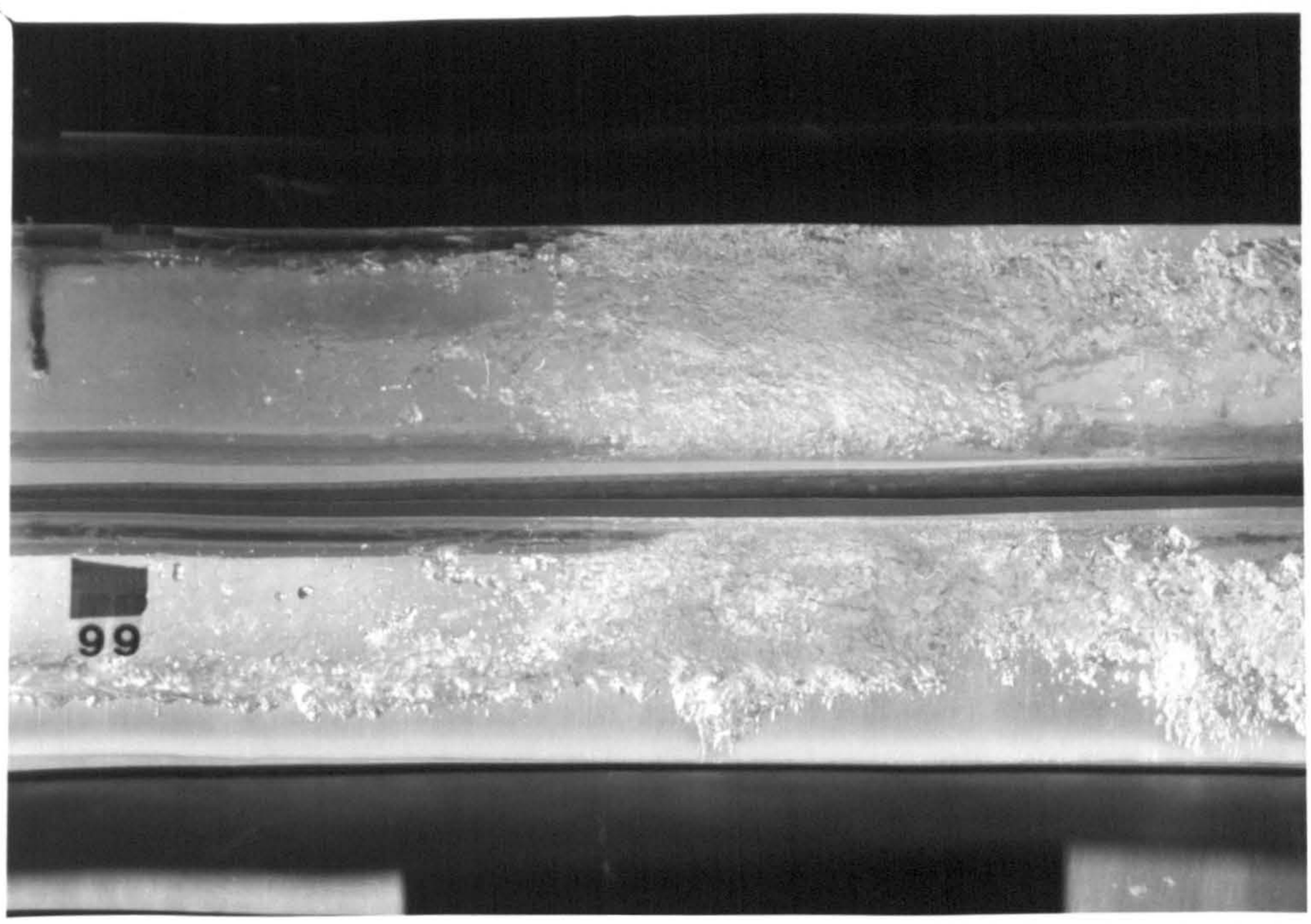

Plate 11

Plate 11 suggests that ultimately the growth of the entrained region is at the expense of the wave which caused the entrainment to begin. The entrained region is sufficiently large that further entrained liquid can come from two possible sources; the underlying liquid beneath the entrained region, or liquid drawn through the now very small wave at the rear (which in this frame is just off to the right of the plate). There is still a region of dispersed entrainment to the front of the denser region, although this is now also rather small.

In the parameter space under consideration it is these densely entrained regions which I shall now refer to as the fully formed slug (in analogy to Coney's "surge").

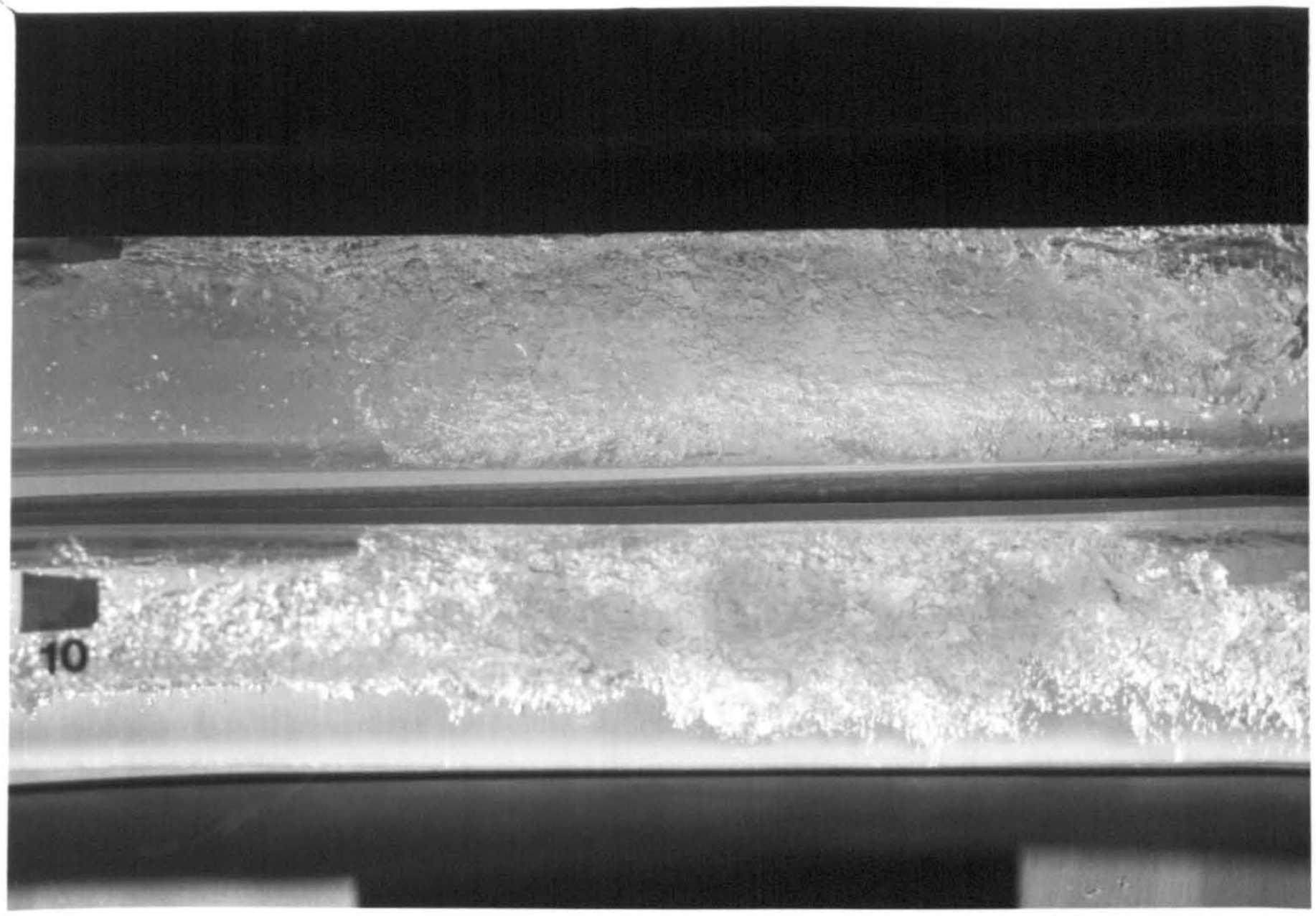

Plate 12

It is observed that these slugs are very fast moving once formed, and within the length of the experimental apparatus used that they continued to grow to lengths longer than that shown on plate 12 which is again a slightly more developed slug than any of the previous ones.

Although the still photographs were very informative about the qualitative nature of the transition to slug flow of a surface instability and provided an adequate account of the stages involved in the transition for the flow parameter space under consideration, only very limited quantitative information could be obtained using this approach.

By taking careful measurements from the photographs, data for the initial depth of liquid in the pipe could be obtained and this is summarised in Appendix B. From such measurements, and taking experimental errors into account, Fig. 3.9 for the variation of the equilibrium liquid level with mixture Froude number was obtained (using a linear least squares fitting routine on the data points) where the

Fig. 3.9

Variation of observed liquid equilibrium depth to tube diameter ratio with mixture Froude number

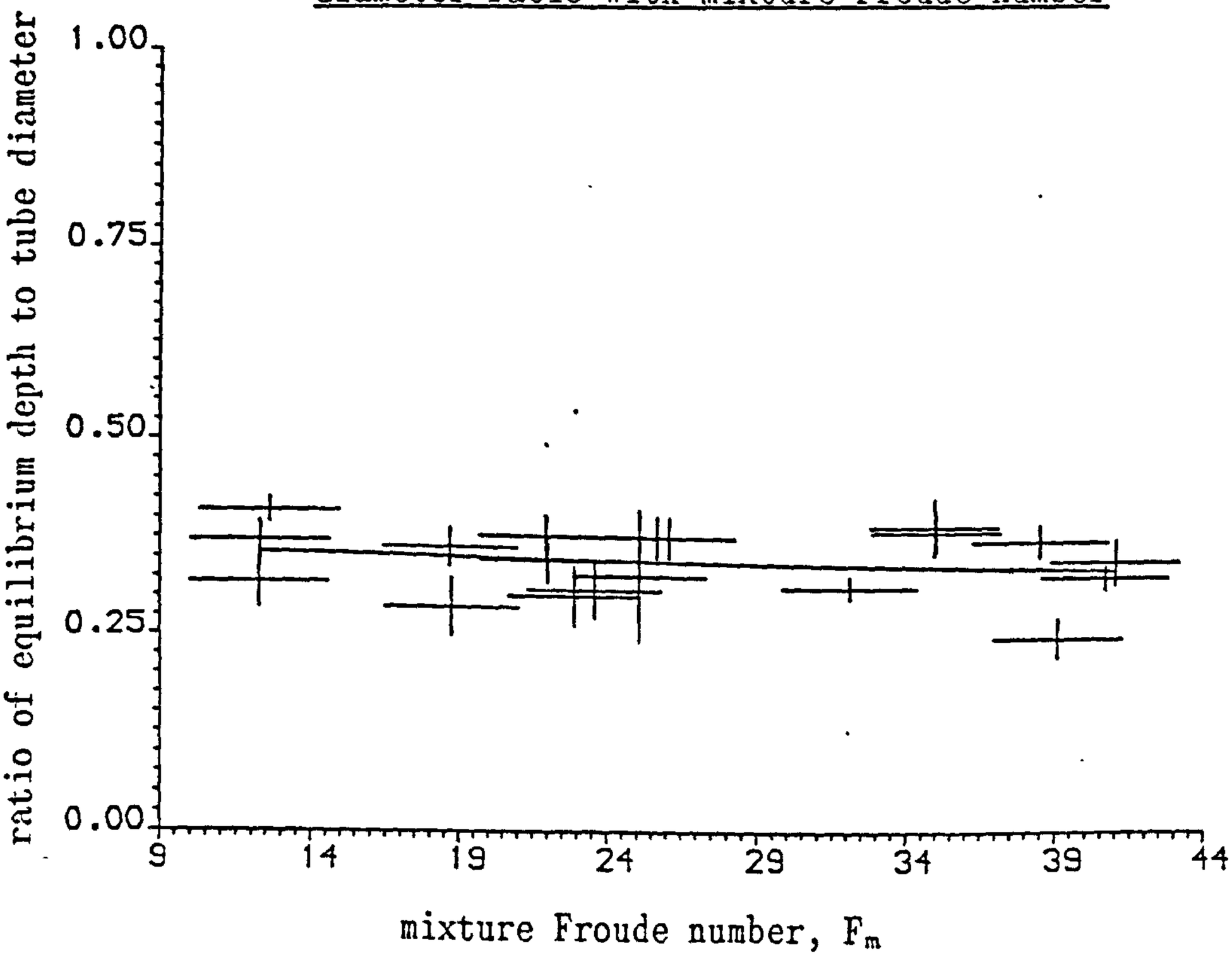

mixture Froude number is given by:

$$F_m = \frac{(U_{GS} + U_{LS})^2}{gH} \qquad (3.6.1)$$

where g is the acceleration due to gravity, H is the tube diameter, and the U_{is} (i=G or L) are the superficial velocities of the respective phases, given by:

$$U_{is} = \frac{Q_i}{\rho_i A} \qquad (3.6.2)$$

where the Q_i is the mass flux and ρ_i is the density of the respective phase, and A is the cross-sectional area of the tube. While the superficial velocities of the phases are easily calculated, and often used in practice (e.g. for the Mandhane flow régime map), they are only the velocities of the respective phases obtained by averaging the flow rates over the entire tube cross-section. For instance, superficial gas and liquid velocities of 4 and 0.2 m s^{-1} respectively fall within the slug flow régime. If instead of averaging the fluxes over the entire cross-sectional area we make some estimate of the specific area occupied by each phase, then we may define a velocity, V, such that:

$$V_i = \frac{Q_i}{\rho_i A_i}$$

where A_i is the cross-sectional area through which phase i may pass. If we assume, for example, that the gas occupies $\frac{2}{3}$ of the total cross-sectional area, then the velocities of the phases as defined by the above equation are 6 and 0.6 m s^{-1} for the gas and liquid respectively. Perhaps, in order to get a better indication of the velocities of the flows, a measurement of velocity like that above is more informative than the superficial velocity (3.6.2). However, this requires knowledge of the partial areas through which the respective

phases pass. Since this is not generally known we shall continue to use the superficial velocity of (3.6.2) as an indication of the velocities of the phases, and consider superficial gas and liquid velocities of 3 and 0.3 m s^{-1} to be typical of the velocities of slug flow.

If waves on oceans or up beaches are studied, the ratio of the initial wave amplitude to equilibrium liquid depth is an important parameter in determining what happens to the wave in shallow water, whether it breaks or not, for instance. To see whether slug formation is sensitive to this parameter, measurements were taken from photographs in which the wavy-stratified flow becomes a slug flow, such as plate 2. However, not all waves like that of plate 2 actually become slugs. Some of these waves try to become slugs, but don't make it; they grow and fall, grow and fall, and so on. Perhaps for these waves, and others that never show the potential of becoming slugs, some parameter, such as the amplitude to depth ratio for example, is below some critical value. This work does not try to identify such parameters, but rather uses analogy with breaking shallow water waves to see whether slug flows and shallow water waves are sensitive to similar parameters. Waves like those in plate 2 are already well developed. Thus, measurements of the "initial" wave amplitude from these photographs are already over-estimates of the true initial wave amplitude. Nevertheless, perhaps such measurements yield an upper-bound for initial amplitude to equilibrium depth ratio for such flows. Fig. 3.10 shows this variation plotted against equilibrium depth to diameter ratio using a linear least squares fitting routine on data in Appendix B.

Fig. 3.10

Variation of observed wave amplitude to equilibrium depth ratio with equilibrium depth to tube diameter ratio

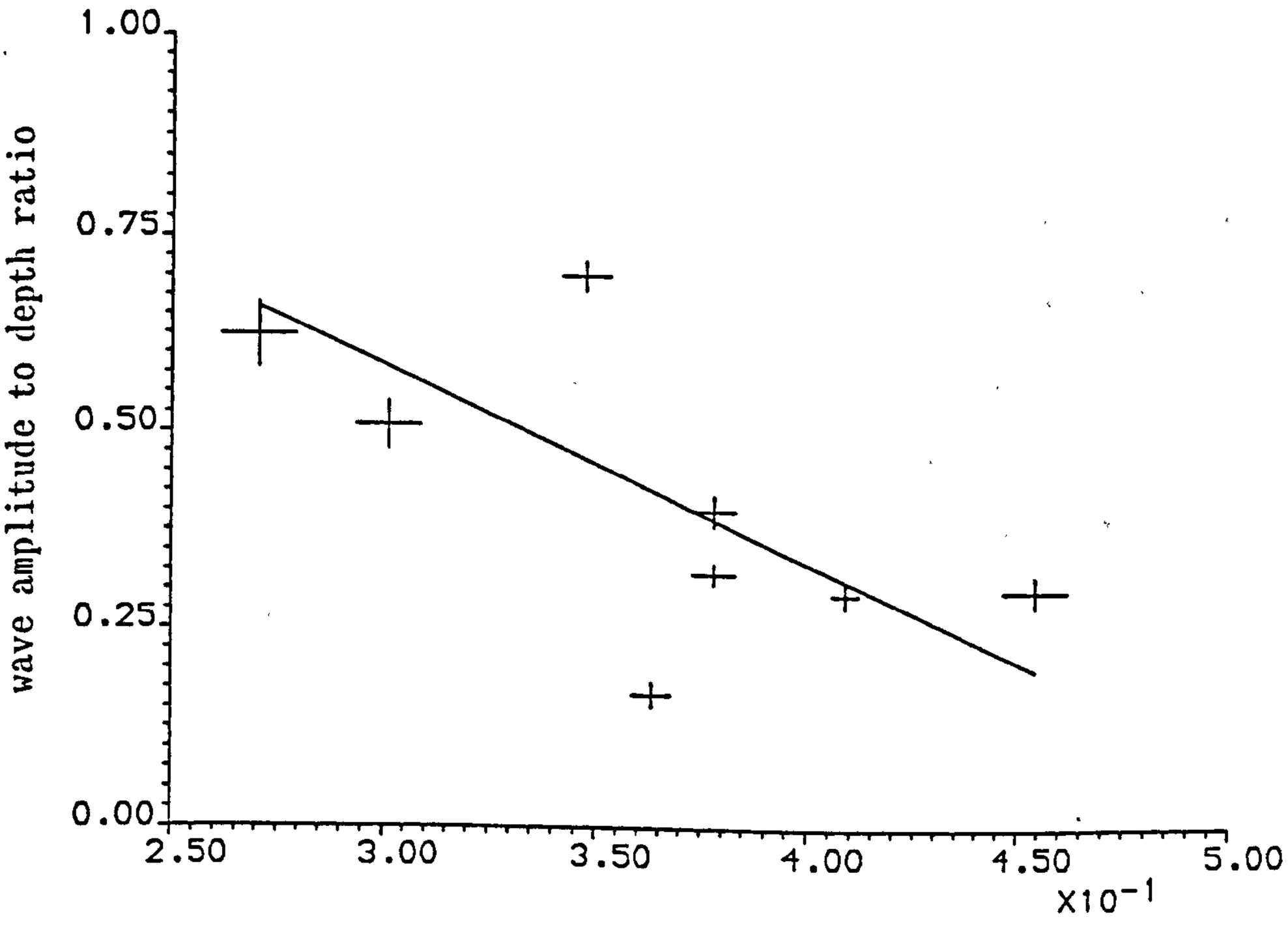

A total of about 200 stills were taken. Approximately 10% were taken in an attempt to obtain a depth to diameter ratio, about 20% to investigate the situation shown on plate 6, approximately 15% were useless, and the remainder to document the stages of the growth of the slug. Thus about twenty points provided data for Fig. 3.9. Despite the large spread of data points, and the relatively large error associated with the mixture Froude number, it can be seen that the equilibrium level of the liquid in the pipe is such that the ratio of liquid level to pipe diameter is in the range 0.33 to 0.38. This is used in the numerical modelling of the two-phase flow within this particular parameter range. In addition, nine points were obtained from these data which provides information for the upper-bound on the wave amplitude to equilibrium depth ratio for the initial waves which do become slugs. This must remain a somewhat tentative parameter as by the time the wave had grown sufficiently to be noticeable it is necessarily somewhat larger than its initial (less noticeable) value. So, if we consider a depth to diameter ratio of about $\frac{1}{3}$, which Fig. 3.9 shows to be reasonable, then Fig. 3.10 would suggest that the initial amplitude to depth ratio must be less than 0.5.

3.7 Results from fast ciné photography

Some experimental work was performed using fast ciné to discover whether, within the domain of interest, the slugs did actually ever bridge the entire tube cross-section. In addition, measurements of the slug growth rate and velocity were desired. Measurements of the growth rate and velocity can be found in Appendix C.

The film obtained was transferred onto VHS video, to increase the portability of the results and allow viewing away from CERL, with one frame of ciné becoming one frame of video (so the time between frames is 4 ms. and 1 s. of film is equivalent to 0.1 s. of flow). To analyse the flow the video was then played back on a good quality video recorder and FST (Flatter, Squarer Tube) television from which a tracing paper copy was made of the transition.

Some (reduced) copies of the tracings are shown in Figs.3.11 to 3.14. In these figures the scale of the waves is 1:1 i.e. the waves appeared in the tube as they appear in the text. The solid lines represent the continuous liquid phase, the dashed lines the approximate envelope of the entrained flow and the numbers on the two represent the counted frame number from the beginning of the sequence of measurements, so solid line 32 with dashed line 32 correspond to the continuous liquid and the envelope of entrained flow that make up the slug at frame 32, whilst black dot (•) 32 is the position of a droplet of water at that time. Unfortunately, it was difficult to resolve the position of many of the droplets accurately.

Fig. 3.11

Results of fast ciné film observations for the transition to slug flow by a small disturbance within a horizontal perspex tube

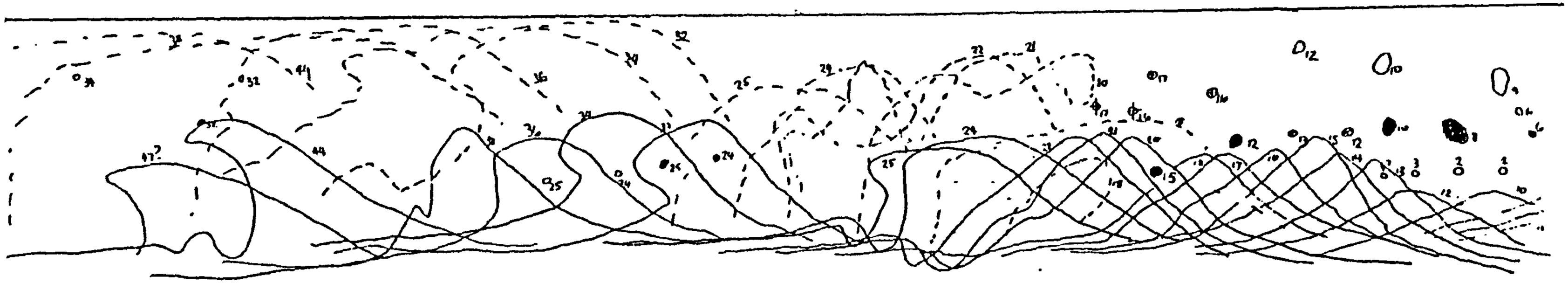

scale 1:1

Fig. 3.12

Results of fast ciné film observations for the transition to slug flow by a small disturbance within a horizontal perspex tube

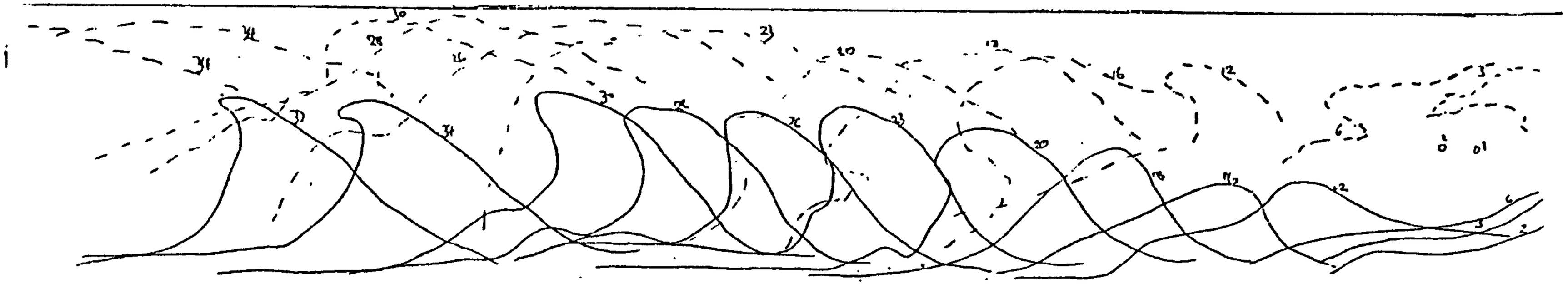

scale 1:1

Fig. 3.13

Results of fast ciné film observations for the transition to slug flow by a small disturbance within a horizontal perspex tube

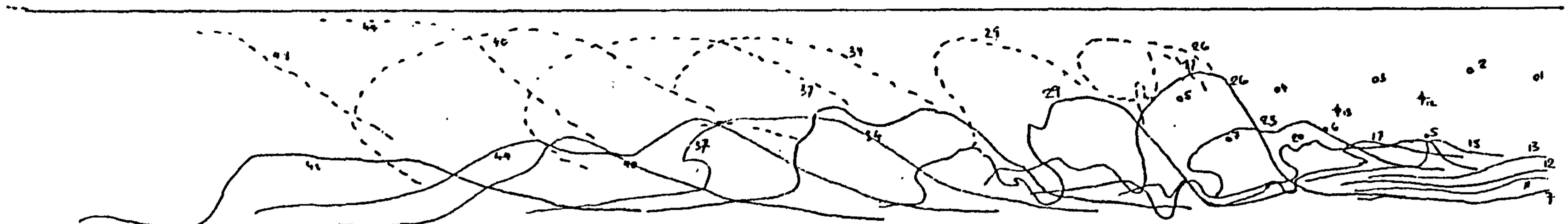

scale 1:1

Fig. 3.14

Results of fast ciné film observations for the transition to slug flow by a small disturbance within a horizontal perspex tube

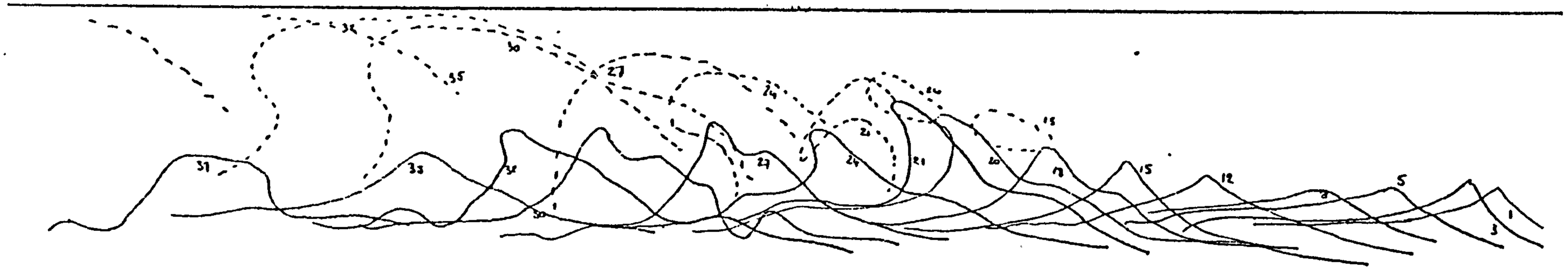

scale 1:1

Although the sequences provide a lot of information, little more of a qualitative nature beyond what has already been said of the quality stills can be added. They all show waves growing, entrainment beginning, and slugs forming. Although they clearly show the close approach of the breaking wave profile to the top of the tube, none of them show a wave actually bridging the tube, and this is in agreement with the experiments of Coney (1974) for this sub-domain of the slug flow régime.

From the films, and the tracing copies that were taken for the sequences shown in Figs. 3.11 to 3.14 measurements were made. These provided data on the velocity of the peak of the disturbance, both horizontal and vertical, as the transitions to slug flow took place. These are illustrated by the graphs in Figs. 3.15 to 3.18.

Fig. 3.15

Measured variation of the horizontal and vertical velocity components for the crest of the wave in Fig. 3.11

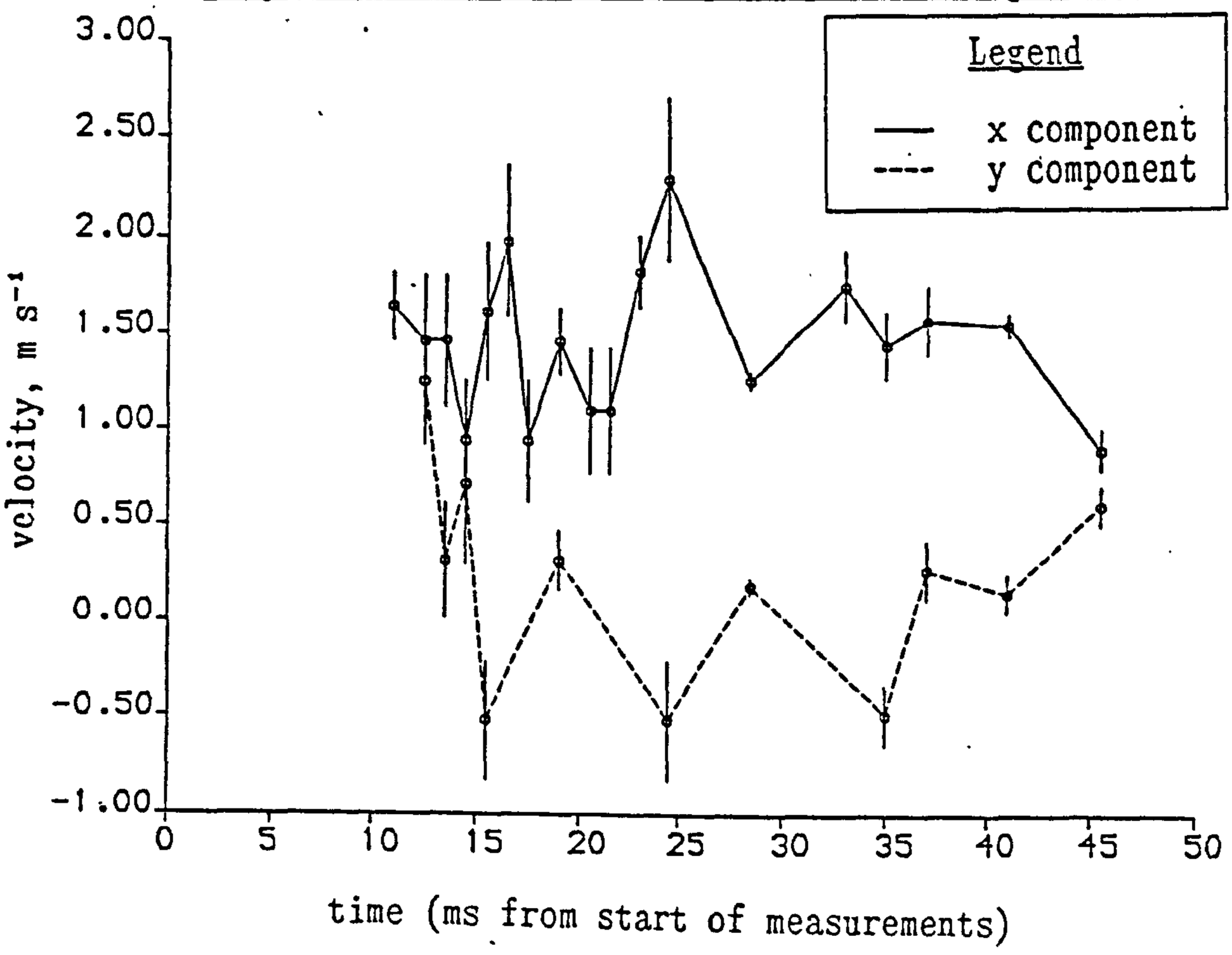

Fig. 3.16

Measured variation of the horizontal and vertical velocity components for the crest of the wave in Fig. 3.12

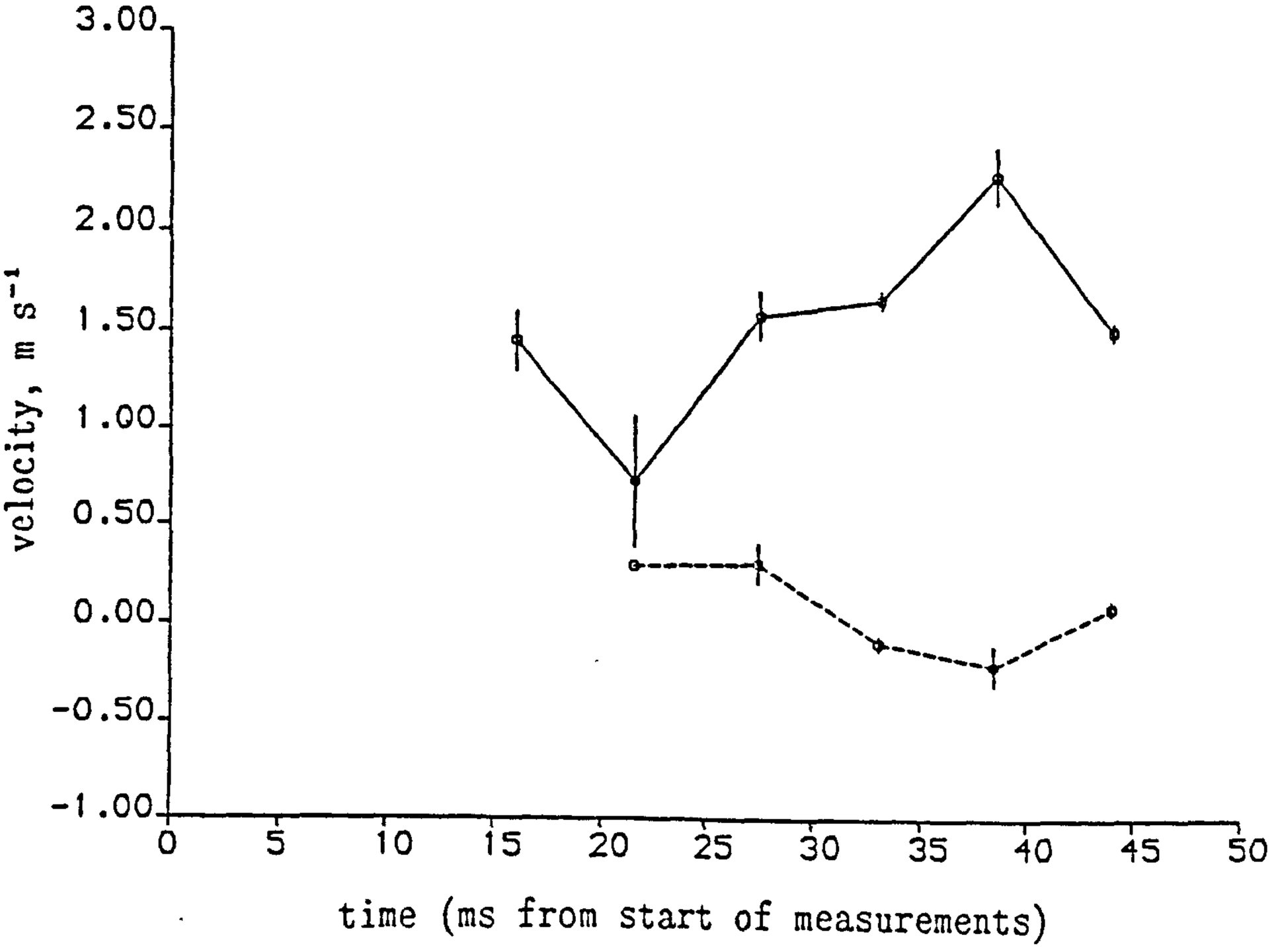

Fig. 3.17

Measured variation of the horizontal and vertical velocitv components for the crest of the wave in Fig. 3.13

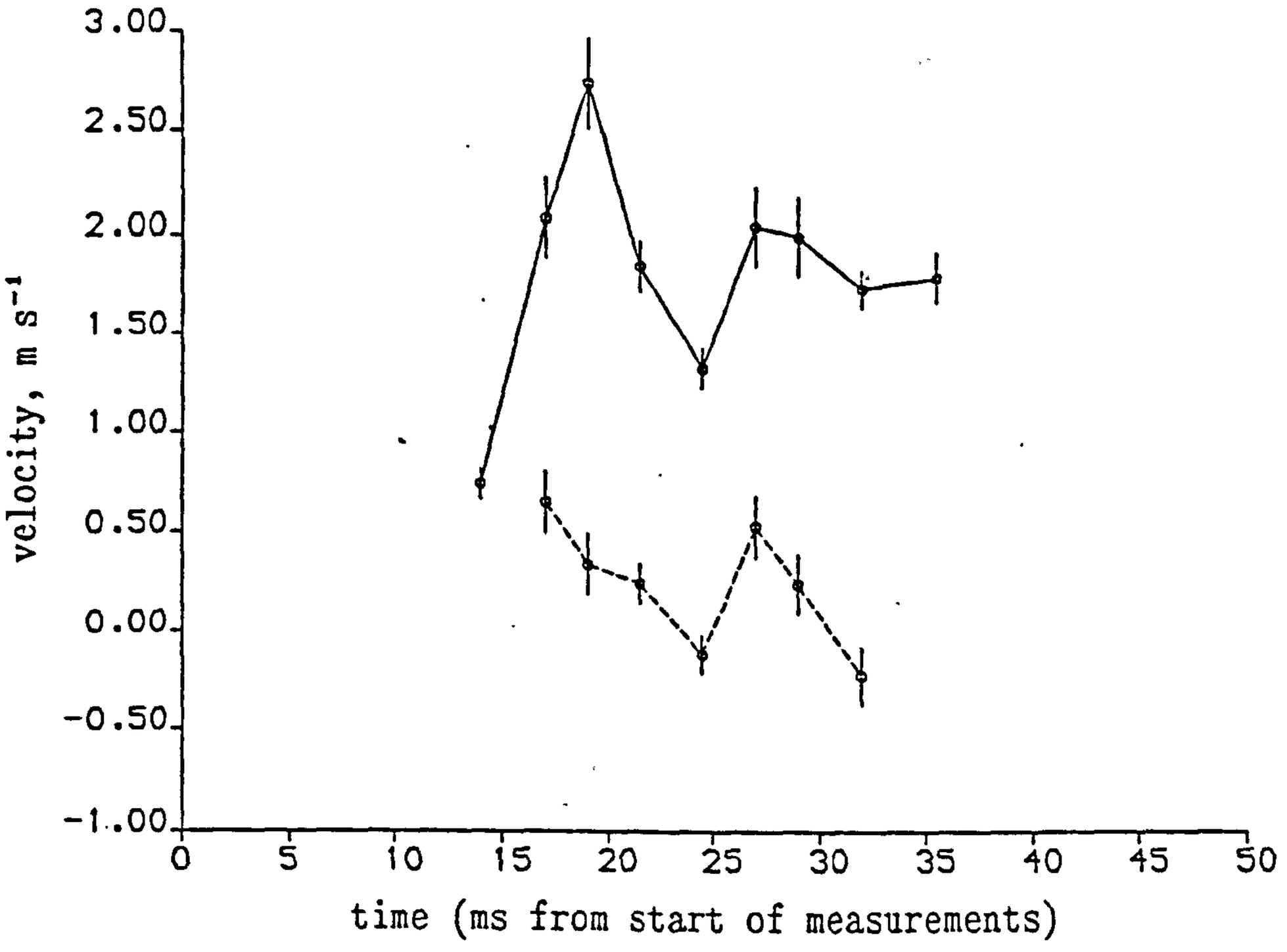

Fig. 3.18

Measured variation of the horizontal and vertical velocitv components for the crest of the wave in Fig. 3.14

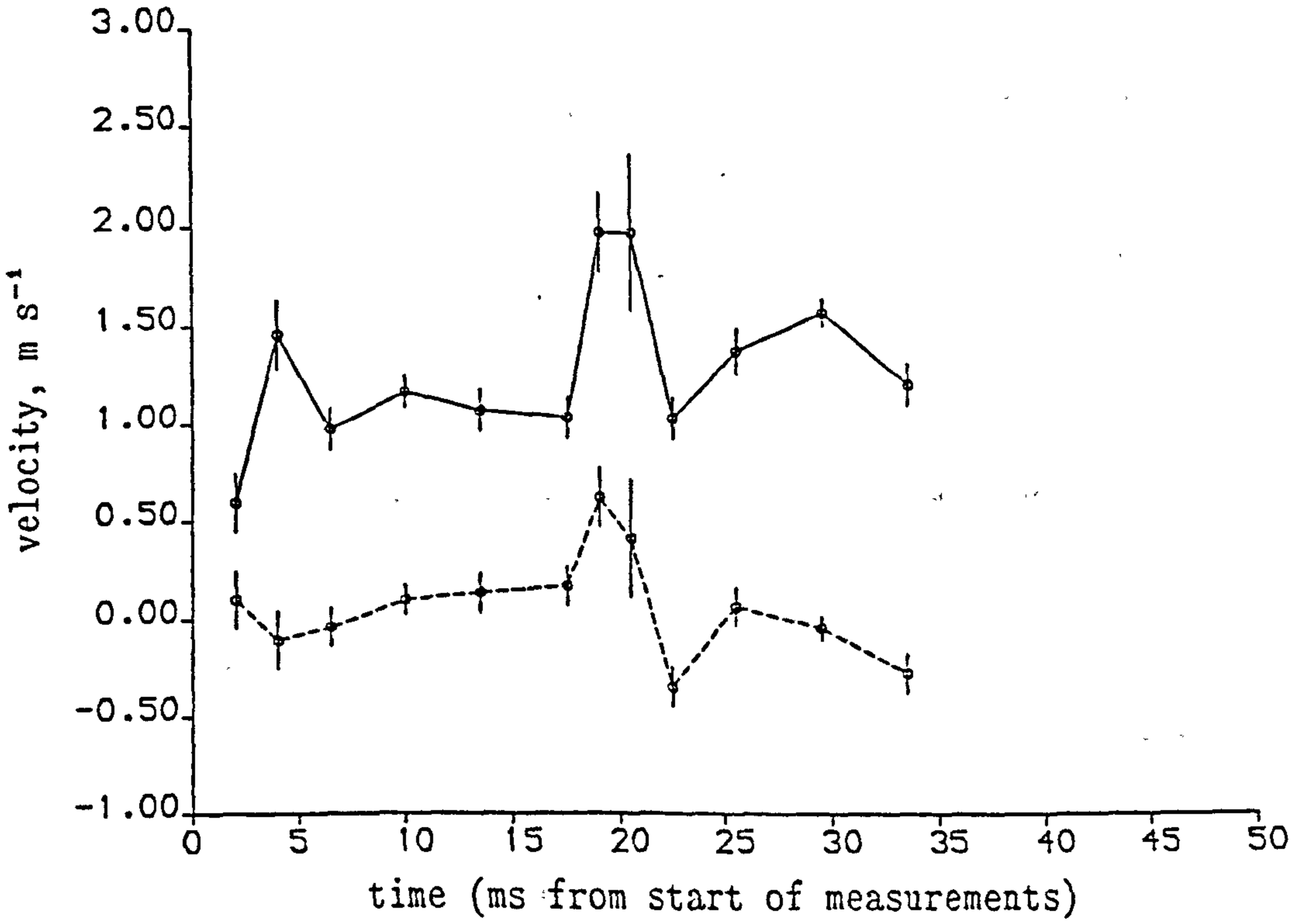

Since these flows may be rotational and are probably turbulent, the data for the velocities vary considerably. However, a trend can still be seen in the velocities as the slug is formed. The horizontal velocity of the liquid peak is seen to remain roughly constant, between about 1 and 1.5 m s^{-1}. This would seem rather a strange result because a slug is "observed" to move very quickly down the tube (perhaps even at the gas velocity). The vertical velocity also behaves other than would be expected from a bridging model.

Perhaps an explanation for this is that these fully formed slugs do not block the entire tube. Rather, they undergo two distinct evolutionary stages. In the first stage the liquid amplitude increases. There is little or no entrainment. The wave reaches a "critical" amplitude, and the second stage begins. Liquid droplets are now entrained into the gas flow at the expense of the wave and from the liquid to the front of the slug. No further substantial increase in the wave amplitude is made. Indeed, the wave amplitude may even decrease. The behaviour of the slug is not as would be expected from the bridging model. Figs. 3.15 to 3.18 show the variation of the velocity of the wave peak. They do not show what happens to the entrained droplets. I suggest that the "observed" fast moving slugs are, in this case, fast moving regions of entrained droplets (in analogy with Coney's "surges"). More data for these figures can be found in Appendix C.

Although the fast ciné provided much information about the growth rates and forms of the surface profile, they were a costly and wasteful means by which to obtain the information because so many 16 second runs produced no useful data - lots of fully blown slugs or hardly any slugs, instead of the desired growing waves. So a third method was employed to obtain further data to expand the parameter space under consideration.

3.8 Results from colour photography

The following plates are some of those obtained from the double coloured flash photography. Where the flashes are blue and yellow, that is the order in which they were fired, and where the flashes are red and blue that is the order. Further data for these flows may be found in Table 3.1 on page 85.

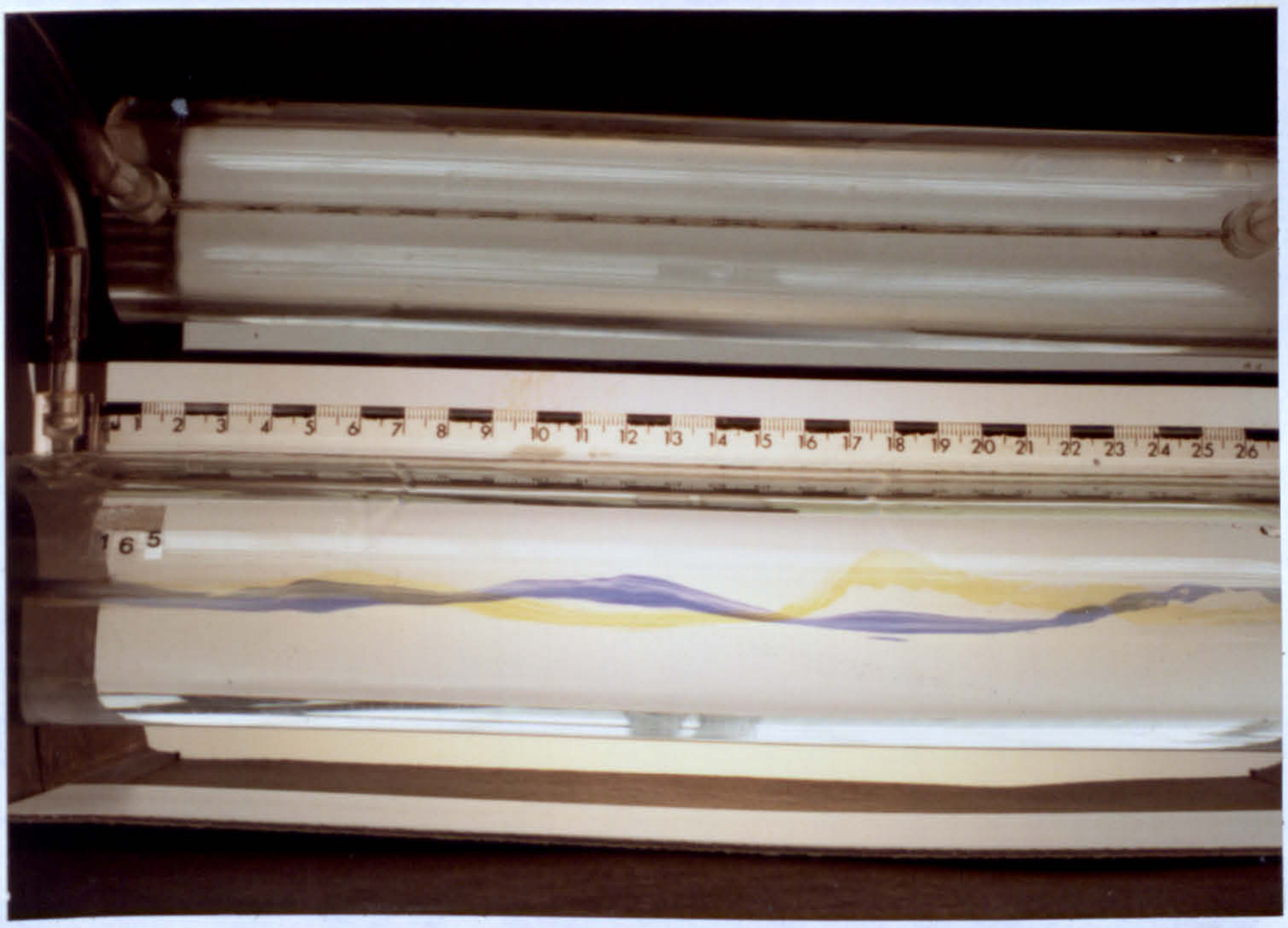

Plate 13

The interface as shown in plates 13 and 14 yielded information about the viewing angle of the photographic equipment to the interface, and verified that the flow type was as suggested by the modified Baker flow régime map - in this case, wavy-stratified flow.

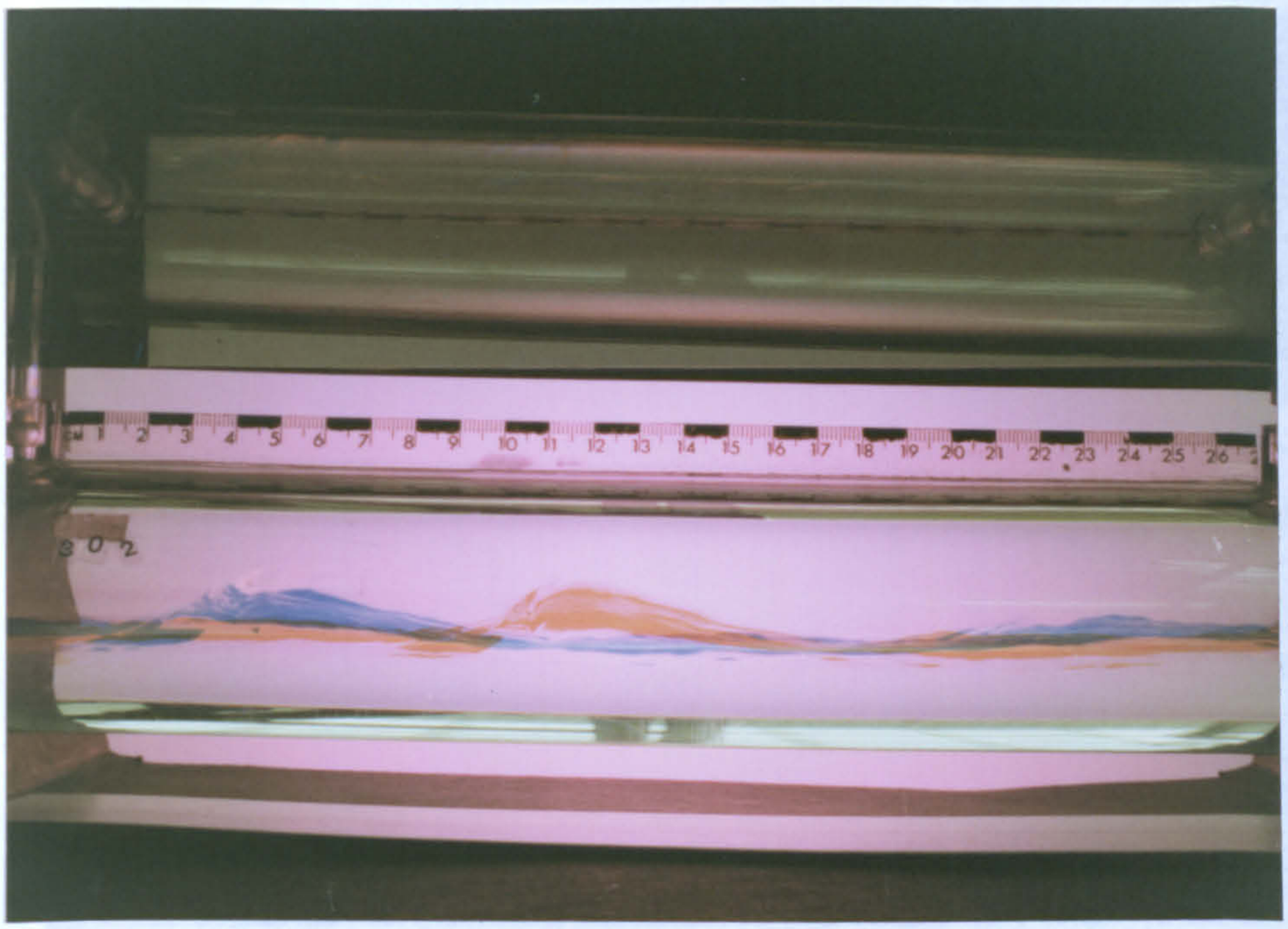

Plate 14

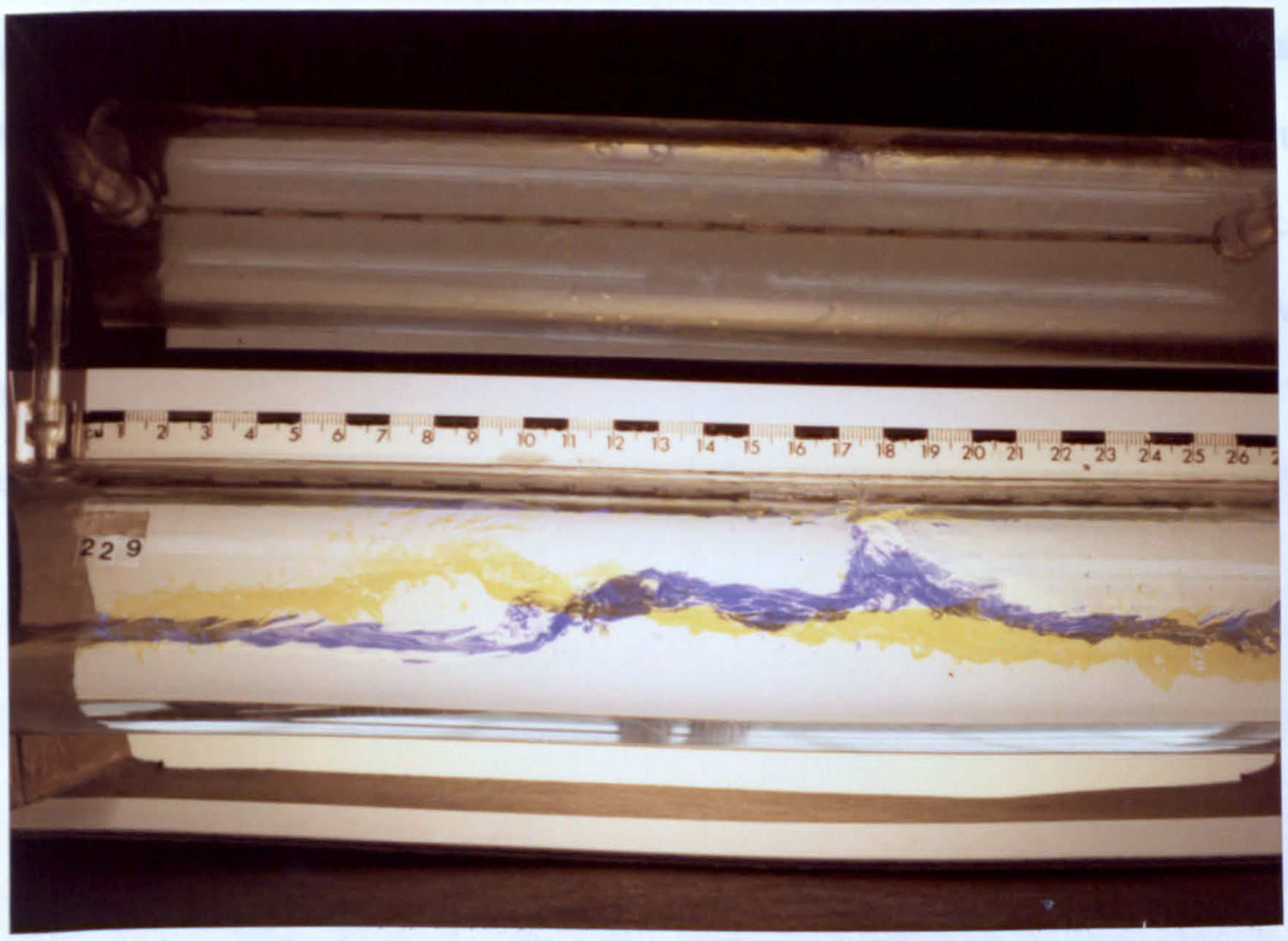

Plate 15

Plate 15 shows an instability growing (as did plate 3 earlier). The blue wave between 17 and 19 cm. along the scale on the tube moves by between 7 and 9 cm. along the tube in 69.76 ms. - a wave velocity of c. 1.5 m s^{-1} , which also appears to be the liquid velocity, in comparison with a superficial liquid velocity of c. 0.2 m s^{-1}.

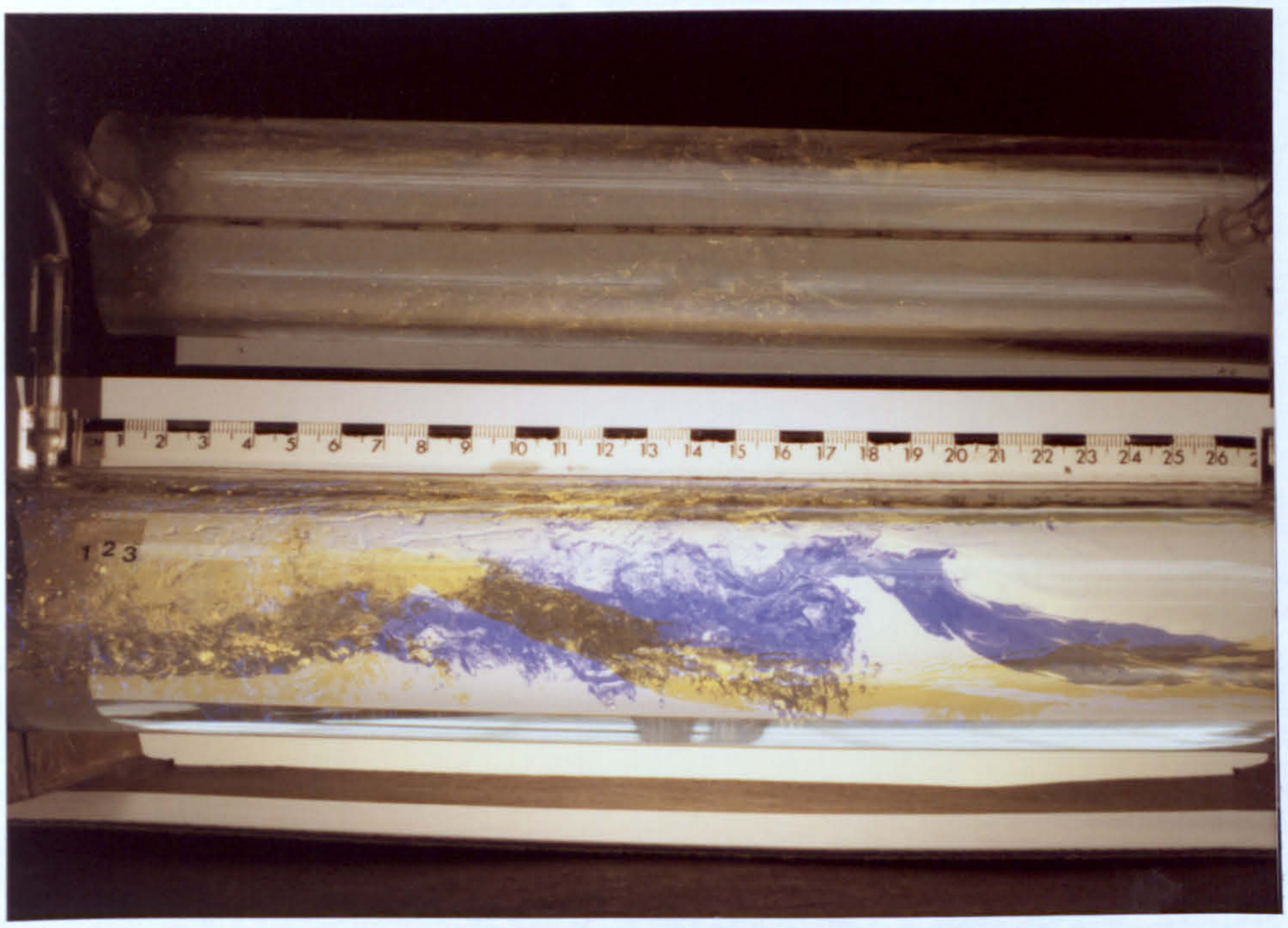

Plate 16

Plate 16 resembles plate 6. Both the blue and the yellow images of the rear of the wave show the surface to be smooth. Unfortunately, little information can be obtained from this shot as the front of the yellow image is off to the left of the picture. Note, this wave, like some others, actually failed to become a slug. The reason for this is unclear from the photographs.

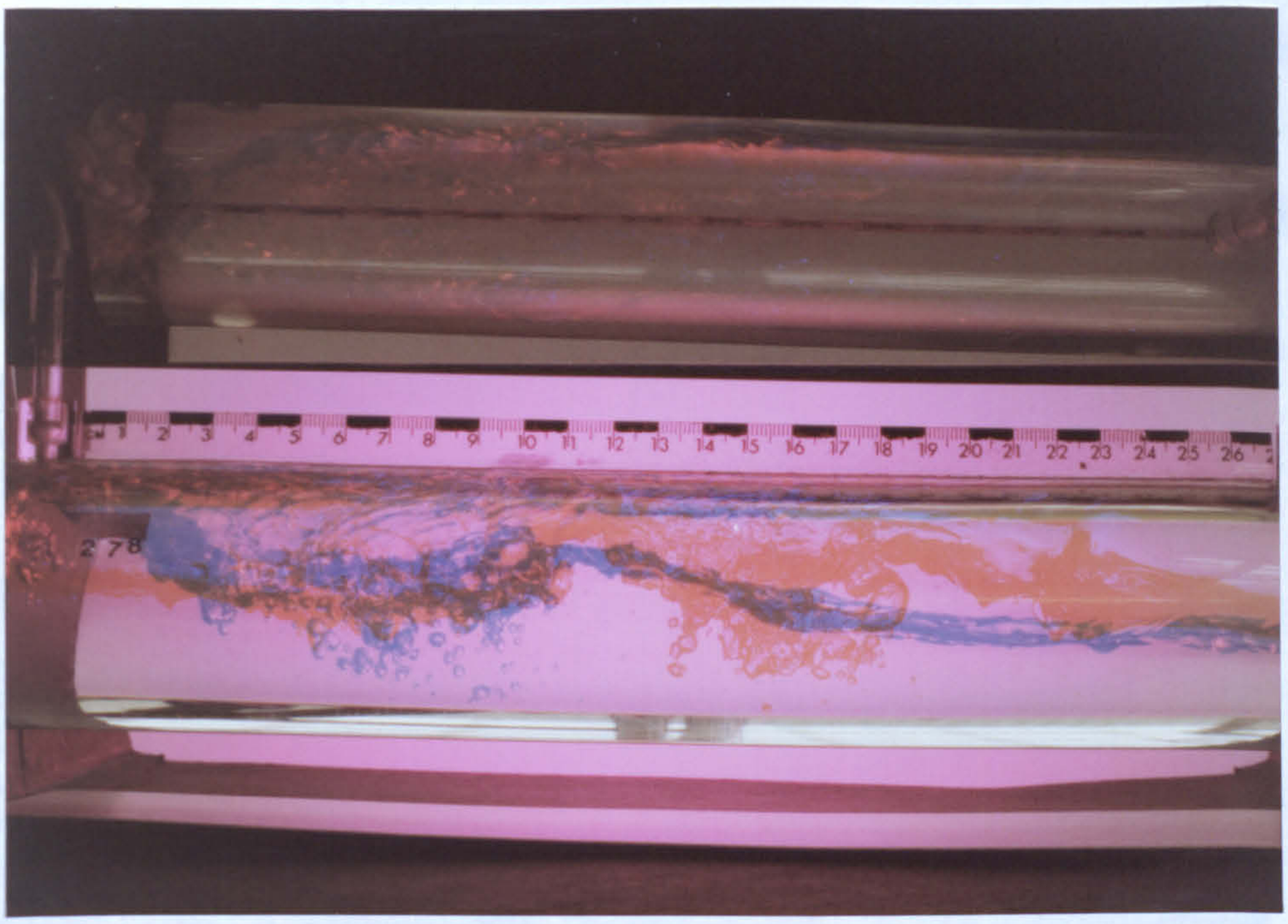

Plate 17

Plate 17 The red wave at between 10 and 13 cm. is actually equivalent to the blue wave at 0 to 3 cm.. The smaller red wave between 19 and 17 cm. actually falls into the rear of the larger wave causing the entrained air as seen in the blue image. The rise in the maximum level of the liquid is at 0.1 m s^{-1} in the 63.5 ms. between the shots.

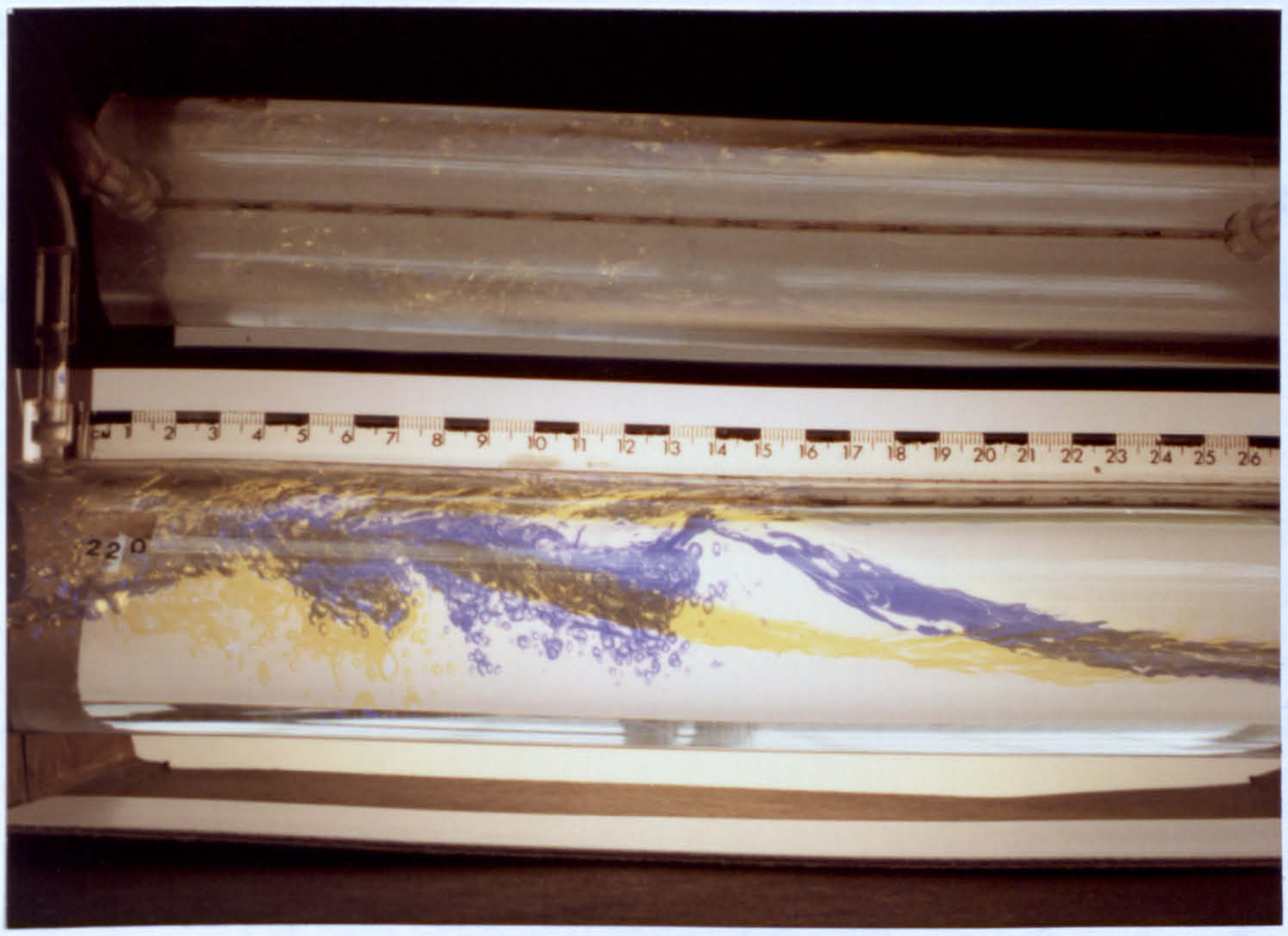

Plate 18

Plate 18 when analysed, shows that the height of the crest has

decreased at a velocity of circa 0.04 m s^{-1} between the flashes (in 69.82 ms.). This is indicative of what the fast ciné has shown to occur after the continuous wave's maximum amplitude has been attained, and entrainment increases resulting in the ultimate destruction of the wave.

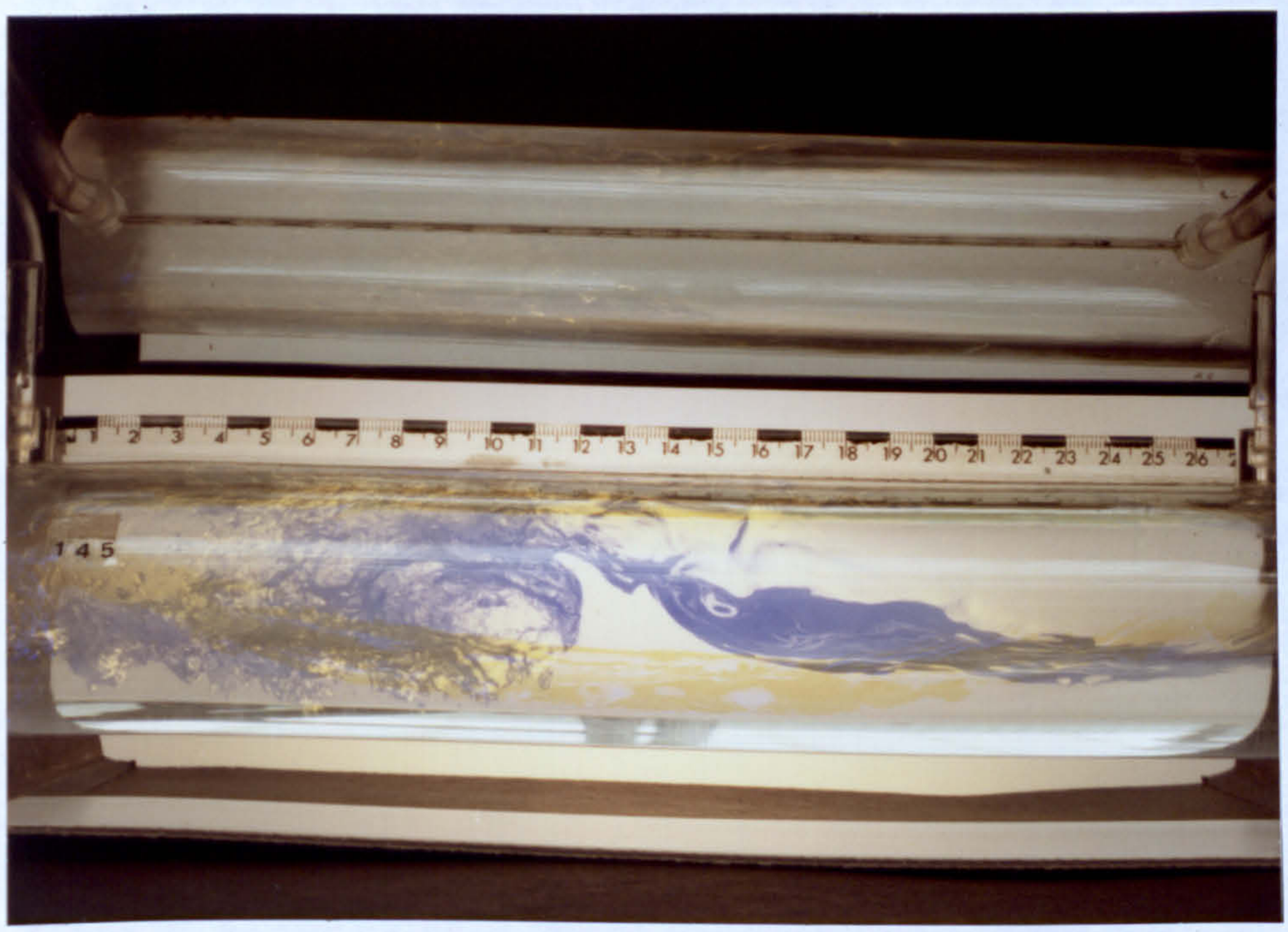

Plate 19

Plates 19 and 20 enable one to obtain more data about the growth rates etc.. Where possible these growth rates were checked with those obtained from measurements taken from the fast ciné photography. In addition, plate 19 affirms that there appears to be a strong rotational flow immediately in front of the wave. The small hump in the liquid interface can also be seen to the far left of the photograph.

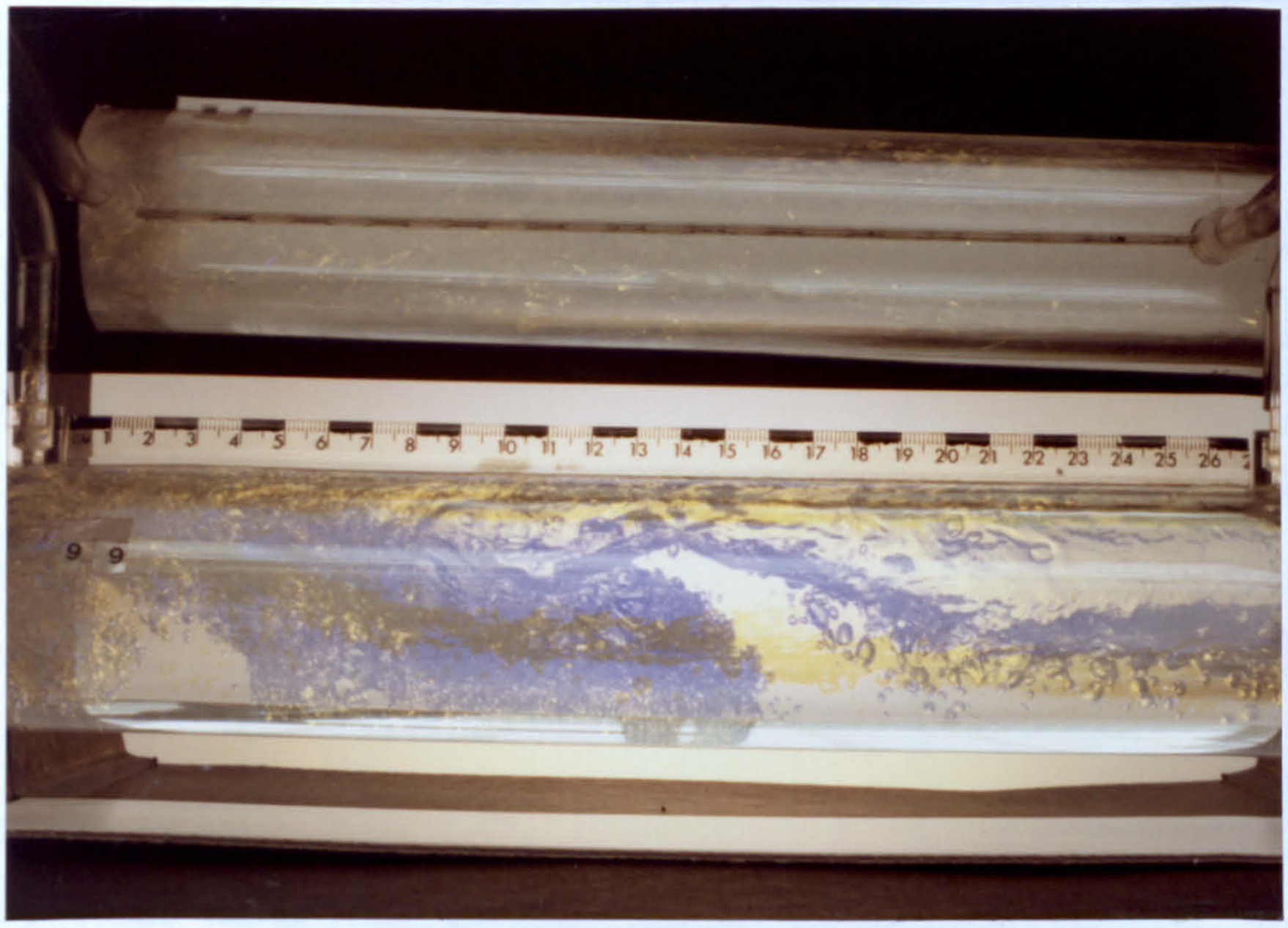

Plate 20

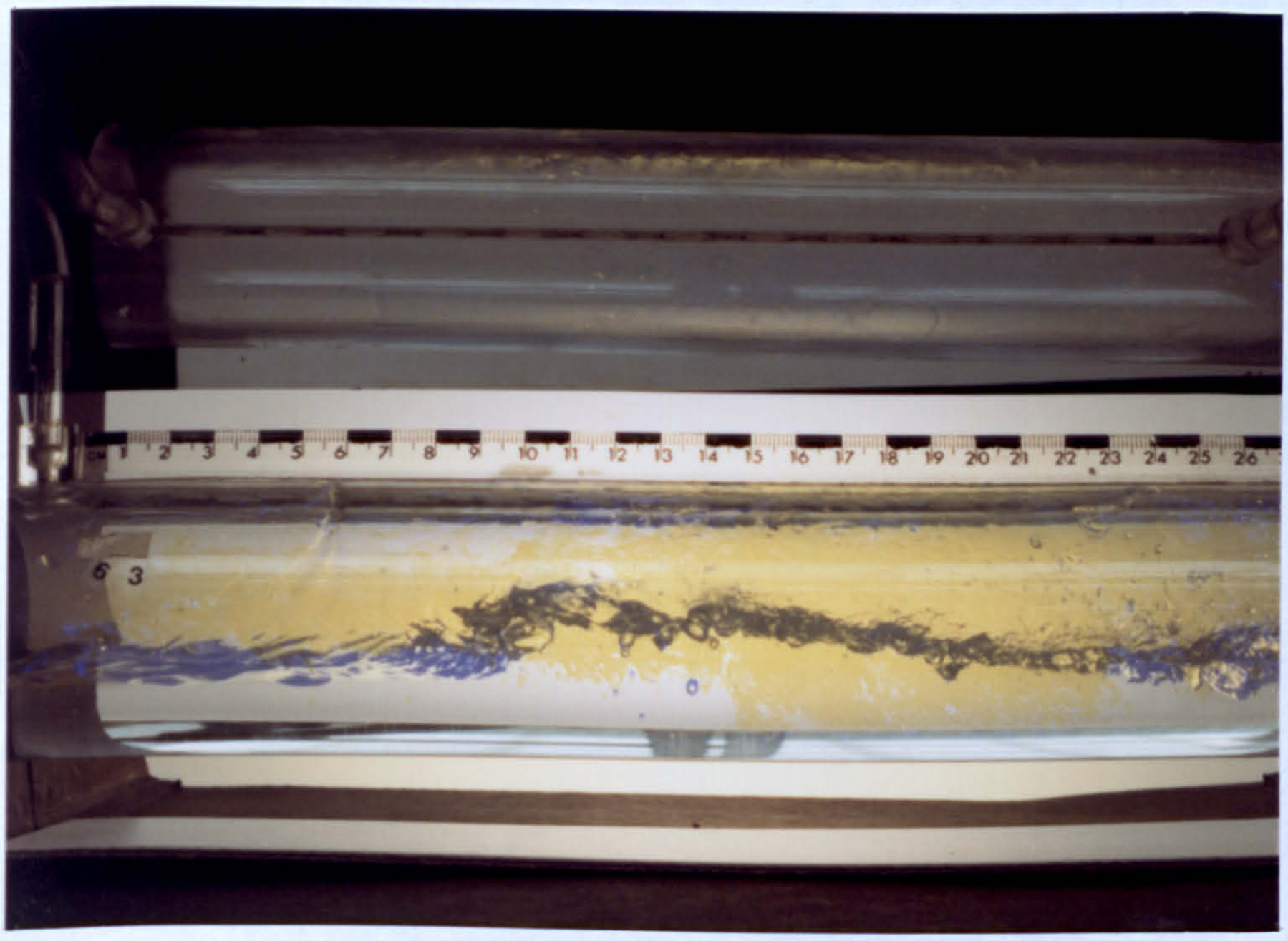

Plate 21

Plate 21 gives an indication of the speed with which the fully formed slug travels (flashes separated by 69.76 ms.). Table 3.1 shows how the vertical velocity of the peak varies for different flows as photographed using this twin flash technique. In the table the Q_i are the mass fluxes of the respective phases, $\frac{a}{d}$ is the amplitude to depth ratio (as defined for the black and white photographs) of the first

photographed wave profile. Also, v is the vertical velocity of the crest and V_G is the gas velocity defined by

$$V_G = \frac{Q_G}{\rho_G A_G} \tag{3.8.1}$$

where Q* is the "relative" mass flux of the gas relative to the liquid (i.e. in the frame of reference moving with the liquid) and is calculated from

$$Q^* = Q_G - \frac{\rho_G A_G}{\rho_L A_L} Q_L \tag{3.8.2}$$

where the ρ_i (i=G or L) are the densities of the respective phases, and the A_i are the actual cross-sectional areas occupied by those fluids on entry to the pipe i.e. those calculated from equilibrium depth of the surface.

Table 3.1

Data concerning some of the twin flash photographs.

Frame	Q_G x 10^{-3} kg s^{-1}	Q_L kg s^{-1}	a/d	v m s^{-1}	V_G m s^{-1}	Q^* x 10^{-3} kg s^{-1}
68	9.51	0.43	0.57	-0.08	4.88	7.85
86	8.75	0.41	1.68	-0.02	4.21	6.64
117	7.19	0.39	1.23	0.04	4.03	6.10
123‡	12.49	0.39	2.13	-0.04	5.76	9.91
129	11.08	0.39	0.86	0.08	5.25	8.87
134	11.08	0.39	0.77	0.07	5.12	8.54
148	8.98	0.45	0.53	0.02	4.72	7.41
155	7.77	0.46	0.62	0.01	4.12	6.21
165‡	6.86	0.46	0.37	0.05	4.44	6.01
175†	5.80	0.46	0.42	0.04	3.26	4.53
186	10.65	0.39	0.45	0.01	5.80	9.45
191	6.73	0.39	0.50	0.12	3.97	5.80
198†	6.73	0.39	1.24	0.01	3.20	4.56
203†	4.67	0.53	0.38	0.01	3.28	3.86
220‡	4.73	0.44	2.03	0.01	2.36	2.80
223	10.21	0.41	1.22	0.01	5.10	8.43
229‡	10.21	0.41	0.92	0.03	5.31	8.72
243†	4.73	0.41	0.21	0.03	2.50	3.32
247	10.21	0.30	1.76	-0.12	4.62	7.94
252	7.22	0.30	0.88	0.01	3.27	4.95
254	7.22	0.30	1.52	0.03	3.50	5.73
255	7.22	0.30	1.93	0.02	3.08	3.37
260	9.08	0.41	1.01	0.02	6.82	8.54
278‡	9.08	0.41	1.06	0.10	9.45	8.78
291	8.69	0.52	1.09	0.01	4.19	6.01
302†	5.86	0.52	0.54	-0.02	3.00	3.83
309	9.27	0.37	1.07	0.18	4.90	8.00
312	9.27	0.37	0.98	0.13	4.90	8.00
314	8.13	0.37	0.53	0.03	4.56	7.10

† data was not in the slug flow régime.
‡ the photograph is in the text.

One major drawback of using the two flash guns was that although the adjustable time interval dictated by the TTL circuitry was adjustable to times of the order of 10 ms., the flash guns would not fire reliably if the time interval was reduced much below 63 ms. (see discussion of the experimental technique later) which limited the usefulness of the information that could be obtained. So, with the experimental apparatus that was available it was impossible to follow the individual droplets by using this method and so the aim of gaining some understanding of the local gas velocity from the droplets was not achieved.

3.9 Discussion of experimental technique

The black and white still photographs of the tube and the inclined mirror impart a lot of information about the mode of the transition to slug flow. These were the easiest of the photographs to obtain, as once the lighting was suitably adjusted no further adjustments needed to be made. The only difficulties with this experimental work, and indeed with all the other experimental work, was actually photographing the slugs in various different stages of growth. Since more versatile equipment was not available this meant that the camera needed to be triggered manually. However, these photographs provide the least quantitative information about the flow. For this reason, and to verify some of the results from the black and white photography, the fast ciné films were taken.

The fast ciné provide most of the quantitative information about the flows. The experimental arrangement was similarly as simple as the black and white photography to arrange, but using fast ciné was very expensive. One draw-back of this method was that the lighting used to film the flow would cause the perspex tubes to sag.

It was desired to obtain information about the pressure fluctuations during slug formation. However, no suitable pressure transducers were readily available. An attempt to obtain some data for the pressure within the gas flow was made using an inclined water manometer to measure the relative pressure between pressure taps on the top of the tube at 30 cm. intervals. A second camera, coupled to the first, both triggered by another circuit (shown in Appendix D) was used to photograph the liquid levels within the manometer corresponding to the stage of slug flow captured in the picture by the first camera. This

was rapidly abandoned because the response of the manometer was so slow and damped, as anticipated.

With the apparatus available the only way of obtaining some knowledge of the gas velocity was by measuring the velocities of small distinct liquid droplets entrained in the gas flow. To this end the multiple flash colour photography was developed. This proved the least successful of all the experimental work. Although the effective design and manufacture of a multiple flash controlling mechanism by means of TTL circuitry had been achieved (Appendix D), the limitations of accurate control of the flash guns did not allow the interval between flashes to be decreased to a sufficiently small interval to really be of any use. This was probably due to poor design of the TTL circuitry by the author. So the photographs, while imparting more information about the interfacial growth rates, slug velocities and qualitative nature of the transition via the breaking wave stage, did not permit measurements of the droplet velocities to be made. So no further understanding of the gas dynamics could be achieved.

Upon reflection, although the theory of using the different coloured flashes to enable two distinct images on one frame to be filtered and studied, triggered with a known time interval was good, perhaps some other means should have been devised, or some more robust electronics manufactured by a more able person than the author. In essence, this is where the problem in the adopted method lay.

Consideration of other methods of illumination, by strobe for instance, still left the problem of filtering the images, since the second image was necessarily further downstream than the first and hence obscured it. The only way around this problem was to use different

colours, or return to the (relatively) expensive fast ciné technique, although this posed its own problems since one could never ensure that in one 16 second reel of film any slugs would form in the camera's field of view, and even if they did, the resolution with the given lighting was not sufficiently good to be able to resolve the movement of the smaller droplets.

It is therefore the robustness of the electronics that needs more attention. The flash guns operated on a "shorting" principle (i.e. when one shorted across the input terminal of the flash gun, the flash gun would trigger). What was needed then was to be able to short each flash gun successively in a known (adjustable) time. This was achieved by means of 5 v. reed relays (Appendix D), the second of which was unreliable, because it in turn was triggered by a signal from the 121 monostable multivibrator which did not trip the relay when the time interval became small. Perhaps the easiest way to have changed this would be to use a smaller capacitor in place of the 3.5 μF capacitor between poles 10 and 11 of the 121 chip, although this may not have solved the problem at the end of the day (i.e the effective shorting of the second flash gun's input).

3.10 Discussion of experimental results

The purpose of conducting this experimental work was basically two-fold. Firstly, a deeper understanding of the mode of transition to slug flow was desired, and secondly, some data pertinent to the flow parameters under consideration was sought.

The exercise to gain deeper understanding of the transition within this particular parameter space was largely successful. The still photographs captured in detail the movement of the liquid within the tube, and even some dispersed droplets and their trajectories could be studied. Entrainment of water droplets into the gas may be due to either, or both, of the following mechanisms. Either droplets can be entrained into the gas from the crest of the growing wave, or from the front of the growing wave. The former is clearly a means by which droplets are initially entrained. If we suggest the possible existence of an eddy or vortex to the front of the growing wave, droplets may be entrained as a result of this. The latter mechanism may be the result of the local interfacial shear stress being high, and droplets being entrained as a result. These photographs also allow estimates of the change in the cross-section of the tube through which the gas may flow to be made. These estimates, together with knowledge of the gas velocity on entry to the pipe, allow estimates of the local gas velocity to be made by using, for instance, the theory of one-dimensional, steady, compressible gas dynamics.

From the "sideways" and "overhead" images no situation where the liquid ever continuously bridged the tube was found. Since the flows under consideration had a small liquid fractional depth a continuous blockage was not expected.

This is verified in the fast ciné films. The high speed ciné confirmed that, for the parameter space under consideration, it would be inappropriate to model slug flow as a bridging of the tube. Indeed, Coney (1974) noted that for a certain sub-domain of the slug flow régime the liquid layer never completely bridged the entire tube cross-section. He termed such flows surge flows, and our experimental observations are in agreement with his. The ciné film showed that once the entrainment of water droplets began, the growth of the waves seemed to be promoted. The waves were then observed to grow rapidly. As the waves grow, their profile closely resembles that of a breaking wave, although it differs from that of a shallow water wave breaking. These waves were considerably steeper than those of a similar initial amplitude to depth ratio on shallow water. The transition to slug flow within the particular domain of interest was always observed to involve the transition through this breaking wave stage. Plates 6, 20 and 21 are typical of the observed surface profile in this breaking wave stage. Furthermore, the fully formed slugs were never observed to be fast moving regions of continuous liquid due to the small liquid fractional depth. Indeed the experiments suggested that in this particular régime the slug is essentially a fast moving body of entrained liquid and that no appreciable wave of water exists for long in the full slug flow.

In addition to increasing understanding about the qualitative nature of the flow, the high speed ciné permitted data for these flows to be gathered. By accurately knowing the framing rate (250 frames per second, accurate to one frame per second), and in conjunction with the gas and liquid mass fluxes, the speed of the slug, growth rates and some tentative idea of the speed of the gas from the droplet velocities could be obtained. This data allows theoretical models to be checked via comparisons with interfacial velocities etc.

3.11 Conclusions

The experiments provided a greater understanding of the qualitative nature of the slug flow for the particular parameter space under consideration. The "bridging model" suggested by Dukler & Hubbard (1975) would appear to be inadequate at modelling this particular slug flow for which the liquid fractional depths of circa $\frac{1}{3}$ are small, whilst the observations of this work are in general agreement with those of Wallis & Dobson (1973), and in good agreement with those of Coney (1974).

The resemblance of an intermediate stage in the transition to slug flow with breaking water waves is clear, and for the flows considered such a profile appeared to be a characteristic of the transition. Furthermore, it appears that within this domain a fully formed slug is not a region of continuous (slightly aerated) liquid. Rather, it is essentially a region of densely entrained droplets. So, whilst no entrainment can begin without the growing wave, the wave ultimately becomes the slug, but in an entrained droplet form rather than in a more-or-less continuous form.

Data obtained from the fast ciné, and to some extent from the multi-flash colour photography, provides the initial conditions and checks that are used in the theoretical modelling and numerical work on flows in this parameter range. The results suggest that for mixture Froude numbers in the range of 9 to 44 and equilibrium depth to tube diameter ratio between 0.33 and 0.38, the initial disturbance amplitude to equilibrium depth ratio appears to be in the range 0.15 and 0.30.

4. SLUG FLOW AS A WAVE MOTION

4.1 Introduction

In the experimental work in Chapter 3 we saw that as the slug grew from its initially small size to its fully formed state - largely consisting of entrained droplets - it appeared to go through a breaking wave stage, when the slug almost filled the entire tube. Perhaps then, we could model the initial stages of the growth of the slug in a similar manner to breaking water waves, and perhaps even model the slug growth up to its breaking stage (as shown in plate 6 on page 57).

Stoker (1957) Art. 10.10 discusses breaking shallow water waves. He points out that there is a great difference in the modes of propagation of the front and of the back of a wave. The backs generally smooth out, while the fronts tend to steepen and even break. This difference arises because the speed of propagation of the wave tends to increase with the wave height: the higher points within a wave tend to travel faster than their lower neighbours, and so the higher points overtake the lower ones and the wave steepens and breaks.

Stoker also discusses the form that the wave profile may take. He discusses solitary waves in great detail. A solitary wave is the only steady, single-humped wave that can propagate over a liquid which is at rest at infinity. In fact, Stoker defines a solitary wave as "a wave of finite amplitude consisting of a single elevation of such a shape that it can propagate unchanged in form". Solitary waves are a good choice of initial wave profile because water waves are often observed to have a similar shape, while the treatment of wave motions as a sinusoidal wave train, say, is not a good representation in many situations.

Furthermore, solutions of the weakly non-linear Korteweg-de Vries equation for initial value problems by using the inverse scattering transform show how solitary waves are a dominant feature of moderately long water-wave dynamics.

Most two-phase flow models rely upon some feature which can be thought to be a characteristic trait of that flow (bridging the tube cross-section for example). The above experimental work suggests that, within the parameter range under consideration, a bridging model for slug flow is inappropriate. Rather, the initial stages of slug growth resemble that of a breaking wave motion. Perhaps by treating the initial stages of slug growth as a water wave phenomenon, the form of the wave profile and other relevant information about the initial stages can be obtained.

Various numerical techniques have been developed to compute the breaking of water waves, the most successful of which is the boundary integral method which we briefly describe in the following section.

4.2 The boundary-integral method

Dold & Peregrine (1986) review boundary-integral methods for numerically calculating inviscid water wave motions, and they outline an efficient and accurate Cauchy-theorem boundary-integral method. The following discussion concentrates upon the Cauchy integral theorem method.

The motion of an inviscid, irrotational, incompressible fluid can be determined by the motion of the boundary (free surface) alone. Thus, numerically, the motion of a fluid may be determined from a point discretisation of the surface, and this greatly reduces the number of variables compared with discretisations of the entire liquid volume within the problem leading to increased numerical efficiency. The boundary-integral approach was first used by Longuet-Higgins & Cokelet (1976). The method used here was developed by Dold, Peregrine and Lewy at the University of Bristol to describe fluid motions, building on work by Baker, Merion & Orszag (1982), amongst others.

By assuming that a liquid is incompressible and irrotational we may define a velocity potential of the liquid, ϕ_L, where ϕ_L is a harmonic function of the spatial co-ordinates, and satisfies Laplace's equation:

$$\nabla^2 \phi_L = 0 \qquad (4.2.1)$$

We shall restrict our attention to two-dimensional flows. If we consider a fluid motion over an impermeable, horizontal bottom at $y = -h_B$, then the boundary condition on this boundary is:

$$\frac{\partial \phi_L}{\partial y}(x,-h_B,t) = 0 \qquad (4.2.2)$$

The time-varying free surface is expressed as:

$$\underline{r} = \underline{R}(\zeta,t) \qquad (4.2.3)$$

where ζ is a parameter which is chosen to be a Lagrangian co-ordinate following particles in the surface. Then, given ϕ_L on the surface we may obtain $\frac{\partial \phi_L}{\partial s}$ where s is a co-ordinate along the surface, but in order to step forward in time we must find $\frac{\partial \phi_L}{\partial n}$ where n is a co-ordinate normal to the surface, and then we don't need to know ϕ_L within the bulk of the liquid. The kinematic and dynamic boundary conditions on the surface may be written as:

$$\frac{DR}{Dt} = \underline{u} = \underline{\nabla}\phi_L \qquad (4.2.4)$$

$$\frac{D\phi_L}{Dt} = \tfrac{1}{2}\underline{u}^2 - \left(\frac{p}{\rho_L} + gy\right) \qquad (4.2.5)$$

respectively, and $\frac{D}{Dt}$ is the convective derivative and where the dynamic boundary condition is Bernoulli's equation for the liquid, p is the pressure on the surface and ρ_L is the liquid density. With these we may obtain the necessary information for time stepping the surface profile. Much previous work has dealt with water waves, such as waves up beaches, in which the surface pressure distribution could be taken as a constant, and arbitrarily zero. To model various different solutions the surface pressure distribution needs to be defined in accordance with the problem. For example, surface tension could be included in the model by defining a pressure such that:

$$p = p_o - \sigma_s K$$

where p_o is the pressure above the surface, σ_s is the surface tension

and K is the curvature of the surface. In order to follow the motion of the surface profile (the wave) a number of methods for solving Laplace's equation have been developed. They differ in their accuracy, efficiency and stability. Here we outline the Cauchy-theorem approach.

Cauchy's Integral Theorem. Cauchy's integral theorem can be applied to a complex velocity:

$$q(z) = u - iv$$

where q(z) is an analytic function of the complex position, z = x + iy. Then the normal gradient of ϕ_L may be written (Dold & Peregrine (1986))

$$\pi\frac{\partial\phi_L}{\partial n} = \int_C \mathrm{Im}\left[\frac{1}{z'-z}\,\frac{\partial z}{\partial s}\right]\frac{\partial\phi_L'}{\partial n}dS' + \int_C \mathrm{Re}\left[\frac{1}{z'-z}\,\frac{\partial z}{\partial s}\right]\frac{\partial\phi_L'}{\partial s}dS'$$

where primes denote integration variables and where differentiation with respect to s and n are with respect to the arclength and the normal respectively and the integrals are for principal values. The arclength is measured in a clockwise sense, and C is the contour around the fluid. The resulting equations may be solved iteratively.

Since successive Eulerian time derivatives of the liquid velocity potential (ie. ϕ_{Lt}, ϕ_{Ltt}, etc.) satisfy both Laplace's equation and the same bottom boundary condition as ϕ_L, and these derivatives are the potential functions for the appropriate Eulerian time derivatives of the liquid velocity, they can be efficiently evaluated. With these derivatives the time dependent motion of the surface profile, and the velocity potential, can be expressed in terms of Taylor series expansions in time, following the fluid particle.

The implementation of the Cauchy integral formulation in this fashion is introduced and discussed in Dold & Peregrine (1986). They show that the scheme is efficient and accurate for describing a variety of wave phenomena. The Cauchy formulation has been used extensively. It has been used to model the run up of waves on beaches and the motion of fluids around submerged structures, or over various bottom topographies. These applications either modify the surface discretisation (to deal with the end point of the fluid domain; where it comes into contact with a beach, say), or the domain of the conformal mapping (to take into account the submerged structure).

With these advantages in mind, and because of expertise in using this scheme by colleagues of the author, the numerical scheme of Dold & Peregrine (1986) as extended by Tanaka, Dold, Lewy & Peregrine (1987) to study breaking solitary waves was used as the basis for the numerical scheme to describe the initial stages of slug flow in a channel. It must be stressed that the above outline of boundary integral methods is only intended as a brief introduction, and that a comprehensive review of boundary integral methods and the detail concerning the implementation of the Cauchy theorem algorithm may be found in Dold (1990 - to appear).

4.3 Using a boundary integral method for the initial stages of slug growth in horizontal two-phase flow.

To correctly describe a surface motion the pressure distribution on the surface must be defined in accordance with the particular problem that is being modeled. In modelling the initial stages of the wave growth in co-current two-phase gas-liquid slug flow it is necessary to model the motion of the gas over the underlying liquid. In particular, the modification of the interfacial pressure distribution on the interface is required.

Consider gas flowing through a slowly varying converging-diverging nozzle. In such a case the gas is often treated as being quasi-steady and one-dimensional. One-dimensional because the slopes in the nozzle are gentle and so the flow in a direction to the free stream flow is relatively insignificant. Quasi-steady because the entire flow is established quickly due to the fast communication of flow conditions throughout the entire flow field. If we consider our two-dimensional liquid flow in a closed channel to define a nozzle for the overlying gas flow. Then provided that the liquid surface has only gentle slopes (in analogy with the slowly varying nozzle) and that the motions of the liquid are sufficiently slow so that changes in the "liquid nozzle" geometry are communicated throughout the gas much faster than these changes occur within the liquid, then perhaps we may, to a first approximation, treat our gas-liquid two-phase flow as an unsteady two-dimensional liquid motion with a coupled quasi-steady onedimensional gas motion. If the gas is also considered to be an ideal gas, then we may use well known relationships to determine the variation of the gas pressure with changing liquid height (e.g. Schreier (1982) p.50).

Using these assumptions, and provided that there is no separation of the gas flow over the liquid layer, we consider the gas in the form of a

quasi-steady one-dimensional model. Then we may use the following standard results for one-dimensional compressible ideal gas flow

$$\frac{A_{Go}}{A_G} = \frac{M}{M_o}\left[\frac{1 + \frac{\gamma-1}{2}M^2}{1 + \frac{\gamma-1}{2}M_o^2}\right]^{\frac{1}{2}-\frac{\gamma}{\gamma-1}} \qquad (4.3.1)$$

and

$$\frac{\rho_{Go}}{\rho_G} = \left[\frac{1 + \frac{\gamma-1}{2}M^2}{1 + \frac{\gamma-1}{2}M_o^2}\right]^{\frac{1}{\gamma-1}} \qquad (4.3.2)$$

with reference to Fig. 4.1,where γ is the ratio of the specific heats for the gas and where A_G is the cross-sectional area through which the gas may flow with density ρ_G at some position along the tube and where the Mach number is M. A_{Go} is a reference cross-section where the gas density, ρ_{Go} and the Mach number, M_o are known.

Diagram of definition for terms used in the one-dimensional equations of motion of the gas

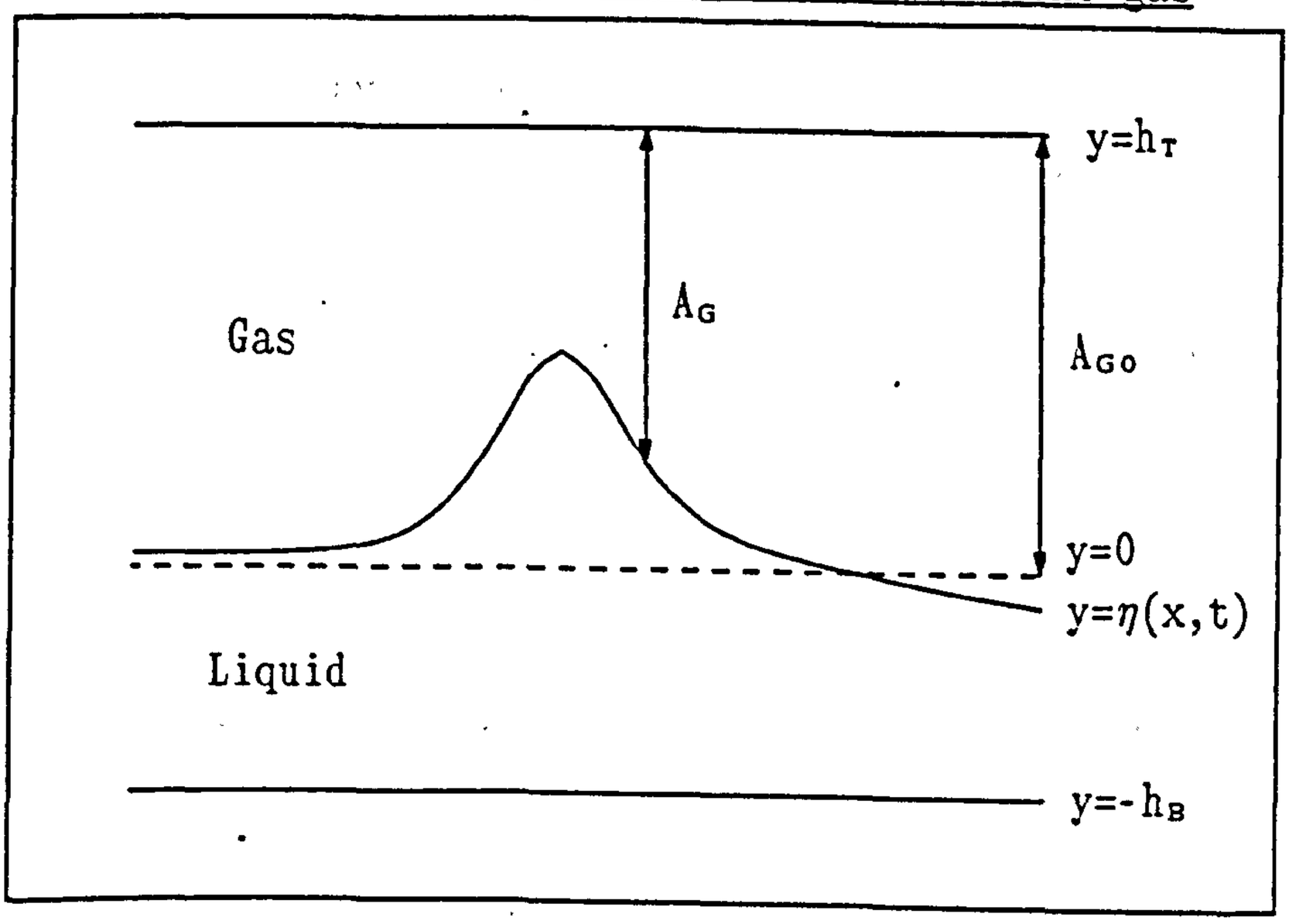

Fig. 4.1

In the case of one-dimensional gas flow through a two-dimensional pipe, the areas through which the gas is free to flow, A_G may be expressed as

a height per unit width:

$$A_G = h_G b \tag{4.3.3}$$

where b is the width. In principle, then, given any initial surface profile, $y=\eta(x,0)$, we know the size of the gas gap through which the gas may flow:

$$h_G(x,0) = h_T - \eta(x,0) \tag{4.3.4}$$

and given the Mach number of the gas and its density on entry to the pipe (far upstream), we may then derive the gas density everywhere from (4.3.2), and thus the pressure everywhere since:

$$p = \kappa \rho_G^{\gamma} \tag{4.3.5}$$

for an ideal gas, where κ is a gas constant and γ is the ratio of the specific heats. Having defined the pressure everywhere on the surface we may then use the boundary integral scheme to calculate the motion of the liquid, and then step the time forward and repeat the process for the new surface profile $y=\eta(x,t)$. In this way the motion of the wave profile may be predicted and followed.

The numerical scheme requires the first and second Lagrangian derivatives of the surface pressure distribution with time. Consider the steady compressible Bernoulli equation:

$$\frac{\gamma}{\gamma-1}\frac{p}{\rho_G} + \tfrac{1}{2}u_G^2 = \text{const} \tag{4.3.6}$$

For a gas flow where the gas mass flux, Q_G, is known and constant

and given by

$$Q_G = \rho_G u_G A_G \tag{4.3.7}$$

We may differentiate (4.3.6) with respect to the Eulerian spatial position, and hence:

$$\frac{d\rho}{dx} = \frac{\frac{Q_G^2}{A}\frac{dA_G}{dx}}{\gamma\kappa A^2\rho_G^\gamma - \frac{Q_G^2}{\rho_G}} \tag{4.3.8}$$

Similarly, we may obtain the second derivative

$$\frac{d^2\rho}{dx^2} = \frac{-\frac{Q_G^2}{A_G^2}\left[\frac{dA_G}{dx}\right]^2 + \frac{Q_G^2}{A_G}\frac{d^2A_G}{dx^2} - \left[\gamma^2\kappa A_G^2\rho^{\gamma-1} + \frac{Q_G^2}{\rho_G^2}\right]\left[\frac{d\rho_G}{dx}\right]^2 - 2\gamma\kappa A_G\rho_G^\gamma\frac{dA_G}{dx}\frac{d\rho_G}{dx}}{\gamma\kappa A_G^2\rho_G^\gamma - \frac{Q_G^2}{\rho_G}} \tag{4.3.9}$$

Now, using (4.3.5) we may relate pressure variations to density variations

$$\left.\begin{aligned}\frac{dp}{dx} &= \kappa\gamma\rho_G^{\gamma-1}\frac{d\rho_G}{dx}\\ \frac{d^2p}{dx^2} &= \kappa\gamma\rho_G^{\gamma-1}\left[\frac{\gamma-1}{\rho_G}\left(\frac{d\rho_G}{dx}\right)^2 + \frac{d^2\rho_G}{dx^2}\right]\end{aligned}\right\} \tag{4.3.10}$$

Similarly we may relate the Eulerian derivatives (4.3.10) to the Lagrangian derivatives on the surface:

$$\left.\begin{aligned}\frac{Dp}{Dt} &= \frac{\partial p}{\partial t} + u_L\frac{\partial p}{\partial x}\\ \frac{D^2p}{Dt^2} &= \frac{\partial p}{\partial x}\frac{Du_L}{Dt} + u_L^2\frac{\partial^2 p}{\partial x^2}\end{aligned}\right\} \tag{4.3.11}$$

Consider the first of equations (4.3.11). The first term on the right hand side is the partial pressure derivative with respect to time.

Since we have assumed that changes in the gas flow occur much more rapidly than changes in the liquid surface, and that we may then regard the gas as quasi-steady, we set this term to zero. While this term is not quite zero even on the liquid time scale, as we notice that the pressures do change throughout our calculations, we maintain this approximation for simplicity. Likewise, the second term should take the form $\underline{u}_L.\hat{\underline{s}}\frac{\partial p}{\partial s}$, where s is the arclength along the surface, rather than that shown in (4.3.11), though in principle we assume that such differences are negligible. These simplistic approximations are made to avoid having to write a substantial new program for an exercise which is primarily aimed at giving a physical "feel" for the problem.

So, given the initial variation of A_G ($=h_G b$) with x we may solve (4.3.1) for the Mach number of the gas everywhere. Hence, from (4.3.2), we know ρ_G everywhere, and then (4.3.5) and (4.3.11) supply the value of the pressure and the first two of its derivatives on the surface. These values and derivatives are required in Bernoulli's equation (and the derivatives of Bernoulli's equation), giving:

$$\frac{\partial \phi_L}{\partial t} = - \left\{ \frac{p}{\rho_L} + gy + \tfrac{1}{2}\underline{u}_L^2 \right\}$$

$$\frac{\partial^2 \phi_L}{\partial t^2} = - \left\{ \frac{1}{\rho_L}\frac{Dp}{Dt} + \underline{u}_L . \left[\frac{D\underline{u}_L}{Dt} + \frac{\partial \underline{u}_L}{\partial t} + g\hat{j} \right] \right\}$$

$$\frac{\partial^3 \phi_L}{\partial t^3} = - \left\{ \frac{1}{\rho_L}\frac{D^2 p}{Dt^2} + \underline{u}_L \cdot \left[\frac{D^2 \underline{u}_L}{Dt^2} + 2\frac{\partial^2 \underline{u}_L}{\partial t^2} + \underline{\nabla}\left(\underline{u}_L \cdot \frac{\partial \underline{u}_L}{\partial t}\right) + \left[\frac{\partial \underline{u}_L}{\partial t}\cdot\right]^2 \right] + \frac{D\underline{u}_L}{Dt} \cdot \left[\frac{D\underline{u}_L}{Dt} + g\hat{j} \right] \right\}$$

And thus we may set up the Taylor series (in time) for advancing the surface profile. This Taylor series is one feature of the program which gives it stability and efficiency, Tanaka, Dold, Lewy & Peregrine (1987).

4.4 Numerical results for air-water two-phase flow

In the following numerical work we shall consider gas and liquid flowing from right to left (in common with the experimental results of Chapter 3). We shall also take the shape of the initial wave profile to be that of a solitary wave. While this may not be considered an obvious choice for the initial profile for a slug flow, there are several reasons why this choice is, perhaps, an adequate one.

Firstly, we are interested in the mode of growth of a single wave, and not of a wave train. Secondly, solitary waves may often be used to describe other water waves, and so comparisons with these wave motions, such as breaking shallow water waves, is possible. Thirdly, this is a convenient family of waves specified by one parameter, the initial amplitude to depth ratio (Fig. 4.2). This provides all of the information about the solitary wave; its shape, its speed and whether the wave is stable or whether it breaks. Finally, and most importantly, as mentioned in §4.1, solitary waves emerge as "natural waves" in shallow water systems. If we consider travelling waves a shallow water wave system which may be described by the Korteweg-de Vries equation, then solitary waves naturally evolve out of these travelling waves.

Diagram of definition for amplitude to depth ratio

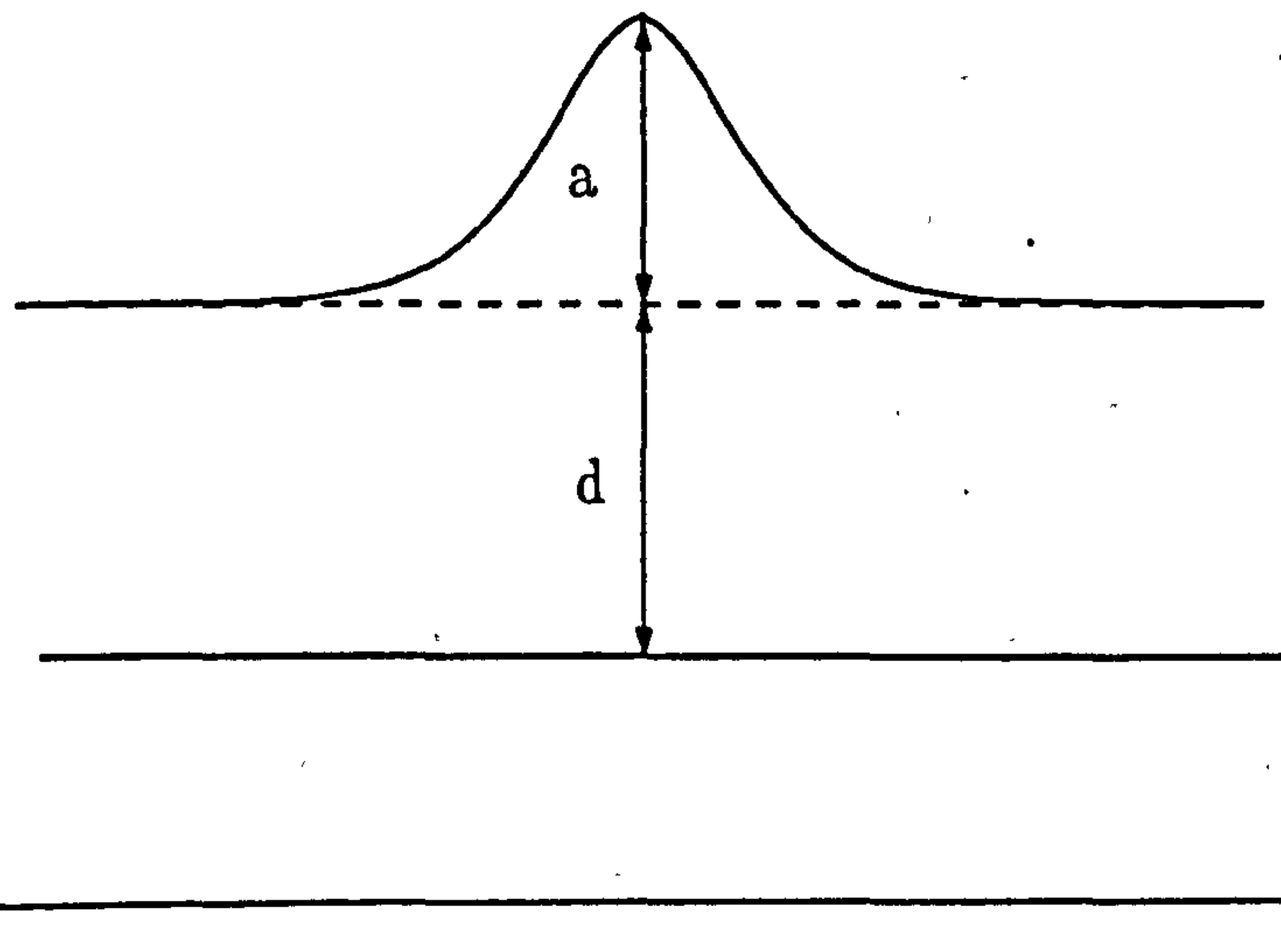

Fig. 4.2

In this chapter we are primarily concerned with the motion of the liquid phase. To make the scheme independent of particular situations we need to define representative dimensionless parameters. For the motion of liquids such as water gravity and inertia are the dominant influences on the flow. To reflect this we define the following dimensionless variables (dimensionalised with respect to the equilibrium depth of liquid, h_B, and the acceleration due to gravity, g, and the liquid density, ρ_L):

$$\tau = t\sqrt{\frac{g}{h_B}} \ , \ \xi = \frac{x}{h_B} \ , \ u = \frac{u_G}{\sqrt{gh_B}} \ , \ v = \frac{u_L}{\sqrt{gh_B}} \ , \ \rho = \frac{\rho_G}{\rho_L} \ , \ \sigma = 1 \ , \ p = \frac{p}{\rho_L g h_B}$$

where τ is the dimensionless time, ξ the dimensionless position. u and v the velocities, ρ the dimensionless gas density, σ the dimensionless liquid density and p is the dimensionless pressure.

Consider a solitary wave of amplitude to depth ratio 0.5, say, on a depth of 1.0 (where this is the dimensionless depth). We know that for this ratio the wave amplitude is preserved for all time in the absence of surface pressures. However, if we define a wave with amplitude to depth ratio of 0.5 on a depth of 1.0, and then put the wave profile with these characteristics onto a depth of 0.5, then the wave may no longer be stable.

This numerical scheme is capable of modelling the growth of a wave, or a wave train, and the subsequent breaking of the wave(s). Fig. 4.3 shows what happens to a solitary wave with the characteristics of a wave of amplitude to depth ratio 0.5 when put on a depth of 0.5. The motion of the wave, and its subsequent breaking, is calculated using the above mentioned Cauchy theorem boundary-integral scheme.

Breaking wave profile of a wave of amplitude to depth ratio 0.5 on a depth of 0.5.

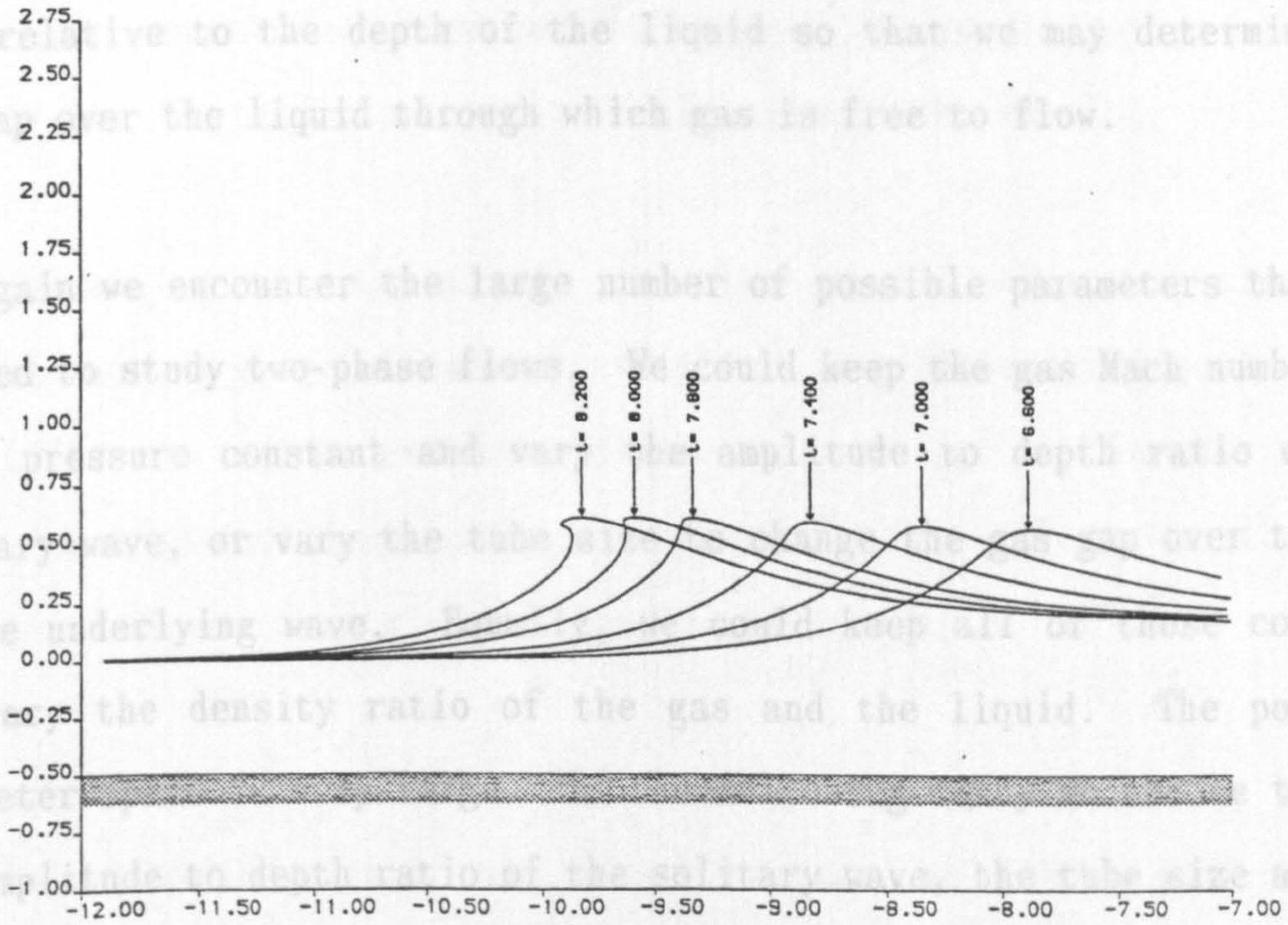

Fig. 4.3

When including the motion of a one-dimensional gas flow over the liquid we have a few problems with implementation to overcome. Clearly we may suspect that the gas flow over a liquid motion like that of

Fig. 4.3 is no longer one-dimensional. Indeed, as soon as either the front or the rear surface of the wave profile becomes steep we can expect inaccuracy.

In practice we also find that the calculation becomes inaccurate because as the surface is drawn upwards curvatures near the crest become large, and points on the sloping surfaces are being rapidly drawn apart. By this time the slopes are usually very steep, and as a result, the calculation is terminated.

Whilst we know everything we need to know about the motion of the liquid by specifying the amplitude to depth ratio of the solitary wave, in order to model two-phase flows we must specify two more parameters. One of these is the speed of flow of the gas, and hence the gas Mach number, relative to the liquid motion. The other is the size of the tube relative to the depth of the liquid so that we may determine the gas gap over the liquid through which gas is free to flow.

Again we encounter the large number of possible parameters that can be used to study two-phase flows. We could keep the gas Mach number and entry pressure constant and vary the amplitude to depth ratio of the solitary wave, or vary the tube size to change the gas gap over the top of the underlying wave. Equally, we could keep all of these constant and vary the density ratio of the gas and the liquid. The possible parameter space is very large. In the following study we choose to keep the amplitude to depth ratio of the solitary wave, the tube size and the density ratio constant and vary only the gas Mach number and the gas entry pressure. While this does not allow all of the possible effects to be studied, it is felt that such a study would be impractical at present.

Once these are specified, the one-dimensional motion of the gas, and hence the surface pressure variation on the gas-liquid interface, may be determined at each time step, and so the motion of both fluids predicted within this approximation.

From the experiments of Chapter 3 in which the gas entry pressure is approximately atmospheric, the undisturbed liquid level is about $\frac{1}{3}$ of the way up from the bottom of the tube (the ratio of liquid to gas cross-sectional area for a liquid depth of $\frac{1}{3}$ is circa 0.4 .). We may then choose the liquid level, and hence the tube diameter in our two-dimensional model, in various ways. We may preserve the area ratio, so for liquid of depth 1.0 we require a tube diameter of 3.5; or we may preserve the depth of liquid in the tube which gives a tube diameter of 3.0 for a liquid depth of 1.0; or we may use some more sophisticated approach. In our numerical calculations the depth ratio (liquid fractional depth) is preserved. However, it would be possible to examine how the variation of this ratio affects the results.

Determining the appropriate relative gas velocity, on the other hand, is not as easy. In actual two-phase slug flows the liquid and gas velocities are determined by effects that we exclude in the present study, such as turbulent shear stresses, and these affect the flow over a longer time and length scale than we are interested in.

Our model, however, is a simple wave motion model. We can specify any liquid velocity and gas velocity, and the scheme will give a resulting wave motion. This arises because we have neglected viscosity, vorticity and turbulence, and have not entirely modeled the physics of the problem.

Clearly, this is an important limitation of the model and numerical algorithm - we may get numerical answers for totally unphysical flows.

The numerical scheme requires the gas velocity (or more precisely, the gas Mach number) to be known everywhere within the computational domain so that the steady one-dimensional model may be used to determine the gas density (and hence, the pressure). Rather than use the superficial gas velocity (defined over the tube cross-section) to obtain the gas Mach number, we obtain a better approximation by considering the (approximate) cross-sectional area of the tube that the gas actually flows through when the gas-liquid interface is in its undisturbed position. Since we know the gas and liquid mass fluxes, then

$$M_G = \frac{u_G}{a} = \frac{Q_G}{a\rho_G A_G} \qquad (4.4.1)$$

We may similarly define a dimensionless gas flux per unit width:

$$Q_G^* = \frac{Q_G}{\rho_L h_B \sqrt{g h_B}} \qquad (4.4.2)$$

Table 4.1 shows some experimentally determined gas and liquid mass fluxes, the corresponding equilibrium depth of liquid in the tube and the Mach number of the gas defined by (4.4.1). We are primarily concerned with Mach numbers ~0.02. We expect compressibility effects to go as the square of the Mach number, and so we expect compressibility to have a small effect. At this stage we retain compressibility so that we may compare compressible and incompressible calculations. In the table we assume that the entry gas density is 1.225 kg m^{-3} (corresponding to atmospheric entry conditions at 15°C). We consider a tube of internal diameter 50 mm and liquid of density 1000 kg m^{-3}.

Table 4.1

Relationship of gas and liquid mass fluxes to the gas Mach number for various depths of liquid

depth of liquid mm	Q_L kg s^{-1}	Q_G $x10^{-3}$ kg s^{-1}	M_G
12	0.390	11.084	0.024
12	0.390	12.457	0.026
13	0.409	8.752	0.019
16	0.368	7.774	0.017
16	0.455	8.977	0.020
16	0.455	9.266	0.021
17	0.407	9.804	0.022

If we assume a different gas entry pressure, and hence a different gas entry density and sound speed (at the same temperature) then, from equation (4.4.1), are be considering different gas Mach numbers (because the gas velocity remains constant since the gas mass flux is constant, while the sound speed changes). Table 4.2 shows how the gas Mach number varies with entry pressure for constant gas mass flux.

Table 4.2

Relationship between gas Mach numbers at various entry pressures

M_G 1 atm	M_G 1.1 atm	M_G $x10^{-3}$ 5 atm	Q_G $x10^{-3}$ 1 atm
0.01	0.0092	2.517	8.74
0.02	0.0184	5.034	17.48
0.03	0.0276	7.551	26.22
0.04	0.0369	10.100	34.96
0.05	0.0461	12.603	43.70
0.06	0.0553	15.101	52.44

Below we present the results for entry pressures of 1 atm, 1.1 atm and 5 atm. For all these results we consider a dimensional depth of liquid of $\frac{1}{3}$ of 50 mm (which is our dimensionless depth of 1.0) and we

consider waves of amplitude to depth ratio of 0.2, which appears to be representative of the propagating smooth water waves observed in the experiments of Chapter 3. By fixing the parameters for the solitary wave to these values (within the range of values found experimentally) we may then investigate the effect of changing the gas Mach number to see whether we promote slug growth.

Figs. 4.4 to 4.7 relate to two-phase flows for which the gas entry pressure is 1 atmosphere. In obtaining these results we find that the rapid growth of the amplitude of the wave (which we shall refer to as the initiation of slug growth) occurs very suddenly. For instance, Fig. 4.4 depicts a flow with gas mass flux corresponding to a gas Mach number of 0.0388. The surface starts to grow very rapidly, and the numerical calculation ceases after a dimensionless time of τ=6.75 (dimensional time of t=0.278 s).

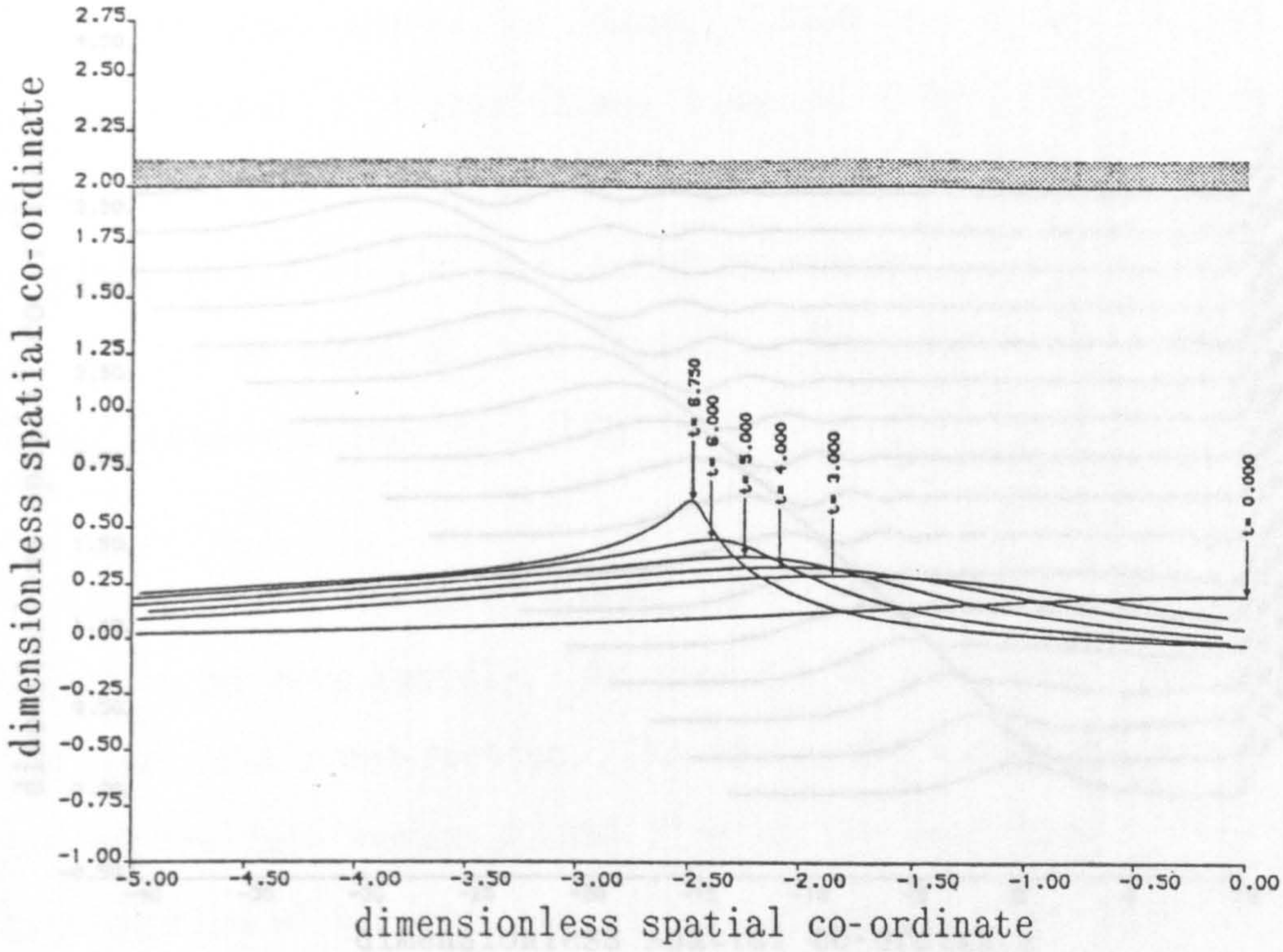

Fig. 4.4

Fig. 4.4 just showing the transition to slug flow with gas at 1 atm. entry pressure and Mach number 0.0388 at dimensional times t≃0, 0.37, 0.49, 0.62, 0.74 and 0.83 s.

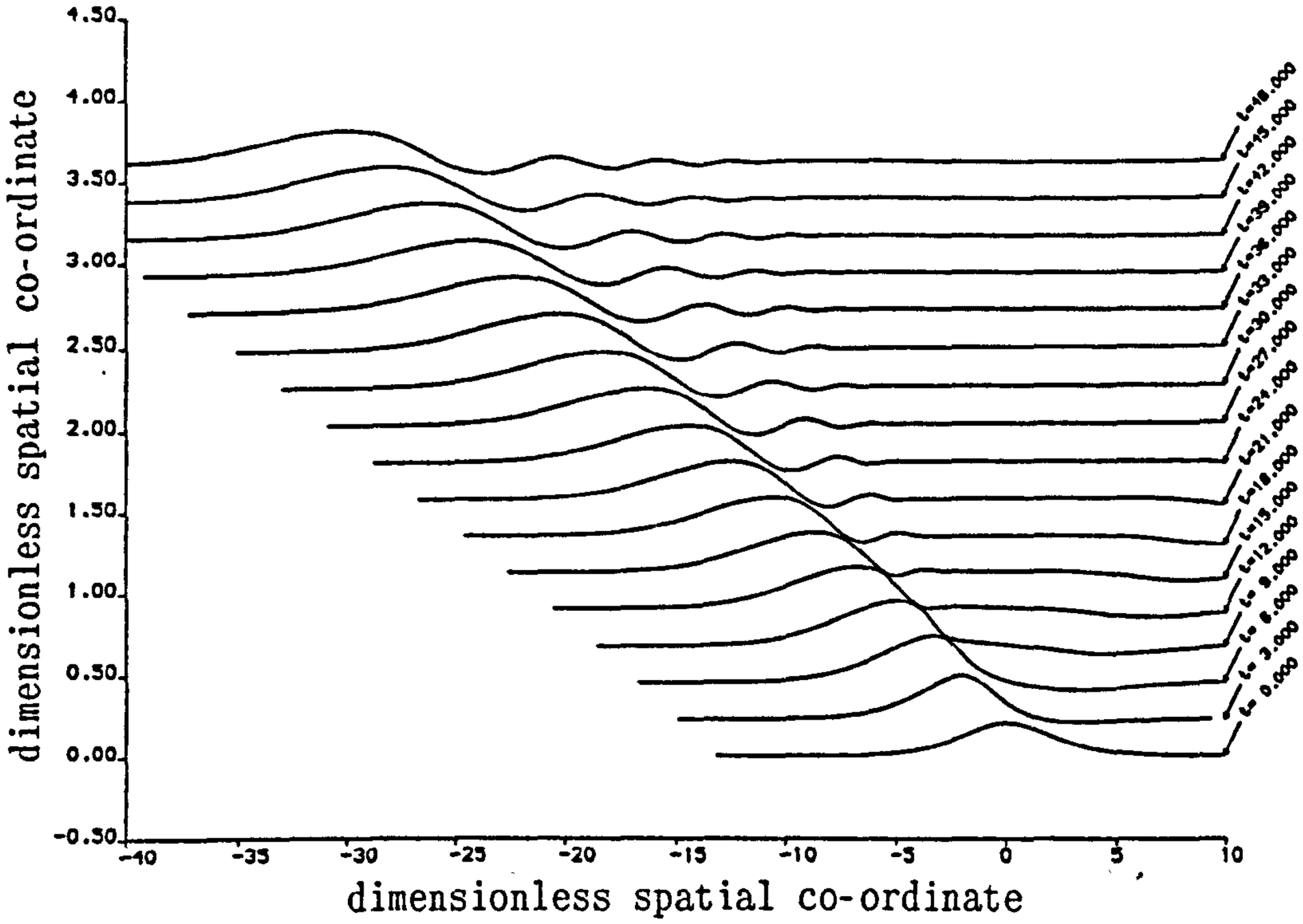

Fig. 4.5

Fig. 4.5 showing a family of wave surfaces with gas at 1 atm. entry pressure and Mach number 0.0380 up to a dimensional time of t≃2 s. The rapid growth of the gas-liquid interface is not observed.

If the Mach number is lower, 0.0380 say, then the calculation continues until a dimensionless time of τ=100 when the calculation ceases because of limits on the computational size of the problem, with no rapid growth of the gas-liquid interface. This is illustrated in Fig. 4.5 up to times of τ=48 (t≃2 s). The profiles are separated by a dimensionless distance of 0.225.

If the entry gas Mach number is increased to 0.045 (Fig. 4.6) the surface grows more rapidly. At time τ=4.25 the liquid blocks more than $\frac{2}{3}$ of the tube cross-section. In fact, the amplitude is almost twice that of the Mach number 0.0388 flow at the same time. Fig. 4.7 shows the variation of the pressure within the gas as given by:

$$\bar{p} = \frac{p - p_o}{p_o}$$

on the left hand axis (which is used for comparisons with the results of Chapter 5), and by:

$$\Delta p = p - p_o$$

on the right hand axis, which is the pressure change on the water wave scale in units non-dimensionalised with respect to $\rho_L g h_B$. The term p is the dimensionless pressure within the gas, and p_o is the dimensionless entry pressure. The curves are for times τ=0.0, 2.0, 3.0, 3.5 and 4.0.

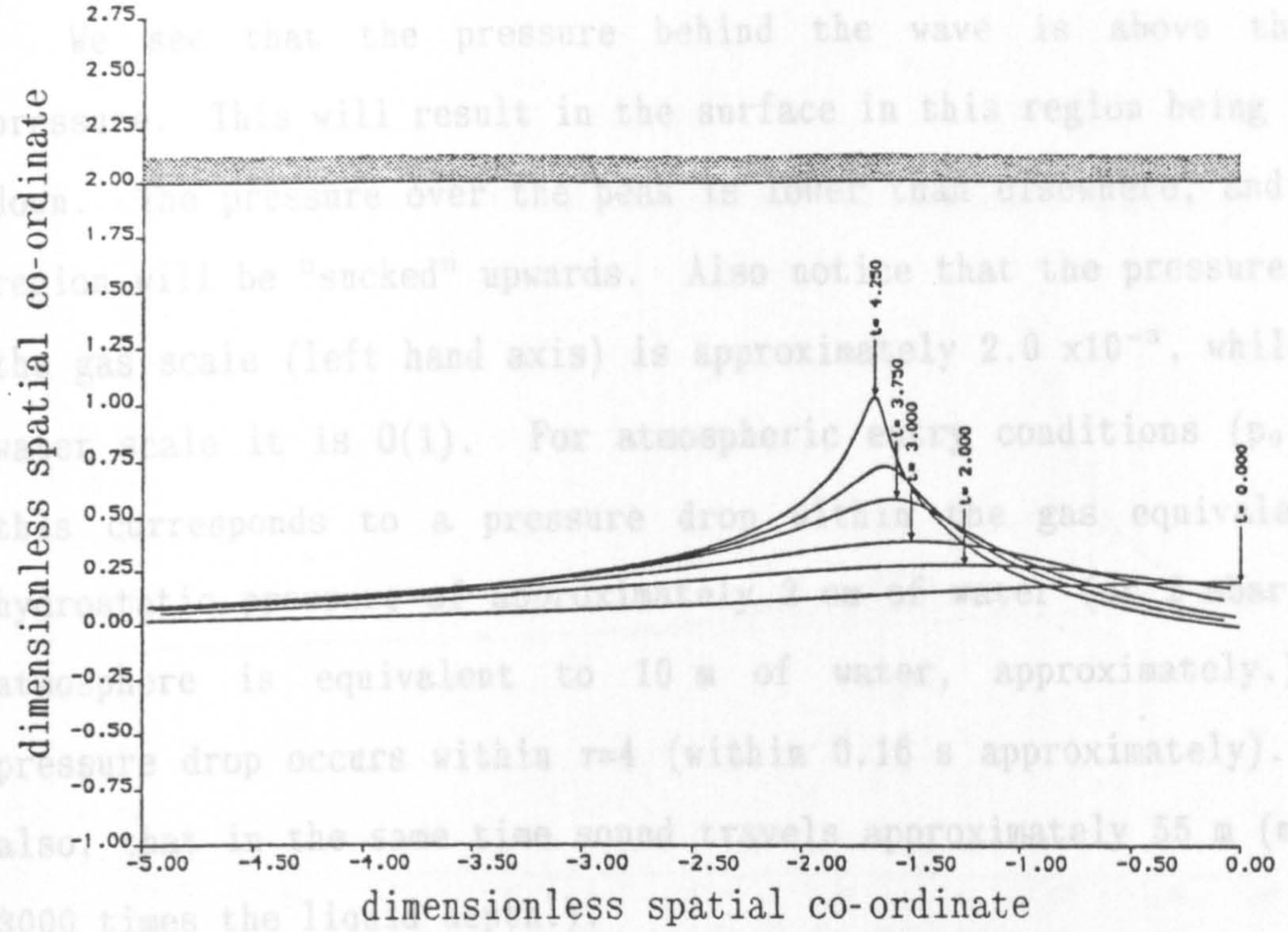

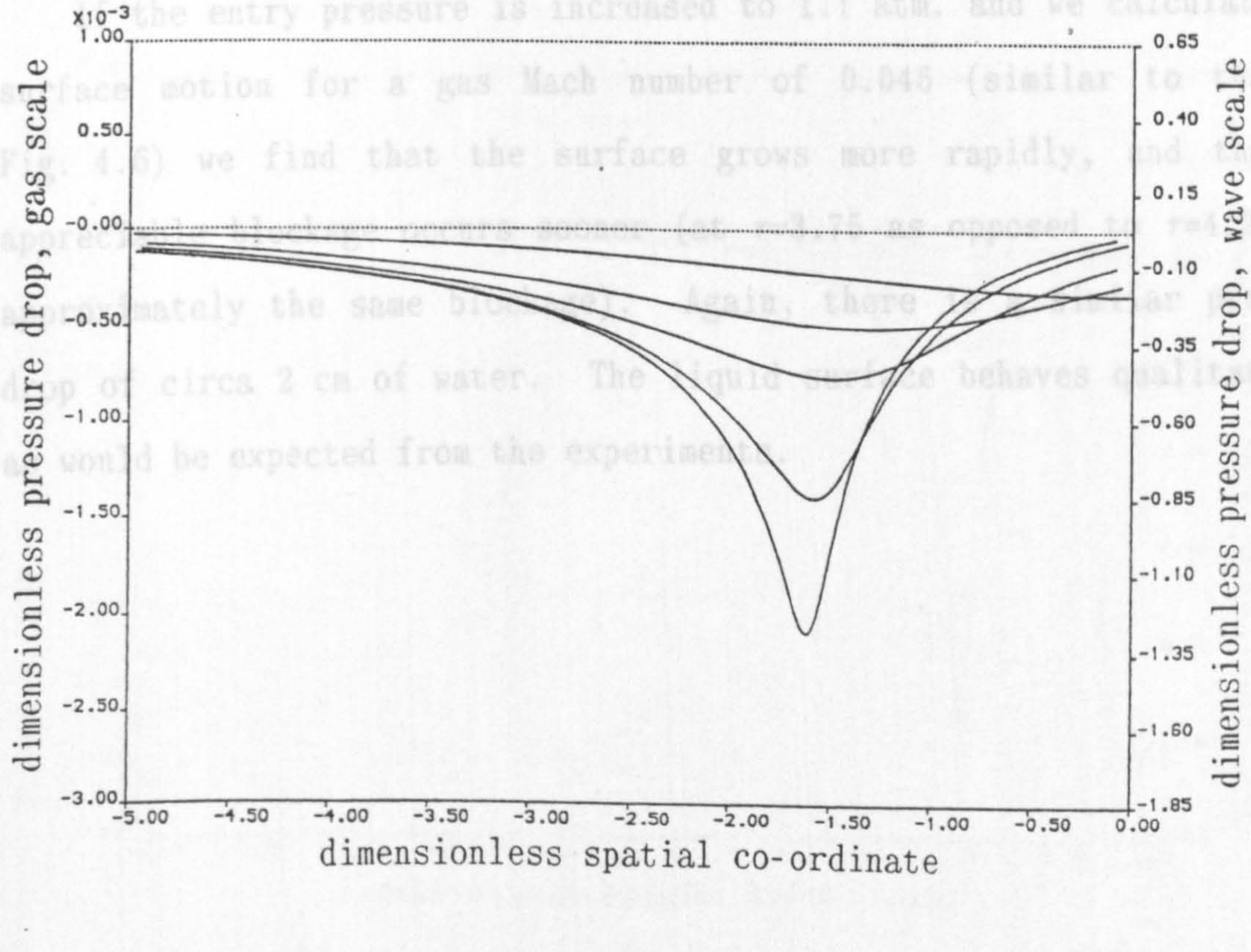

Fig. 4.6 (top) and 4.7

Fig. 4.6 showing the transition to slug flow with gas at 1 atm entry pressure and Mach number 0.045 at dimensional times t≃0, 0.25, 0.37, 0.46, 0.49 and 0.53 s.
Fig. 4.7 shows the dimensionless pressure variation corresponding to the conditions for the wave in Fig. 4.6 at times t≃0, 0.25, 0.37, 0.43 and 0.49 s (left hand axis shows dimensionless pressure on the gas scale, while the right hand axis shows dimensionless pressure on the wave scale).

We see that the pressure behind the wave is above the entry pressure. This will result in the surface in this region being "pushed" down. The pressure over the peak is lower than elsewhere, and so this region will be "sucked" upwards. Also notice that the pressure drop on the gas scale (left hand axis) is approximately 2.0 $x10^{-3}$, while on the water scale it is O(1). For atmospheric entry conditions (p_o=1 atm.) this corresponds to a pressure drop within the gas equivalent to a hydrostatic pressure of approximately 2 cm of water (or 2 mbar). (One atmosphere is equivalent to 10 m of water, approximately.) This pressure drop occurs within τ=4 (within 0.16 s approximately). Notice also, that in the same time sound travels approximately 55 m (more than 3000 times the liquid depth!).

If the entry pressure is increased to 1.1 atm. and we calculate the surface motion for a gas Mach number of 0.045 (similar to that of Fig. 4.6) we find that the surface grows more rapidly, and that an appreciable blockage occurs sooner (at τ=3.75 as opposed to τ=4.25 for approximately the same blockage). Again, there is a similar pressure drop of circa 2 cm of water. The liquid surface behaves qualitatively as would be expected from the experiments.

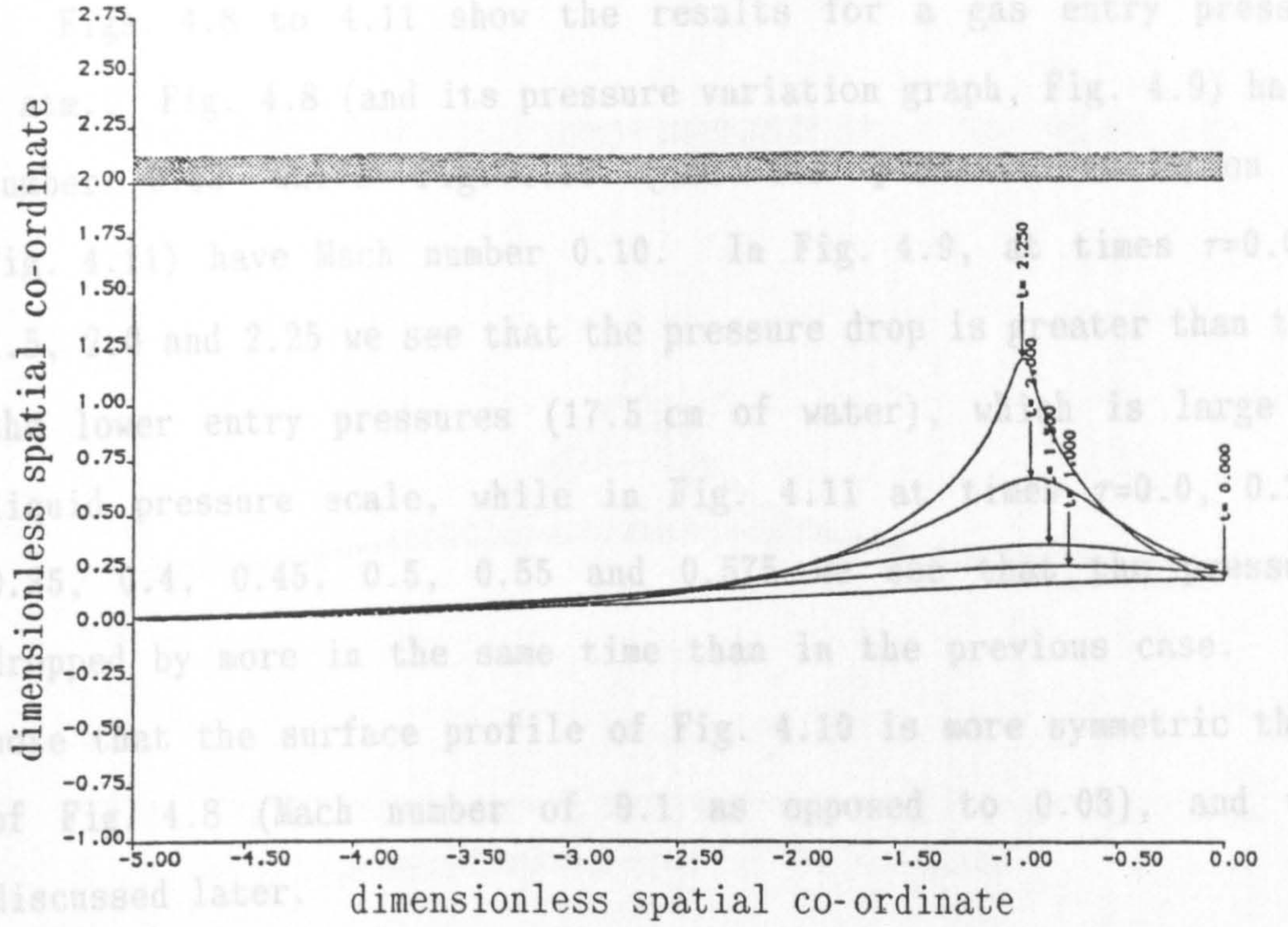

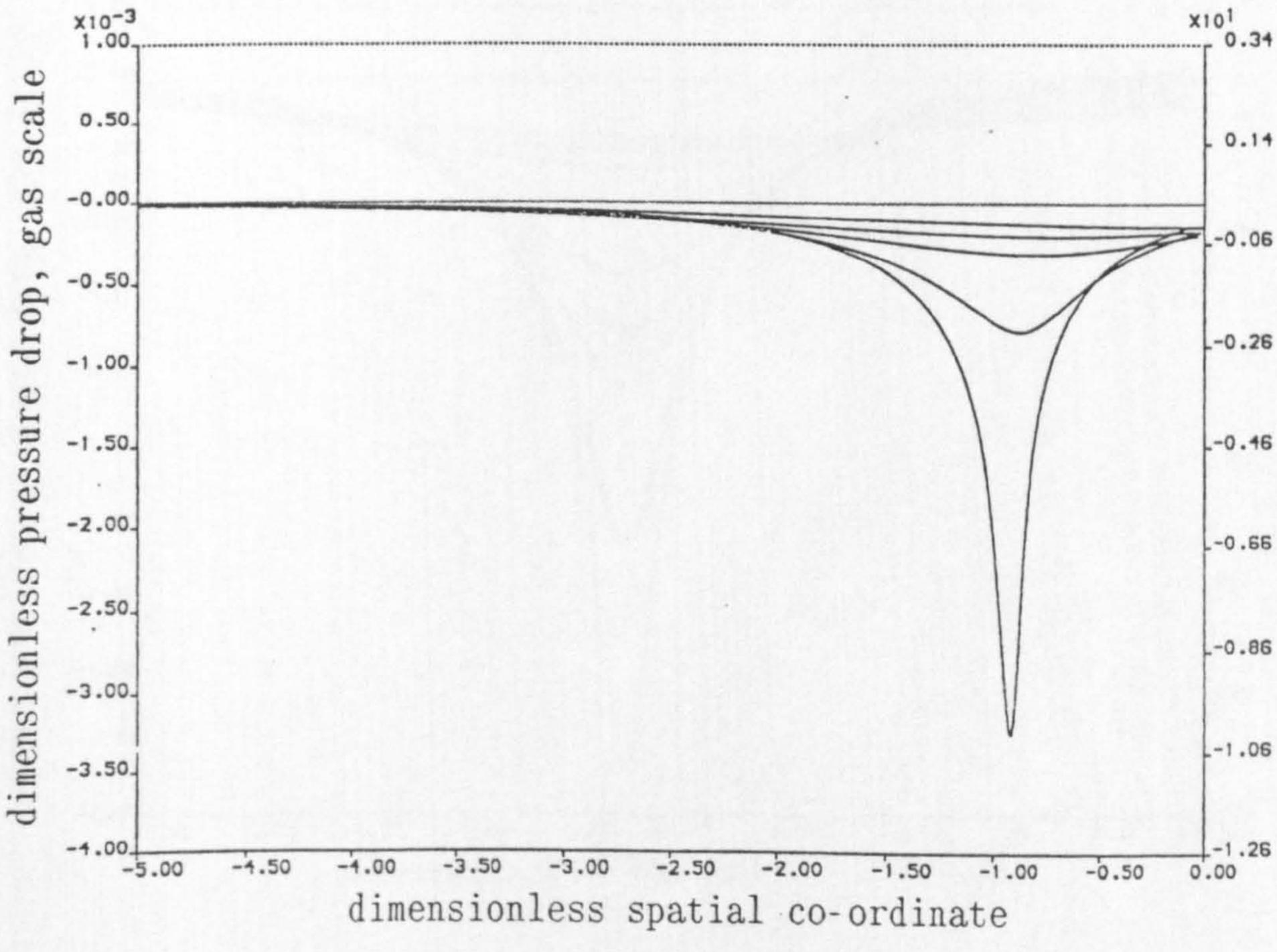

Figs. 4.8 (top) and 4.9

Fig. 4.8 showing the transition to slug flow with gas at 5 atm entry pressure and Mach number 0.030 at dimensional times t≃0, 0.12, 0.19, 0.25 and 0.28 s.
Fig. 4.9 shows the dimensionless pressure variation corresponding to the conditions for the wave in Fig. 4.8 at times t≃0, 0.12, 0.19, 0.25 and 0.28 s.

Figs. 4.8 to 4.11 show the results for a gas entry pressure of 5 atm.. Fig. 4.8 (and its pressure variation graph, Fig. 4.9) have Mach number 0.03 while Fig. 4.10 (and its pressure variation graph, Fig. 4.11) have Mach number 0.10. In Fig. 4.9, at times τ=0.0, 1.0, 1.5, 2.0 and 2.25 we see that the pressure drop is greater than those at the lower entry pressures (17.5 cm of water), which is large on the liquid pressure scale, while in Fig. 4.11 at times τ=0.0, 0.2, 0.3, 0.35, 0.4, 0.45, 0.5, 0.55 and 0.575 we see that the pressure has dropped by more in the same time than in the previous case. We also note that the surface profile of Fig. 4.10 is more symmetric than that of Fig. 4.8 (Mach number of 0.1 as opposed to 0.03), and this is discussed later.

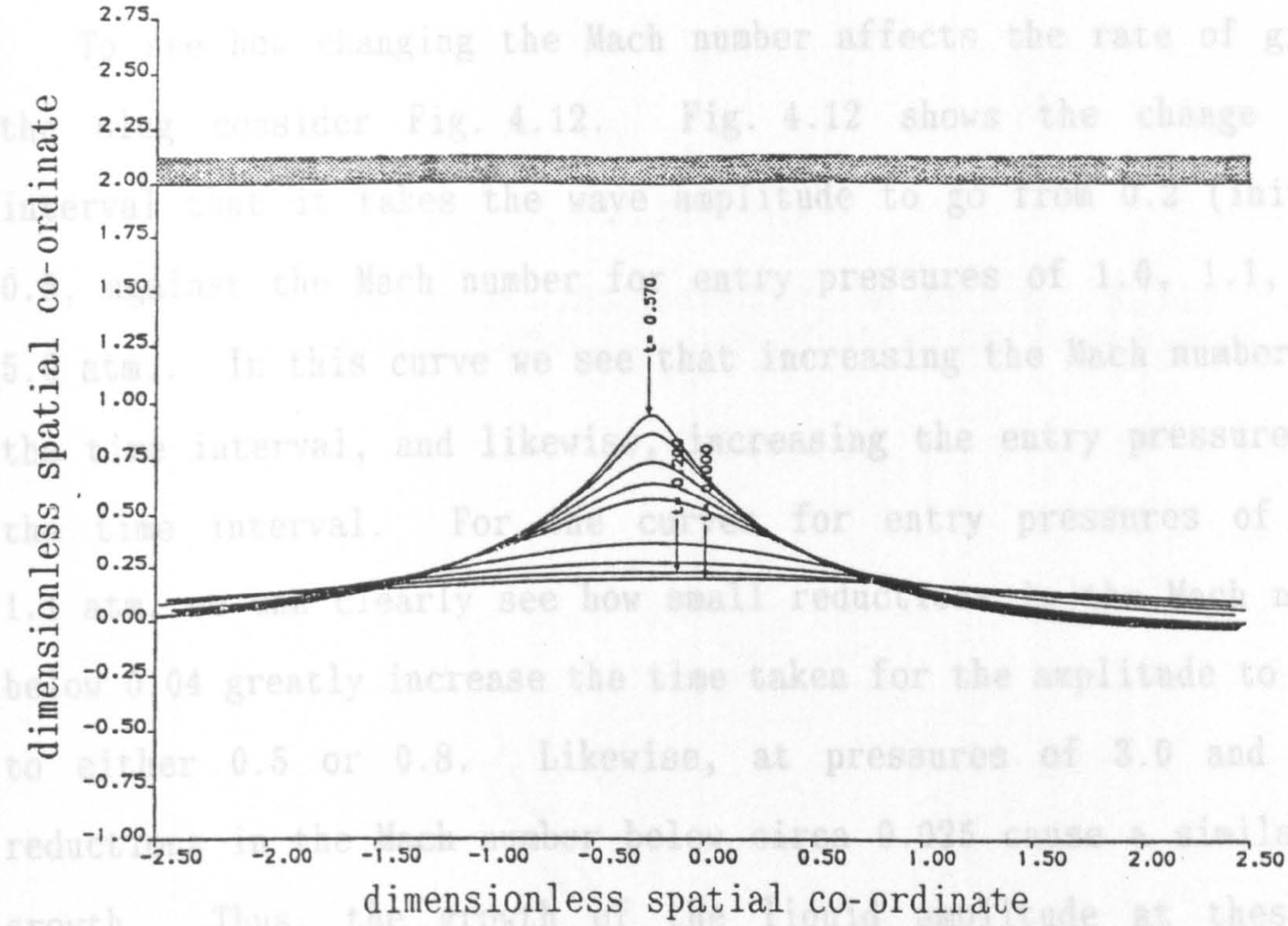

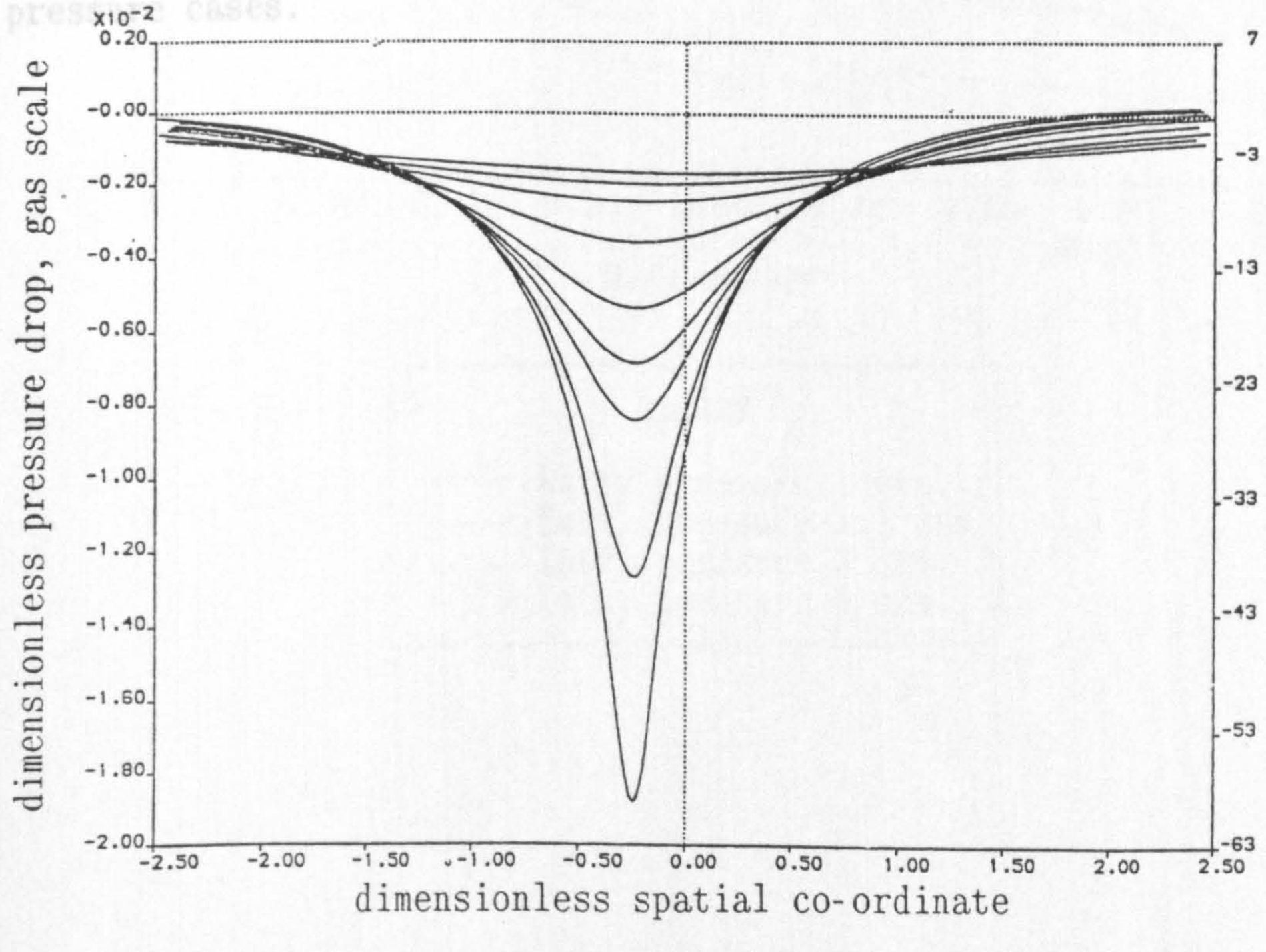

Figs. 4.10 (top) and 4.11

Fig. 4.10 showing the transition to slug flow with gas at 5 atm entry pressure and Mach number 0.100 at dimensional times t≃0, 0.025, 0.037, 0.050, 0.059, 0.062, 0.065, 0.068 and 0.074 s.
Fig. 4.11 shows the dimensionless pressure variation corresponding to the conditions for the wave in Fig. 4.6 at those times.

To see how changing the Mach number affects the rate of growth of the slug consider Fig. 4.12. Fig. 4.12 shows the change in time interval that it takes the wave amplitude to go from 0.2 (initial) to 0.5, against the Mach number for entry pressures of 1.0, 1.1, 3.0 and 5.0 atm.. In this curve we see that increasing the Mach number reduces the time interval, and likewise, increasing the entry pressure reduces the time interval. For the curves for entry pressures of 1.0 and 1.1 atm. we can clearly see how small reductions in the Mach number to below 0.04 greatly increase the time taken for the amplitude to increase to either 0.5 or 0.8. Likewise, at pressures of 3.0 and 5.0 atm. reductions in the Mach number below circa 0.025 cause a similarly slow growth. Thus, the growth of the liquid amplitude at these higher pressures is very sensitive to the gas Mach number, as in the lower pressure cases.

Fig. 4.12

Variation of the time taken for the initial amplitude of the wave to reach 0.5 with relative gas Mach number

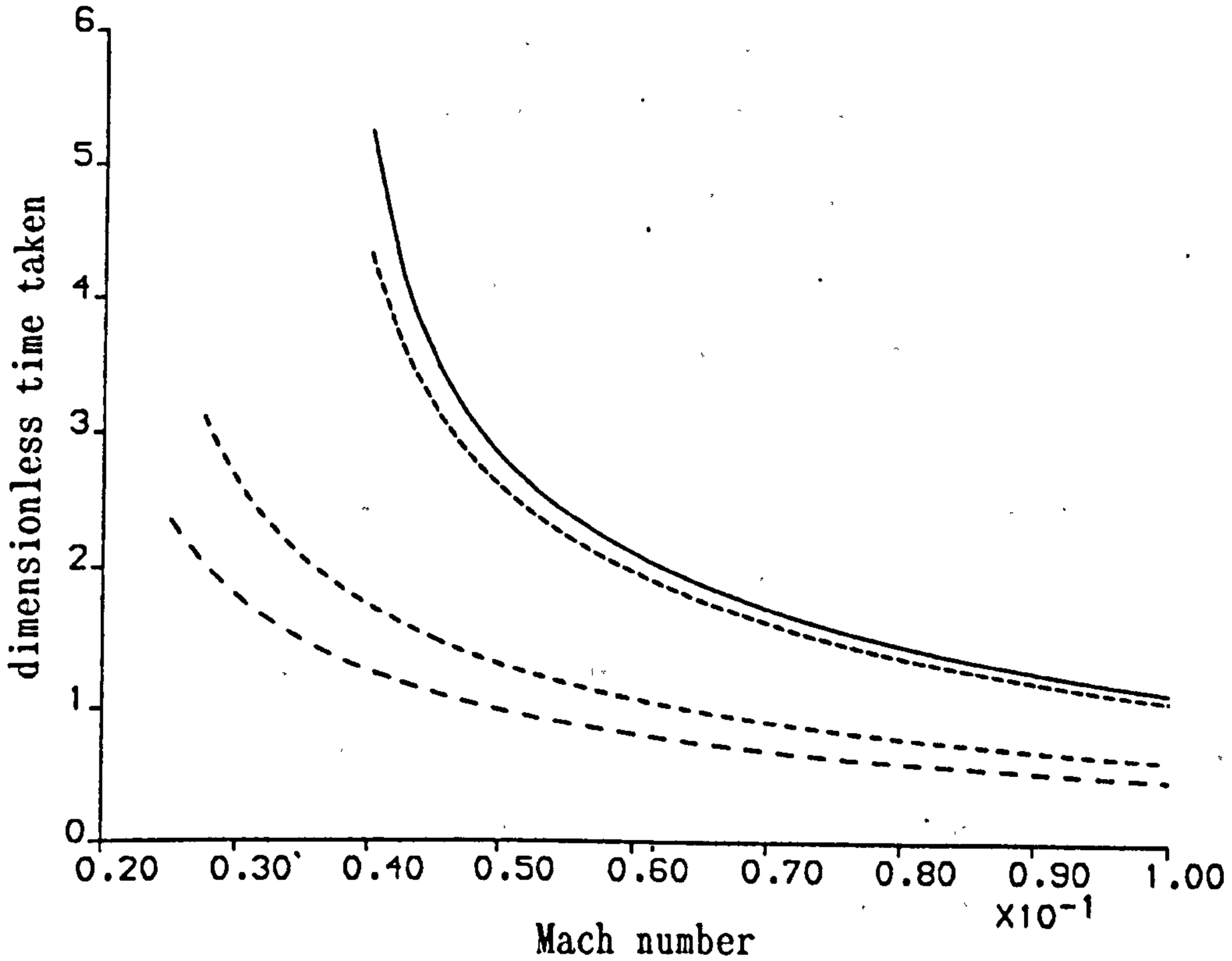

It is interesting to consider the effect that ignoring compressibility has on the motion of the surface. If we now consider our gas to be incompressible and obtain a curve for the time taken for the wave amplitude to increase from 0.2 to 0.5 (similar to Fig. 4.12) and plot this against the entry gas velocity, in fact, plotted against the equivalent compressible gas Mach number, for a gas entry pressure of 1 atm. we obtain Fig. 4.13. Fig. 4.13 shows that the incompressible gas takes longer to increase the wave amplitude by this amount than the compressible gas. Further, if we consider an incompressible gas at entry pressure of 5 atm. then when the entry velocity is equivalent to Mach number 0.03 for the compressible gas the time taken for the amplitude to increase through this range is 2.298 dimensionless time units as opposed to 2.096 units (a 9.6% increase). Similarly for a velocity equivalent to Mach number 0.04 the times for the incompressible and compressible flows are 1.674 and 1.472 units respectively (13.7% difference). So, by considering the gas to be a compressible gas rather than an incompressible one we obtain faster growth rates for the surface amplitude, and these effects are noticeable even for low pressure, low Mach number gas flows.

Fig. 4.13

Comparison of times taken for the initial amplitude of the wave to reach 0.5 for an entry pressure of 1 atm. but for compressible and incompressible gases.

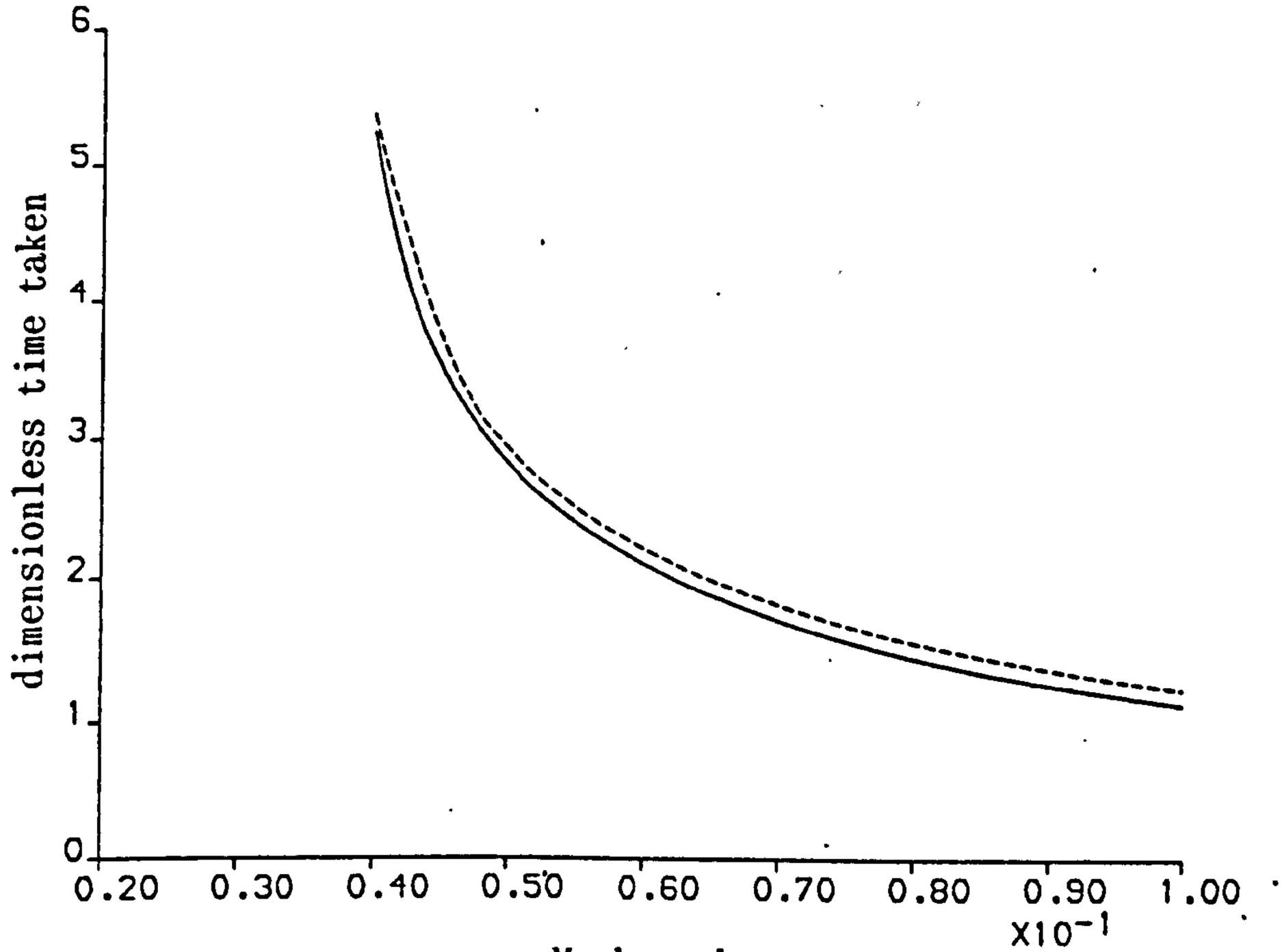

In addition to the speed with which the amplitude of the waves increases, another interesting effect can be seen from the surface profiles. When the Mach number or the entry pressure is low, as in Fig. 4.6, the profile is noticeably asymmetric about the amplitude maximum, whilst for higher pressures and Mach numbers, as in Fig. 4.10, the wave remains virtually symmetric. In order to gauge the importance of the effect of the gas to the effect of gravity on the wave we shall measure the asymmetry of the wave by taking the ratio of the lengths from the crest to the positions on the surface at half that height (see Fig. 4.14), $\frac{L_1}{L_2}$, and plot this against:

$$\mathcal{P} = \frac{\frac{1}{2}\rho_G u_G^2}{\rho_L g a}$$

where a is the wave amplitude. In fact, we plot $\frac{L_1}{L_2}$ against the following analog of $\mathcal{P}$:

$$\bar{\mathcal{P}} = \frac{\frac{1}{2}\rho u^2}{\sigma a}$$

where a is the dimensionless liquid amplitude and σ is the dimensionless liquid density. This dimensionless number measures the affect of the gas pressure (numerator) to the asymmetric liquid velocity profile through the hydrostatic liquid pressure at the crest (denominator). When the gas pressure and Mach number are large and the liquid hydrostatic pressure at the crest is relatively small, changes in the gas occur rapidly.

Schematic diagram showing the asymmetry of a growing wave.

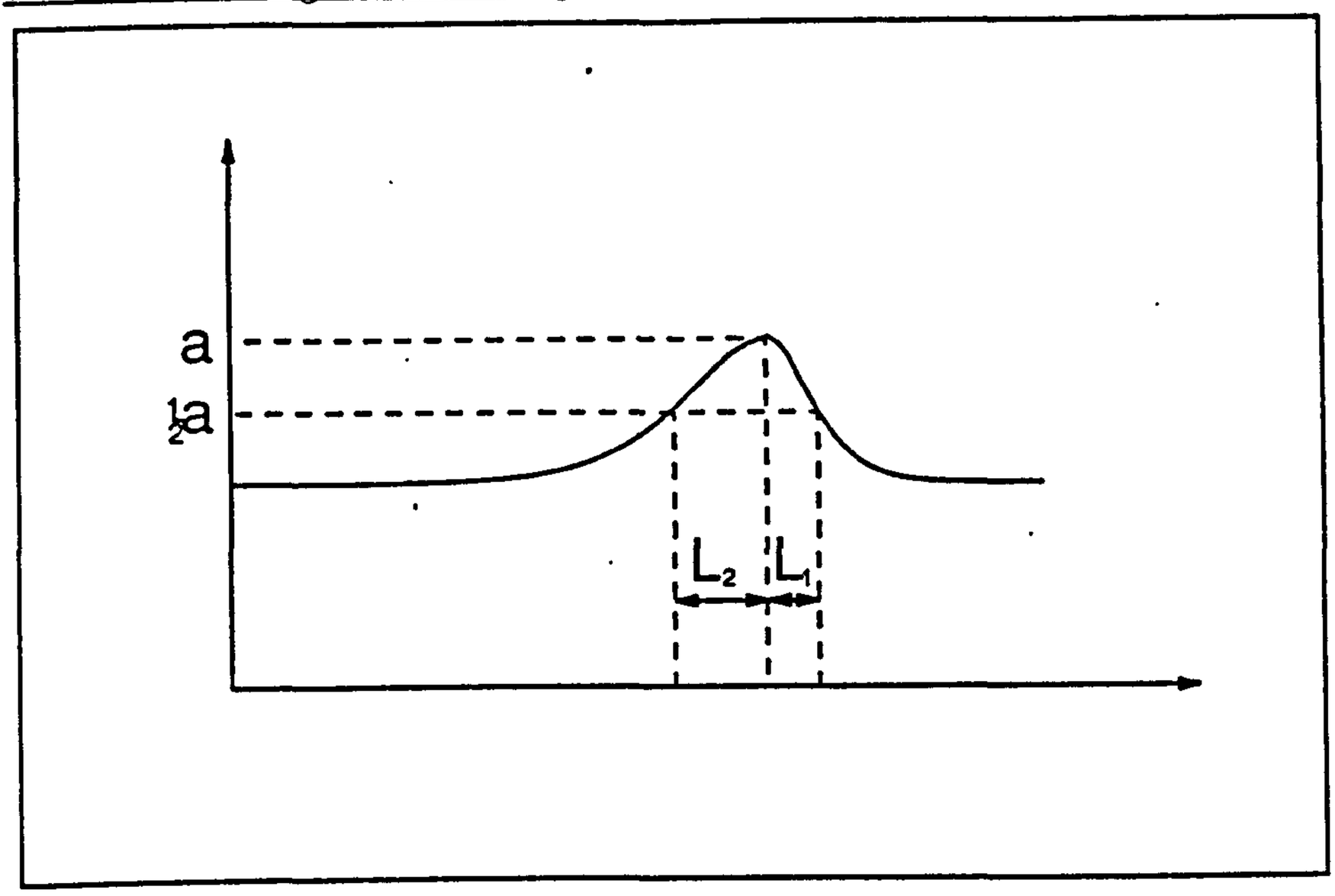

Fig. 4.14

Using this to gauge the asymmetry we obtain Fig. 4.15. Notice that the points for this curve were taken by measurements from plotted surface profiles, such as Fig. 4.4. In addition it is desirable to measure the ratio $\frac{L_1}{L_2}$ for identical amplitudes, 0.5 for example. However, the numerical scheme allows specification of specific dimensionless times for outputting data but not for specific dimensional heights for outputting data. Thus, these ratios were not always measured for amplitudes of exactly 0.5, and this may account for the spread in the data, indicated by the "error" bars. Since the data for Fig. 4.15 is not ideal we shall regard this graph merely as a qualitative indication of the effect of the dimensionless pressure parameter, $\bar{P}$, on the asymmetry.

Fig. 4.15

Measurements of the asymmetry of growing waves.

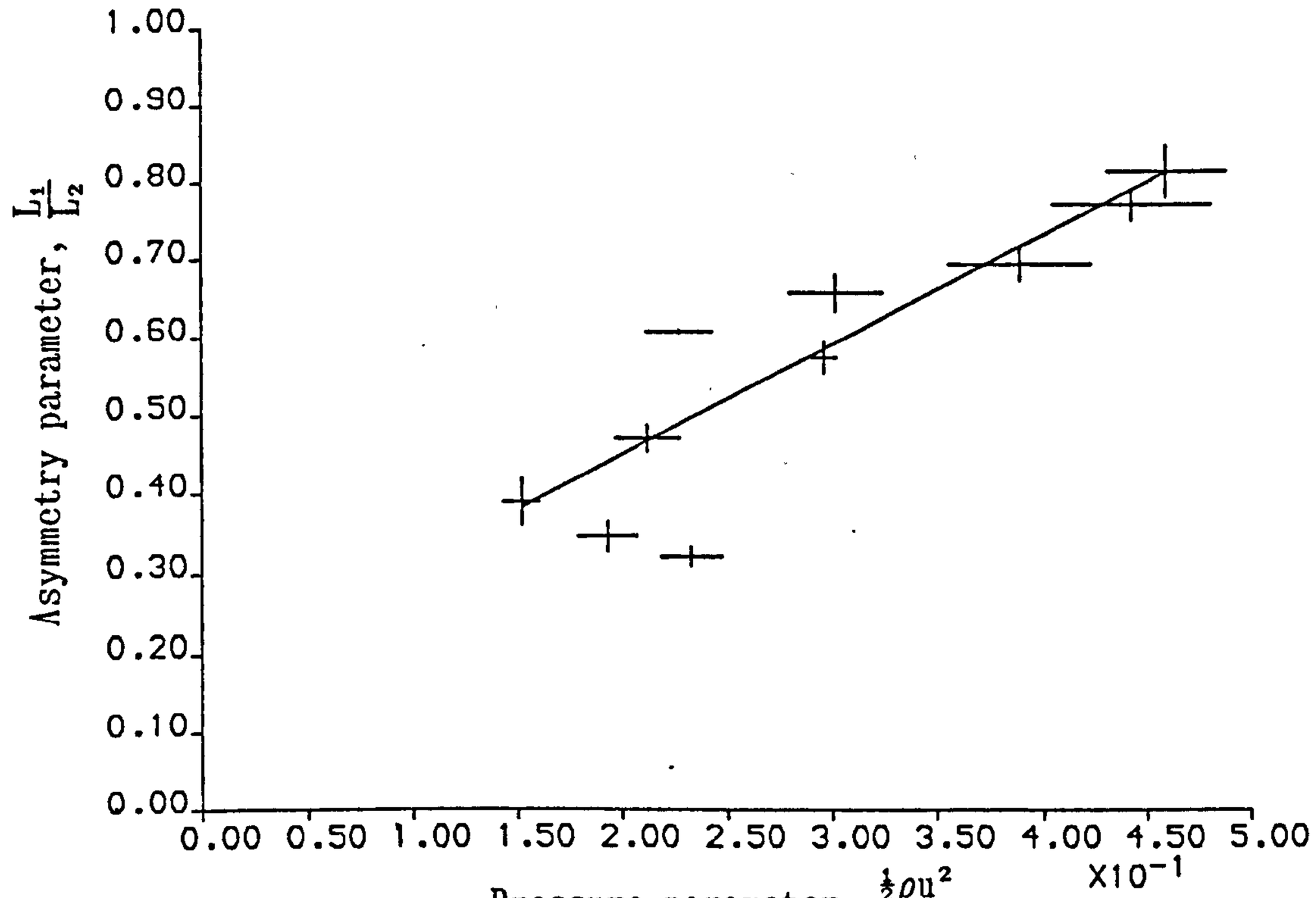

We can see that for gas flows for which the gas entry pressure is low and/or the gas Mach number is low (and thus $\bar{\mathcal{P}}$ is low) then the asymmetry is great ($\frac{L_1}{L_2}$ is small), while for higher pressure flows and/or flows for which the Mach number is large then the asymmetry is small. This is clearly seen if Figs. 4.6 and 4.10 are compared. Both fluids are considered to be inviscid and the initial elevation of the liquid surface is symmetric, thus any asymmetry is due to the liquid velocity profile, through the initial form of ϕ_L, which is asymmetric. This affects the motion of the liquid surface. If the gas pressure and Mach number are relatively small, then the liquid velocity profile has a greater effect on the surface profile than the motion due to the gas. The dimensionless number $\bar{\mathcal{P}}$ has been chosen as a measure of the ratio of the gas to liquid velocity effects.

4.5 Discussion of the numerical air-water flow results

A striking result from the air-water flow calculations is the apparent abruptness with which the flow of the liquid changes from one which appears to be steady for long times into a flow in which the wave amplitude rapidly increases. In the case of the air-water like flow at 1 atm. entry pressure we found that when the Mach number was 0.0380 the surface profile changed, but the amplitude never increased rapidly, but for a Mach number of 0.0388 the amplitude increased rapidly. The transition seems to have occurred very rapidly. To illustrate this, consider Fig. 4.16. Fig. 4.16 is the Mandhane flow régime map. If we convert the relative gas Mach numbers of 0.0380 and 0.0388 into relative gas velocities and hence into relative superficial gas velocities we obtain the long dashed curve. The former Mach number is analogous to a flow on the left hand edge of that curve, while the higher Mach number is one on the right hand edge. There is hardly any difference in the flow, and yet our model gives different effects. Additionally, the Mach number 0.0380 flow (for which we observe no rapid surface movement) can be seen to lie well within the established slug flow domain.

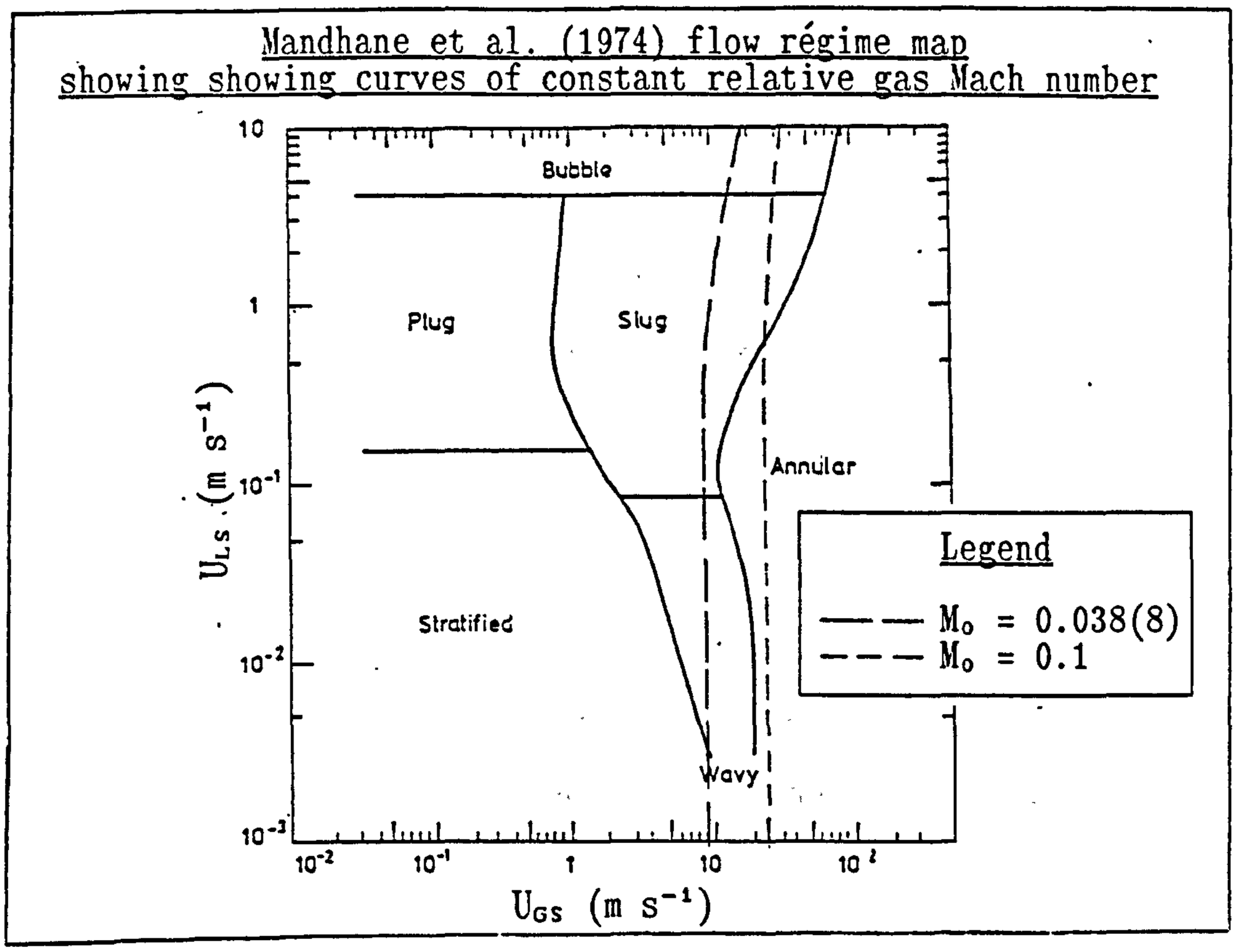

Fig. 4.16

One would expect our model to predict slug flow for such a Mach number. Perhaps one reason why we do not may be that our initial choice of wave amplitude to depth ratio was too small. Perhaps had we chosen 0.25 we might have obtained slug flow. Likewise, by varying the initial liquid depth in the tube (and hence changing the gas gap) we may have been able to predict slug flows further within the region shown on the flow régime map. However, as already explained, we decided not to explore the entire parameter space, but concentrate on only one or two effects.

When we consider flows for which the gas Mach number is relatively large, 0.1 for example, we also find that the surface growth occurs very rapidly indeed. If we convert the relative gas Mach number of 0.1 into a relative superficial velocity we obtain 24.0 m s^{-1}, approximately corresponding to the small dashed curve on Fig. 4.16. We can see that a large proportion of this curve lies outside the slug flow régime. This highlights a major problem with the scheme used. Since we are

considering only inviscid, irrotational and non-turbulent flows, and provided that our system is inertial, then we are at liberty to superimpose any velocity on our system that we choose. The scheme as it stands uses only the relative velocity between the gas and the liquid (which we define through the relative gas Mach number). As a result, we do not know our exact position on the flow régime map. We may be anywhere along such curves for each Mach number we specify.

We may attempt to find a unique velocity for the liquid from considerations of the turbulent shear stresses. If we suppose some form for the velocity profiles of the gas and the liquid, such as log-law profiles (Tritton (1988) p.342), and with suitable modelling of the wall and interfacial shear stresses perhaps we may obtain a measure of the unique liquid velocity. While this is possible, such an analysis has not been performed here.

The numerical and experimental work are qualitatively similar in the early stages. The front and rear surfaces of the wave steepen greatly as the slug grows, as may be seen from the fast ciné tracings, and the time scale of the numerically predicted growth compares reasonably with that of the fast ciné. For the early stages of slug growth the experimental maximum growth rates are in the range 0.3 to 0.7 m s^{-1}, and for similar numerical calculations the growth rates are typically 0.4 to 0.9 m s^{-1}.

It is interesting to compare breaking shallow water waves with slug wave-like motions in a pipe. Both the experimental and the numerical work show that the liquid surfaces of the slug wave growth are much steeper than the surfaces of the shallow water waves, particularly the rear surface. In the numerical calculations, this causes the crest of

the slug wave to become very sharp. The sharpness of the crest would suggest that in a real flow separation and droplet entrainment from the crest region are likely to occur.

Despite the limitations of the gas model (quasi-steady, one-dimensional flow) and of the liquid (inviscid, irrotational and laminar flow) perhaps this scheme can be used to model the initial stages of two-phase flows that are of more interest to industry, such as steam-water flows. With this in mind, the following extension to the gas dynamics part of the problem is carried out. However, it should be stressed that in the following extension any phase changes and heat transfers are ignored. Thus the flows under consideration are not steam-water flows, bu very idealised steam-water like flows.

4.6 Numerical results for the two-phase flow of steam-water treated as a wave motion

The numerical results of the above section, §4.4, were for air-water, co-current two-phase flows. Steam-water flows, are of interest for their industrial applications, such as within condensers at power stations.

In this section we shall use the numerical scheme developed for air-water flows and apply it to co-current steam-water flows at various entry pressures and temperatures.

To use the numerical scheme it is necessary to model the steam density variation as a steady, one-dimensional flow. We continue to assume that our steam-water flow continues to obey this criterion. Whilst this may not be a good model to use for the density variation of steam with spatial co-ordinate, since all the slug flows under consideration are expected to behave in a turbulent, unsteady three-dimensional fashion, it is necessary to choose this simple model so that the numerical scheme outlined above can be used. In §4.4 we treated the air as an ideal gas and we could express its equation of state as

$$p = \kappa \rho_G^{\gamma}$$

but for many industrial applications steam does not behave as an ideal gas. For steam-water flows we really require an equation of state for the steam. And such an equation of state exists. In fact, all the values in the steam tables are calculated from the equation of state for steam, Keenan et al. (1978) p.128 . Thus, to continue to use the above numerical scheme we need to obtain relations analogous to (4.3.1) and (4.3.2) so that the variation of the steam density with available cross-sectional area may be obtained. In order to do so we may use the

following thermodynamic relationships which hold for all gases for which there is no heat transfer outside the system and for which there is no phase change - condensation or evaporation:

$$\rho_G u_G A_G = Q_G \tag{4.6.1}$$

$$\rho_G u_G \frac{du_G}{dx} + \frac{dp_G}{dx} = 0 \tag{4.6.2}$$

$$\frac{d}{dx}(h + \tfrac{1}{2}u_G^2) = 0 \tag{4.6.3}$$

$$\frac{dh}{dx} - \frac{1}{\rho_G}\frac{dp_G}{dx} = T\frac{dS}{dx} = 0 \tag{4.6.4}$$

where Q_G is a mass flux, h is the specific enthalpy and S is the entropy of the gas (Schreier (1982) p.38 or Clarke & McChesney (1964)). For isenthalpic gases (4.6.4) is a consequence of (4.6.2) and (4.6.3). If the gas is assumed to be ideal then the above relations and the equation of state for the ideal gas:

$$p_G = \rho_G RT$$

yield equations (4.3.1) and (4.3.2). If, however, we consider a non-ideal (real) gas, while equations (4.6.1) to (4.6.4) still hold, we can no longer obtain a simple relationship between area changes and Mach number or density. Instead, the following relationship holds (Schreier (1982) p. 39):

$$\frac{dS}{dx} = \frac{c_p}{T}\frac{dT}{dx} + \frac{dc_p}{dx} - \frac{A}{T\rho_G^2 u^2}(1 - M^2)\frac{dA_G}{dx}$$

and using (4.6.1) this becomes:

$$\frac{dS}{dx} = \frac{c_p}{T}\frac{dT}{dx} + \frac{dc_p}{dx} - \frac{A^3}{TQ^2}(1 - M^2)\frac{dA_G}{dx} \tag{4.6.5}$$

For real gases, the specific heat at constant pressure is a function of both the density and the thermodynamic temperature. We may express the specific enthalpy as:

$$h = I + \frac{p_G}{\rho_G}$$

where I is the specific internal energy. Then we may write c_P (and c_V) as:

$$c_V = \left[\frac{\partial I}{\partial T}\right]_\rho \tag{4.6.6}$$

$$c_P = \left[\frac{\partial h}{\partial T}\right]_\rho - \frac{\left[\frac{\partial h}{\partial \rho_G}\right]_T \left[\frac{\partial p_G}{\partial T}\right]_\rho}{\left[\frac{\partial p_G}{\partial \rho_G}\right]_T} \tag{4.6.7}$$

If the equation of state for steam is relatively simple in form (like that of an ideal gas) then perhaps the analysis of equation (4.6.5) can be pushed further. However, the equation of state for steam is not at all simple in form, being a complicated function of both ρ_G and T, and so no simple relations like equations (4.3.1) and (4.3.2) arise.

This is somewhat of a draw-back as all the remaining analysis that is required to implement the problem is simple. Thus, to see what effect the specific form of the equation of state of steam has on the liquid interface, neglecting phase changes and heat transfer, we make the assumption that the steam density (one of the fundamental thermodynamic quantities) varies in an ideal fashion, and the pressure varies in a non-ideal fashion. While this appears to be a contradiction, Clarke & McChesney (1964) say that for nozzle flows at pressures of up to 200 atm. little error is incurred by treating the density of the gas in an ideal fashion provided that all of the other quantities are calculated correctly. Undoubtedly, since we are neglecting phase changes and heat transfer we are neglecting some very important effects, effects as important if not more so than

compressibility. However, for the flows under consideration it is still interesting to look at the very over simplified problem. Now, by considering the density to vary ideally we may use equations (4.3.1) and (4.3.2) to determine the variation of the gas density with cross-section. In order to do this we calculate the ratio of specific heats using (4.6.6) and (4.6.7).

The equation of state is expressed in terms of the fundamental thermodynamic parameter called the Helmholtz free energy which is a function of the fluid density, ρ_G, and the thermodynamic temperature (on the Kelvin scale), T, which is given by Keenan et al (1978) p. 128:

$$H(\rho,T) = H_o(T) + RT[\ln\rho + \rho Q(\rho,\tau)] \qquad (4.6.8)$$

where:

$$H_o(T) = \sum_{i=1}^{6} \frac{C_i}{\tau^{i-1}} + C_7 \ln T + C_8 \ln\frac{T}{\tau} \qquad (4.6.9)$$

$$Q(\rho,\tau) = (\tau-\tau_c)\sum_{j=1}^{7}(\tau-\tau_{aj})^{j-2}\left[\sum_{i=1}^{8} A_{ij}(\rho-\rho_{aj})^{i-1} + e^{-E\rho}\sum_{i=9}^{10} A_{ij}\rho^{i-9}\right] \qquad (4.6.10)$$

and where τ=1000/T, R is the gas constant in J kg^{-1} K^{-1}, and:

$$\tau_c = 1000/T_{crit} = 1.544912$$

$$E = 4.8$$

$$\tau_{aj} = \begin{cases} \tau_c & j=1 \\ 2.5 & j>1 \end{cases}$$

$$\rho_{aj} = \begin{cases} 0.634 & j=1 \\ 1.0 & j>1 \end{cases}$$

The values of the constants C_i and A_{ij} can be found in Appendix E. Any desired thermodynamic property can be obtained from differentiation of the Helmholtz free energy. For the purposes of our study we are interested in the pressure variation corresponding to a density

variation along the tube, and the pressure is given by:

$$p = \rho^2 \left[\frac{\partial H}{\partial \rho}\right]_\tau \tag{4.6.11}$$

which may be written:

$$p = \rho^2 RT\left[\frac{1}{\rho} + Q(\rho,\tau) + \rho\left[\frac{\partial Q}{\partial \rho}\right]_\tau\right] \tag{4.6.12}$$

where:

$$\left[\frac{\partial Q}{\partial \rho}\right]_\tau = (\tau-\tau_c)\sum_{j=1}^{7}(\tau-\tau_{aj})^{j-2}\left\{\sum_{i=1}^{8}A_{ij}(i-1)(\rho-\rho_{aj})^{i-2} + e^{-E\rho}\sum_{i=9}^{10}A_{ij}[(i-9)\rho^{i-10}-E\rho^{i-9}]\right\} \tag{4.6.13}$$

Similarly, the pressure gradient at constant temperature is given by:

$$\frac{dp}{dx} = \frac{dp}{d\rho}\frac{\partial \rho}{\partial x} \tag{4.6.14}$$

where:

$$\frac{\partial p}{\partial \rho} = \frac{2p}{\rho} + \rho^2 RT\left[\rho\left[\frac{\partial^2 Q}{\partial \rho^2}\right]_\tau + 2\left[\frac{\partial Q}{\partial \rho}\right]_\tau - \frac{1}{\rho^2}\right]$$

and:

$$\left[\frac{\partial^2 Q}{\partial \rho^2}\right]_\tau = (\tau-\tau_c)\sum_{j=1}^{7}(\tau-\tau_{aj})^{j-2}\left\{\sum_{i=1}^{8}A_{ij}(i-1)(i-2)(\rho-\rho_{aj})^{i-3} + e^{-E\rho}\sum_{i=9}^{10}A_{ij}[E^2\rho^{i-9}-2E(i-9)\rho^{i-10}]\right\} \tag{4.6.15}$$

Likewise, the second derivative of the pressure at constant temperature is:

$$\frac{d^2 p}{dx^2} = \frac{\partial p}{\partial \rho}\frac{d^2 \rho}{dx^2} + \frac{\partial^2 p}{\partial x^2}\left[\frac{d\rho}{dx}\right]^2 \tag{4.6.16}$$

and:
$$\frac{\partial^2 p}{\partial \rho^2} = -\frac{2p}{\rho^2} + \frac{2}{\rho}\frac{\partial p}{\partial \rho} + 2\rho RT\left[\rho\left[\frac{\partial^2 Q}{\partial \rho^2}\right]_T + 2\left[\frac{\partial Q}{\partial \rho}\right]_T - \frac{1}{\rho^2}\right]$$
$$+ \rho^2 RT\left[3\left[\frac{\partial^2 Q}{\partial \rho^2}\right]_T + \rho\left[\frac{\partial^3 Q}{\partial \rho^3}\right]_T + \frac{2}{\rho^3}\right] \qquad (4.6.17)$$

where:

$$\left[\frac{\partial^3 Q}{\partial \rho^3}\right]_T = (\tau-\tau_c)\sum_{j=1}^{7}(\tau-\tau_{aj})^{j-2}\left\{\sum_{i=1}^{8}A_{ij}(i-1)(i-2)(i-3)(\rho-\rho_{aj})^{i-4}\right.$$
$$\left.+e^{-E\rho}\sum_{i=9}^{10}A_{ij}[3E^2(i-9)\rho^{i-10} - E^3\rho^{i-9}]\right\} \qquad (4.6.18)$$

This gives us our Eulerian derivatives of pressure (analogous to (4.3.10)) from which we obtain the Lagrangian derivatives (analogous to (4.3.11)) to use in the numerical scheme.

We again assume that the initial wave profile is that of a solitary wave of amplitude to depth ratio 0.2.

Figs. 4.17 to 4.22 show the results obtained for the steam-water calculation using the approximate equation of state for steam to obtain the pressure on the steam-water interface. Fig. 4.17 has entry pressure of 100 atm. and gas Mach number of 0.00625 (the initial steam density is ρ_{Go}=55.49 kg m^{-3}, the specific heat at constant pressure is c_P=5.8298 kJ kg^{-1} K^{-1} and the ratio of specific heats is γ=4.8044). For this value of the entry pressure the Mach number just causes the rapid growth of the liquid surface. If the Mach number were 0.00620 then the surface does not grow rapidly, analogous to Fig. 4.5 for the 1 atm. gas flow at Mach number 0.0380. If we compare the pressure variation for this flow (Fig. 4.18) with those of the air-water flows we see that the relative dimensionless pressure drop on the gas scale is somewhat smaller. It in fact corresponds to a pressure drop of 1.6 atm.; similar to the drop in the air-water flows.

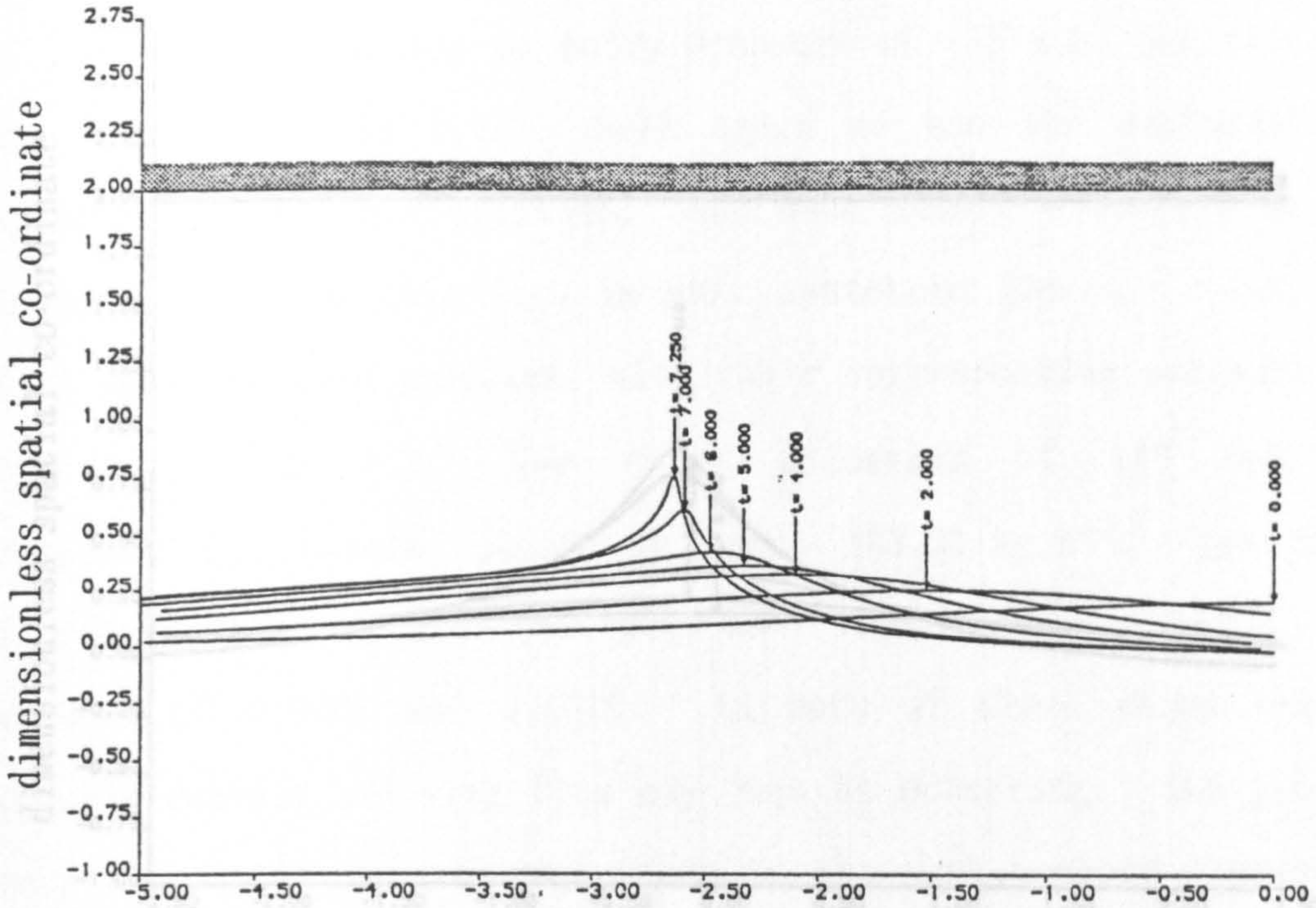

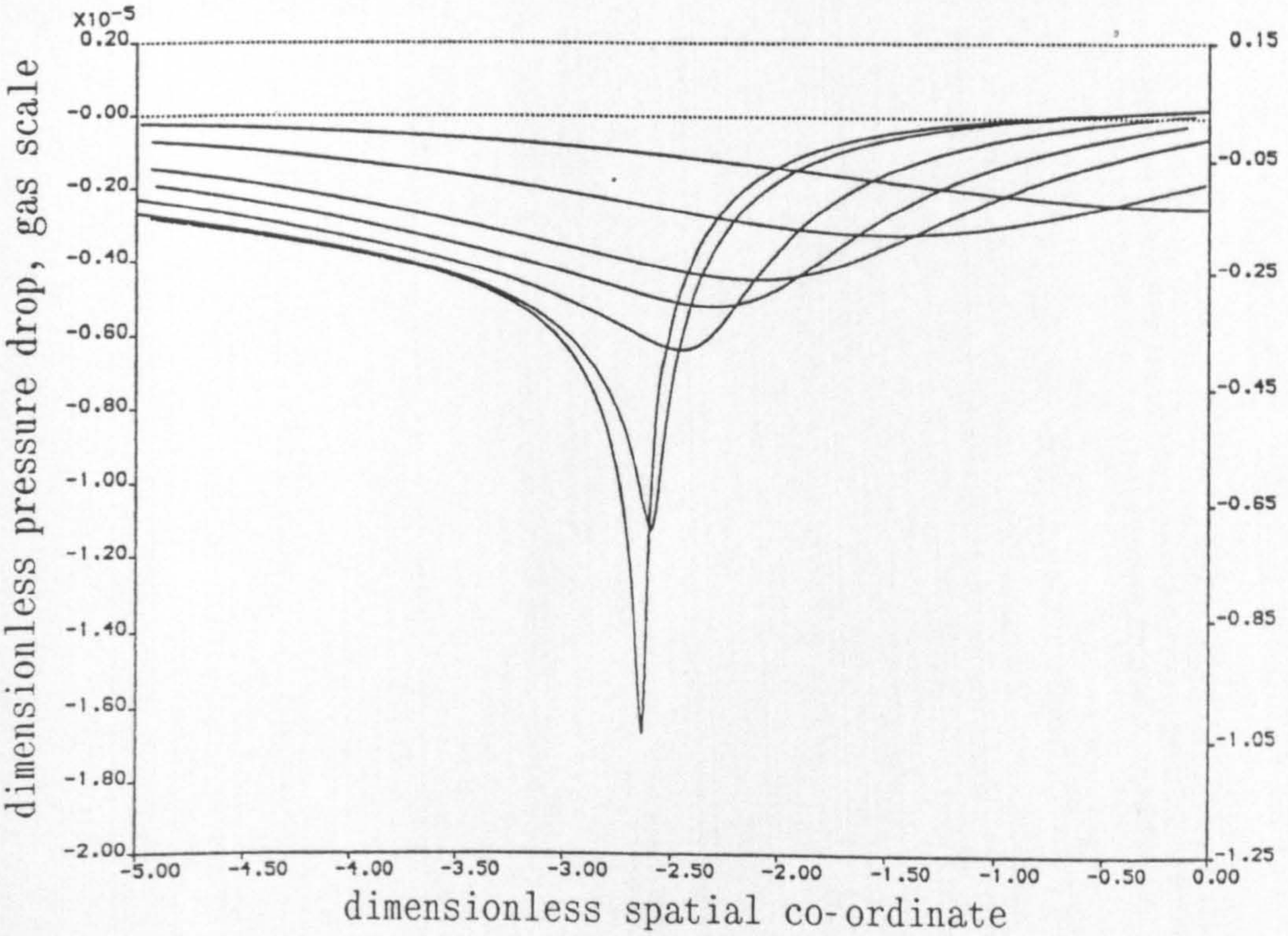

Figs. 4.17 (top) and 4.18

Fig. 4.17 showing the transition to slug flow with steam at 100 atm entry pressure (c_P=5.8298 kJ kg^{-1} K^{-1}, γ=4.8044) at temperature 310.96°C and Mach number 0.00625 at dimensional times t≃0, 0.25, 0.49, 0.62, 0.74, 0.87 and 0.90 s.
Fig. 4.18 shows the dimensionless pressure variation corresponding to the conditions for the wave in Fig. 4.17 at times shown above.

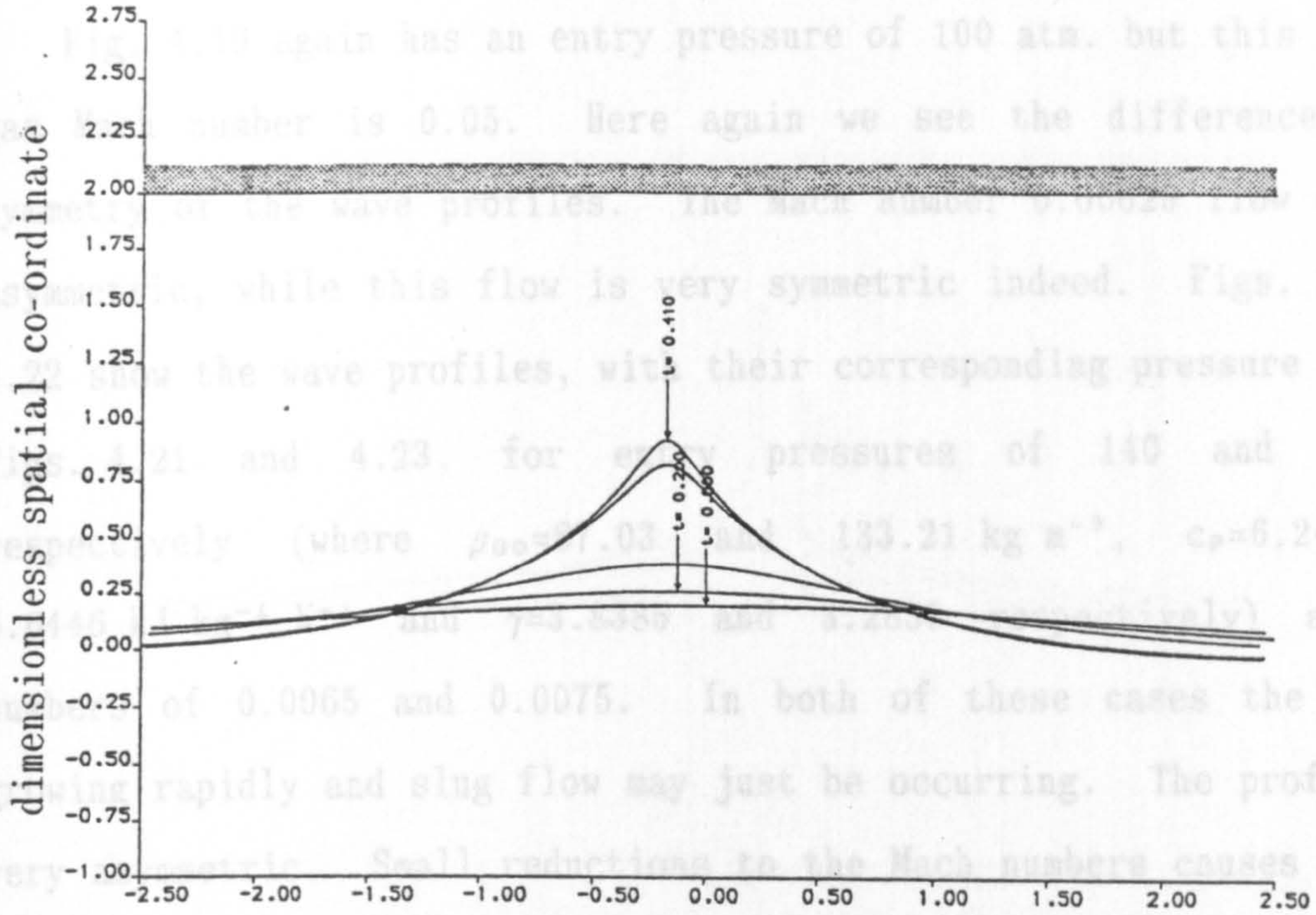

Fig. 4.19

Fig. 4.19 shows the transition to slug flow with steam at 100 atm entry pressure and Mach number 0.050 at dimensional times t≃0, 0.021, 0.025, 0.029, 0.033, 0.035 and 0.036 s.

Fig. 4.19 again has an entry pressure of 100 atm. but this time the gas Mach number is 0.05. Here again we see the difference in the symmetry of the wave profiles. The Mach number 0.00625 flow was very asymmetric, while this flow is very symmetric indeed. Figs. 4.20 and 4.22 show the wave profiles, with their corresponding pressure profiles Figs. 4.21 and 4.23, for entry pressures of 140 and 180 atm. respectively (where ρ_{Go}=87.03 and 133.21 kg m^{-3}, c_p=6.2461 and 6.6446 kJ kg^{-1} K^{-1} and γ=3.8385 and 3.2830 respectively) and Mach numbers of 0.0065 and 0.0075. In both of these cases the wave is growing rapidly and slug flow may just be occurring. The profiles are very asymmetric. Small reductions to the Mach numbers causes no rapid growth of the liquid surface. While these curves are seen to be qualitatively similar to those obtained for the air-water flows a few important points arise.

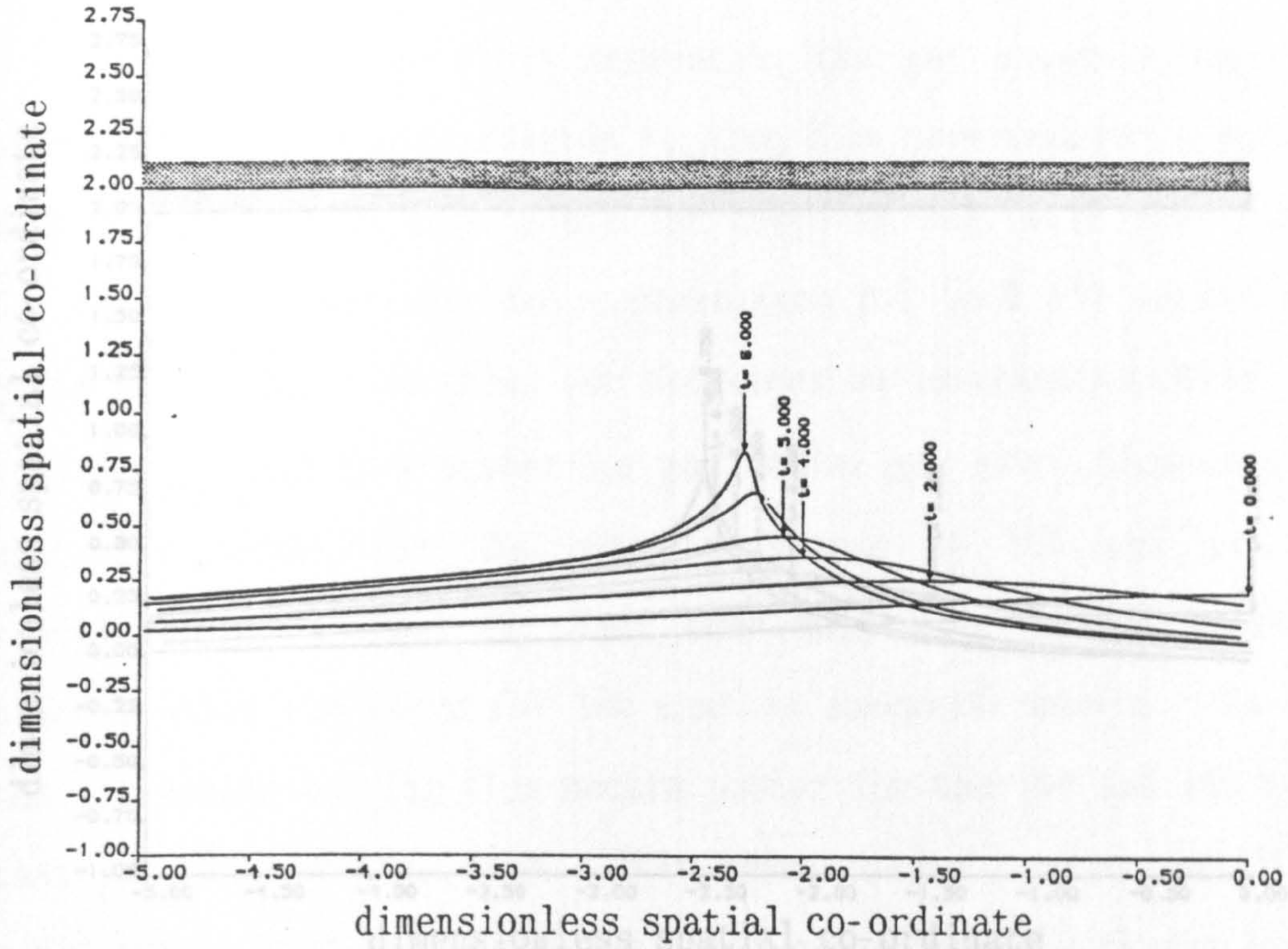

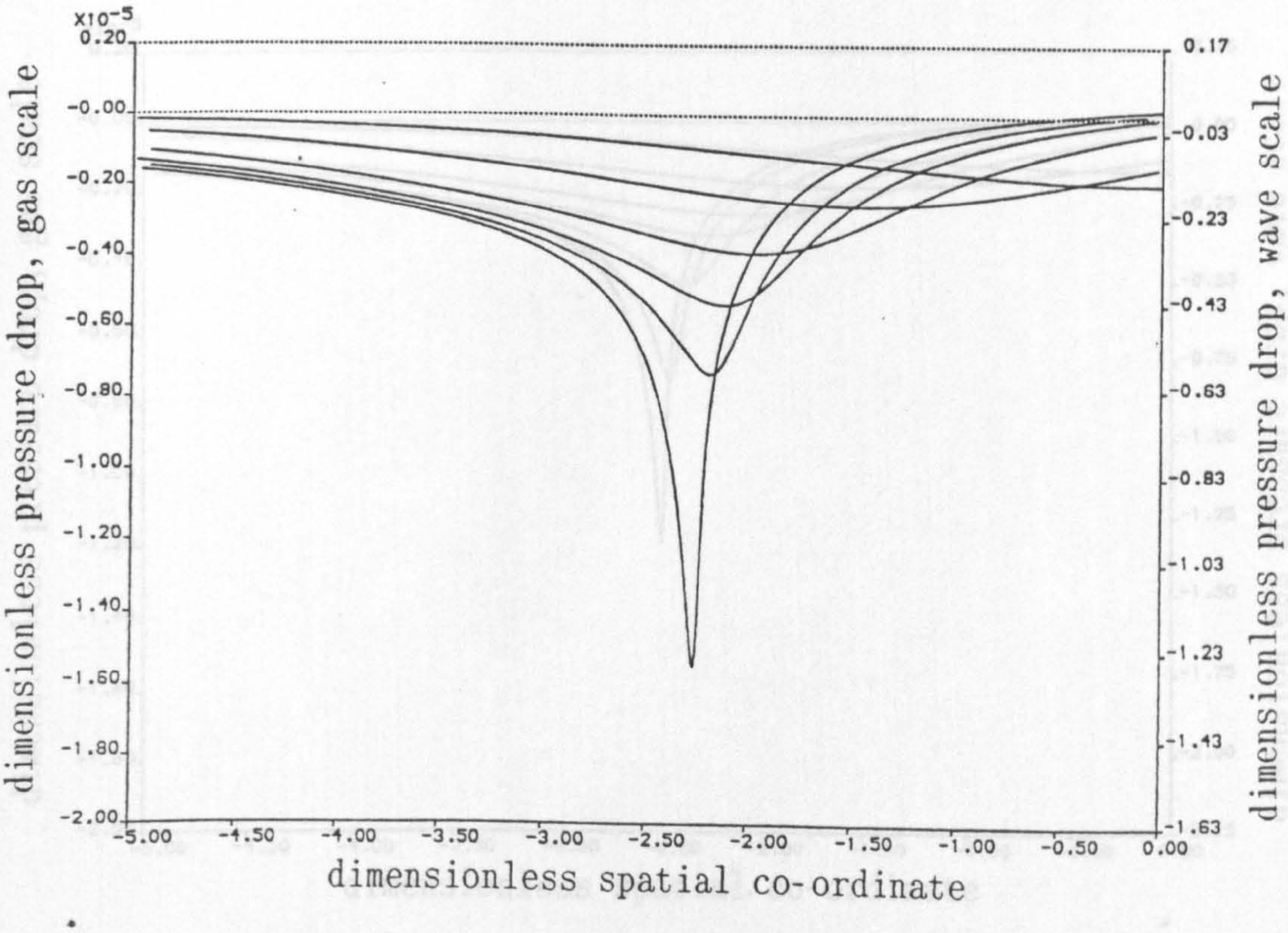

Figs. 4.20 (top) and 4.21

Fig. 4.20 shows the transition to slug flow with steam at 140 atm entry pressure (c_P=6.2461 kJ kg^{-1} K^{-1}, γ=3.8385) at temperature 336.63°C and Mach number 0.0065 at dimensional times t≃0, 0.25, 0.49, 0.62, 0.68 and 0.74 s

Fig. 4.21 shows the dimensionless pressure variation corresponding to the conditions for the wave in Fig. 4.20 at dimensional times t≃0, 0.12, 0.25, 0.37, 0.49, 0.62, 0.68 and 0.74 s.

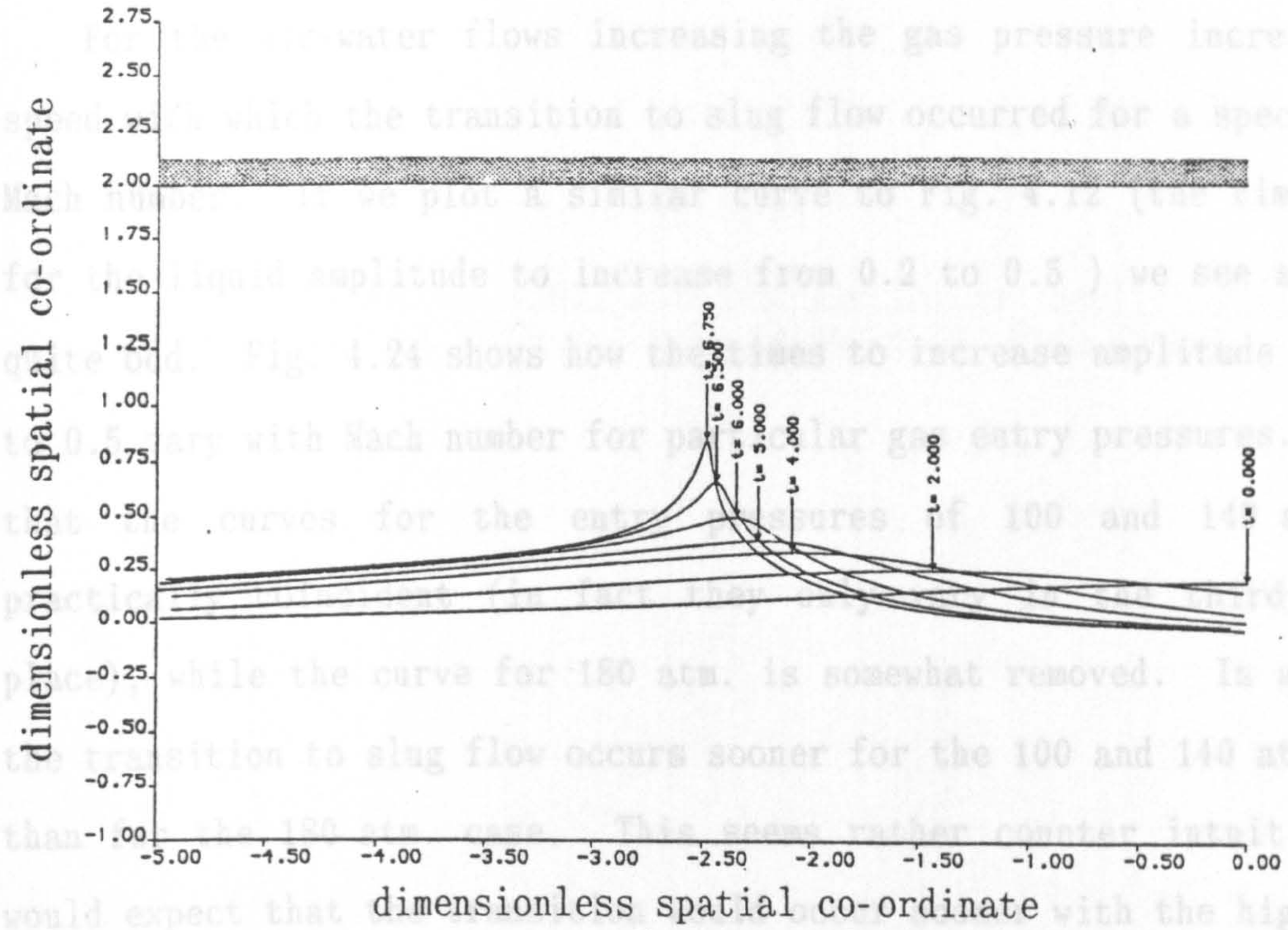

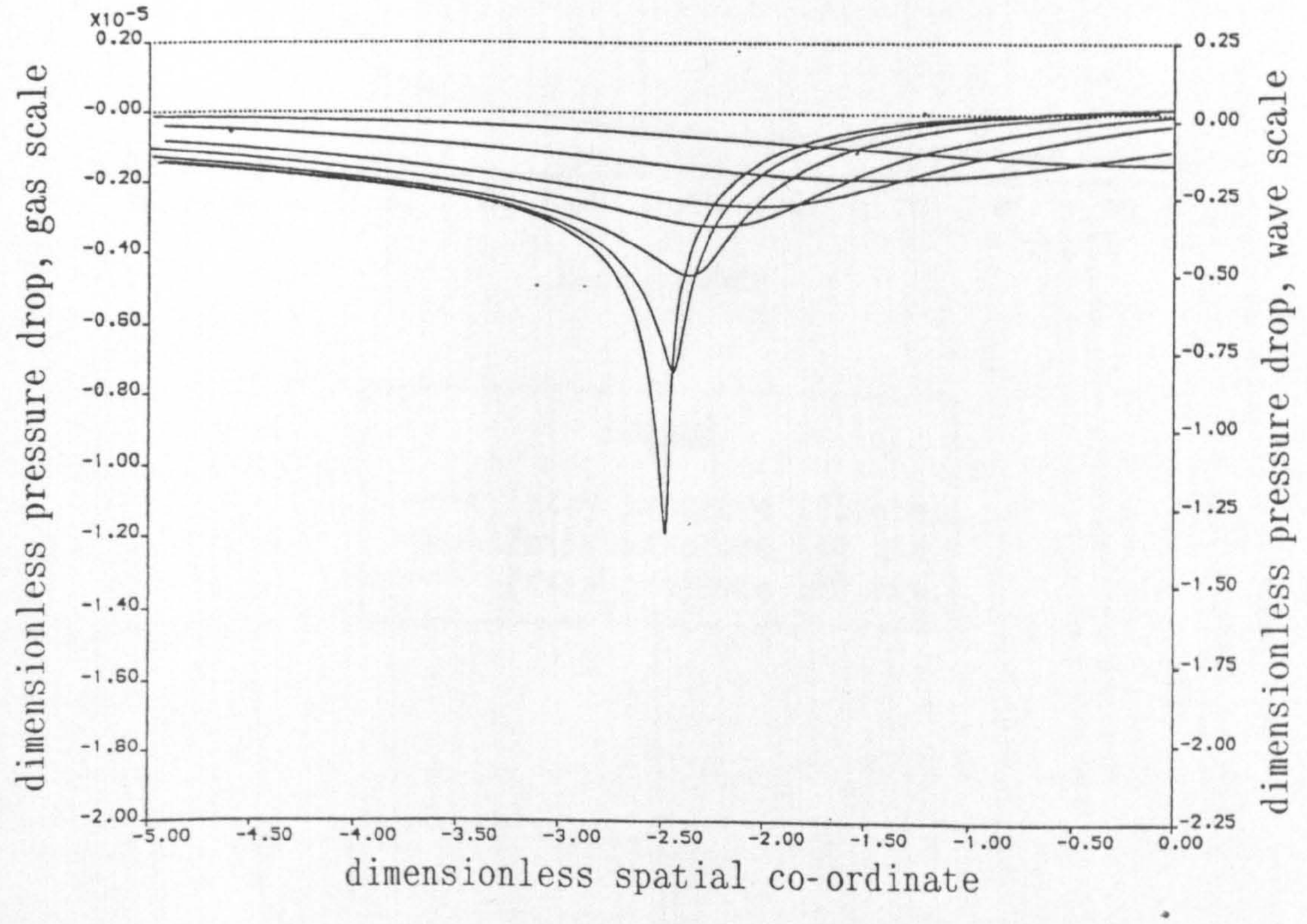

Figs. 4.22 (top) and 4.23

Fig. 4.22 shows the transition to slug flow with steam at 180 atm entry pressure (c_P=6.6446 kJ kg^{-1} K^{-1}, γ=3.2830) at temperature 356.96°C and Mach number 0.0075 at dimensional times t≃0, 0.25, 0.49, 0.62, 0.74, 0.80 and 0.83 s.
Fig. 4.23 shows the dimensionless pressure variation corresponding to the conditions for the wave in Fig. 4.22 at dimensional times t≃0, 0.25, 0.37, 0.49, 0.62, 0.74, 0.80 and 0.83 s.

For the air-water flows increasing the gas pressure increased the speed with which the transition to slug flow occurred for a specific gas Mach number. If we plot a similar curve to Fig. 4.12 (the times taken for the liquid amplitude to increase from 0.2 to 0.5) we see something quite odd. Fig. 4.24 shows how the times to increase amplitude from 0.2 to 0.5 vary with Mach number for particular gas entry pressures. We see that the curves for the entry pressures of 100 and 140 atm. are practically coincident (in fact they only vary in the third decimal place), while the curve for 180 atm. is somewhat removed. In addition, the transition to slug flow occurs sooner for the 100 and 140 atm. flows than for the 180 atm. case. This seems rather counter intuitive. We would expect that the transition would occur sooner with the higher Mach number flows (as it does for the air-water like flows).

Fig. 4.24

Variation of the time taken for the initial amplitude of the wave to reach 0.5 with relative gas Mach number

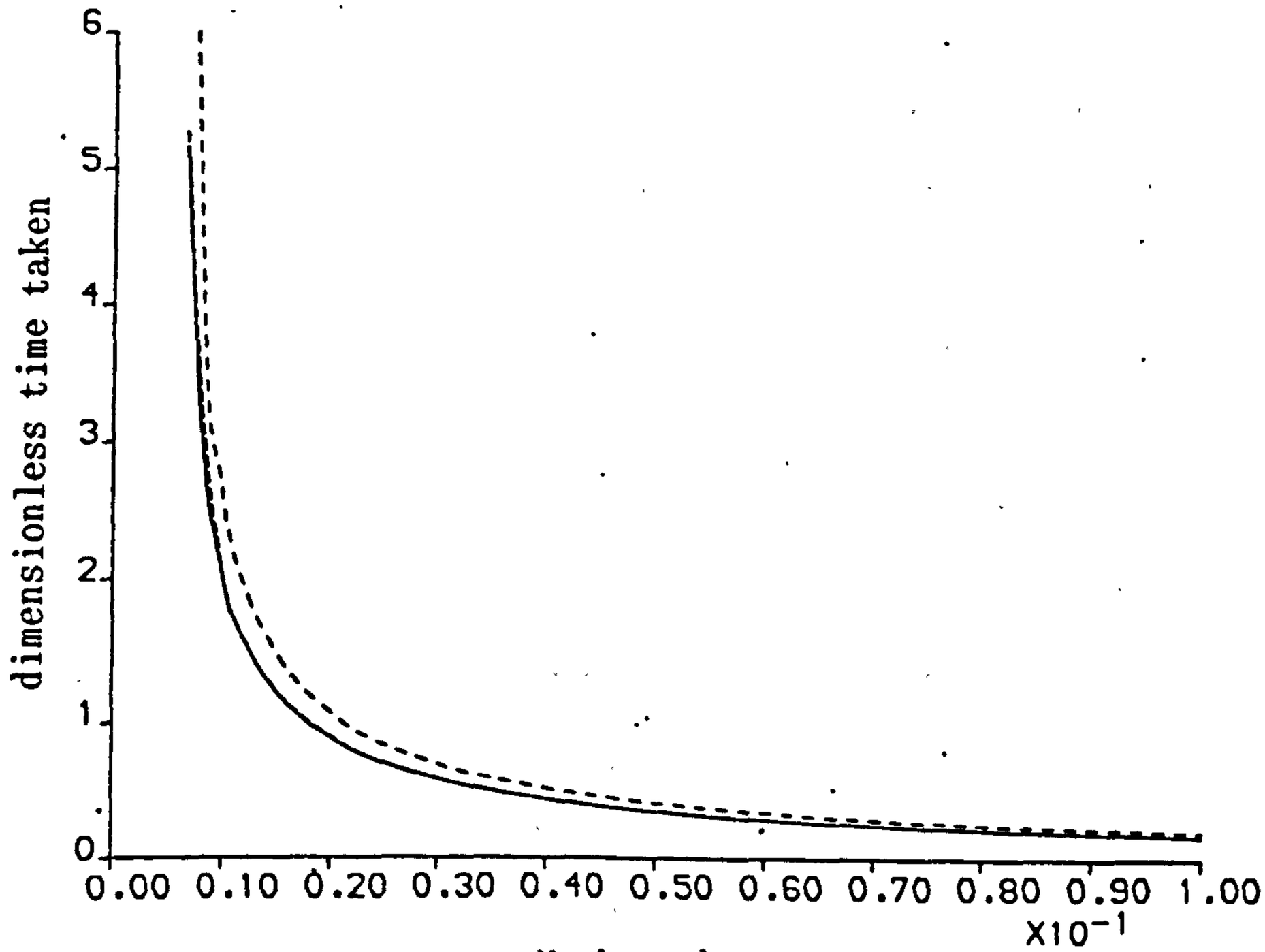

Legend

—— Entry pressure 100 atm.
----- Entry pressure 140 atm.
---- Entry pressure 180 atm.

This, then, seems like another situation where intuition is false. The behaviour of steam at these high pressures cannot easily be compared with our day-to-day knowledge of ideal-like gases such as air. Indeed, steam under such conditions is closer to behaving like steam at its thermodynamic critical point than steam from a kettle spout, and to think of steam in such a fashion is misleading. Instead, perhaps we should consider the steam under these really high pressure conditions to be liquid-like in behaviour. If we consider the steam to water density ratio at these high pressures we have some justification in such an assumption since the density ratio is typically ~0.10 (as opposed to 0.001 for air-water). (Steam at 180 atm. has a density of 133.21 kg m^{-3}.) If we consider the steam to be liquid-like then perhaps the easier transition at 100 and 140 atm. than at 180 atm. may be explained. A true liquid is not affected as much by compressibility as a gas or a vapour. Perhaps the very high (180 atm.) pressure steam flow is less of a compressible flow than its lower pressure counterparts (despite the sound speed in steam at 180 atm. being ~169 m s^{-1} while steam at 140 atm. has a sound speed ~248 m s^{-1}: these values are obtained from the equation of state for steam). Then the flow of the steam through the constriction over the crest of the wave will produce a significantly smaller pressure drop than the lower pressure flows. This will then affect the surface pressure distribution and slugging will be hampered. If we compare Figs. 4.18, 4.21 and 4.23 we see that this is in fact the case. The pressure drops for the 100 and 140 atm. flows being very similar at the same times, while the 180 atm. flow pressure drop is considerably smaller. As to why the 180 atm. flow behaves in a less compressible fashion than its counterparts is somewhat speculative. Perhaps the greater proximity to the steam critical point is an important factor. Also, perhaps neglecting the thermodynamic effects may give rise to such anomalous answers.

4.7 Discussion of the numerical scheme

Let us now consider the numerical calculation itself. The results from the numerical calculation initially use 300 surface points between $-14 < \xi < 14$ (dimensionless spatial co-ordinate) to describe the solitary wave of amplitude to depth ratio 0.2. The maximum number of points that the calculation can cope with on an IBM 3090/150S is 1200. The accuracy of the calculation is controlled by specifying the tolerance to which the equilibrium level at either end of the calculation must be maintained. To maintain these tolerances points are either added to the calculation, increasing the length of the computational domain, or removed, when necessary. In this fashion the propagation of the wave may be followed.

For the purposes of these numerical calculations it was found necessary to describe the initial solitary wave with 300 points. When less than 300 points were used it was found that spurious oscillations appeared on the gas-liquid interface which disappeared when more points were added, or if numerical smoothing was used. Numerical smoothing, however, inhibited the surface level from rising as quickly as it does in the case when more points are used. To maintain accuracy, numerical smoothing was not employed.

The dimensionless time limit of the calculations was chosen to be τ=100 (4 s real time). For this value of the time limit either the total number of points needed to describe the surface was in excess of 1200 (the computational virtual memory limit), or the elapsed cpu time was becoming prohibitive, and so the calculation was stopped. In fact, on an IBM 3090/150S computer it was found that for the breaking wave problem (like that shown in Fig. 4.3) the calculation took approximately

12 ms per grid node per time step, while for the air-water like flows it took approximately 20 ms per grid node per time step and 30 ms for the steam-water flows. In principle by choosing the equilibrium level tolerances adequately, and with no limit on cpu time, the problem could be computed to any arbitrary time limit. This would make the study of "slow" slugging (i.e. when it takes a relatively long dimensional time for slugs to occur) a possibility.

In addition to stopping the calculation when the number of points or cpu time were becoming large, the calculation may be terminated by the numerical scheme itself. Within the scheme is incorporated a "roughness" parameter which is responsible for the termination of the above calculations at the times shown. In this instance, the roughness parameter may be regarded as a measure of how fast the points on the surface are being drawn apart in the regions where the surface slope is greatest, and pushed together in regions like the peak, and the inadequacy of the point adding and removing routines at the ends of the computational domain to cope with this point movement. So, even while the surface in many of the above figures appears to be well described, the rapid stretching and concentrating of the surface points in some regions is enough to stop the calculation.

Clearly, it would be desirable to develop a model that allows us to track the rapidly growing fluid motion for longer times. This, however, would require the gas to be modeled as an unsteady, two-dimensional flow, or as a first step, at least as a two-dimensional flow for the class of surface motions and time scales involved. Since this was not possible at this time, the results from the one-dimensional model can only be used to describe the initiation of slug growth, and not the stages of growth as shown in plate 6 of Chapter 3.

4.8 Discussion

We have seen in the above sections that modifying the surface pressure distribution over a solitary wave may cause the surface amplitude to grow rapidly if the conditions are correctly chosen. The qualitative results are very encouraging. The interface is seen to remain "wavy-stratified" for gas flows below a certain Mach number, while the surface wave is seen to grow rapidly (as expected for slugging flows) when the Mach number increases beyond a certain point.

With this in mind, the scheme was extended to cover steam-water flows by using an approximate equation of state for steam. The aim of this work was to see whether slug flow could be predicted from numerical calculations. Indeed, the results of the previous section suggest that slug flow may occur for steam-water like flows with no real thermodynamic relations in which the gas Mach number is very small - Mach numbers in the region of 0.006 for gas pressures of 100 atm and 0.007 for gas pressures of 180 atm. No comparison with an "incompressible" steam was performed. This then shows that there is an anomalous behaviour when we consider high pressure steam-water like flows. The very high pressure steam appears to slug more slowly than slightly lower pressure steam. Perhaps this may account for the fact that experimenters who have tried to produce a flow régime map for steam at 180 atm. have been largely unsuccessful in finding a sub-domain in which slug flow has been proven to exist, Pearce (1982).

In fact, Pearce (1982) catalogues experiments using Refrigerant-12 at 30 atm. At these pressures the refrigerant and its vapour have a similar density ratio to steam-water at 180 atm. It was hoped that in this way a flow régime map that could be applied to steam-water flows

could be obtained. Pearce finds that slug flow may occur for certain values of the gas and liquid superficial velocities ($0.2 \lesssim U_{Ls} \lesssim 1.0$ m s^{-1} and $0.75 \lesssim U_{Gs} \lesssim 1.2$ m s^{-1}) and this is in reasonable agreement with our slug growths at the lower Mach numbers. For a gas Mach number of 0.008 and entry pressure of 180 atm. we have a superficial gas velocity of 0.83 m s^{-1} since the sound speed is ~169 m s^{-1}. However, if the Mach number is increased to 0.1, say, which is a reasonable Mach number for steam annular flow, then for the 100 atm flow case the surface profile blows up within a dimensionless time of τ=0.2 (very fast!). Perhaps, then, this is indicative that there is a transition to a different flow type (perhaps annular flow) rather than to slug flow at high Mach numbers.

Whether this numerical scheme can be used to accurately predict wave like transitions to slug flow must remain to be verified. There are, however, several reasons for using such a scheme. This boundary integral scheme has been used extensively in the past to model breaking shallow water waves with great success, and the scheme has proved to be both accurate and efficient (Tanaka, Dold, Lewy & Peregrine (1987)). Further, this scheme has not been found to suffer from the "saw-tooth" numerical instability which an alternative, a Green's identity boundary-integral approach, has been found to suffer from (Dold & Peregrine (1986)).

There are naturally some limitations with the approach used. For example, analogies between this numerical work and the experimental work of the previous chapter must be tenuous. The experimental results are for two-phase flows within a pipe (three-dimensional geometry) while the numerics consider the two-dimensional channel case. Experimental work on two-phase flows in a really broad horizontal rectangular channel,

like that of Wallis & Dobson (1973), may enable firmer conclusions to be made. Perhaps the greatest limitation of this model is the treatment of the gas as a quasi-steady one-dimensional flow. With improvements in this aspect of the modelling the numerical results may agree further with any rectangular channel two-phase flow experiments.

4.9 Conclusions

The treatment of air-water like flows by modifying the surface pressure distribution by using a quasi-steady one-dimensional ideal gas motion has permitted the initial growth of slug flow to be modeled. The results from these calculations suggest that the transition to slug flow will occur sooner if the entry pressure is increased, or if the gas Mach number is increased. At higher gas Mach numbers the effect of the motion (and velocity) of the liquid layer, and the effect of gravity on the interface is outweighed by the fast motion of the gas and the resulting rapid pressure changes. This causes the more symmetric growth of the wave.

Since the numerical scheme deals with an inviscid, laminar, irrotational flow of a homogeneous system it only requires the relative velocity of the gas and the liquid. The result of this is that we are not in a position to uniquely define both the liquid and gas velocity, and so our precise position on a flow régime map is in question. Only by trying to define some length-scale (such as a turbulent length-scale) in the direction of the liquid and gas flow may we obtain the unique positions on the flow régime map for the flows that we are considering.

For the steam-water flows we find a further interesting result. We find that the speed with which the liquid surface grows increases with the Mach number of the steam (in the same fashion as air-water like flows), while increasing the entry pressure retards this surface growth. For very low Mach number flows we get relatively slow growth rates and for such Mach numbers slug flow is predicted by the experimental work of Pearce (1982). Further, in that study flows with higher Mach numbers were found to be typically annular flows. This suggests that while we

may always obtain some wave growth by increasing the Mach number, these flows may not be physical. Perhaps these flows may instead be flows in a different flow régime.

5. THE EFFECT OF ENTRAINED DROPLETS ON GAS DYNAMICS IN A PIPE

5.1 Introduction

Our experiments recorded that a wave would grow until it almost blocked the entire tube cross-section. As the wave grows droplets of liquid become entrained into the gas flow. Initially, the amount of entrained liquid is small. However, as the wave reaches its maximum height in the tube, entrainment increases greatly. In addition to droplets being entrained into the gas, some gas is entrained into the liquid.

To understand the nature of the interaction of entrained drops with the gas let us perform the following thought experiment:

1. Consider gas flowing through a converging-diverging nozzle. Mass conservation and Bernoulli's equation tell us that as the sub-sonic gas flows through the nozzle it speeds up through the contraction, and then slows down again as it flows through the expansion. Consequently, the pressure decreases then increases again.

2. Consider now the gas flowing down a tube of constant cross-section. Some liquid droplets are added to the pipe at a lower velocity than the gas velocity. Now, the gas again flows through a constriction, the dispersed droplets. This time we cannot simply tell whether we will always get a pressure drop. While the gas speeds up through the constriction (hence, a drop in pressure) it loses momentum to the droplets so the gas slows down and pressure rises. So, there is a trade off. Will the pressure drop due to the constriction always out-weigh the pressure rise due to the momentum transfer?

In most models of two-phase flow, the effect that the droplets have on the gas dynamics, and hence on the liquid dynamics, is not taken into account. The models of Wallis & Dobson (1973) (inverse Benjamin bubble), Dukler & Hubbard (1975) (bridging phenomenon), and most empirical models, do not consider the effect of the entrained droplets on the flow.

However, the effect of droplets on the gas flow has been investigated by Kreibel (1964) and more recently, in the fine paper by Comfort III & Crowe (1980). From their theoretical modelling they conclude that for high Mach number flows a pressure shock is often formed. This shock, and the abruptness of its formation, is very sensitive to droplet size. For small drops the gas-liquid mixture behaves like a continuum and shocks can occur for flows with velocity below the vapour sonic velocity. They conclude that for droplets of diameter between 1 and 2 μm the mixture behaves like a continuum.

Bouré et al. (1976) derive a criterion for the maximum two-phase flow rate, their "critical" rate. They also define a "critical region", analogous to the region in which a single phase compressible flow becomes choked. They conclude that for two-phase flows, like their single phase counterparts, the flow is critical when disturbances initiated downstream of the critical region cannot propagate upstream. They attribute this effect to the strong coupling between the phases. Soo (1976) formulates the conservation of mass, momentum and energy equations for a two-phase system, including coupling terms between the phases.

Drew (1983) reviews dispersed two-phase flow models, and examines this type of flow from a continuum-mechanical approach. More is said about the continuum-mechanical approach in the following section.

5.2 Equations of motion

By definition, two-phase flows are flows in which there is an interface separating the phases, unless we consider thermodynamically critical two-phase flows in which the ideas about interfaces are notional ones. On a small scale a two-phase system consists of a number of single phase regions which are bounded by moving interfaces. So "in theory, the [two-phase flow] problem could be formulated in terms of standard balance equations applicable to single phase flow with appropriate matching boundary conditions at the interfaces" (Ishii & Kocamustafaogullari (1983)). However, to model a two-phase flow using a multi-boundary formulation with the positions of the interfaces unknown would be rather difficult and impractical. To model two-phase flows without explicit knowledge of the fluid motions on a microscale, yet modelling these microscale effects in macroscopic quantities, one of the following approaches is generally used to obtain the equations of motion (Ishii & Kocamustafaogullari (1983)):

1. Interacting continua assumption
2. Control volume modelling
3. Averaging method

The first and second approaches are based on empiricism, hypothesis and physical insight, while the third is mathematically rigorous but requires much mathematical manipulation.

Many authors have employed the averaging approach. While the mathematical manipulations of the averaging method may become tedious, there are several advantages in using this method. For instance, by obtaining macroscopic equations from microscopic considerations specific microscopic effects can be traced (such as the effect of microscopic stresses) to what they correspond to macroscopically. In this way some

physical understanding of the macroscopic quantities can be achieved. Furthermore, if terms appear in the system of equations obtained by the averaging method that do not appear in a postulated or empirical system, then one is in a position to comment on why the terms are insignificant, or to modify the hypothesised systems to comply with the averaged system.

For these reasons, a macroscopic system of equations based on the averaging method that describes two-phase flows will be used. However, it is not the intention of the author to reproduce the analysis involved in the averaging method, which may be found in the very well documented articles of Drew (1983), Ishii & Kocamustafaogullari (1983), Ishii (1975) and Soo (1967), to name but a few. Rather, it is intended to give a flavour of the averaging method and then briefly discuss the macroscopic equations of the two-phase system prior to employing these equations to look at dispersed two-phase flows and the gas dynamics in particular.

The averaging method is basically a means by which high frequency fluctuations of the microscopic variables are eliminated (like low pass filtering), and yet the statistical effects of the collective variations are retained. By analogy, consider a cup of tea. Statistical thermodynamics allows us to study every particle of the tea. Some particles have great energy and some less, and together these particles possess a particular energy distribution, a Boltzmann distribution for instance. The particles with large enough energy may evaporate and leave the system resulting in a new energy distribution, with new (lower) mean energy. This may all be analysed statistically by looking at the small fluctuations of the energies. However, sometimes a macroscopic model will suffice. Then we may say "blowing on the tea

(removing the high energy particles from the system) lowers the tea's temperature (reduces its mean energy)".

For two-phase flows, one of two possible averaging methods is most commonly used, depending on whether a fully three-dimensional representation is required, or whether a quasi-one-dimensional system, with constitutive relations for flow properties normal to the main flow, will suffice. These may be termed Eulerian (time) statistical or Eulerian area averaging respectively. Drew (1983) discusses these, and other averaging methods, at some length. An important point about averaging arises in Ishii & Kocamustafaogullari (1983) and also from statistical thermodynamic considerations, Kittel & Krömer (1980) that is, the average of the product of variables is not equal to the product of the averages. So, care must be taken when using the averaging method to ensure that the correctly calculated averages are used.

In addition to the various different methods for obtaining the macroscopic equations of the system, there are also two different basic formulations of the macroscopic equations themselves. These are the two-fluid model and the mixture model.

The two-fluid model considers each phase separately. Each phase has its own mass, momentum and energy conservation equations, and these sets of equations for the two phases are coupled to describe the system as a whole, while the mixture model dispenses with the coupling terms by formulating the conservation equations for the whole system as a mixture with a constitutive equation to describe the relative velocity of the phases (Drew (1983)).

The two-fluid model contains at least two transient forces; the virtual mass force and the Basset force, in addition to the drag and interfacial shear forces. When the averaging method is used on the microscale continuity equations (see Drew (1983) p.271 equations (25), (26), (28) and (30) or Ishii & Kocamustafaogullari (1983) p.6 equations (1), (2), (3) and (5)) several interfacial transfer terms arise. Constitutive relations are then used on these transfer terms to transform the averaged microscale quantities into macroscale quantities. Hence we obtain what Drew refers to as the "interfacial momentum transfer term" (Drew (1983) p.281 equation (77), analogy with Ishii & Kocamustafaogullari (1983) p.7 equation (9)). Ishii & Kocamustafaogullari (1983) end their discussion on the two-fluid model by pointing out that although the averaging method is very rigorous, the constitutive relations for the interfacial transfer terms provide most of the error in the final modelling, and hence in the macroscopic equations.

The mixture model, on the other hand, considers the motion of the two-phase system as a whole. This model assumes that there is a very strong coupling between the phases. So, the mixture model is a good approximation to the two-fluid model only when interaction time or the domain of the two-phase flow is sufficiently long. Certain two-phase flows, such as those in which one phase is being rapidly accelerated with respect to the other phase, cannot be described using the mixture model. Various different mixture models exist, such as the homogeneous flow model, or the drift-flux model to name but two, and these depend on the treatment of the non-equilibrium thermodynamic effects between the phases (Soo (1967)).

Since none of the mixture models can cope with the rapid accelerations of one phase with respect to the other, the two-fluid model will be used.

Drew (1983) points out that the crucial modelling for two-phase flows is done via the interfacial momentum transfer terms. He, in common with Ishii (1975), defines an interfacial momentum transfer term that contains the forces on the "particulate phase due to viscous drag, wake and boundary layer formation, and unbalanced pressure distributions leading to lift or virtual mass effects, except for the mean interfacial pressure". So, the interfacial momentum transfer term can be considered as consisting of a drag force, a virtual mass force, a Basset force and a force due to the effect of average interfacial viscous stress, neglecting any phase change. From Drew (1983) this term is of the form:

$$\underline{M} = A_1(\underline{u}_G - \underline{u}_L) + A_2\left[\left[\frac{\partial \underline{u}_G}{\partial t} + \underline{u}_L.\underline{\nabla}\,\underline{u}_G\right] - \left[\frac{\partial \underline{u}_L}{\partial t} + \underline{u}_G.\underline{\nabla}\,\underline{u}_L\right]\right]$$
$$+ A_5(\underline{u}_G - \underline{u}_L).\underline{\nabla}(\underline{u}_G - \underline{u}_L) + A_6(\underline{u}_L - \underline{u}_G).[\underline{\nabla}(\underline{u}_L - \underline{u}_G)]^T$$
$$+ A_3(\underline{u}_G - \underline{u}_L).\underline{D}_{L,b} + A_4(\underline{u}_G - \underline{u}_L).\underline{D}_{G,b} \qquad (5.2.1)$$

where the A_i (as used by Drew) are the following scalar functions of the invariants:

$$A_1 = \tfrac{3}{8}\alpha\rho_G\frac{C_D}{r}|\underline{u}_L - \underline{u}_G|$$

$$A_2 = \alpha\rho_G(\tfrac{1}{2} + \tfrac{3}{2}\alpha) = \rho_G B_2$$

$$A_4 = \alpha L$$

$$A_5 = A_2(1 + fn(\alpha))$$

where r is the effective particle radius, C_D the drag coefficient and α

the droplet void fraction (the fractional amount of liquid in the channel), and L and fn(α) are unknown functions. By obtaining the specific form of fn(α) for a particular flow, we are then in a position to obtain the functional form of A_4 (and in principle A_3 and A_6) with respect to A_2. In his discussion Drew concludes that no observations have confirmed the existence of the term in A_6, and the terms in A_3 have no physical basis, so generally, these terms are set to zero. We are largely interested in entrained flows in which the particulate phase is quite disperse, α is small. The drag coefficient, $C_D = C_D(\alpha,Re)$ where Re is the droplet Reynolds number, is given in a table for drag coefficients in multiparticulate systems reproduced by Drew (1983). Drew also discusses the arbitrary function of α, fn(α), and concludes that while no calculations have shown any effect due to varying this function, this function may be found by treating the interfacial momentum transfer term as a uniform conservative field. In this fashion Drew obtains both fn(α) and A_4. However, Drew's final analysis leading to his equation (99) is not wholly correct. Between his equation (77) and (99) he has changed his definition of A_4 from αL to $-\alpha L$, and so the form of L that he obtains has the wrong sign. However, this is a minor error. On the other hand, if we try to work backwards from his equation (99) to his equation (77) we obtain the following:

$$\underline{M} = A_1(\underline{u}_G - \underline{u}_L) + A_2\left[\left[\frac{\partial \underline{u}_G}{\partial t} + \underline{u}_L.\underline{\nabla}\,\underline{u}_G\right] - \left[\frac{\partial \underline{u}_L}{\partial t} + \underline{u}_G.\underline{\nabla}\,\underline{u}_L\right]\right.$$
$$\left. + \tfrac{1}{2}\underline{u}_G.\underline{\nabla}\,\underline{u}_L - \tfrac{1}{2}\underline{u}_L.\underline{\nabla}\,\underline{u}_L\right] + A_5(\underline{u}_G - \underline{u}_L).\underline{\nabla}(\underline{u}_G - \underline{u}_L) + A_4(\underline{u}_G - \underline{u}_L).\underline{D}_{G,b}$$

where the terms in italics are spurious terms that arise from Drew's equation (99). Thus, his equation (99) is in error, and so his values for fn(α) and A_4 may be wrong. In his subsequent analysis of the interfacial momentum transfer term he finds that in order to satisfy $A_1 \geq 0$, and by assuming that fn(α) and L are constants, he finds that

$fn(\alpha) = 2$ and $L = -\rho_G B_2$. If we perform the analysis to express the interfacial momentum transfer term in conservation form we find that Drew's value for $fn(\alpha)$ is in fact correct and $fn(\alpha) = 2$. However, we find that $A_4 = 2A_2$. Equation (5.2.1) then becomes

$$\underline{M} = A_1(\underline{u}_G - \underline{u}_L) + A_2\left[\left[\frac{\partial \underline{u}_G}{\partial t} + \underline{u}_G.\nabla\,\underline{u}_G\right] - \left[\frac{\partial \underline{u}_L}{\partial t} + \underline{u}_L.\nabla\,\underline{u}_L\right]\right] \tag{5.2.2}$$

In addition to this interfacial momentum transfer term we wish to consider a sudden addition of liquid to the gas flow, such as a source term corresponding to liquid being suddenly entrained.

5.3 The effect of the virtual mass term

For one dimensional flows equation (5.2.2) becomes:

$$M = A_1(u_G - u_L) + A_2\left[\left[\frac{\partial u_G}{\partial t} + u_G\frac{\partial u_G}{\partial x}\right] - \left[\frac{\partial u_L}{\partial t} + u_L\frac{\partial u_L}{\partial x}\right]\right] \quad (5.3.1)$$

Drew points out that in order for the virtual mass term to be important, the time scale of the flow must be $O(\frac{r}{V})$, where V is the velocity scale. Since r is typically small, and V large, then the virtual mass effects are only important at high frequencies. This is also noted by Soo (1976). This formulation enables us to show that the terms in A_2 are not responsible for the dominant coupling between the phases in agreement with Drew. We may then (tentatively) gauge the importance of the A_2 term relative to the A_1 term, the drag term, for the case of a suddenly entrained flow. The equations of mass and momentum conservation for the system are then:

$$\rho_L\frac{\partial \alpha}{\partial t} + \rho_L\frac{\partial}{\partial x}(\alpha u_L) = \rho_L E \quad (5.3.2)$$

$$\frac{\partial}{\partial t}[(1-\alpha)\rho_G] + \frac{\partial}{\partial x}[(1-\alpha)\rho_G u_G] = 0 \quad (5.3.3)$$

$$\rho_L\frac{\partial}{\partial t}(\alpha u_L) + \rho_L\frac{\partial}{\partial x}(\alpha u_L^2) = -\alpha\frac{\partial p_G}{\partial x} + A_1(u_G-u_L) + A_2\left[\left[\frac{\partial u_G}{\partial t} + u_G\frac{\partial u_G}{\partial x}\right] - \left[\frac{\partial u_L}{\partial t} + u_L\frac{\partial u_L}{\partial x}\right]\right] + u_{LI}E \quad (5.3.4)$$

$$\frac{\partial}{\partial t}[(1-\alpha)\rho_G u_G] + \frac{\partial}{\partial x}[(1-\alpha)\rho_G u_G^2] = -(1-\alpha)\frac{\partial p_G}{\partial x} - A_1(u_G-u_L) - A_2\left[\left[\frac{\partial u_G}{\partial t} + u_G\frac{\partial u_G}{\partial x}\right] - \left[\frac{\partial u_L}{\partial t} + u_L\frac{\partial u_L}{\partial x}\right]\right] \quad (5.3.5)$$

where u_{LI} is the velocity of the liquid interface from which entrainment begins, and $\rho_L E$ is the entrained liquid. Equations (5.3.4) and (5.3.5) may be re-written in the following form:

$$Du_L - \frac{A_2}{\rho_L\alpha + A_2} Du_G + \frac{\alpha}{\rho_L\alpha + A_2} \frac{\partial p_G}{\partial x} = \frac{\hat{u}_L\rho_L E + A_1(u_G-u_L)}{\rho_L\alpha + A_2}$$

$$Du_G - \frac{A_2}{\rho_G(1-\alpha) + A_2} Du_L + \frac{(1-\alpha)}{\rho_G(1-\alpha) + A_2} \frac{\partial p_G}{\partial x} = - \frac{A_1(u_G-u_L)}{\rho_G(1-\alpha) + A_2}$$

where $Du_i = \frac{\partial u_i}{\partial t} + u_i\frac{\partial u_i}{\partial x}$ for i=G or L, and $\hat{u}_L=u_{LI}-u_L$. The Du_i may now be decoupled and we obtain:

$$Du_L + \frac{\rho_G(1-\alpha) + A_2}{\rho_L\rho_G\alpha(1-\alpha) + A_2(\rho_L\alpha + \rho_G(1-\alpha))}\left[\alpha + \frac{\alpha A_2}{\rho_G(1-\alpha) + A_2}\right]\frac{\partial p_G}{\partial x}$$

$$= \frac{\rho_G(1-\alpha) + A_2}{\rho_L\rho_G\alpha(1-\alpha) + A_2(\rho_L\alpha + \rho_G(1-\alpha))}\left[\hat{u}_{LI}\rho_L E + A_1(u_G-u_L) - \frac{A_1A_2(u_G-u_L)}{\rho_G(1-\alpha) + A_2}\right] \quad (5.3.6)$$

$$Du_G + \frac{\rho_L\alpha + A_2}{\rho_L\rho_G\alpha(1-\alpha) + A_2(\rho_L\alpha + \rho_G(1-\alpha))}\left[(1-\alpha) + \frac{\alpha A_2}{\rho_L\alpha + A_2}\right]\frac{\partial p_G}{\partial x}$$

$$= \frac{\rho_L\alpha + A_2}{\rho_L\rho_G\alpha(1-\alpha) + A_2(\rho_L\alpha + \rho_G(1-\alpha))}\left[\frac{A_2}{\rho_L\alpha + A_2}(\hat{u}_L\rho_L E + A_1(u_G-u_L)) - A_1(u_G-u_L)\right] \quad (5.3.7)$$

If we also assume that the gas is isentropic, then

$$\frac{\partial p_G}{\partial x} = \frac{dp_G}{d\rho_G}\frac{\partial \rho_G}{\partial x} \quad (5.3.8)$$

where $\frac{dp_G}{d\rho_G} = a^2$, the square of the sound speed in the gas. Equations (5.3.2), (5.3.3), (5.3.6), (5.3.7) and (5.3.8) now express the conservation laws for the partially decoupled two-phase system.

The above problem can be forced no further analytically. By assuming that $\frac{\rho_G}{\rho_L} \ll 1$ (which is a reasonable assumption for many flows, including air-water flows and steam-water flows sufficiently far from the critical point) and remembering that $A_2 = \rho_G B_2$ they may be re-written as:

$$Du_L + \frac{1}{\rho_L \alpha}\left[\alpha + \frac{(1-\alpha)B_2}{(1-\alpha) + B_2}\right] \frac{\partial p_G}{\partial x} = \frac{1}{\rho_L \alpha}\left[\hat{u}_L \rho_L E + a_1(u_G - u_L) - \frac{A_1 B_2 (u_G - u_L)}{(1-\alpha) + B_2}\right] \tag{5.3.9}$$

$$Du_G + \frac{(1-\alpha)}{\rho_G[(1-\alpha) + B_2]} \frac{\partial p_G}{\partial x} = - \frac{A_1(u_G - u_L)}{\rho_G[(1-\alpha) + B_2]} \tag{5.3.10}$$

Using the method of characteristics to tackle this partial differential system yields the following characteristic equation;

$$(u_G-\lambda)^2(u_L-\lambda)^2 - \frac{\rho_G}{\rho_L}\left[\alpha + \frac{(1-\alpha)B_2}{(1-\alpha) + B_2}\right]\frac{1}{1-\alpha}\frac{dp_G}{d\rho_G}(u_G-\lambda)(u_L-\lambda)$$

$$- \frac{(1-\alpha)\alpha}{(1-\alpha) + B_2}\frac{1}{\alpha}\frac{dp_G}{d\rho_G}(u_L-\lambda)^2 - \frac{\rho_G}{\rho_L}\left[\alpha + \frac{(1-\alpha)B_2}{(1-\alpha) + B_2}\right]\frac{1}{1-\alpha}\frac{dp_G}{d\rho_G}(u_G-\lambda)(u_L-\lambda) = 0$$

Again, by discarding terms in $\frac{\rho_G}{\rho_L}$ ($\ll 1$) the above characteristic equation becomes:

$$(u_L-\lambda)^2\left[(u_G-\lambda)^2 - \frac{(1-\alpha)}{(1-\alpha) + B_2}\frac{dp_G}{d\rho_G}\right] \simeq 0 \tag{5.3.11}$$

And hence the eigenvalues are:

$$\lambda = u_L \text{ or } u_G \pm \sqrt{\frac{(1-\alpha)}{(1-\alpha) + B_2}\frac{dp_G}{d\rho_G}}$$

where the term within the square root is the sound speed in the system. Note, as $\alpha \longrightarrow 0$ then $B_2 \longrightarrow 0$ also. So as $\alpha \longrightarrow 0$ then the sound speed becomes the single phase sound speed, as expected.

5.4 Interim comments

Drew (1983) presents an expression for the interfacial momentum transfer between the phases of a dispersed two-phase flow. The expression contains the forces on the particulate phase due to viscous drag, wake and boundary layer formation and virtual mass. Recall equation (5.2.1) in which:

$$\underline{\underline{D}}_{i,b} = \tfrac{1}{2}(\underline{\nabla}\,\underline{u}_i + (\underline{\nabla}\,\underline{u}_i)^T)$$

Drew mentions that the terms included in the interfacial momentum transfer expression are there through a desire to model two-phase flows. So, while velocity gradients (expressing rate of deformation) are included, displacement gradients (expressing deformation) are not. And while we undoubtedly have cause to worry that something important may have been omitted, we continue with this formulation which is already fairly intractable.

Thus we arrive at our expression (5.2.3). We are interested in disperse two-phase flows where α is small. So, we may also suspect that the terms including A_2 are small in this case because $A_2 = O(\alpha)$. (Note however, that the A_1 term is $O(\frac{\alpha}{r})$, where both α and r are small, and so this term is not negligible.)

Nevertheless, to see what sort of effect the A_2 term has on the motion of the phases we express the interfacial momentum transfer term in conservation form, retaining the coupling via the A_1 (large) term.

So, by assuming that $\frac{\rho_G}{\rho_L} \ll 1$ we have obtained the eigenvalues of the system, but in doing so we have simplified the system a great deal. We

are confined to systems such as air-water systems by this approximation. Nevertheless, a large number of systems are of this type, and so for this class of problem we are in a position to comment on the effect of the virtual mass terms on the flow.

For the case of a gas flow in a pipe of constant cross-section, the characteristics of the flow are:

$$\lambda_C = u_G \pm a$$

By including the virtual mass term in the two-phase flow case we can see that the sound speed has been modified. The two-phase sound speed, a_{TP} is:

$$a_{TP} = a \sqrt{\frac{(1-\alpha)}{(1-\alpha) + \alpha(\frac{1}{2}+\frac{3}{2}\alpha)}}$$

where a is the sound speed in the gas alone. From this expression we can see that for the case when $\alpha \ll 1$ (which is necessarily the case when entrainment begins) then $a_{TP} \rightarrow a$, as would be expected.

Prior to this analysis we already knew that $A_2 = O(\alpha)$, and since we are interested in effects in which α is small, we could have just neglected it from the start. Rather than do this, we have found that the decoupled system is influenced by the virtual mass only through a modification of the gas sound speed. Perhaps we would have expected some influence to the motion of the particulate phase through the virtual mass term. This effect, however, would have been removed from the system by the assumption that $\frac{\rho_G}{\rho_L} \ll 1$, which is like saying that the virtual mass effects are too small (in some sense) to influence the motion of the really heavy phase.

So, we have further corroboration of the insignificance of the virtual mass term to dispersed two-phase flows when the liquid void fraction is small. It may now be neglected.

We are now in a position to study the effects of the drag term on disperse two-phase flow. The only remaining coupling is via the A_1 terms of the interfacial momentum transfer expression (see equation (5.3.1)).

5.5 The effect of the drag term

By assuming that $\alpha \ll 1$, and thus neglecting the A_2 term because it has little effect on the sound speed of the gas, the conservation equations for the system may be written as:

$$\frac{\partial \alpha}{\partial t} + \frac{\partial}{\partial x}(\alpha u_L) = E \tag{5.5.1}$$

$$\frac{\partial \rho_G}{\partial t} + \frac{\partial}{\partial x}(\rho_G u_G) = 0 \tag{5.5.2}$$

$$\alpha\left[\frac{\partial u_L}{\partial t} + u_L\frac{\partial u_L}{\partial x}\right] = -\frac{\alpha}{\rho_L}\frac{\partial p}{\partial x} + \frac{A_1}{\rho_L}(u_G - u_L) + \hat{u}_L E \tag{5.5.3}$$

$$\rho_G\left[\frac{\partial u_G}{\partial t} + u_G\frac{\partial u_G}{\partial x}\right] = -\frac{\partial p}{\partial x} - A_1(u_G - u_L) \tag{5.5.4}$$

If we consider an entrainment such that $E \begin{cases} \neq 0 & t=0 \\ =0 & \forall t>0 \end{cases}$ then $\forall t>0$ the equations describing the system is the same as above but with the omission of the terms in E.

Furthermore, if we assume that the gas is in fact ideal, and if we also consider the system to be one in which there is no heat transfer into or out of the system, then the First Law of Thermodynamics:

$$dI = dQ - dW$$

may be written as

$$\frac{\partial I}{\partial t} + \frac{\partial}{\partial x}[(I + p)u_G] = 0 \tag{5.5.5}$$

In order to proceed with the problem it necessary to determine which of the terms in equations (5.5.1) to (5.5.5) are of importance to the system, and which may be neglected. In order to do so the following non-dimensional variables (different from those used in Chapter 4) are

defined:

$$u = \frac{u_G}{a_o},\ v = \frac{u_L}{a_o},\ \xi = \frac{x}{D},\ \tau = \frac{ta_o}{D},\ p = \frac{p_G - p_o}{p_o},$$

$$\rho = \frac{\rho_G a_o^2}{\gamma p_o}\ ,\ \sigma = \frac{\rho_L a_o^2}{\gamma p_o},\ I = p_o e$$

where p_o is the pressure in the gas on entry to the pipe, and:

$$e = \frac{p + 1}{\gamma - 1} + \tfrac{1}{2}\gamma\rho u^2$$

and U_o is the free stream gas velocity, a_o the sound speed in the gas at pressure p_o, and D is the effective diameter of the tube (not necessarily the actual tube diameter). Thus (5.5.1) to (5.5.5) become:

$$\frac{\partial\alpha}{\partial\tau} + \frac{\partial}{\partial\xi}(\alpha v) = 0 \qquad \forall\tau>0 \qquad (5.5.6)$$

$$\frac{\partial\rho}{\partial\tau} + \frac{\partial}{\partial\xi}(\rho u) = 0 \qquad (5.5.7)$$

$$\sigma\left[\frac{\partial v}{\partial\tau} + v\frac{\partial v}{\partial\xi}\right] = -\frac{1}{\gamma}\frac{\partial p}{\partial\xi} + kC_D^* D\rho(u - v)^2 \qquad (5.5.8)$$

$$\rho\left[\frac{\partial u}{\partial\tau} + u\frac{\partial u}{\partial\xi}\right] = -\frac{1}{\gamma}\frac{\partial p}{\partial\xi} - kC_D^* D\rho\alpha(u - v)^2 \qquad (5.5.9)$$

$$\frac{\partial e}{\partial\tau} + \frac{\partial}{\partial\xi}[(p+e+1)u] = 0 \qquad (5.5.10)$$

by using $A_i = k\alpha\rho_G C_D^* |\underline{u}_L - \underline{u}_G|$ and $k=\frac{3}{8}$, $C_D^* = \frac{C_D}{r}$ where r is the radius of the droplets which is assumed to be small and constant. Remembering that we are considering $1-\alpha\approx 1$, equations (5.5.8) and (5.5.9) may be written in conservation form as:

$$\frac{\partial}{\partial\tau}(\alpha v) + \frac{\partial}{\partial\xi}(\alpha v^2) = kC_D^* D(u - v)^2\frac{\rho}{\sigma} \qquad (5.5.11)$$

$$\frac{\partial}{\partial\tau}(\rho u) + \frac{\partial}{\partial\xi}\left(\rho u^2 + \frac{p+1}{\gamma}\right) = -kC_D^* D\rho\alpha(u - v)^2 \qquad (5.5.12)$$

Equations (5.5.6), (5.5.7) and (5.5.10) are already in conservation form. Note, that in going to (5.5.11) from (5.5.8) the pressure gradient term has been omitted. This is because the pressure gradient term is of smaller order than the remaining terms, and so has little effect on the disperse liquid flow.

In order to pursue the modelling of the flow and since this system is used by other authors, so the comparison of results is possible, we must resort to a numerical solution of the equations to gain a deeper understanding of the flow.

5.6 Choice of numerical scheme for the equations of disperse two-phase flow

Our system of partial differential equations may be written in the general form:

$$\frac{\partial \underline{u}}{\partial t} + \frac{\partial}{\partial x}\left[\underline{F}(\underline{u})\right] = \underline{Q}(\underline{u}) \qquad (5.6.1)$$

where $\underline{F}$ is such that the Jácobian matrix, $\underline{\underline{A}} = \frac{\partial \underline{F}}{\partial \underline{u}}$, has only real eigenvalues, i.e is purely hyperbolic. There is a large class of partial differential systems of the form:

$$\frac{\partial \underline{u}}{\partial t} + \frac{\partial}{\partial x}\left[\underline{F}(\underline{u})\right] = 0 \qquad (5.6.2)$$

for which various analytic techniques, such as the method of characteristics, Jeffrey (1976), and numerical techniques, such as finite difference schemes, Roache (1972), exist. The solutions of the scalar conservation law:

$$\frac{\partial u}{\partial t} + \frac{\partial}{\partial x}\left[f(u)\right] = 0 \qquad (5.6.3)$$

have been extensively developed. The theory for non-homogeneous systems, such as (5.6.1), is less well developed.

Let us begin by considering the problem at hand. It is possible that a shock wave may form in the two-phase system, Comfort III & Crowe (1980). So we need to use a numerical scheme that can capture and follow any shock waves that are created. Finite difference schemes lend themselves most suitably to this problem (Allen (1987)). If we consider a compressible flow of the form (5.6.2) then Roache (1972) points out that when the partial differential system for gas dynamics are expressed in conservation form, then the Rankine-Hugoniot relations for a normal

shock wave are based only on this gross conservation and are not dependent on the microscopic behaviour within the shock front. However, use of the conservation form of the partial differential system alone does not guarantee conservation, and the finite difference method must also be conservative and stable. Then the correct jump condition is produced at the shock.

For the scalar conservation laws the theory of stability of finite difference schemes is well established (Courant et al. (1967)), but for nonlinear systems of equations this is less so. The most frequently used criterion for the stability of a centrally differenced one-dimensional compressible finite difference scheme is that the CFL number is

$$\nu = (V + a)\,\frac{\Delta t}{\Delta x} < 1$$

where Δt is the time step size, Δx the grid spacing, V the continuum advection speed and a the sound speed, Richtmeyer & Morton (1967). This can be translated as meaning that we are not allowing sound waves to travel more than one cell length per time interval. This aids in shock capturing. Another important quantity is the "total variation" of grid, which is a function of u^n (a function of u at time step n):

$$TV(u^n) = \sum_i |u^n_{i+1} - u^n_i|$$

finite difference schemes which are total variation diminishing (TVD), i.e.:

$$TV(u^n) \geq TV(u^{n+1})$$

will be good shock capturing schemes, Allen (1987).

Up-wind finite difference schemes (as opposed to centrally differenced schemes) of a one-time-step explicit nature achieve stability for the advection terms of a hyperbolic system, Roache (1972) p.64 (Roache also discusses the other terminology used in the literature to mean the same as "upwind differencing"). To illustrate what is meant by up-wind differencing, consider the linear advection equation:

$$\frac{\partial u}{\partial t} + a\frac{\partial u}{\partial x} = 0 \qquad a > 0 \qquad (5.6.4)$$

Then (5.6.4) may be approximated by the following explicit equation for a numerical scheme:

$$\frac{u_i^{n+1} - u_i^n}{\Delta t} + a\frac{(u_i^n - u_{i-1}^n)}{\Delta x} = 0 \qquad (5.6.5)$$

where u_i^n is the value of u at the i^{th} grid point at time level n, for example. Roache discusses the advantages of explicit numerical schemes over implicit schemes for hyperbolic conservation laws. He points out that while many explicit schemes are unconditionally stable for incompressible flows, they may not be for compressible flows, and that explicit down-wind differencing schemes are unconditionally unstable. So, to leading order, we may find u_i at the next time level from:

$$u_i^{n+1} = u_i^n - a\frac{\Delta t}{\Delta x}(u_i^n - u_{i-1}^n) \qquad a > 0 \qquad (5.6.6)$$

or:
$$u_i^{n+1} = u_i^n - a\frac{\Delta t}{\Delta x}(u_{i+1}^n - u_i^n) \qquad a < 0 \qquad (5.6.7)$$

One of the advantages of using an upwind finite differencing scheme is that it requires no additional initial and boundary conditions beyond those required by the original partial differential system. This makes the scheme, and the above difference equations, generally easy to

implement. Indeed, many upwind finite difference schemes possess the "transportive property" (Roache & Müller (1970)). This is stated as: "A finite difference formulation of a flow equation possesses the transportive property if the effect of a perturbation in a transport property is advected only in the direction of the velocity."

Many other methods, such as centrally differenced schemes for the advection terms, do not possess this property. If, in addition to the transportive property, we summarise what Roache means by "conservative property" as:

A finite difference formulation of the flow equations possesses the conservative property if the finite difference description of the mass conservation equation neither adds nor subtracts mass from the system through sources or sinks other than those prescribed within the original integral formulation of the equation.

Then, finite difference schemes like (5.6.6) and (5.6.7) are conservative and transportive providing the advection speed, a, is always positive- or negative-definite (and never goes through zero). If the sign of the advection speed switches, the conservative property of this finite difference scheme is violated.

For instances when a switches we may average a as follows:

$$a_r = \tfrac{1}{2}(a_{i+1} + a_i)$$

$$a_l = \tfrac{1}{2}(a_{i-1} + a_i)$$

where, in this case, the r and l refer to right and left, and:

$$u_r = u_i \quad a_r > 0 \;, \quad u_r = u_{i+1} \quad a_r < 0$$

$$u_l = u_{i-1} \quad a_l > 0 \;, \quad u_l = u_i \quad a_l < 0$$

and (5.6.6) and (5.6.7) then become:

$$u_i^{n+1} = u_i^n - \frac{\Delta t}{\Delta x}(a_r u_r^n - a_l u_l^n) \qquad (5.6.8)$$

which is both conservative and transportive regardless of the sign of the advection velocity, a.

Clearly, finite difference schemes of the above form cannot be applied directly to systems of the form (5.6.2), Allen (1987). Now, equation (5.6.2) may be written as:

$$\frac{\partial \underline{u}}{\partial t} + \underset{\sim}{A} \frac{\partial \underline{u}}{\partial x} = 0 \qquad (5.6.9)$$

In order to solve this problem using the ideas of the above finite difference scheme, we need to split this system of n conservation equations into a set of simple equations of the form of (5.6.3). This may be done by solving a succession of Riemann problems. Given the initial condition:

$$\underline{u}(x,0) = \underline{u}_0(x) \qquad (5.6.10)$$

then the Riemann problem is the initial value problem obtained when this is expressed as:

$$\underline{u}(x,0) \equiv \underline{u}_l \quad (x < 0) \; ; \; \underline{u}(x,0) \equiv \underline{u}_r \quad (x > 0) \qquad (5.6.11)$$

To incorporate the Riemann problem into a numerical scheme one usually takes $(\underline{u}_i^n, \underline{u}_{i+1}^n)$ for each successive i as pairs of states which define a sequence of Riemann problems, each of which provides the solution within each interval (i,i+1), Roe (1981a).

To solve a system like (5.6.9), a piecewise constant matrix $\tilde{\underline{A}}$ which is dependent on the local conditions, is constructed. This matrix is a constant approximation of $\underline{A}$, such that:

$$\tilde{\underline{A}} = \tilde{\underline{A}}(u_l, u_r) \tag{5.6.12}$$

which is constructed over a single cell in the following fashion:

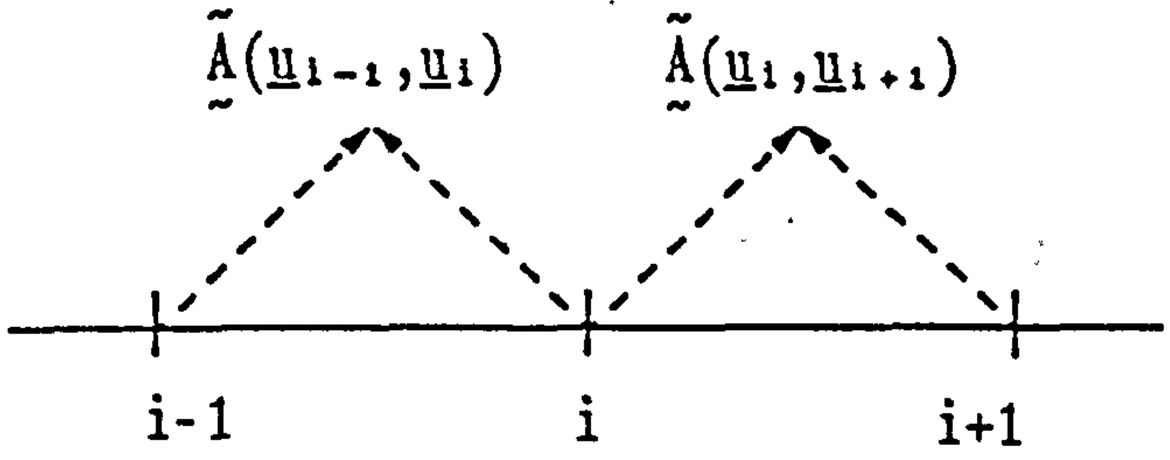

However, the choice of $\tilde{\underline{A}}$ is not trivial. In order to obtain a scheme which possesses both the transportive and the conservative properties, Roe (1981a) finds that the matrix $\tilde{\underline{A}}$ must satisfy the following properties (hereafter called Roe's properties):

1. It constitutes a linear mapping from vector space $\underline{u}$ to vector space $\underline{F}$.
2. As $\underline{u}_l \longrightarrow \underline{u}_r$, $\tilde{\underline{A}}(\underline{u}_l, \underline{u}_r) \longrightarrow \underline{A}(\underline{u})$ where $\underline{A} = \frac{\partial \underline{F}}{\partial \underline{u}}$.
3. For any $\underline{u}_l$, $\underline{u}_r$ $\tilde{\underline{A}}(\underline{u}_l, \underline{u}_r)$ X $(\underline{u}_l - \underline{u}_r) = \underline{F}_l - \underline{F}_r$
4. The eigenvectors of $\tilde{\underline{A}}$ are linearly independent.

Of all these conditions, condition 3 is the most important when considering shocks or discontinuities, and is also the most difficult to satisfy. Perhaps the two following forms for the matrix $\tilde{\underline{A}}$ seem the most obvious:

$$\tilde{\underline{A}}(\underline{u}_l, \underline{u}_r) = \tfrac{1}{2}(\underline{A}(\underline{u}_l) + \underline{A}(\underline{u}_r))$$

or:

$$\tilde{\underline{A}}(\underline{u}_l, \underline{u}_r) = \underline{A}(\tfrac{1}{2}(\underline{u}_l + \underline{u}_r))$$

However, neither of these satisfies condition 3. Roe (1981a) suggests a method for constructing $\tilde{\underline{A}}$. Roe (1981b) shows that condition 3 is a sufficient condition for the scheme to be conservative, and that both conditions 3 and 4 are necessary and sufficient conditions for the numerical scheme to detect a shock, i.e. that $\underline{u}_l$ and $\underline{u}_r$ satisfy the jump condition:

$$(\underline{F}_l - \underline{F}_r) = S(\underline{u}_l - \underline{u}_r) \tag{5.6.14}$$

where S is a scalar, and by condition 3, an eigenvalue of $\tilde{\underline{A}}$. If we approximate (5.6.2) as:

$$\frac{\partial \underline{u}}{\partial t} = - \frac{1}{\Delta x} \Delta \underline{F} \tag{5.6.15}$$

then we need to construct the matrix $\tilde{\underline{A}}$ to map $\Delta \underline{u}$ to $\Delta \underline{F}$, and we need $\tilde{\underline{A}} = \tilde{\underline{A}}(\underline{u}_l, \underline{u}_r)$, so that (5.6.15) may be written:

$$\frac{\partial \underline{u}}{\partial t} = - \frac{1}{\Delta x} \tilde{\underline{A}} \Delta \underline{u} \tag{5.6.16}$$

and $\tilde{\underline{A}}$ satisfies Roe's conditions, Roe (1981a). Roe (1981a) introduces a parameter vector, $\underline{w}$ such that:

$$\underline{F} = \underline{F}(\underline{w}) \tag{5.6.17}$$

$$\underline{u} = \underline{u}(\underline{w}) \tag{5.6.18}$$

and then finds matrices to map $\Delta \underline{u} \longrightarrow \Delta \underline{F}$ and $\Delta \underline{w} \longrightarrow \Delta \underline{u}$, such that:

$$\Delta \underline{u} = \tilde{\underline{B}}(\underline{w}) \Delta \underline{w} \tag{5.6.19}$$

$$\Delta \underline{F} = \tilde{\underline{C}}(\underline{w}) \Delta \underline{w} \tag{5.6.20}$$

which can combine to give:

$$\Delta \underset{\sim}{F} = \tilde{\underset{\sim}{C}}\ \tilde{\underset{\sim}{B}}^{-1}\ \Delta \underset{\sim}{u} \tag{5.6.21}$$

and so, $\tilde{\underset{\sim}{A}}$ may be expressed as:

$$\tilde{\underset{\sim}{A}} = \tilde{\underset{\sim}{C}}\ \tilde{\underset{\sim}{B}}^{-1} \tag{5.6.22}$$

(Note: all values $\tilde{p}$ refer to values for the piecewise constant problem defined over a cell.) To find the eigenvalues of this mapping we solve:

$$(\tilde{\underset{\sim}{C}}\ \tilde{\underset{\sim}{B}}^{-1} - \tilde{\lambda}\ \underset{\sim}{I})\Delta \underset{\sim}{u} = 0 \tag{5.6.23}$$

where $\underset{\sim}{I}$ is the identity matrix, and $\tilde{\lambda}$ is the eigenvalue for the piecewise constant problem. Using (5.6.18) this then becomes:

$$(\tilde{\underset{\sim}{C}} - \tilde{\lambda}\ \tilde{\underset{\sim}{B}})\Delta \underset{\sim}{w} = 0 \tag{5.6.24}$$

Then we may find the right eigenvectors, $\underset{\sim}{r}$, and the left eigenvectors, $\underset{\sim}{l}$, such that:

$$\tilde{\underset{\sim}{C}}\ \tilde{\underset{\sim}{B}}^{-1}\ \tilde{\underset{\sim}{r}}_k = \tilde{\lambda}_k\ \tilde{\underset{\sim}{r}}_k \tag{5.6.25}$$

$$\tilde{\underset{\sim}{l}}_k\ \tilde{\underset{\sim}{C}}\ \tilde{\underset{\sim}{B}}^{-1} = \tilde{\lambda}_k\ \tilde{\underset{\sim}{l}}_k \tag{5.6.26}$$

We may then form a basis by projecting $\Delta \underset{\sim}{u}$ onto either the right or left eigenvectors, and then:

$$\Delta \underset{\sim}{u} = \sum_{k=1}^{n} a_k \tilde{\underset{\sim}{r}}_k \tag{5.6.27}$$

and so:
$$\Delta\underline{F} = \tilde{\underline{A}}\,\Delta\underline{u} = \sum_{k=1}^{n} \tilde{\lambda}_k a_k \tilde{\underline{r}}_k \qquad (5.6.28)$$

where $\tilde{\lambda}_k$ is the wave speed in the k^{th}. co-ordinate field direction. Hence, we may find the coefficients a_k. Donnelly & Li (1984) in their analysis, show that the scheme is both TVD and stable.

Whilst this basis is sufficient to solve systems like (5.6.2) Roe (1986b), when considering problems like (5.6.1), finds it necessary to use both sets of eigenvectors, and does not define a set of basis vectors as in (5.6.27).

We are interested in a system of partial differential equations of the form of (5.6.1). Using a Roe-type scheme similar to that in Roe (1986b) should provide a scheme with both the transportive and the conservative properties, is characteristic following (in the above sense) and shock capturing. From Roe (1986b) we find that the following scalar quantity measures the fluctuation in the solution due to the k^{th}. wave:

$$\phi_k = \tilde{\lambda}_k \tilde{\underline{l}}_k.(\underline{u}_{i+1} - \underline{u}_i) - \tfrac{1}{2}\Delta x \tilde{\underline{l}}_k.(\underline{Q}_i + \underline{Q}_{i+1}) \qquad (5.6.29)$$

Then the up-wind differencing scheme is:

$$\underline{u}_k^{n+1} = \underline{u}_k^n - \frac{\Delta t}{\Delta x}\tilde{\lambda}_k[\tilde{\underline{l}}_k.(\underline{u}_{k+1} - \underline{u}_k)]\tilde{\underline{r}}_k + \tfrac{1}{2}\Delta t[\tilde{\underline{l}}_k.(\underline{Q}_i + \underline{Q}_{i+1})]\tilde{\underline{r}}_k \qquad \tilde{\lambda}_k < 0 \qquad (5.6.30)$$

$$\underline{u}_{k+1}^{n+1} = \underline{u}_{k+1}^n - \frac{\Delta t}{\Delta x}\tilde{\lambda}_k[\tilde{\underline{l}}_k.(\underline{u}_{k+1} - \underline{u}_k)]\tilde{\underline{r}}_k + \tfrac{1}{2}\Delta t[\tilde{\underline{l}}_k.(\underline{Q}_i + \underline{Q}_{i+1})]\tilde{\underline{r}}_k \qquad \tilde{\lambda}_k > 0 \qquad (5.6.31)$$

Notice, that when the switching occurs ($\tilde{\lambda}_k = 0$) the first term on the right-hand-side of (5.6.29) disappears, but the second may not. So the effects of the source term switch discontinuously (Roe (1986b)). Whilst this is realistic for some flows, it may not be always, and this remains to be investigated.

Although this Roe-type scheme has (to date) no formal stability analysis, it is desirable because it is characteristic following and shock capturing, and we know that it comes from a family of schemes which are proven to be stable and TVD.

This scheme is used to study the two-phase system (5.5.6), (5.5.7), (5.5.10), (5.5.11) and (5.5.12), but because the stability of the scheme may be questionable, we must always critically consider whether the calculated solutions are plausible or not.

5.7 Numerical solution of the equations of disperse two-phase flow

The equations of disperse two-phase flow in dimensionless form (5.5.6) to (5.5.10), may be written:

$$\frac{\partial}{\partial\tau}(\alpha v) + \frac{\partial}{\partial\xi}(\alpha v^2) = \alpha k C_D^* D(u-v)^2 \frac{\rho}{\sigma} \qquad (5.7.1)$$

$$\frac{\partial}{\partial\tau}(\rho u) + \frac{\partial}{\partial\xi}(\rho u^2 + \frac{p+1}{\gamma}) = -\alpha k C_D^* (u-v)^2 \qquad (5.7.2)$$

$$\frac{\partial}{\partial\tau}(\rho) + \frac{\partial}{\partial\xi}(\rho u) = 0 \qquad (5.7.3)$$

$$\frac{\partial}{\partial\tau}(\alpha) + \frac{\partial}{\partial\xi}(\alpha v) = 0 \qquad \forall t>0 \qquad (5.7.4)$$

$$\frac{\partial e}{\partial\tau} + \frac{\partial}{\partial\xi}[(p+e+1)u] = 0 \qquad (5.7.5)$$

where $k=\frac{3}{8}$. This may be expressed in the form of (5.6.1):

$$\underline{u}^* = \begin{bmatrix} \rho u \\ \alpha v \\ \rho \\ \alpha \\ e \end{bmatrix} \qquad (5.7.6)$$

$$\underline{F}^* = \begin{bmatrix} \rho u^2 + \frac{p+1}{\gamma} \\ \alpha v^2 \\ \rho u \\ \alpha v \\ (p+e+1)u \end{bmatrix} \qquad (5.7.7)$$

In section 5.3 when we formed the characteristic equation of the partial differential system we found that there was a repeated eigenvalue corresponding to $\lambda = v$ for the dimensionless system. Thus, we would expect to find that the piecewise constant system would also have a doubly degenerate eigenvalue, and indeed, this can be verified.

The doubly degenerate eigenvalue causes problems for the Roe-type scheme of the previous section. Roe's condition 4 says that the eigenvectors of $\tilde{\underline{A}}$ (the piecewise constant matrix) must be linearly independent, and the doubly degenerate eigenvalue prevents this.

However, this problem is easily overcome. The problem arises for the (simplified) disperse two-phase flow equations because, in obtaining them, we have over specified the system. The problem may be reconciled as follows. From a physical point of view, we can have no liquid velocity where there are no liquid droplets, while we can have droplets where we have no liquid velocity. However, it is more desirable to retain the liquid velocity, v, in our system and consider the liquid existence, α, separately. We can do this if we ensure that the liquid velocity never becomes zero, or if we are careful, we can "program the physics" of the problem into the scheme to ensure that the first physical statement is always obeyed. In practice, the latter option is employed, and the system may be expressed in the form:

$$\underline{u} = \begin{bmatrix} \rho u \\ v \\ \rho \\ e \end{bmatrix} \tag{5.7.8}$$

$$\underline{F} = \begin{bmatrix} \rho u^2 + \dfrac{p+1}{\gamma} \\ \frac{1}{2}v^2 \\ \rho u \\ (p+e+1)u \end{bmatrix} \tag{5.7.9}$$

$$\underline{Q} = \begin{bmatrix} -kC_D^* D\alpha\rho(u-v)^2 \\ kC_D^* D\dfrac{\rho}{\sigma}(u-v)^2 \\ 0 \\ 0 \end{bmatrix} . \tag{5.7.10}$$

and:

$$\frac{\partial \alpha}{\partial \tau} + \frac{\partial}{\partial \xi}(\alpha v) = 0 \qquad \forall t > 0$$

is up-winded using the eigenvalue and vectors obtained for v. By analogy with Roe (1986b) we define a parameter vector $\underline{w}$, where:

$$\underline{w} = \begin{bmatrix} \sqrt{\rho}u \\ v \\ \sqrt{\rho} \\ \frac{p+e+1}{\sqrt{\rho}} \end{bmatrix} \qquad (5.7.11)$$

Denoting the components of $\underline{w}$ as w_1, w_2, w_3 and w_4 respectively, we can write:

$$\underline{u} = \begin{bmatrix} w_1 w_3 \\ w_2 \\ w_3^2 \\ \frac{w_3 w_4}{\gamma} + \frac{\gamma-1}{2\gamma} w_1^2 \end{bmatrix} \qquad (5.7.12)$$

and:

$$\underline{F} = \begin{bmatrix} \frac{\gamma-1}{\gamma} w_3 w_4 + \frac{\gamma+1}{2\gamma} w_1^2 \\ \frac{1}{2} w_2^2 \\ w_1 w_3 \\ w_1 w_4 \end{bmatrix} \qquad (5.7.13)$$

We seek piecewise constant matrices $\tilde{\underline{B}}$ and $\tilde{\underline{C}}$ which satisfy:

$$\Delta \underline{u} = \tilde{\underline{B}} \, \Delta \underline{w}$$

$$\Delta \underline{F} = \tilde{\underline{C}} \, \Delta \underline{w}$$

where $\Delta(.) = (.)_i - (.)_{i+1}$ (i.e. $(.)_l - (.)_r$) and $\bar{(.)} = \frac{1}{2}((.)_i + (.)_{i+1})$, then:

$$\tilde{\underline{B}} = \begin{bmatrix} \bar{w}_3 & 0 & \bar{w}_1 & 0 \\ 0 & 1 & 0 & 0 \\ 0 & 0 & 2\bar{w}_3 & 0 \\ \frac{\gamma-1}{\gamma}\bar{w}_1 & 0 & \frac{\bar{w}_4}{\gamma} & \frac{\bar{w}_3}{\gamma} \end{bmatrix} \qquad (5.7.14)$$

$$\tilde{\underline{C}} = \begin{bmatrix} \frac{\gamma+1}{\gamma}\bar{w}_1 & 0 & \frac{\gamma-1}{\gamma}\bar{w}_4 & \frac{\gamma-1}{\gamma}\bar{w}_3 \\ 0 & \bar{w}_2 & 0 & 0 \\ \bar{w}_3 & 0 & \bar{w}_1 & 0 \\ \bar{w}_4 & 0 & 0 & \bar{w}_1 \end{bmatrix} \qquad (5.7.15)$$

We seek eigenvalues, $\tilde{\lambda}$ which satisfy:

$$|\tilde{\underline{C}} - \tilde{\lambda}\,\tilde{\underline{B}}| = 0$$

which may be written:

$$\begin{vmatrix} \frac{\gamma+1}{\gamma}\bar{w}_1 - \tilde{\lambda}\bar{w}_3 & 0 & \frac{\gamma+1}{\gamma^2}\bar{w}_4 - \tilde{\lambda}\bar{w}_1 & \frac{\gamma-1}{\gamma^2}\bar{w}_3 \\ 0 & \bar{w}_2 - \tilde{\lambda} & 0 & 0 \\ \bar{w}_3 & 0 & \bar{w}_1 - 2\tilde{\lambda}\bar{w}_3 & 0 \\ \bar{w}_4 - \tilde{\lambda}(\gamma-1)\bar{w}_1 & 0 & -\frac{\tilde{\lambda}\bar{w}_4}{\gamma} & \bar{w}_1 - \frac{\tilde{\lambda}\bar{w}_3}{\gamma} \end{vmatrix} = 0$$

Hence, the following characteristic equation:

$$(\tilde{\lambda}-\tilde{v})(\tilde{\lambda}-(\tilde{u}-\tilde{c}))(\tilde{\lambda}-(\tilde{u}+\tilde{c}))(\tilde{\lambda}-\tilde{u}) = 0 \qquad (5.7.16)$$

where:

$$\tilde{u} = \frac{\sqrt{\rho}_{i+1}u_{i+1} + \sqrt{\rho}_i u_i}{\sqrt{\rho}_{i+1} + \sqrt{\rho}_i}$$

$$\tilde{v} = \frac{v_{i+1} + v_i}{2}$$

$$\tilde{c}^2 = \tfrac{1}{2}\left[\frac{p_{i+1} + 1}{\rho_{i+1}} + \frac{p_i + 1}{\rho_i}\right]$$

We obtain the following right eigenvectors:

$$\left\{\frac{2(\tilde{u} \pm 2\tilde{c})}{\gamma[\tilde{u}^2 \pm 4\tilde{u}\tilde{c} + \frac{2(2\gamma-1)}{\gamma-1}\tilde{c}^2]} \ , \ 0 \ , \frac{2}{\gamma[\tilde{u}^2 \pm 4\tilde{u}\tilde{c} + \frac{2(2\gamma-1)}{\gamma-1}\tilde{c}^2]} \ , \ 1\right\}^T \qquad \tilde{\lambda}=\tilde{u}\pm\tilde{c}$$

$$\left\{\frac{2\tilde{u}}{\gamma[\tilde{u}^2 - \frac{2\tilde{c}^2}{\gamma-1}]} \ , \ 0 \ , \ \frac{2}{\gamma[\tilde{u}^2 - \frac{2\tilde{c}^2}{\gamma-1}]} \ , \ 1\right\}^T \qquad \tilde{\lambda}=\tilde{u}$$

$$\{0 \ , \ 1 \ , \ 0 \ , \ 0\}^T \qquad \tilde{\lambda}=\tilde{v}$$

and the following left eigenvectors:

$$\left\{-\gamma[\tilde{u} \mp \frac{\tilde{c}}{\gamma-1}] \ , \ 0 \ , \ \frac{\gamma}{2}[\tilde{u}^2 \mp \frac{2\tilde{u}\tilde{c}}{\gamma-1}] \ , \ 1\right\} \qquad \tilde{\lambda}=\tilde{u}\pm\tilde{c}$$

$$\left\{-\gamma\tilde{u} \ , \ 0 \ , \ \frac{\gamma}{2}[\tilde{u}^2 - \frac{2\tilde{c}^2}{\gamma-1}] \ , \ 1\right\} \qquad \tilde{\lambda}=\tilde{u}$$

$$\{0 \ , \ 1 \ , \ 0 \ , \ 0\} \qquad \tilde{\lambda}=\tilde{v}$$

We may now use the criterion of (5.6.30) and (5.6.31) to up-wind the scheme and find the state at a later time, given suitable initial conditions. Criterion (5.6.30) and (5.6.31) allows the contributions from each eigenvalue to be calculated. To determine the total contribution for all eigenvalues, the individual contributions from each eigenvalue at all the grid points must be summed. In this way we can determine the time evolution of the vector $\underline{u}$.

5.8 Difficulties implementing the numerical scheme.

The implementation of the numerical scheme was not trivial, although the code writing (in FORTRAN 77) proved trouble free.

The major problem, and one that was not obvious at first, was that the dispersed two-phase flow problem has two distinct time scales. This can be seen from the eigenvalues of the piecewise constant matrix, for instance. One is a sonic time scale from the gas dynamics, while the other is a much slower time scale due to the entrained liquid. Since the CFL number for centrally differenced compressible flow is given by:

$$\nu = (V + a)\frac{\Delta t}{\Delta x} \leq 1$$

and the condition for up-wind differencing schemes is more restrictive than this (Roache (1972) p.229), say:

$$\nu = (V + a)\frac{\Delta t}{\Delta x} \lesssim \tfrac{1}{2}$$

then we would expect $\frac{\Delta t}{\Delta x} \lesssim \frac{1}{600}$ for air-water flows for example. For a suitable grid resolution (sufficiently small Δx) we then require a very small Δt , much smaller than is required for the particulate (droplet) flow, and this is naturally computationally expensive. Indeed, the value of "V + a" (the eigenvalue) is not known, *a priori*, for each cell (i,i+1), So, to upwind whichever variable is fastest correctly (i.e. whichever has the largest eigenvalue) and thus the other variables, the time step at each stage of the calculation is obtained from:

$$\nu = \tilde{\lambda}_{max}\frac{\Delta t}{\Delta x}$$

where $\tilde{\lambda}_{max}$ is the largest of the piecewise calculated eigenvalues, and ν is a suitable CFL number to ensure stability and convergence. With $\nu \leq 1$ we ensure that the calculated information never travels across more than one space cell per time step and so we can follow the fastest, and consequently the slowest, information. Thus, the scheme has a constant spatial step size, Δx, but varying time step size. This naturally means that the shortest steps are always used. Thus the scheme is cpu intensive, even when only moderate spatial resolution is required.

There is no point in completely neglecting the motion of the (slower) particulate phase. There are two main reasons for this.

The first is that to neglect the particulate motion necessarily changes the character of the system we are studying - it is no longer the same physical problem.

The second is that there is no reason to do so from a computational view point as the large cpu times are a manifestation of the gaseous effects with their very fast time scales, and up-winding the particulate phase is easy and computationally cheap.

5.9 Results of the numerical modelling.

In this chapter, unlike all of the previous chapters, the graphical information depicts flows moving from left to right so that comparisons with other authors' work can be most easily drawn. Also note, that in this chapter the dimensionless variables differ from those of Chapter 4. This is because in Chapter 4 we concentrated on the wave dynamics, and this chapter concentrates on the gas dynamics.

The numerical results presented here concern the flow of a gas through a region of (initially) stationary droplets, and the subsequent motion of the droplets themselves.

We consider a two-dimensional pipe of constant cross-section and rigid walls of infinite extent. The entry pressure to the tube is specified, and the pressure is initially considered to be uniform throughout the tube. In addition, the entry gas Mach number (the dimensionless relative gas velocity) is also specified. In this work the region of entrained droplets may have one of two possible distributions. Either a Gaussian distribution of the form

$$\alpha = \alpha_{max} e^{-0.4\xi^2} \tag{5.9.1}$$

centred on $\xi = 0$, or a broad step distribution of the form

$$\alpha = \begin{cases} 0 & -\infty < \xi < 0 \\ \alpha_{max} & 0 \leq \xi \leq 20 \\ 0 & 20 < \xi < +\infty \end{cases} \tag{5.9.2}$$

where ξ is the dimensionless position co-ordinate and α_{max} is the maximum droplet fraction of the liquid, is used. The form of both distributions was of an arbitrary choice, but both were chosen to

investigate different phenomena. They are not chosen because they are "like" any physically occurring distribution of entrained droplets. Indeed, the author has found no literature in which the initial spatial distribution of droplets and their effect on gas dynamics phenomena is discussed.

The Gaussian form is centred on $\xi = 0$ and the factor of 0.4 is chosen so that, for most sizes of spatial discretised cell length, there are a reasonable number of nodes through the distribution. A Gaussian form is considered because it is a smooth function, and so any discontinuities that arise in the calculations are not the result of the propagation of an initial discontinuity.

The step function, on the other hand, is chosen to see the effect that a large region of disperse droplets has on the gas dynamics of the flow, and in particular, to study the gas dynamics within that region.

In principle, the system could be considered to be entirely consisting of entrained droplets with no regions of purely gas flow, and the void fraction, α, to have some specified initial distribution throughout. The evolution of the system could then be studied. It was desired to investigate how "narrow" (Gaussian) and "broad" (step) regions of initially stationary droplets would affect the gas dynamics within a pipe, and how these droplets would subsequently move. To this end we consider a dimensionless flow corresponding to the following physical situation.

We consider an air-water flow in which the air is an ideal gas. Firstly we consider an entry gas pressure of 1.1 atm. and initial uniform gas velocity with Mach number 0.1 . For these parameters we

consider a narrow (Gaussian) band of droplets of various maximum void fraction (0.01, 0.05 and 0.1) - chosen so that our assumption that $1 - \alpha \simeq 1$ still holds, although the void fraction of 0.1 is testing this somewhat. We further consider two different droplet radii, 0.1 mm and 0.01 mm, although it was intended to consider a third, 1 μm so that comparisons with the work of Comfort III & Crowe (1980) could be made. The third radius, however, could not be used with this numerical scheme (see discussion later).

These conditions are repeated for an entry gas pressure of 5.0 atm. and initial gas Mach numbers of 0.1 and 0.25 with the narrow band of droplets, and with an initial gas Mach number of 0.1 for the broad band of droplets.

And finally, the conditions are repeated for an entry gas pressure of 20.0 atm and initial gas Mach number of 0.1 for the narrow band of droplets.

The dimensional computational domain is initially of length -6 to +6 m and of height 25 mm. There were either 400 grid points per 6 m, or 800 per 6 m (hereafter referred to as 400 point or 800 point grids). On both the positive and negative sides of the grid there were "is the grid long enough?" check points (for instance at ±4.5 m). After each iteration the scheme would check that at these points the conditions were unchanged from the previous iteration. If any one of the flow parameters had changed at one of these points the scheme would then add 3 m to that side of the grid (and another 200 or 400 points to the calculation) and move the check point to 1.5 m from the end of the grid. This extension of the grid was performed (as opposed to specifying non-reflecting boundary conditions) so that any interesting changes in

the motions of the fluids could always be tracked. In this way it was hoped that cpu time could be kept to a necessary minimum, and yet the flow could always be calculated. Clearly, however, if the flow after a long time is desired, there may be very many points in the calculation.

One problem arises immediately. When writing the program it is necessary to specify the array dimensions, and clearly there is a limit to the size of the arrays that a computer will allow a program to have. So, rather than specify a large number of large arrays, a time limit is given to the calculation so that the total number of grid points is maintained at less than some sensible value. This is achieved by trial and error, although a value of 10 ms was generally used. Times up to 100 ms were possible with a coarsening of the spatial grid, although this sometimes caused problems.

The higher density of grid nodes (800 points) was used to check that the lower density calculations were accurate, or where the 400 point grid showed signs of numerical inaccuracy (eg. oscillations). Some calculations with less than 400 points per 6 m were performed, but these were sometimes found to vary somewhat from the 400 point calculations, which are generally in good agreement with 800 point calculations. As a result, the 400 point grids were generally used.

Prior to presenting some computational results, it should be noted that the CFL number for these calculations was 0.48 for the entire range of initial conditions. This CFL number was found by trial and error, and if it were increased, to 0.5 say, the computation became unstable. Further, recall that the time stepping within the scheme is determined by the size of the maximum eigenvalue of the Riemann problem, and as a result, the dimensional (and dimensionless) times for the data presented

in the following graphs are not all of uniform step size.

Figs. 5.1 to 5.5 show the computed variation of the dimensionless gas pressure with spatial co-ordinate for a gas with initial undisturbed pressure p_o=1.1 atm. and for initial gas relative Mach number of 0.1. The initial distribution of the liquid droplets is of the Gaussian form.

Fig. 5.1 shows the computations for the spatial variation of the dimensionless pressure ($p = \frac{p_G - p_o}{p_o}$) at dimensionless times τ = 0.54, 1.09, 1.64, 2.18, 3.82, 6.54, 9.81 and 13.08 (corresponding to dimensional times of t = 0.04, 0.08, 0.12, 0.16, 0.28, 0.48, 0.71 and 0.95 ms) approximately. The maximum initial void fraction is α=0.01 and the droplets have radius 0.1 mm. In Fig. 5.1 we see a maximum dimensionless pressure drop of $1x10^{-2}$ (corresponding to approximately 11 cm of water hydrostatic pressure in 0.5 ms). While the pressure within the entrained region barely changes, outside there is a broad region in which the pressure has fallen. After a dimensionless time of τ=13.08 the pressure pulse has propagated circa 15 dimensionless units downstream. The front of the pressure pulse is smoothly varying (there is no sign of a shock wave), while the magnitude of the pressure drop is large (and fairly constant) over a reasonably large dimensionless distance. Likewise, the back pressure remains constant over a similarly large region in the upstream direction.

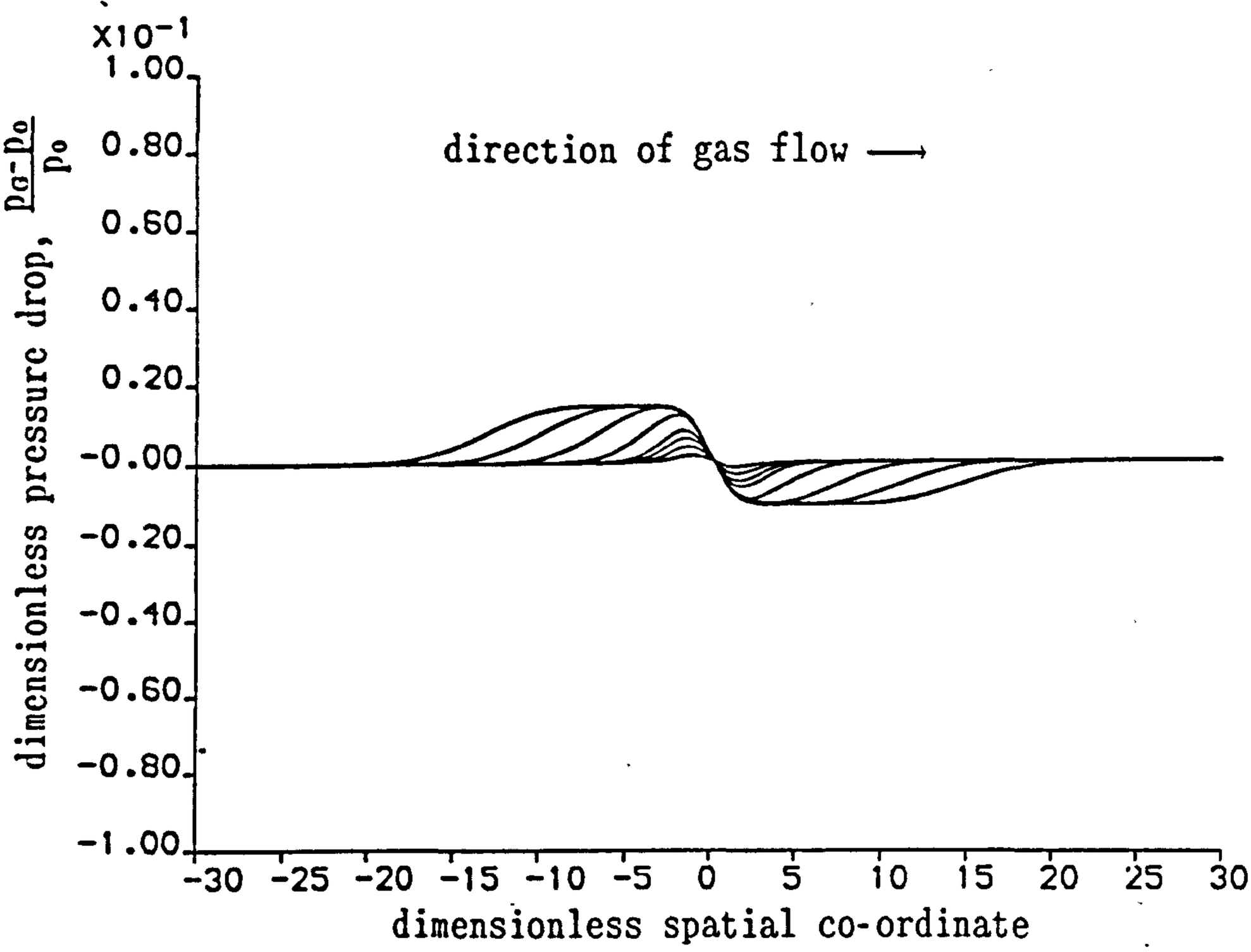

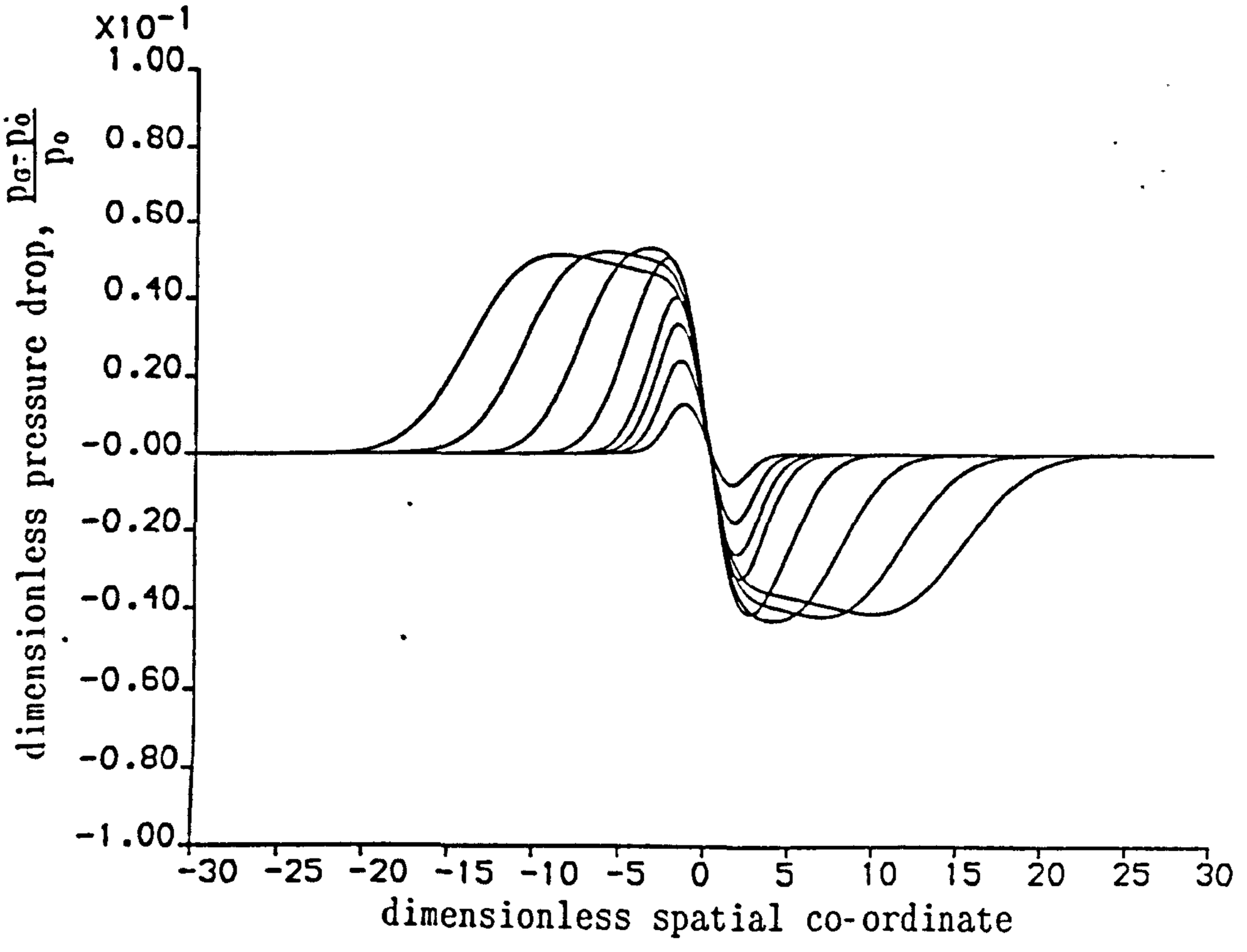

Figs. 5.1 (top) and 5.2

Fig. 5.1 has gas entry pressure of 1.1 atm. at Mach number 0.10, void fraction, α=0.01, droplet radius, r=0.1 mm
Fig. 5.2 has gas entry pressure of 1.1 atm. at Mach number 0.10 void fraction, α=0.01, droplet radius, r=0.01 mm
All of these curves are at dimensionless times of $\tau\simeq$0.55, 1.09, 1.64, 2.18, 3.83, 6.54, 9.81 and 13.08 (dimensional times of t$\simeq$40.4, 80.1, 120.5, 160.2, 281.5, 480.6, 721.0 and 961.3 μs) with a narrow distribution of droplets initially at ξ=0.

Fig. 5.2 shows the same gas flow as in Fig. 5.1 but with the liquid droplets of radius 10 μm (0.01 mm). The magnitude of the back pressure and the pressure drop is greater than in previous cases (approximately $-4\text{x}10^{-2}$ and $5\text{x}10^{-2}$ respectively - a pressure drop of almost 50 cm of water hydrostatic pressure in 0.5 ms!). The fluctuations propagate in a similar fashion to those of the previous case; the pressure pulses travelling similar distances up- and down-stream after similar times. However, the magnitude of the pressure variations is not as constant over the spatial dimension as previously. The pressure behind the front of the wave surface rises toward zero as opposed to remaining constant.

If we now consider an initial droplet distribution with maximum void fraction α=0.1 and droplet radius 0.1 mm we obtain the results of Fig. 5.3. We see that the magnitude of the pressure fluctuation is very similar to (but slightly larger than) that shown in Fig. 5.2 , but that the pressure drop remains relatively constant with distance behind the front of the pressure pulse, in a similar fashion to that of Fig. 5.1. So it appears that increasing the void fraction increases the magnitude of the pressure fluctuation, as expected.

If we now consider a similar flow to that shown in Fig. 5.3 but with droplets of radius 10 μm we obtain Fig. 5.4. Fig. 5.4 shows a dramatic increase in the magnitude of the pressure fluctuations. The maximum pressure drop is now $\sim -9\text{x}10^{-2}$ while the back pressure is $\sim 1\text{x}10^{-1}$; considerably larger than that shown in Fig. 5.2 (at the lower void fraction) and that shown in Fig. 5.3 (with the smaller droplet radius). It appears, then, that decreasing the droplet radius increases the magnitude of the pressure pulse variation, and this is in line with the results of Comfort III & Crowe (1980).

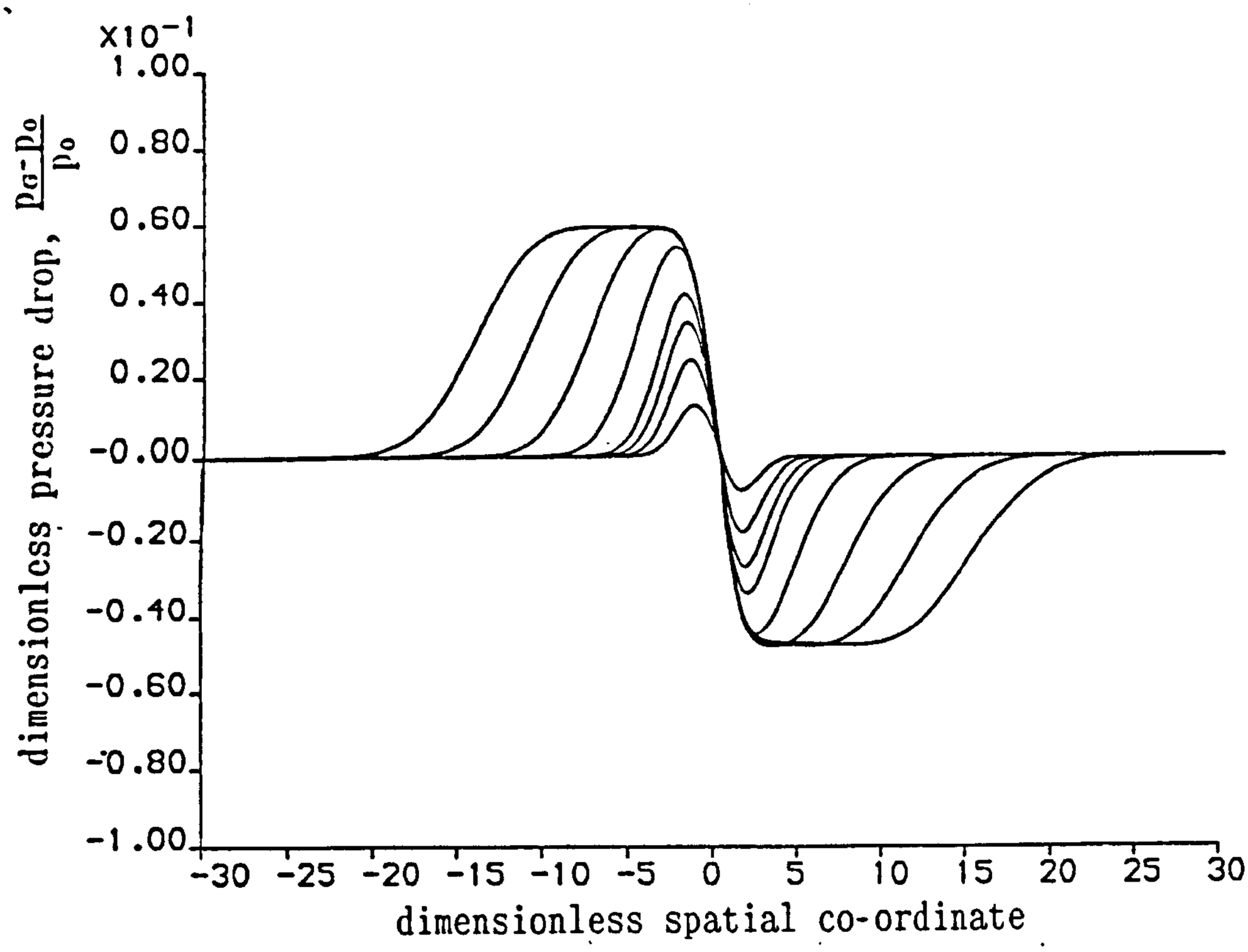

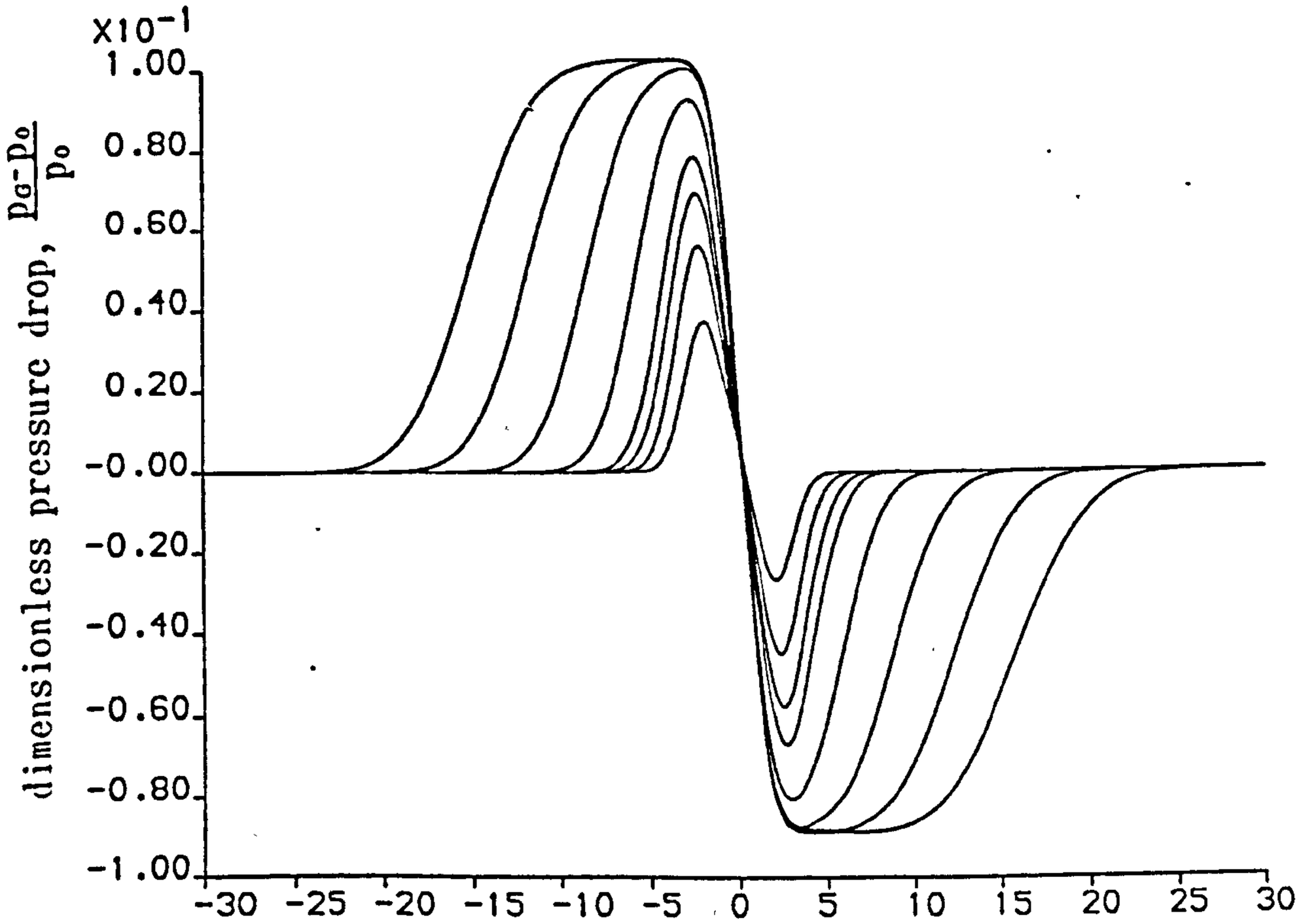

Figs. 5.3 (top) and 5.4

Fig. 5.3 has gas entry pressure of 1.1 atm. at Mach number 0.10, void fraction, α=0.10, droplet radius, r=0.1 mm
Fig. 5.4 has gas entry pressure of 1.1 atm. at Mach number 0.10, void fraction, α=0.10, droplet radius, r=0.01 mm
All of these curves are at dimensionless times of $\tau \simeq 0.54$, 1.09, 1.64, 2.18, 3.82, 6.54, 9.81 and 13.08 (dimensional times of $t \simeq 40.4$, 80.1, 120.5, 160.2, 281.5, 480.6, 721.0 and 961.3 μs) with a narrow distribution of droplets initially at ξ=0.

For the class of Mach numbers and entry pressures that we are interested in we find that the more interesting phenomena occur early in our calculations (as in the above figures). If we are interested in what happens to the flow at larger times, such as up to $\tau \simeq 46$ ($t \simeq 3.3$ ms) we obtain results like that of Fig. 5.5 (where the profiles are plotted at times τ = 13.08, 22.98, 32.70 and 42.52). Fig. 5.5 has the same flow conditions as the flow of Fig. 5.2 (and the same droplet size and void fraction). We see the trend of Fig. 5.2 being continued. The pressure variation behind the front of the pressure pulse increases from its minimum towards zero (as in Fig. 5.2) and no steepening of the front of the pulse is observed. It seems unlikely that a shock wave will form.

Fig. 5.6 illustrates the variation in the droplet distribution for a flow like that shown on Figs. 5.2 and 5.5 but at times τ = 3.27, 35.98, 68.68, 101.38 and 134.11 (corresponding to t = 0.23, 2.61, 5.00, 7.35 and 9.72 ms). Initially we have a narrow entrained region of maximum void fraction 0.01. After a dimensionless time of $\tau \simeq 134$ ($t \simeq 9.72$ ms) the centre has moved to $\xi \simeq 3.75$ ($x \simeq 93.75$ mm - a velocity of 9.65 m s^{-1} from rest). So while the droplet position does change, it does so only for times much longer than changes in the pressure take to occur.

Graphs of the variation of the void fraction show that the system is conservative. Indeed, the code checks that the total mass of the liquid is constant. They also show that the entrained droplets become more disperse - the maximum in the peak of the droplets decreases. And this in turn affects the pressure distribution. If we consider Figs. 5.1 and 5.3 we see that different droplet distributions lead to different pressure variations - the greater the void fraction the greater the pressure drop and the back pressure.

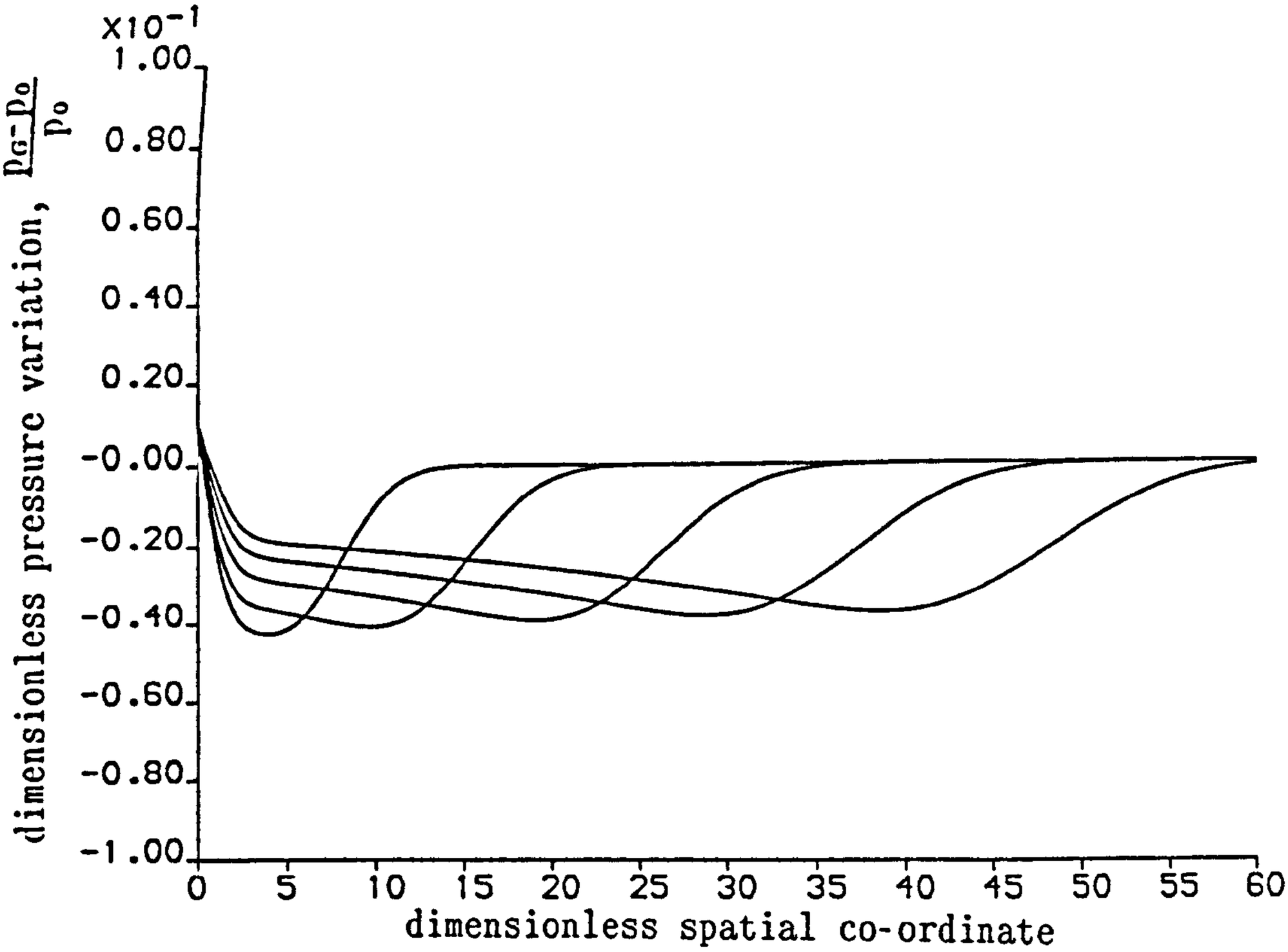

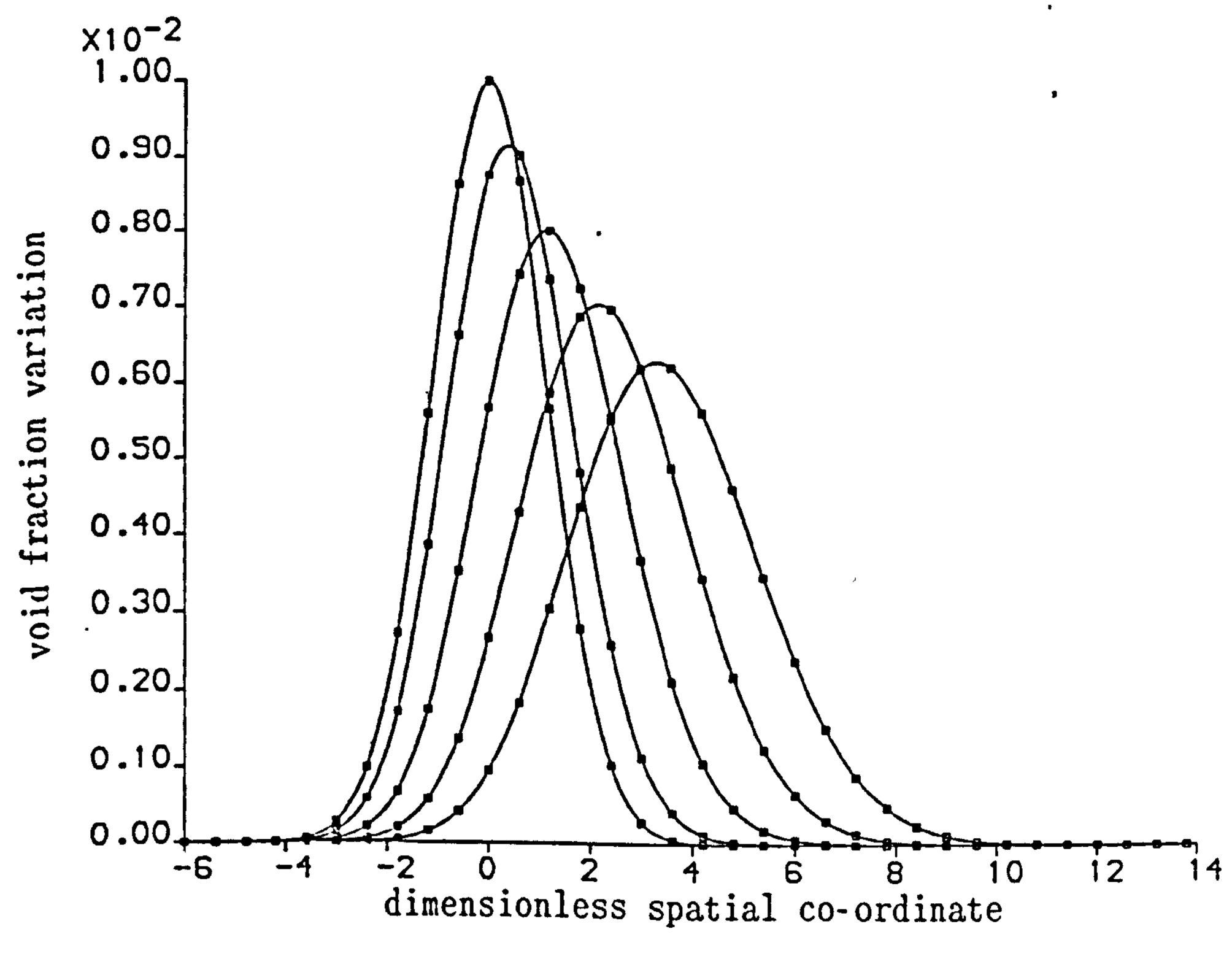

Figs. 5.5 (top) and 5.6

Fig. 5.5 has gas entry pressure of 1.1 atm. at Mach number 0.10, void fraction, α=0.01, droplet radius, r=0.01 mm and is at times $\tau \simeq$13.08, 22.98, 32.70 and 42.52 (dimensional times of t$\simeq$0.95, 1.67, 2.37 and 3.08 ms.)
Fig. 5.6 shows how the pulse distribution of droplets varies for gas flows corresponding to Fig. 5.2 at times $\tau \simeq$3.27, 35.98, 68.68, 101.38 and 134.11 (dimensional times of t$\simeq$0.23, 2.61, 5.00, 7.35 and 9.72 ms.)

If we turn our attention to gas flows with an initial pressure of 5 atm. and initial relative gas Mach number of 0.1 we may obtain similar results to those with an initial pressure of 1.1 atm. as above. Fig. 5.7 illustrates the pressure fluctuations for such a gas pressure and Mach number when the maximum liquid void fraction is 0.1 and the droplet radius is 10 μm. If we compare Figs. 5.4 and 5.7 we see a similar dimensionless pressure drop (but remember, that the dimensional pressure drop, $\Delta p = p_G - p_o$ is larger in the latter case). In addition, the profiles have a similar shape. The profiles of Fig. 5.7 are at dimensionless times of τ = 0.54, 1.09, 1.64, 2.18, 3.82, 6.54, 9.81 and 13.08 (corresponding to dimensional times of t = 0.03, 0.06, 0.10, 0.13, 0.22, 0.38, 0.57 and 0.76 ms) approximately. So, while the dimensionless pressures and times are very similar we see that the dimensional result of changing the gas entry pressure is an increased pressure pulse magnitude in a shorter time. If data for the motion of the entrained region is studied (or a graph like Fig. 5.6 produced) we find that after a dimensionless time $\tau \simeq 128$ ($t \simeq 7.52$ ms) the maximum in the distribution has moved to $\xi \simeq 5.75$ ($x \simeq 143.75$ mm - a velocity of 19.12 m s^{-1}) and that the droplets to the front of the entrained region again travel faster. So the effect of changing the gas pressure is to increase the speed of propagation of the entrained region and increase the pressure drop in the gas in a smaller time than the lower pressure flow.

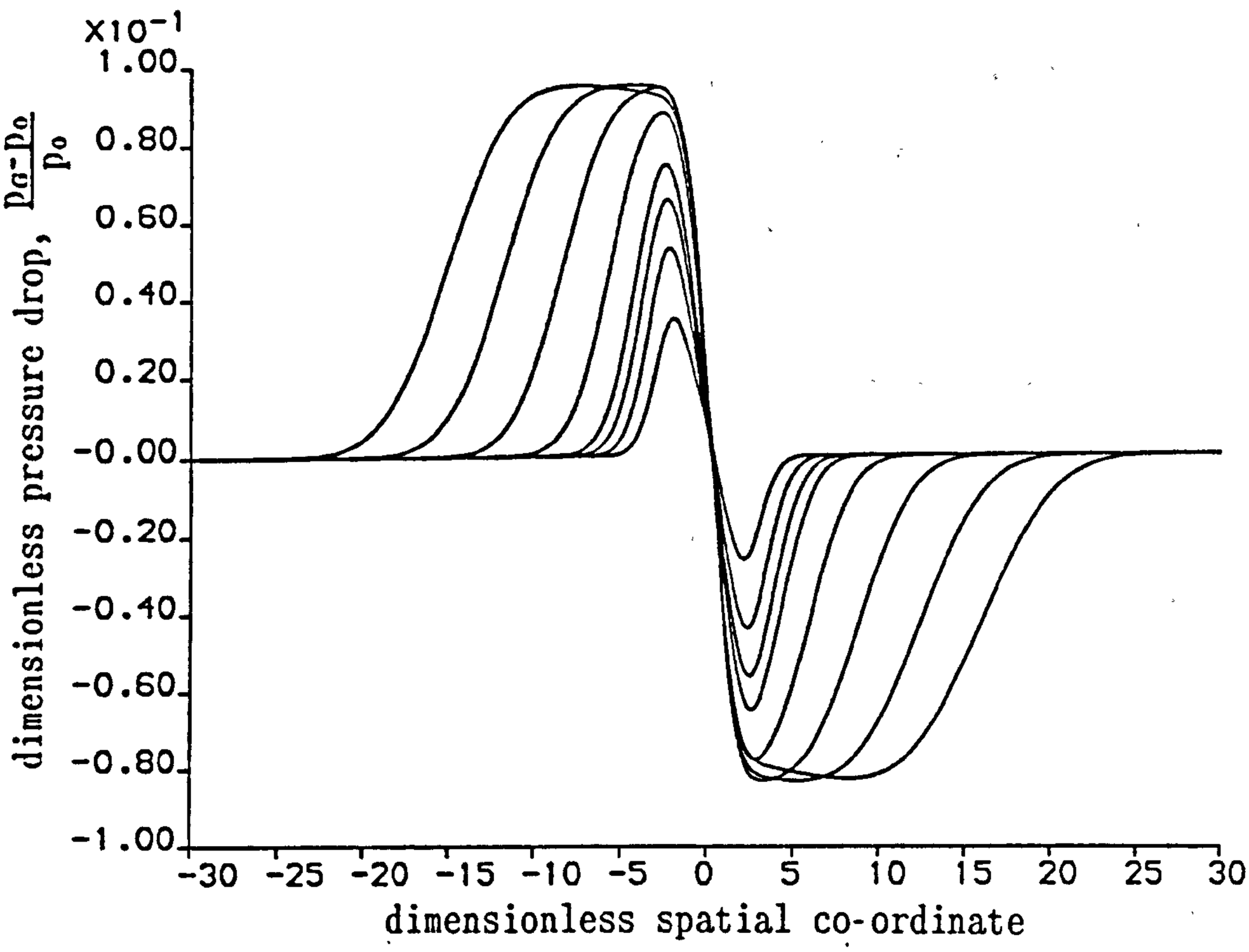

Fig. 5.7

Fig. 5.7 has gas entry pressure of 5.0 atm. at Mach number 0.10, void fraction, α=0.10, droplet radius, r=0.01 mm and these curves are at dimensionless times of $\tau \simeq$0.54, 1.09, 1.64, 2.18, 3.82, 6.54, 9.81 and 13.08 (dimensional times of t$\simeq$32.1, 63.7, 95.8, 127.3, 223.7, 381.9, 572.9 and 763.8 μs) with a narrow distribution of droplets initially at ξ=0.

We now turning our attention to the relative Mach number of the gas. If we consider a gas in which the initial pressure is 5 atm. and the gas Mach number is 0.25 and the void fraction is Gaussian in form with initial maximum 0.01 with droplets of radius 0.1 mm then we obtain Fig. 5.8 for the variation of the dimensionless pressure. The profiles are plotted at dimensionless times of τ = 0.54, 0.96, 1.44, 1.92, 2.40, 4.80, 7.20, 9.60, 12.00, 14.40 and 16.80 (corresponding to dimensional times of t = 0.03, 0.06, 0.08, 0.11, 0.14, 0.28, 0.42, 0.56, 0.70, 0.84 and 0.98 ms) approximately. If we compare Figs. 5.1 and 5.8 we see that the form of the pressure variation is now quite different. Further, the magnitude of the pressure fluctuation in the larger Mach number flow is itself larger. The maximum pressure drop is $\sim -4\times10^{-2}$; about four times greater than that with initial pressure 1.1 atm. and Mach number 0.1 (Fig. 5.1) and four times greater than a flow with initial pressure 5 atm. and Mach number 0.1. Likewise, the maximum back pressure is $\sim 7\times10^{-2}$; about four times greater than flows with initial pressures of 1.1 and 5 atm. at Mach number 0.1. The pressure in the region behind the front of the pressure pulse rapidly increases toward zero in a similar fashion to that shown in Fig. 5.2. Indeed, if we plot the pressure variation corresponding to the above conditions but change the droplet radius to 10 μm then the falling back of the pressure behind the front of the pressure pulse is more noticeable.

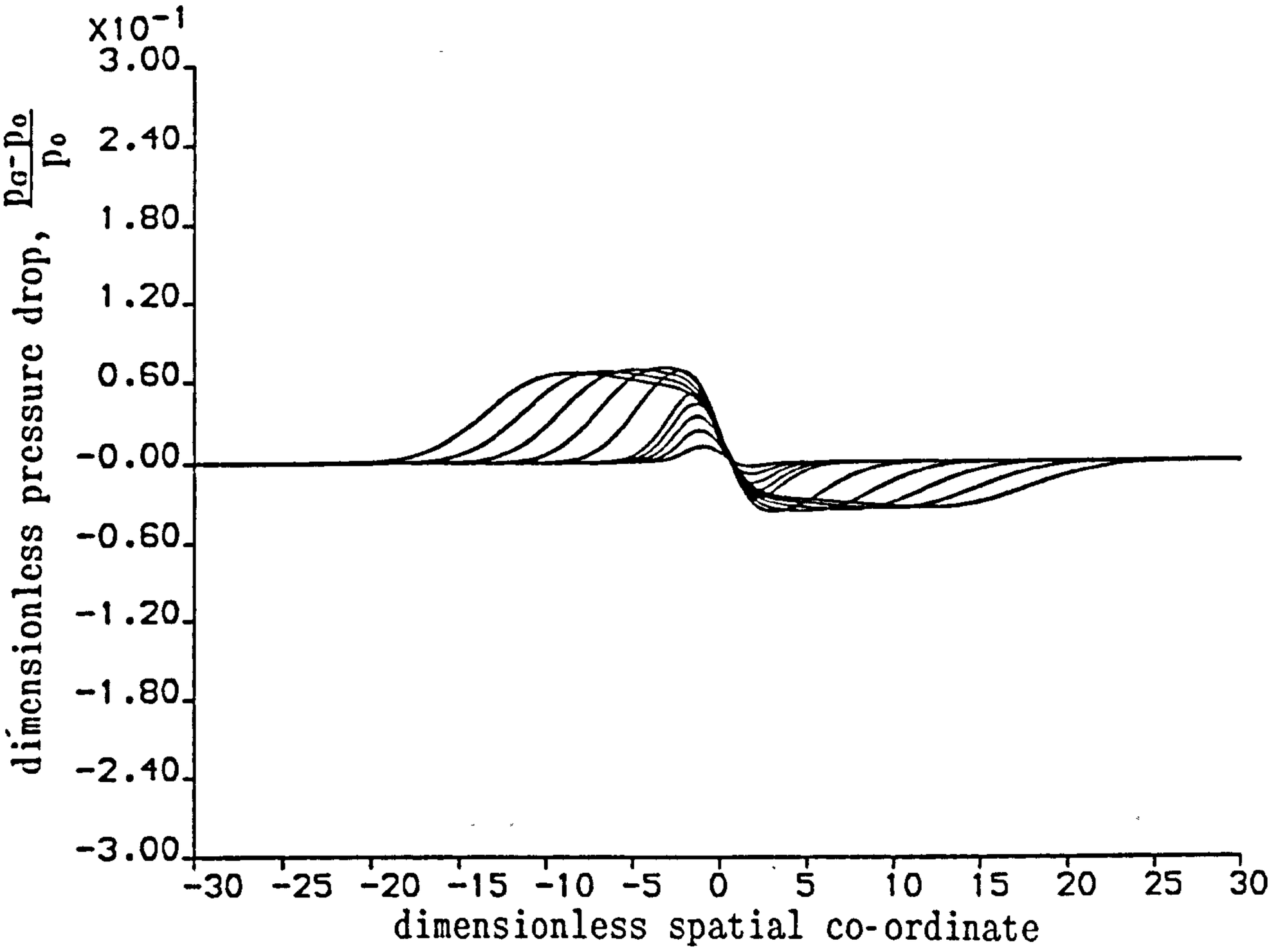

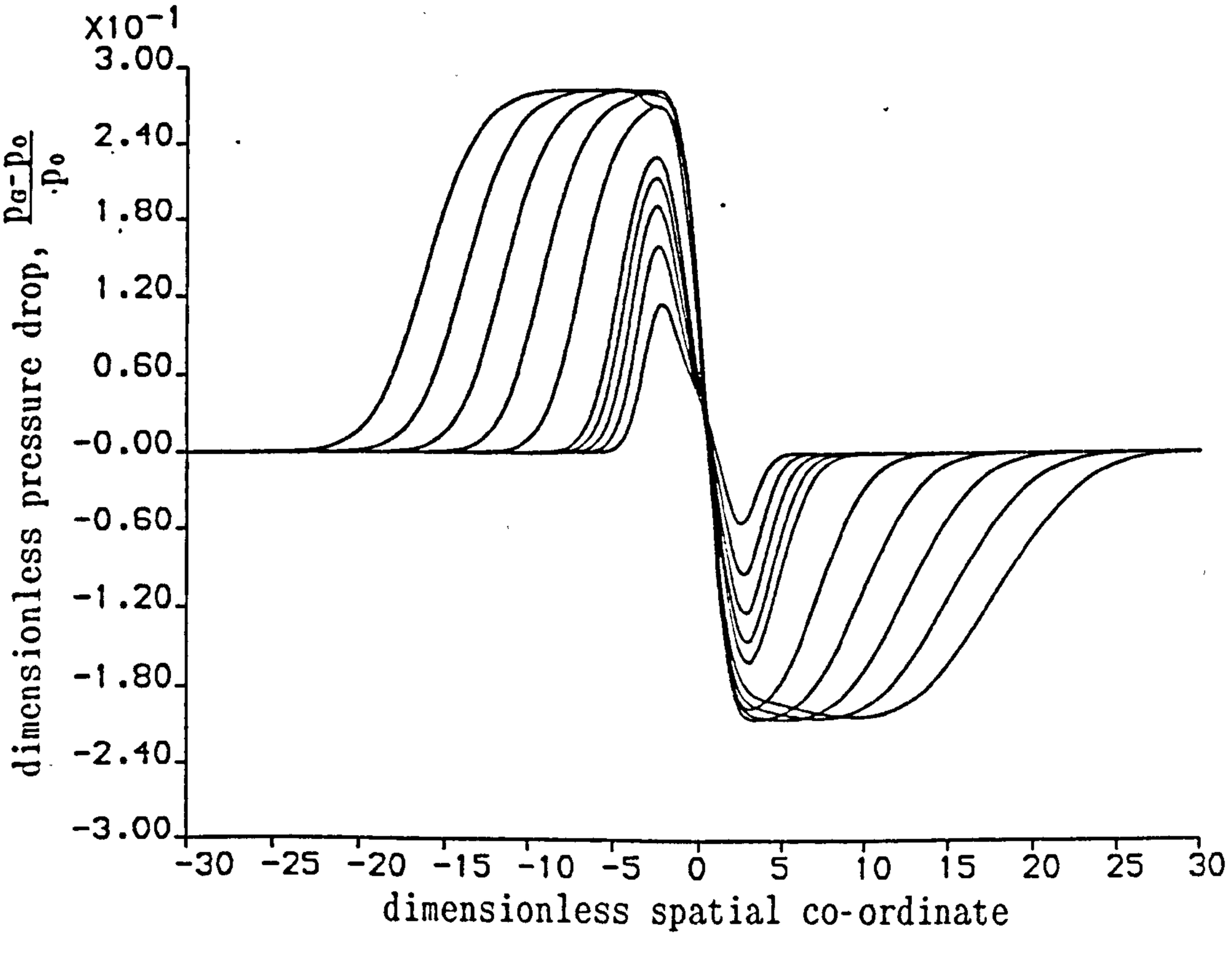

Figs. 5.8 (top) and 5.9

Fig. 5.8 has gas entry pressure of 5.0 atm. at Mach number 0.25, void fraction, α=0.01, droplet radius, r=0.1 mm
Fig. 5.9 has gas entry pressure of 5.0 atm. at Mach number 0.25, void fraction, α=0.10, droplet radius, r=0.01 mm
All of these curves are at dimensionless times of $\tau \simeq$0.54, 0.96, 1.44, 1.92, 2.40, 4.80, 7.20, 9.60, 12.00 and 14.40 (dimensional times of t$\simeq$32.1, 56.1, 84.1, 112.1, 140.2, 280.3, 420.5, 560.6, 700.8 and 840.9 μs) with a narrow distribution of droplets initially at ξ=0.

Fig. 5.9 shows the variation of the pressure fluctuations for similar conditions as shown in Fig. 5.8 but for which the maximum of the initial void fraction is 0.1 and the droplets have radius 10 μm. In Fig. 5.9 we see a huge pressure fluctuation. The maximum in the pressure drop is $\sim -2\times10^{-1}$ while the maximum in the back pressure is $\sim 3\times10^{-1}$. This is a considerable fraction of the initial pressure. Figs. 5.8 and 5.9 suggest that both the form of the pressure fluctuation and its magnitude are strongly influenced by the initial gas Mach number.

To study the effect of the droplet void fraction distribution on the pressure fluctuation we now consider a gas with entry pressure 5 atm. and relative Mach number 0.1 and a droplet distribution in the form of a broad step. In Fig. 5.10 the initial maximum in the void fraction is α=0.01 and the droplet radius is 0.1 mm. The profiles are plotted at dimensionless times of τ = 0.54, 1.09, 1.64, 2.18, 3.82, 6.54, 9.81 and 13.08 (corresponding to dimensional times of t = 0.03, 0.06, 0.10, 0.13, 0.22, 0.38, 0.57 and 0.76 ms) approximately. We see that the ends of the region of entrained droplets cause first a back pressure to propagate in the upstream gas direction, while there is a smaller pressure drop propagating in the downstream gas direction from the other side of the entrained region. Within the entrained region, the pressure is largely slightly above the entry pressure, but there is a small region in which the pressure drops to below the initial entry pressure.

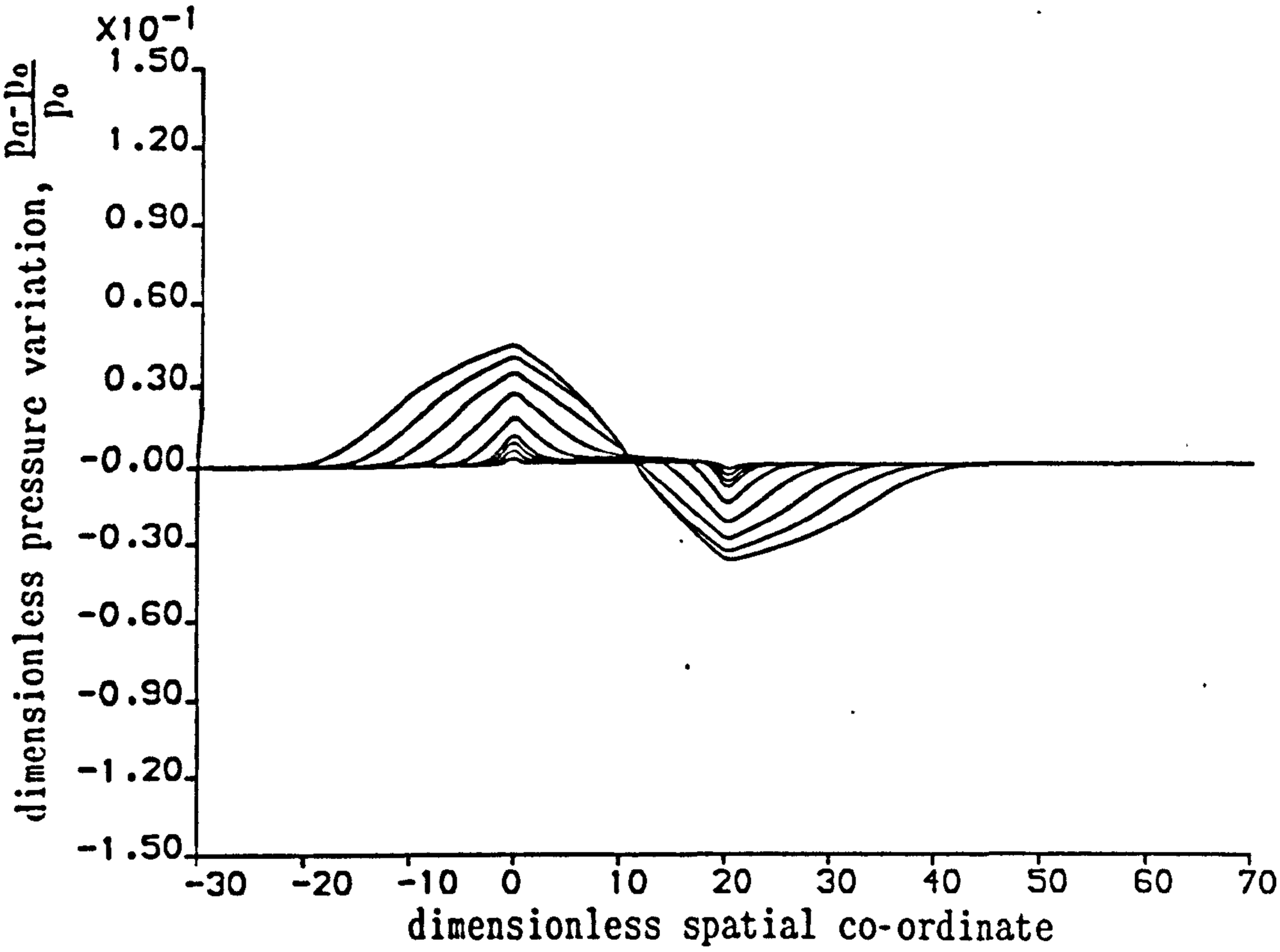

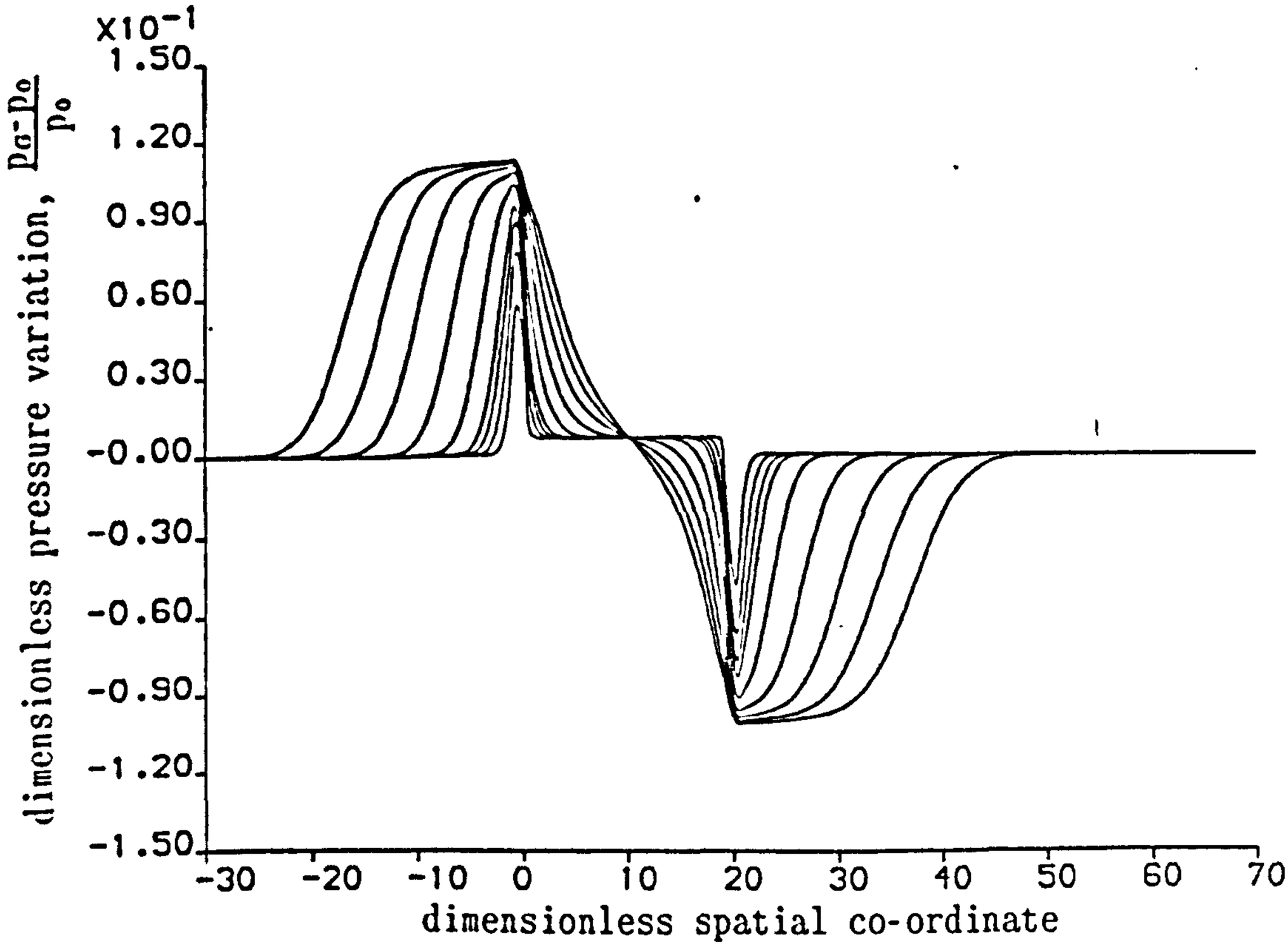

Figs. 5.10 (top) and 5.11

Fig. 5.10 has gas entry pressure of 5.0 atm. at Mach number 0.10, void fraction, α=0.01, droplet radius, r=0.1 mm
Fig. 5.11 has gas entry pressure of 5.0 atm. at Mach number 0.10, void fraction, α=0.10, droplet radius, r=0.01 mm
All of these curves are at dimensionless times of $\tau \simeq 0.54$, 1.09, 1.64, 2.18, 3.82, 6.54, 9.81 and 13.08 (dimensional times of t≃32.1, 63.7, 95.8, 127.3, 223.7, 381.9, 572.9 and 763.8 μs) with a broad distribution of droplets initially at ξ=0.

If we now consider the effect of increasing the initial maximum in the liquid void fraction to α=0.1 and consider smaller droplets of radius 10 μm we obtain Fig. 5.11. In Fig. 5.11 we see that the ends of the entrained region again cause pressure pulses to propagate. These pressure pulses are initially very sharp. The magnitude of the pressure differences within the entrained region are smaller than in the previous case, the pressure rapidly dropping toward slightly greater than the initial entry pressure. *In both* Figs. 5.10 and 5.11 we see that the magnitude of the pressure pulse is greater than in their narrow droplet distribution counterparts, Fig. 5.7 for example.

If we consider the variation of the droplet void fraction corresponding to the case shown in Fig. 5.10 at dimensionless times τ = 3.14, 22.89, 34.35, 65.93, 97.33 and 128.73 (corresponding to dimensional times of t = 0.18, 1.33, 2.00, 3.85, 5.68 and 7.52 ms) approximately we obtain Fig. 5.12. We see that the entrained region moves in the direction of the gas flow, and that the front of the entrained region moves faster than the remainder. The front of the entrained region is thus becoming more disperse.

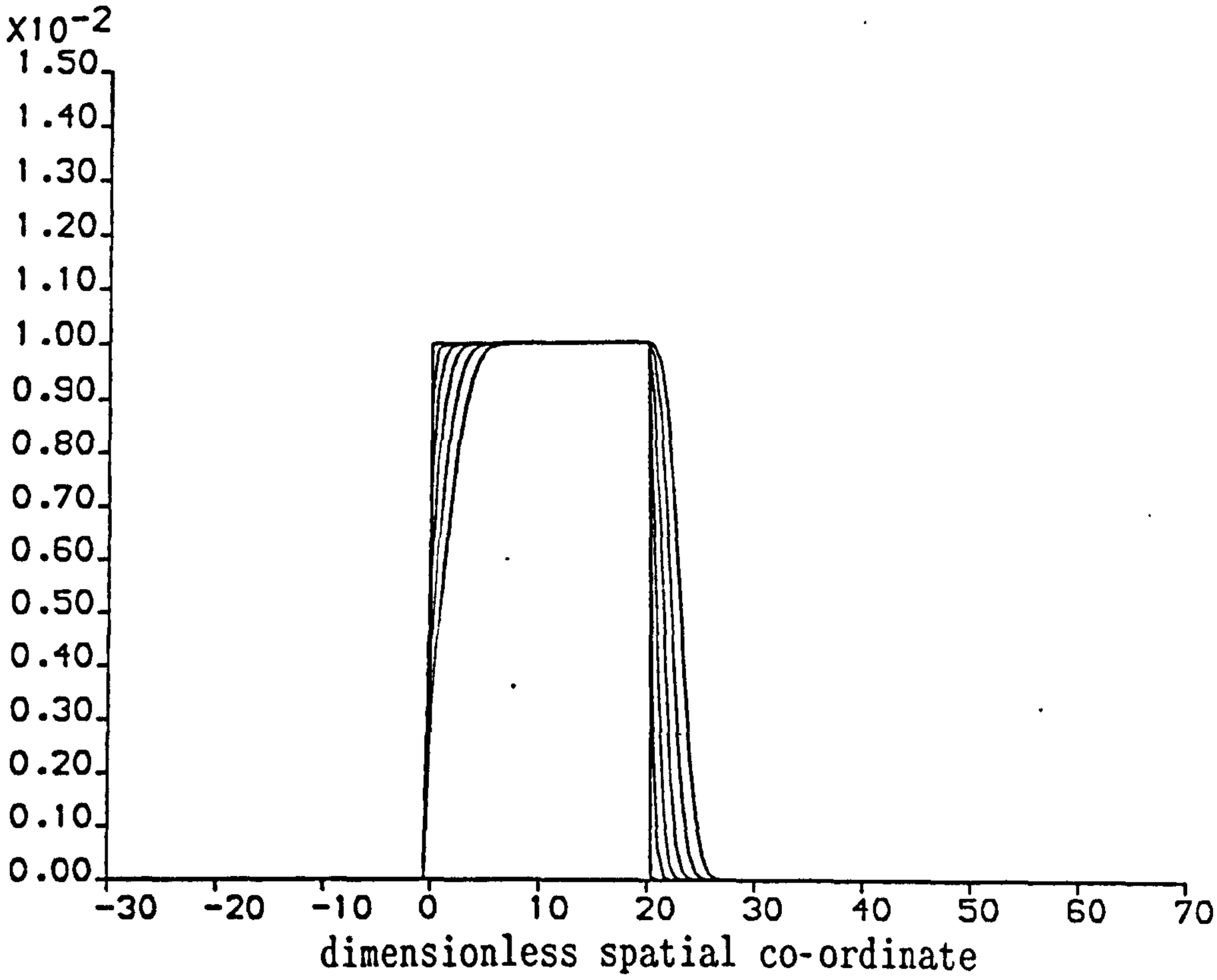

Fig. 5.12

Fig. 5.12 shows the variation of the droplet distribution corresponding to the conditions of the wave shown in Fig. 5.10 at dimensionless times $\tau \simeq 3.14$, 22.89, 34.35, 65.93, 97.33 and 128.73 (corresponding to dimensional times of $t \simeq 0.18$, 1.33, 2.00, 3.85, 5.68 and 7.52 ms.).

5.10 Discussion of numerical results

The results of the numerical modelling of the effect of disperse droplets on the gas dynamics of a two-phase flow are quite interesting. While all of the results are qualitatively similar - even when α=0.1 which is relatively large - they do show the effect increasing the pressure has on the flow and also the effect of changing the initial Mach number of the gas flow. Furthermore, the broad band of disperse droplets (a dimensionless distance of 20 is equivalent to 0.5 m in our dimensional units), and its effect on the gas flow through it, is quite informative.

To summarise the various effects, consider Figs. 5.13 and 5.14. Fig. 5.13 shows the magnitude of the dimensionless pressure drop at time τ = 6.54 (just chosen for convenience) plotted against $\bar{\alpha}$, where:

$$\bar{\alpha} = \log_{10}(100\alpha)$$

for entry pressures of 1.1, 5.0 and 20.0 atm. and all with a relative gas Mach number of 0.1. There are two sets of curves, one for droplets with radius 0.1 mm, and the other for droplets with radius 10 μm. For droplets with the 0.1 mm radius the dimensionless pressure drop is largest for an entry pressure of 1.1 atm. and smallest for an entry pressure of 20.0 atm.. This trend is maintained when the droplet radius is 10 μm. Fig. 5.14, on the other hand, has a set of curves all at an entry pressure of 5.0 atm., but for Mach number 0.1 with the narrow and broad distributions of droplets, and Mach number 0.25 for the narrow distribution.

Fig. 5.13

Variation of the dimensionless pressure drop with liquid void fraction for various entry pressures of gas flow all at Mach number 0.1

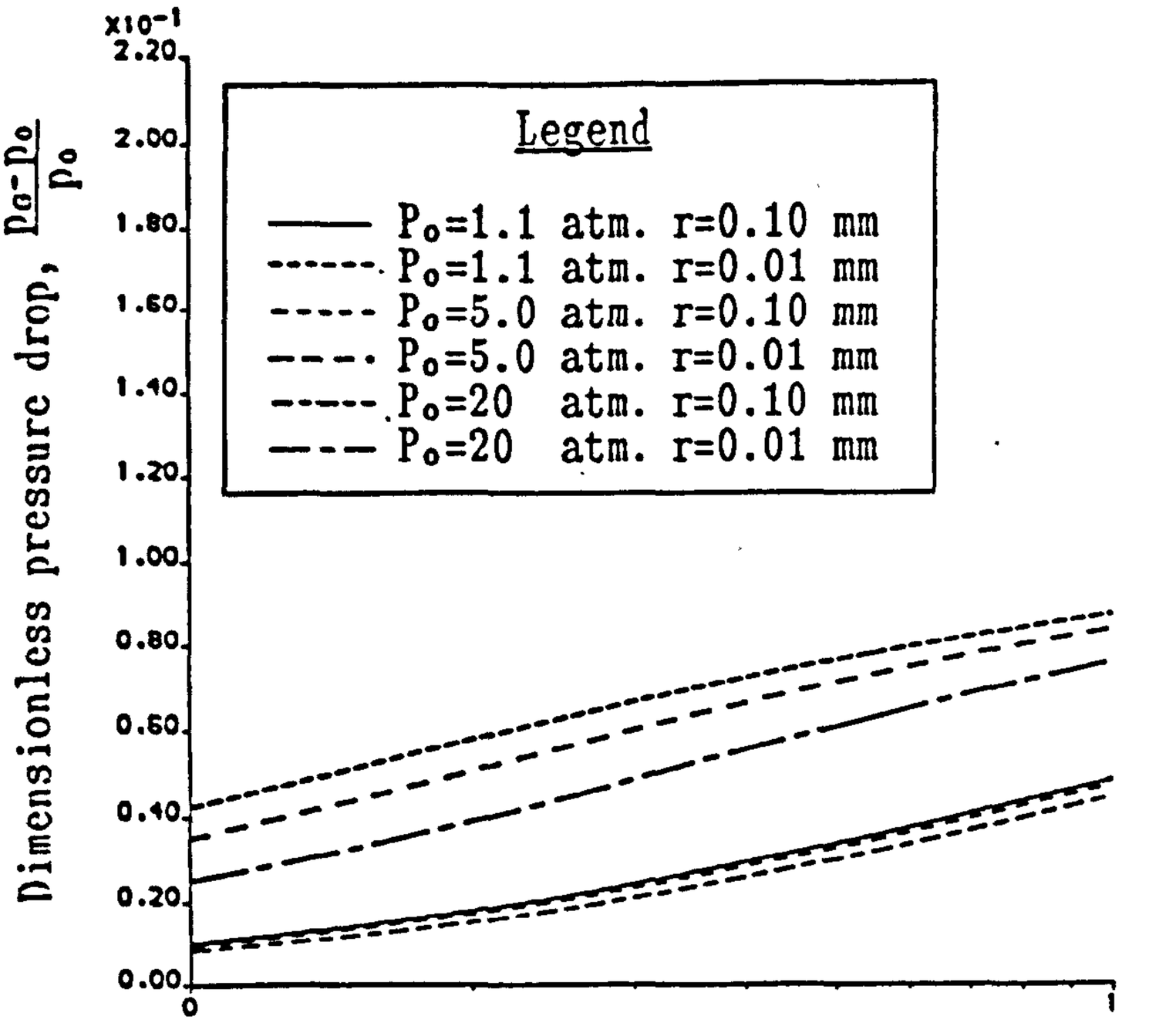

Fig. 5.14

Variation of the dimensionless pressure drop with liquid void fraction for various different gas Mach numbers or droplet distributions all at entry pressure 5.0 atm.

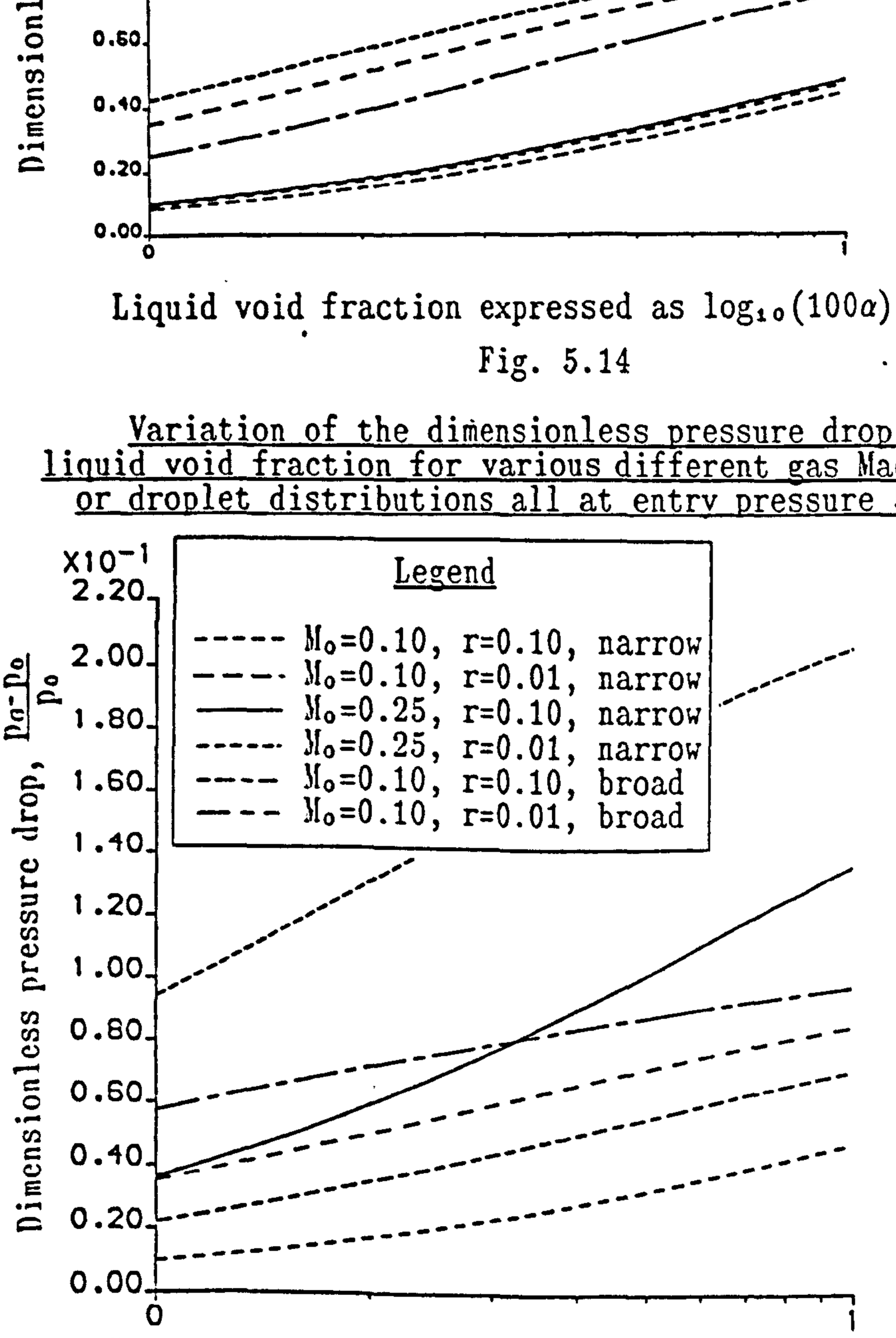

Both Figs. 5.13 and 5.14 show the following points:

1. increasing the entry pressure decreases the dimensionless pressure drop,
2. decreasing the droplet radius increases the dimensionless pressure drop,
3. increasing the void fraction increases the dimensionless pressure drop,
4. increasing the relative gas Mach number increases the dimensionless pressure drop, and
5. changing the droplet distribution affects the pressure drop.

While these figures summarise the effects on the pressure drop for various situations, Figs. 5.1 to 5.12 show how these changes quantitatively affect the individual pressure profiles. However, the actual validity of these results must remain questionable at this time, since the author has found no experimental results with which to check the numerical calculation.

Since no check could be made with existing experimental results, the qualitative nature of the results must be scrutinised. Comfort III & Crowe (1980) concluded that for the two-phase disperse flow through a converging-diverging nozzle, shocks will form in the pressure distribution when the droplet diameter is of the order 1 μm, and that for droplet diameters greater than this the variation in pressure and gas velocity is smoother than this. They considered flows with large Mach numbers, when shocks were more likely to occur. So, for flows of relatively low Mach number, and relatively large droplet diameter, perhaps it is reasonable not expect shocks to form. Indeed, we find this. It was originally intended to also study the effect of entrained

droplets of radius 1 μm on the gas dynamics of the flow. However, this could not be done, since when this radius was chosen the source terms in the two-phase system of equations became very large, and it would have been necessary to rescale all of the variables in order to retain the same computational scheme. If no such rescaling is performed, and the radius set to this low value, the numerical scheme is not stable. *Comfort III & Crowe (1980) conclude that when the droplet diameter is* small the medium behaves more like a homogeneous medium, and that the two-phase interaction problem reduces to a gas flow-like problem.

The numerical scheme was checked to see if it behaved sensibly. If the drag factor between the gas and the liquid droplets was set to zero, then the liquid became transparent to the gas and no modification in the pressure, or any of the other gas flow parameters, occurred. And in absence of gravitational effects, the droplet distribution remained unaltered (with no sign of numerical diffusion even after very many iterations) as would be expected if the interaction between the phases through the drag term were omitted. The choice of the magnitude of the drag factor for the flows under consideration was calculated from Drew (1983), in which there is a table for the drag factors of multidisperse two-phase flows. The drag factor in the calculations was of the order 0.6 . This is indicative of a fairly strong coupling between the phases through the drag.

If the liquid void fraction is reduced greatly ($\alpha \simeq 1 \times 10^{-4}$ or less) we would expect very little change in the gas flow parameters. After all, there is hardly any liquid for the gas to interact with. For very small void fractions the pressure fluctuation is found to be $O(10^{-14})$ or less, as expected.

Checking the numerical scheme by using other partial differential systems of equations was not really possible due to the specific nature of this scheme; however, it was possible to check the scheme with:

$$\frac{\partial u}{\partial t} + a\frac{\partial u}{\partial x} = 0 \qquad (5.10.1)$$

or:

$$\frac{\partial u}{\partial t} + u\frac{\partial u}{\partial x} = 0 \qquad (5.10.2)$$

or other similar (easy to program) equations with various initial conditions. If we consider the most simple check, (5.10.1) with some original profile for u, then this is advected properly for all time with no measurable numerical diffusion. Likewise, checks with other equations were all very encouraging.

No further checks could be made to test the accuracy of the numerical model beyond those outlined above, but all of these indicated that the scheme was performing in the desired fashion and that it was accurate for the test functions used. The calculated numerical results then, may be representative of the transition for the given initial conditions. They indicate that, in addition to a transmitted pressure drop, due to interaction with the droplets, there is also a back pressure of similar magnitude to the pressure drop. Indeed this would seem reasonable for systems in which the total energy is constant, ie. no heat enters or leaves the system. However, whether this is the case for real gas-droplet flows remains to be verified.

The pressure variations in the gas as a result of interaction with the various disperse regions of droplets can be analysed relative to steady one-dimensional gas flow through a change of area, say. We consider the void fraction as equivalent to an area reduction. Then

when the gas of Mach number 0.1 through area A goes through area A(1-α), we may obtain the corresponding gas Mach number through this area and the resulting pressure (eg. when α=0.05 and p_o=5.0 atm we find the pressure given by the one-dimensional steady calculation to be 4.9962 atm. corresponding to a dimensionless pressure drop of -0.7645×10^{-3}). Analysis of the actual numerical results shows that the pressure change is in fact somewhat greater than is calculated from the steady one-dimensional model.

In further evaluating the validity and accuracy of the numerical scheme, entire regions of disperse droplets could be considered so that analogy with fog dynamics calculations and experiments could be made. However, in order to check the scheme with two-phase flow calculations through constrictions such as that of Comfort III & Crowe (1980), a great deal of remodelling and code rewriting would be necessary.

The numerical scheme itself is fairly cpu intensive. All of the calculations were performed on an IBM 3090/150S with vector facility, and great efforts were made to ensure that the code vectorised well. This involved extensive analysis of the code itself. However, run times in excess of one hour cpu time for the 400 point grid, and more than twice that for the 800 point grid, were the norm. In fact, the numerical scheme was found to use approximately 50 μs per grid point per time step. By time stepping the motion on the scale of the fastest eigenvalue, the excessive run times that would be incurred if the time step were chosen to be much less than this, or the numerical inaccuracy incurred by choosing the time step to be large, was avoided. The penalty of this was print-out time steps that were not "nice". In fact, using this time stepping approach greatly improved the efficiency of the scheme.

5.11 Conclusions

The specific form of the equations of motion of the disperse liquid and gas, with the omission of all interactions except the drag , allowed the system of partial differential equations to be solved by using an explicit Roe-type scheme. Whilst the scheme works for individual partial differential equations, the validity and accuracy could not be tested with other partial differential systems. However, various limiting cases of the specific partial differential system were considered, such as no drag, or hardly any droplets, and the results for these were as would be expected. Whilst we may suspect, therefore, that the scheme accurately describes the evolution of the two-phase system, a firm conclusion of this fact will only be possible once data from suitable experiments has been obtained, and comparison with the numerical results made. Until such a time, the numerical results can only be speculative.

In addition, the numerical scheme admits solution to a wider class of two-phase problem than is presented here, such as gas flow within an entirely entrained region, or gas-droplet flow with high gas Mach number (0.75 for instance) for which we may expect shocks to form.

6. CONCLUSIONS

The transition to horizontal slug flow has long been of interest. Early work considered the conditions necessary for slug flow to exist. These conditions were initially determined experimentally and summarised on flow régime maps, but the applicability of these maps, and their inability to cover a wide range of fluids under a wide variety of conditions limits their effectiveness. Subsequently, empirical correlations were sought. There was some success with this approach, but the inability to gain deeper physical understanding of multiphase flows limits the effectiveness of this approach. This has led to the theoretical modelling of multiphase flows. Effective theoretical modelling attempts to avoid the pitfalls of the experimental and empirical modelling.

The inception stage of slug flow from a wavy-stratified type flow has been treated as a growing Kelvin-Helmholtz type of instability by many authors. However, this approach has always considered the gas (like the liquid) to be incompressible. This may seem logical for gas-liquid flows for which the gas Mach number is low. In Chapter 2 we showed that the compressibility of the gas is evident even for low gas Mach number flows. While this approach does not reconcile the difference between the Kelvin-Helmholtz instability, long wave (small wave number) prediction for the onset of slugging with either the experimental observations or with the finite amplitude, "most dangerous" wave (i.e. waves of wave number that grow fastest) predictions, it does clearly show that compressibility destabilises the linear theory.

Models for predicting slug flow stem largely from experimental observations, and attempts to model slug flow have often relied upon what may be regarded as a characteristic trait of that flow from such observations. While such models are undoubtedly relevant for flows that are in a similar sub-domain of the two-phase parameter space as the initial experiments, they may not be relevant for flows in other sub-domains. Consider the tube "bridging" model suggested by Dukler & Hubbard (1975). This model, and the "bridging" phenomenon, are widely used to describe, or characterise, slug flows. However, this model cannot be used to describe all two-phase slug flows. Coney (1974) presents experimental observations for horizontal two-phase slug flows which do not bridge the entire tube diameter (he calls these flows "surge" flows).

Due to the lack of detailed descriptions of the mode of growth of surface waves into fast moving slugs, the experimental work of Chapter 3 was performed. While no measurements of pressure pulse propagation, or of water film thicknesses were obtained, the mode of transition to slug flow within the particular sub-domain of the slug flow parameter space was extensively recorded. The results of the study proved interesting. In both the black and white still photographs, and the fast ciné film, the growth of surface waves into very steep sided large amplitude to depth ratio waves then onto breaking waves can be observed. Simultaneously, the entrainment of drops of liquid into the gas flow can be observed. Initially, the entrainment is small, but by the breaking wave stage it is quite considerable. From the breaking wave stage the wave is not seen to grow further and block ("bridge") the tube. Instead, entrainment is seen to increase at the expense of the wave. Droplets are drawn from the tip of the breaking wave, and from the front surface of the wave, into the gas flow. Ultimately, a fully formed slug

in the form of a fast moving region of entrained droplets propagates down the tube. Careful study of the stills and the fast ciné suggest the following mode of transition to slug flow in this particular sub-domain of the slug flow parameter space:

1. a wave is "sucked" upwards by a region of low pressure over its crest due to the motion of the gas over it
2. the wave grows rapidly and both its front and back surfaces become steep
3. as the liquid grows entrainment of liquid droplets from the crest begins; perhaps an eddy is formed in front of the wave
4. the wave reaches some maximum height in the tube (perhaps resembling a breaking wave) after which entrainment of liquid droplets into the gas flow occurs at a greater rate than liquid is being drawn into the wave body from the underlying liquid
5. entrainment continues to increase at the expense of the wave, whose amplitude decreases
6. a fully formed slug consisting of fast moving entrained droplets is formed from the initial wave.

From the experiments we may conclude that for this particular type of slug flow, the bridging model is inappropriate. We may also conclude that in the initial stages of slug growth (corresponding to point 1 in the above mode of transition) it may be appropriate to treat the motion of the slug in a water wave like fashion, where the water wave motion is two-dimensional and modulated by a compressible gas. In the later stages of slug growth (corresponding to point 3 in the mode of transition), the emphasis is placed on the interaction of the compressible gas with the entrained liquid droplets.

In Chapter 4 we dealt with the wave like motion of the initial stages of slug growth. Since we are primarily concerned with the motion of the gas-liquid interface the problem was scaled accordingly. As a result, since changes in the motion of the gas occurred on a much faster time scale than changes in the motion of the liquid, and since we were concerned with the initial stages of the growth of the wave, when the wave slopes were not steep, we modeled the gas motion as a compressible, quasi-steady one-dimensional motion. The liquid was treated as incompressible, unsteady and two-dimensional. With the gas in a closed channel, we could then determine the interfacial pressure distribution and thus, the motion of the underlying liquid.

The parameter space of variables that affect such a coupled motion is very large. In order to make some progress it was decided that the effect on the motion of the interface of changing the gas dynamics quantities would be investigated. So, from the experimental work of Chapter 3 and considerations of the possible initial wave profile from the non-linear Korteweg-de Vries equation, values for the initial amplitude to depth ratio for a solitary wave profile, the initial undisturbed depth of the liquid in the channel and the initial channel depth were fixed. These values were fixed at 0.2, 1.0 and 3.0 in dimensionless units. By doing this the effects of changing the gas entry pressure and the relative gas entry Mach number could be studied.

The solution of the coupled problem is obtained by a boundary-integral technique (extensively developed by colleagues of the author at the University of Bristol). The results of the modelling carried out in Chapter 4 are interesting. They show that there is a strong influence of the gas, through the gas Mach number, on the motion of the liquid surface. If we consider the time taken for the wave

amplitude to increase from 0.2 (the initial value) to 0.5 we see that this time decreases greatly with increasing gas Mach number. We also see that increasing the gas Mach number increases the symmetry of the growing wave about the amplitude maximum; low Mach number, large asymmetry, large Mach number, little asymmetry. The results from the numerical calculations are very encouraging. The surface grows in a similar fashion to that observed in the experimental work. The dependence of this growth on the gas Mach number (equivalent experimentally to the relative gas mass flux) is strong, and growth rates are similar, although no direct quantitative analysis is performed to compare our numerical two-dimensional growth rates with their three-dimensional experimental counterparts.

The method is then extended to cover a specific type of flow. In the latter part of Chapter 4 steam-water flows are considered. The motion of the steam is again assumed to be quasi-steady and one-dimensional and the effect of steam at 100, 140 and 180 atm. and under saturation conditions, on the liquid motion is studied. Under such conditions the assumptions of quasi-steady, one-dimensionality for the steam, and two-dimensionality for the water are less likely to be valid than they were for the air-water type flows. Both of these flows are in fact, highly turbulent, unsteady and three-dimensional. This study produces a strange result. The results suggest that steam at 100 and 140 atm. have an almost identical effect on the motion of the water surface, while steam at 180 atm. causes a very different effect. The 180 atm. steam appears to retard the growth rate of the water surface. Slugs form more slowly. This result is counter-intuitive. Perhaps due to the intricate nature of steam, steam at this pressure is less compressible than its lower pressure counterparts (despite the much lower sound speed). The result of Chapter 2 showed that compressibility

destabilises two-phase flow, so perhaps we are witnessing a more stable flow due to a decrease in the effects of compressibility. While this result appears strange, Pearce (1982) in experiments on Refrigerant-12 at 30 atm. (for which the vapour liquid density ratio is similar to steam-water at 180 atm.) finds that there may only be a small permissible parameter space for slug flows under these conditions. Perhaps, then, slug flows under these conditions are inhibited.

While modelling slug flow inception as a wave-like phenomenon seems to have met with some success, there are a few limitations. Since we consider inviscid fluids we do not know the velocity, relative to the walls of the channel, of any of the flows that we calculate. While we may consider turbulent shear stresses within the fluids and hence obtain such a velocity, there appears to be no standard approach to this problem, and this has yet to be performed.

We found that the transition to slug flow occurred very abruptly (for very small changes in the gas Mach number), and whilst the gas Mach numbers were often representative of flows well within the established slug flow parameter space, such an abrupt change is indicative of the instability of the liquid layer. The parameter space of variables that affect such slugging flows is large. It would have been interesting to study the effect of how varying the initial amplitude to depth ratio of the solitary wave affects the subsequent gas-liquid interface movement. Perhaps this would sometimes lead to slugging at lower gas Mach numbers.

By solving Laplace's equation within the liquid by a boundary - integral technique we are limiting ourselves to inviscid, irrotational, non-turbulent, two-dimensional flows. As the scheme stands, we are

further limited by the motion of the gaseous layer. When the slopes of the interface become large we can no longer consider the gas to flow in a one-dimensional fashion. Since the liquid layer is already modeled as an unsteady, two-dimensional layer, perhaps one extension to this scheme would be to develop a two-layer irrotational model, in which the gaseous layer is also considered to be two-dimensional. In this way, we could allow the interface to become steeper, and so follow the motion for longer. Another useful extension to the scheme would be to model spray formation and entrainment. From the experimental results we saw that entrainment from the crest of the steepening wave limited the size of the wave. So modelling such entrainment may be important.

The observations of Chapter 3 suggest that in the latter stages of slug growth the effect of the interaction between the gas and the entrained liquid droplets becomes of primary importance. In the light of this, the work of Chapter 5 was performed. Chapter 5 considers the effect that the droplets have on the gas flow. Since we are now primarily concerned with the gas dynamics, the system of equations is scaled suitably. It is now necessary to treat both the gas and the liquid motions as unsteady, but we assume that the motion of both may be adequately described by one-dimensional equations.

Again the parameter space of the possible variables is large, but we again narrow our attention so that we may draw some conclusions relating to Chapters 3, 4 and 5. We choose a uniform channel into which droplets are injected. We also fix the drag coefficient between the gas and the droplets and the form of the initial droplet distribution, for which we have two choices. Then, by varying the maximum in the droplet void fraction distribution, the droplet radius, the gas Mach number and the initial entry pressure we hope to discover how these parameters

influence the flow.

To numerically solve this problem an upwind finite difference scheme was developed. This scheme allowed a system of non-homogeneous partial differential equations to be solved. Again the results of the numerical scheme are interesting. By changing the droplet radius the pressure fluctuation changed; the smaller the droplet the greater the pressure drop (in good agreement with Comfort III & Crowe (1980)). Further, increasing the void fraction increased the pressure drop, and changing the droplet distribution affected the pressure drop. But perhaps the most dramatic effect was seen when the initial gas Mach number was increased. This substantially increased the pressure drop. All of these changes affected the pressure pulse profiles. Sometimes the pressure change behind the front of the pressure pulse remained fairly constant, while at other times the pressure pulse rapidly tended toward its equilibrium value.

The effect of the gas flow on the droplet dynamics was also studied. The greater the gas entry pressure or the gas Mach number, the faster the droplets would move. This behaviour was expected.

While only low gas Mach number flows were studied here, the scheme was a shock capturing scheme, and gas flows with larger Mach number were admissible to the scheme. Perhaps such flows would have been of some interest, and then comparisons with the work of other authors in this field could be made. However, at this time no such extension to the work has been performed.

The results for the magnitude of the pressure pulses are more like those expected for fully formed slug flows, since they are in reasonable

agreement with the experimental observations of Martin & Padmanabhan (1979), Mori et al. (1975) and Comfort III & Crowe (1980). These pressure drops are considerably larger than those predicted from the quasi-steady one-dimensional work of Chapter 4, and this is very encouraging. Likewise, the motion of the droplets is as we would expect from the results of Chapter 3. The entrained region becomes extended with a fast moving region of disperse entrainment to the front of the slug, then a slower, denser region of entrainment, and finally a much slower very disperse region to the rear.

Checks on the numerical scheme were limited, but tests were performed to see whether the scheme *behaved sensibly* and these proved very satisfactory.

Again, there were some limitations. The theory for the implementation of the scheme limited the droplet void fraction to small void fractions. In this fashion the implementation of the scheme was simplified, but the possible parameter space available for study was limited (to circa 0.1 as a maximum void fraction). Secondly, the scaling chosen for the dimensionless parameters was such that droplets of very small radius were excluded from the analysis unless the problem was completely rescaled. Comfort III & Crowe (1980) conclude that the smaller the individual droplets, the more homogeneous the medium, the sharper the fronts of the pressure fluctuations, possibly leading to shock waves at relatively low Mach numbers. It would have been interesting to perform such calculations, but this was not achieved at this time.

In summary, we have seen that by treating the gas as compressible we destabilise the linear, one-dimensional theory (albeit slightly). Analysis of the experimental results for horizontal slug flows in a particular sub-domain of the slug flow parameter space have led to simplified models which give an indication of the importance of certain parameters. Throughout, the effects of compressibility of the gaseous phase have been considered. For air-water like flows this effect is only slight at slug flow initiation. However, the sensitivity of the gas-liquid interface to the relative gas Mach number suggests that the liquid layer is very unstable. Compressibility is more important when assessing the effects of entrained droplets on the gas flow dynamics. The resulting pressure drops within the gas are very sensitive to the droplet radius, liquid void fraction and the gas Mach number, and are influenced by the form of the region of entrainment. These regions of entrainment greatly modify the observed pressure, causing the experimentally measured large pressure fluctuations.

REFERENCES

Andritsos, N. & Hanratty, T.J. (1987)
"Interfacial instabilities for horizontal gas liquid flows in pipelines"
Int.Jour.Multiphase Flow 13 p.583

Allen, C.B. (1987)
"Shock capturing finite difference schemes for non-smooth shallow water flows"
MSc. dissertation, University of Bristol

Azzopardi, B.J. (1983)
"Mechanisms of entrainment in annular two-phase flow"
AERE Harwell report AERE-R 11068

Baker, G.R., Meiron, D.I. & Orszag, S.A. (1982)
"Generalised vortex methods for free surface flow problems"
Jour.Fluid Mech. 123 p.477

Baker, O. (1954)
"Simultaneous flow of oil and gas"
Oil Gas Journal 53 p.185

Bell, K.J., Taborek, J. & Fenoglio, F. (1970)
Interpretation of horizontal in-tube condensation heat transfer correlations with a two-phase flow régime map"
Chem.Eng.Prog.Symposium Series 66(102) p.150

Benjamin, T.B. (1968)
"Gravity currents and related phenomena"
Jour.Fluid Mech. 31 p.209

Bergles, A.E., Collier, J.G., Delhaye, J.M., Hewitt, G.F. & Mayinger, F. (1981)
Two-phase Flow and Heat Transfer in the Power and Process Industries
Hemisphere Publishing Corp., McGraw-Hill Book Co., New York

Bretherton, F.P. (1961)
"The motion of long bubbles in tubes"
Jour.Fluid Mech. 10 p.166

Bouré, J.A., Fritte, A.A., Giot, M.M. & Réocreux, M.L. (1976)
"Highlights of two-phase critical flow: On the links between maximum flow rates, sonic velocities, propagation and transfer phenomenon in single phase and two-phase flows"
Int.Jour.Multiphase Flow 3 p.1

Carrier, G.F. & Greenspan, H.P. (1958)
"Water waves of finite amplitude on a sloping beach"
Jour.Fluid Mech. 4 p.97

Chan, R.K.-C. & Street, R.L. (1970)
"A computer study of finite amplitude water waves"
Jour.Comp.Phys. 6 p.68

Clarke, J.F. & McChesney, M. (1964)
The Dynamics of Real Gases
Butterworth & Co. (Publishers) Ltd., London

Comfort III, W.J. & Crowe, C.T. (1980)
"Dependence of shock characteristics on droplet size in supersonic two-phase mixtures"
Trans.ASME Jour.Fluid Eng. 102 p.54

Coney, M.W.E. (1974)
"The analysis of a mechanism of liquid replenishment and draining in horizontal two-phase flow"
Int.Jour.Multiphase Flow 1 p.647

Courant, R., Friedrichs, K.O. & Lewy, H. (1967)
"On the partial difference equations of mathematical physics"
IBM Journal of Research and Development 11 p.215

Davidson, G.A. (1975)
"Sound propagation in fogs"
Jour.Acoust.Soc.Am. 32 p.2201

Dold, J.W. (1990 - to appear)
"An efficient surface-integral algorithm applied to unsteady water waves"

Dold, J.W. & Peregrine, D.H. (1986)
"An efficient boundary integral method for steep unsteady water waves"
in Numerical Methods for Fluid Dynamics II (eds. K.W. Morton and M.J. Baines), Oxford University Press, Oxford

Donnelly, J.D.P. & Li, Xin Kai (1989)
"Roe's approximation for a two-phase slug flow model"
Oxford University Computing Laboratory Numerical Analysis Group
Report number 89/3

Drazin, P.G. & Reid, W.H. (1985)
Hydrodynamic Stability
Cambridge University Press, Cambridge

Drew, D.A. (1983)
"Mathematical modeling of two-phase flow"
Ann.Rev.Fluid Mech. 15 p.261

Drew, D.A., Cheng, L.Y. & Lahey, R.T. (1979)
"The analysis of virtual mass effects in two-phase flow"
Int.Jour.Multiphase Flow 5 p.233

Dukler, A.E. & Hubbard, M.G. (1975)
"A model for gas-liquid slug flow in horizontal and near horizontal tubes"
Ind.Eng.Chem.Fund. 13 & 14 p.337

Gardner, G.C. (1978)
"Onset of slugging in horizontal ducts"
CEGB internal report CERL RD/L/N 138/78

Govier, G.W. & Omer, M.M. (1962)
"The horizontal pipeline flow of air-water mixtures"
Can.Jour.Chem.Eng. 40 p.93

Gray, W.G. (1983)
"Local volume averaging of multiphase systems using a non-constant averaging volume"
Int.Jour.Multiphase Flow 9 p.755

Harrison, G.S. (1975)
"The effect of tube diameter on the frequency distribution of surge intervals in an air-water serpentine"
CEGB internal report CERL RD/L/N 95/75

Helmholtz, H. (1868)
"Über discontinuirliche Flüßigkeits-bewegnungen"
in Helmholtz: Wissenschaftliche Abhandlungen I, Druck von Metzger und Wittig, Liepzig, p.146

Hewitt, G.F. & Hall-Taylor, N.S. (1970)
Annular Two-phase Flow
Pergamon Press, Oxford

Ishii, M. (1975)
Thermo-fluid Dynamic Theory of Two-phase Flow
Eyrolles, Paris

Ishii, M. & Kocamustafaogullari, G. (1983)
"Two-phase flow models and their limitations"
in Advances in Two-phase Flow and Heat Transfer vol.1 (eds. S. Kakaç and M. Ishii) NATO ASI Series, Martinus Nijhoff Publishers, The Hague

James, P.W., Wilkes, N.S., Conkie, W. & Burns, A. (1987)
"Developments in the modeling of horizontal annular two-phase flow"
Int.Jour.Multiphase Flow 13 p.173

Jeffrey, A. (1976)
Quasilinear Hyperbolic systems and Waves
Pitman Publishing, London

Keenan, J.H., Keyes, F.G., Hill, P.G. & Moore, J.G. (1978)
Steam Tables (S.I. Units)
John Wiley & Sons, Inc., New York

Keller, H.B., Levine, D.A. & Whitham, G.B. (1960)
"Motion of a bore over a sloping beach"
Jour.Fluid Mech. 7 p.302

Kelvin, W. (1871)
"Hydrokinetic solutions and observations"
Phil.Mag. 4 p.374

Kittel, C. & Krömer, H. (1980)
Thermal Physics, 2nd. edition
Freeman Publishers, San Francisco

Korbyban, E.S. (1977)
"Some characteristics of high waves in closed channels approaching Kelvin-Helmholtz instability"
Trans.ASME Jour.Fluid Eng. 37 p.339

Kordyban, E.S. (1963)
"Experimental study of the mechanism of two-phase flow in horizontal tubes"
ASME Multiphase flow symposium, p.1

Kordyban, E.S. (1961)
"A flow model for two-phase slug flow in horizontal tubes"
Trans.ASME Jour.Basic Eng. 83 p.613.

Kordyban, E.S. & Ranov, T. (1970)
"Mechanism of slug formation in horizontal two-phase flow"
Trans.ASME Jour.Basic Eng. 92 p.857

Kreibel, A.R. (1964)
"Analysis of normal shock waves in a particle laden gas"
Trans.ASME Jour.Basic Eng. 86 p.655

Lamb, Sir. H. (1953)
Hydrodynamics (6th. edition)
Cambridge University Press, Cambridge

Lin, P.Y. & Hanratty, T.J. (1987)
"Effect of pipe diameter on flow patterns for air-water flow in horizontal pipes"
Int.Jour.Multiphase Flow 13 p.549

Lin, P.Y. & Hanratty, T.J. (1986)
"Prediction of the initiation of slugs with linear stability theory"
Int.Jour.Multiphase Flow 12 p.79

Lockhart, R.W. & Martinelli, R.C. (1949)
"Proposed correlation of data for isothermal two-phase, two-component flow in pipes"
Chem.Eng.Prog. 45 p.39

Longuet-Higgins, M.S. & Cokelet, E.D. (1976)
"The deformation of steep surface waves on water; A numerical method of computation"
Proc.Royal Soc.Lond. A 350 p.1

Mandhane, J.M., Gregory, G.A. & Aziz, K. (1974)
"A flow pattern map for gas-liquid flow in horizontal pipes"
Int.Jour.Multiphase Flow 1 p.537

Markovich, É.É. (1983a)
"Structure of the leading edge of a liquid slug in the case of a slug flow of a gas-liquid mixture in a horizontal tube"
Fluid Dynamics 17 p.785

Markovich, É.É. (1983b)
"On the transition between slug flow and two-layer flow of a gas-liquid mixture in a horizontal tube"
Fluid Dynamics 18 p.143

Martin, C.S. & Padmanabhan, M. (1979)
"Pressure pulse propagation in two-component slug flow"
Trans.ASME Jour.Fluid Eng. 101 p.44

Miles, J.W. (1962)
"On the generation of surface waves by shear flows, part 4"
Jour.Fluid Mech. 13 p.433

Milne-Thomson, L.M. (1950)
Theoretical Hydrodynamics (2nd. edition)
The MacMillan Company, New York

Mishima, K. & Ishii, M. (1980)
"Theoretical prediction of onset of horizontal slug flow"
Trans.ASME Jour.Fluid Eng. 102 p.441

Mori, Y., Hijikata, K. & Komine, A. (1975)
"Propagation of pressure waves in two-phase flow"
Int.Jour.Multiphase Flow 2 p.139

New, A.L., McIver, P. & Peregrine, D.H. (1985)
"Computations of overturning waves"
Jour.Fluid Mech. 150 p.233

Oliver, D.R. & Wright, S.I. (1964)
"Pressure drop and heat transfer in gas-liquid slug flow in horizontal tubes"
Brit.Chem.Eng. 9 p.590

Pai, Shih-I (1977)
Two-phase Flows
Vieweg & Sohn Verlagsgesellschaft mbH, Braunschweig

Peregrine, D.H. (1968)
"Long waves in a uniform channel of arbitrary cross-section"
Jour.Fluid Mech. 32 p.358

Peregrine, D.H. (1972)
"Equations for water waves and the approximations behind them"
in Waves on Beaches and Resulting Sediment Transport (ed. R.E. Meyer) Academic Press, New York

Priestley, A. (1987)
"Roe type schemes for two-dimensional shallow water equations"
University of Reading Numerical Analysis report number 8/87

Richtmyer, R.D. & Morton, K.W. (1967)
Difference Methods for Initial Value Problems (2nd. edition)
Interscience Publishers, John Wiley & Sons, New York

Roache, P.J. (1972)
Computational Fluid Dynamics
Hermosa Publishers, Albuquerque, New Mexico

Roache, P.J. & Müller, T.J. (1970)
"Numerical schemes of laminar separated flows"
AIAA Journal 8 no.3 p.530

Roe, P.L. (1986a)
"Characteristic based schemes for the Euler equations"
Ann.Rev.Fluid Mech. 18 p.337

Roe, P.L. (1986b)
"Upwind differencing schemes, hyperbolic conservation laws with source terms"
1st. Int.Conf. on Hyperbolic Problems, St.Etienne

Roe, P.L. (1981a)
"Approximate Riemann solvers, parameter vectors, and difference schemes"
Jour.Comp.Phys. 43 no.2 p.357

Roe, P.L. (1981b)
"The use of the Riemann problem in finite difference schemes"
in Proceedings, 7th. Int.Conf. on Num.Methods in Fluid Dynamics, Springer-Verlag, New York

Rony, P.R. & Larsen, D.G. (1979)
The Bugbook II
Howard W. Sams & Co., Inc., Indianapolis

Schreier, S. (1982)
Compressible Flow
John Wiley & Sons, New York

Soo, S.L. (1976)
"On one-dimensional motion of a single component in two-phases"
Int.Jour.Multiphase Flow 3 p.79

Soo, S.L. (1967)
Fluid Dynamics of Multiphase Systems
Blaisdell, Waltham, Massachusetts

Stoker, J.J. (1957)
Water Waves
Interscience Publishers, Inc., New York

Taitel, Y. (1977)
"Flow pattern transition in rough pipes"
Int.Jour.Multiphase Flow 3 p.597

Taitel, Y. & Dukler, A.E. (1976)
"A model for prediction flow régime transitions in horizontal and near horizontal gas-liquid flow"
A.I.Chem.Eng.Jour. 22 no.1 p.47

Taitel, Y. & Dukler, A.E. (1977)
"A model for slug frequency during gas-liquid flow in horizontal and near horizontal tubes"
Int.Jour.Multiphase Flow 3 p.585

Taitel, Y. & Dukler, A.E. (1987)
"The effect of pipe length on transition boundaries"
Int.Jour.Multiphase Flow 13 p.577

Tanaka, M., Dold, J.W., Lewy, M. & Peregrine, D.H. (1987)
"Instability and breaking of a solitary wave"
Jour.Fluid Mech. 185 p.235

Taylor, G.I. (1963)
"Generation of ripples by wind blowing over a viscous fluid"
in The Scientific Papers of Sir G.I. Taylor, III (ed. G.K. Batchelor), Cambridge University Press, Cambridge

Tritton, D.J. (1988)
Physical fluid dynamics (2nd. edition)
Clarendon Press, Oxford

Wallis, G.B. (1969)
One-dimensional Two-phase Flow
McGraw-Hill Book Co., New York

Wallis, G.B. & Dobson, J.E. (1973)
"The onset of slugging in horizontal stratified air-water flow"
Int.Jour.Multiphase Flow 1 p.173

Wei, Rong-jue, Wu,Jun-ru (1981)
"Absorption of sound in water fog"
Jour.Acoust.Soc.Am. 70 no.5 p.1213

Whitham, G.B. (1974)
Linear and Non-linear Waves
Wiley Interscience Publication, John Wiley & Sons, New York

Yu, S.K.W. (1973)
"Surge flows of steam and water in a serpentine at atmospheric pressure", CEGB internal report CERL RD/L/N 261/73

APPENDIX A

If we are merely interested in the very long wave limit for sinusoidal perturbations to the interface between a gas and a liquid, we may do this by considering the shallow water equations for closed channel flow. If we have the same simplifying assumptions as we had in chapter 2:

1. The density of the gas is constant in section

$$\rho_G = \rho_G(x,t) \tag{A.1}$$

2. The interface has gentle slopes.
3. The hydrostatic pressure due to the gas is negligible.
4. The liquid density is constant.
5. Vertical velocities are small in comparison to horizontal ones.
6. The equation of state of the gas has the form

$$p_o = p_o(\rho_G) \tag{A.2}$$

where p_o is the pressure distribution along the top of the tube. If the interface is at $y = \eta(x,t)$, then the kinetic surface condition is:

$$\frac{\partial \eta}{\partial t} + \frac{\partial \eta}{\partial x} u_i - v_i = 0 \qquad \text{on } y = \eta(x,t) \tag{A.3}$$

If the top and bottom of the tube are non-varying spatially, then the top condition on $y = h_T$ and the bottom condition on $y = -h_B$ similarly become:

$$v_G = 0 \tag{A.4}$$

$$v_L = 0 \tag{A.5}$$

respectively. Consider the continuity of the gaseous phase:

$$\frac{\partial \rho_G}{\partial t} + \underline{\nabla}.(\rho_G \underline{u}_G) = 0 \tag{A.6}$$

then integrating with respect to y gives:

$$\int_{\eta}^{h_T} \frac{\partial \rho_G}{\partial t} \, dy + \int_{\eta}^{h_T} \frac{\partial}{\partial x}(\rho_G u_G) \, dy + [\rho_G v_G]_{\eta}^{h_T} = 0 \qquad (A.7)$$

and substituting (A.3) and (A.4) into (A.7) gives:

$$\int_{\eta}^{h_T} \frac{\partial \rho_G}{\partial t} \, dy + \frac{\partial}{\partial x} \int_{\eta}^{h_T} \rho_G u_G \, dy - \rho_G(\eta) \frac{\partial \eta}{\partial t} = 0 \qquad (A.8)$$

And similarly for the liquid:

$$\int_{-h_B}^{\eta} \frac{\partial \rho_L}{\partial t} \, dy + \frac{\partial}{\partial x} \int_{-h_B}^{\eta} \rho_L u_L \, dy + \rho_L(\eta) \frac{\partial \eta}{\partial t} = 0 \qquad (A.9)$$

If we now implement our assumptions in equations (A.8) and (A.9) then we obtain the continuity equations for the gas and liquid:

$$(h_T - \eta) \frac{\partial \rho_G}{\partial t} - \rho_G \frac{\partial \eta}{\partial t} + \rho_G (h_T - \eta) \frac{\partial u_G}{\partial x} +$$

$$u_G (h_T - \eta) \frac{\partial \rho_G}{\partial x} - \rho_G u_G \frac{\partial \eta}{\partial x} = 0 \qquad (A.10)$$

$$\frac{\partial \eta}{\partial t} + (\eta + h_B) \frac{\partial u_L}{\partial x} + u_L \frac{\partial \eta}{\partial x} = 0 \qquad (A.11)$$

The gas and liquid momentum conservation equations are:

$$\left.\begin{aligned} \frac{\partial u_G}{\partial t} + u_G \frac{\partial u_G}{\partial x} + v_G \frac{\partial u_G}{\partial y} &= - \frac{1}{\rho_G} \frac{\partial p_o}{\partial x} \\ \frac{\partial v_G}{\partial t} + u_G \frac{\partial v_G}{\partial x} + v_G \frac{\partial v_G}{\partial x} &= - \frac{1}{\rho_G} \frac{\partial p_o}{\partial y} \end{aligned}\right\} (A.12)$$

$$\left.\begin{aligned} \frac{\partial u_L}{\partial t} + u_L\frac{\partial u_L}{\partial x} + v_L\frac{\partial u_L}{\partial y} &= -\frac{1}{\rho_L}\frac{\partial p_o}{\partial x} - g\frac{\partial \eta}{\partial x} \\ \frac{\partial v_L}{\partial t} + u_L\frac{\partial v_L}{\partial x} + v_L\frac{\partial v_L}{\partial x} &= -\frac{1}{\rho_L}\frac{\partial p_o}{\partial y} \end{aligned}\right\} \quad (A.13)$$

Again, implementing our assumptions in equations (A.12) and (A.13) gives:

$$\frac{\partial u_G}{\partial t} + u_G\frac{\partial u_G}{\partial x} = -\frac{1}{\rho_G}\frac{\partial p_o}{\partial x} \quad (A.14)$$

$$\frac{\partial u_L}{\partial t} + u_L\frac{\partial u_L}{\partial x} = -\frac{1}{\rho_L}\frac{\partial p_o}{\partial x} - g\frac{\partial \eta}{\partial x} \quad (A.15)$$

Equations (A.10), (A.11), (A.14), (A.15) together with equation (A.2), the equation of state for the gas, define our system.

These equations are the shallow water wave equations for flow in a rectangular cross-section channel. These could be used to obtain the long wave limit of Chapter 2.

APPENDIX B

The still photographs presented in Chapter 3, the experimental section, are indicative of the type of flow observed within the parameter range under consideration. Each photograph is numbered, and the flow conditions relevant to that photograph recorded. In the following tables, data concerning those photographs is presented.

Some interesting problems concerning the analysis of the data from the photographs arose when the photographs were studied. For example, due to the nature of the experimental arrangement it was clear that the camera could not always be aligned so that the axis of the lens was perfectly horizontal, nor would the interface always be at the camera axis level. From the photographs it is clear that the camera is often inclined (albeit by a small degree) to the liquid surface in the tube, and so the photographs show two lines of contact of the liquid with the tube. One corresponds to contact with the near side of the tube, the other with the far side. In the following tables the distance from the top of the tube to the lines of contact is recorded, and b_n refers to the near line of contact while b_f refers to the far line. The other data taken from the photographs is the measured diameter of the tube, denoted d_m in the tables, which was used in conjunction with the b's to obtain the real depth of liquid in the tube. Other data concerning the flows, such as the mass fluxes Q_i (i= G or L), were calculated form measurements of pressure, temperature and orifice plate pressure differential as described in Section 3.

In order to obtain the corrected value of the distance from the top of the tube to the liquid interface, as though the camera's lens was perfectly horizontal, the following expression, with reference to the

figure below (Fig. B.1), was derived:

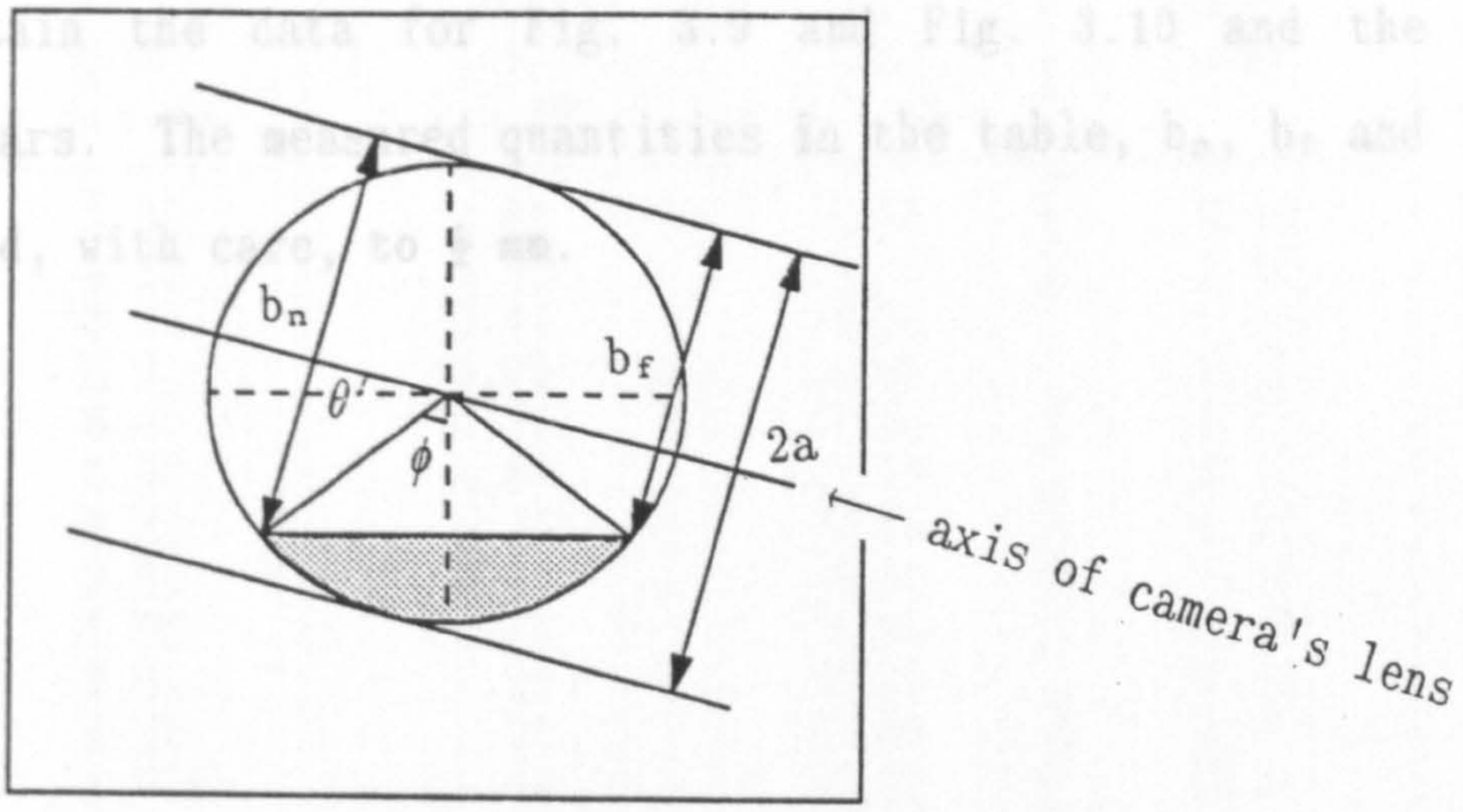

Fig. B.1

$$b_n = a\ (1 + \cos(\theta - \phi))$$

$$b_f = a\ (1 + \cos(\theta + \phi))$$

where θ is the angle of inclination of the axis of the camera's lens to the horizontal, ϕ as indicated on Fig. B.1 and a the radius of the tube. Hence:

$$\frac{1}{\sin^2\theta}\left[\frac{b_n - b_f}{2a}\right]^2 + \frac{1}{\cos^2\theta}\left[1 - \frac{b_n + b_f}{2a}\right]^2 = 1$$

which can be solved for $\cos\theta$, say, and hence:

$$b = a\left[1 - \frac{1}{\cos\theta}\left[1 - \frac{b_n + b_f}{2a}\right]\right]$$

So the depth is:

$$\text{depth} = a\left[1 + \frac{1}{\cos\theta}\left[1 - \frac{b_n + b_f}{2a}\right]\right]$$

The table below, Table B.1, shows a selection of the raw data as measured during the experiments. This table also shows how this data

may be converted into the true depth of liquid in the tube, column "depth" in the table. Subsequent tables show how this data is used to calculate the average viewing angle, and then a subset of this data is considered to obtain the data for Fig. 3.9 and Fig. 3.10 and the associated error bars. The measured quantities in the table, b_n, b_f and d_m, can be measured, with care, to $\frac{1}{2}$ mm.

Table B.1

Conversion of experimental values for the depth into real values for depth.

frame no.	b_n (cm) ± 0.5 mm.	b_f (cm) ± 0.5 mm.	d_m (cm) ± 0.5 mm.	depth (cm)
2	5.00	3.85	8.55	2.49
6	4.10	3.50	8.55	2.87
9	3.95	3.45	8.55	2.93
14	6.80	5.75	8.55	1.37
21	6.40	5.30	8.55	1.63
26	5.90	4.80	7.15	1.29
30	5.20	4.40	7.15	1.69
60	2.50	2.10	3.30	1.56
63	1.90	1.70	3.30	2.35
63†	1.50	1.20	3.30	3.06
68	2.20	1.90	3.30	1.95
68†	1.70	1.40	3.30	2.74
73	2.30	2.10	3.30	1.72
87	2.20	1.90	3.30	1.95
88	2.15	1.80	3.30	2.07
92	2.30	2.00	3.30	1.80
92†	1.50	1.20	3.30	3.06
94	2.10	1.90	3.40	2.13
95	2.45	2.10	3.30	1.60
97	2.00	1.90	3.30	2.35
102	2.00	1.70	3.30	2.27
107	2.20	1.90	3.30	1.95
111	2.20	1.95	3.30	1.92
112	2.15	1.90	3.30	1.99
117	2.40	1.95	3.30	1.64
119	2.55	2.30	3.40	1.48
120	2.30	2.00	3.30	1.80
121	2.20	2.00	3.30	1.88
121†	2.00	1.80	3.30	2.19
123	2.60	2.20	3.30	1.41
123†	2.00	1.70	3.30	2.27
127	2.00	1.80	3.40	2.28
130	2.00	1.90	3.30	2.11
130†	1.70	1.40	3.30	2.74
131	2.15	1.85	3.30	2.03
148	2.20	1.90	3.30	1.96
148†	1.80	1.50	3.30	2.58
152	1.20	1.00	3.30	3.45
153	1.55	1.35	3.30	3.50
154	2.00	1.70	3.30	2.27
181	2.20	1.80	3.30	2.03
186	2.15	1.90	3.30	1.99
187	2.50	2.10	3.30	1.56
187†	1.90	1.70	3.30	2.35
192	2.30	2.20	3.30	1.80
192†	1.50	1.20	3.30	3.06

† additional data taken from a frame that provides information about the initial disturbance amplitude to equilibrium depth ratio for Fig. 3.10 .

The following table shows how the angle of viewing of the photographic equipment varied, from film to film. At first sight, worrying about the angle of the camera's lens to the horizontal may seem unnecessary, but for a 105 mm lens, the field of view is about 6°, and this is the order of the calculated errors. If these angles were ignored, the error bars of Figs. 3.9 and 3.10 would be unnecessarily large. This average angle is used when calculating the actual depth of liquid in the above table, Table B.1, and the following tables, Table B.3 and B.4 ..

Table B.2

The average viewing angle for sets of the above frames.

range of frames	angle (degrees)
2 - 21	6.2
26 - 30	8.6
60 - 73	5.1
87 - 107	5.6
111 - 148	4.8
152 - 154	4.1
181 - 192	5.6

In order to obtain the data for Fig. 3.9 in the Experimental section the above angles were used when calculating the actual liquid depth in the tube, so that errors of measuring the angle in any one frame were averaged out over the number of frames that provided useful data about the viewing angle. In this way, the following table of results for the equilibrium liquid depth to tube diameter ratio against mixture Froude number, defined in equation 3.2.1, Table B.3 was obtained.

Table B.3

Analysis of experimental data of Fig. 3.9; the variation of depth to diameter ratio with the mixture Froude number of the flow

Frame no.	Liquid Mass Flux ($kg\ s^{-1}$)	Error $x10^{-3}$	Gas Mass Flux $x10^{-3}$ ($kg\ s^{-1}$)	Error $x10^{-3}$	Liquid Depth (cm)	Error (mm)	Mixture Froude No.	Error (mm)	Angle (degrees)
14	0.462	2.5	10.77	0.33	1.9	0.20	38.47	2.25	2.2
21	0.462	2.5	9.79	0.37	1.6	0.15	32.10	2.26	8.0
26	0.373	3.1	10.98	0.31	1.3	0.26	39.09	2.13	10.3
30	0.373	3.1	11.20	0.30	1.7	0.16	40.65	2.13	6.8
60	0.373	0.5	8.27	0.42	1.6	0.39	22.86	2.19	7.6
68	0.396	0.5	8.85	0.39	2.0	0.26	26.05	2.19	5.4
87	0.390	0.5	8.08	0.44	2.0	0.26	21.92	2.25	5.4
92	0.390	0.5	8.09	0.44	1.8	0.29	21.96	2.28	5.5
95	0.390	0.5	8.40	0.42	1.6	0.36	23.55	2.25	6.6
107	0.390	0.5	8.08	0.44	2.0	0.26	21.89	2.25	5.4
111	0.393	0.5	5.93	0.60	1.9	0.25	12.29	2.30	4.5
117	0.393	0.5	5.92	0.60	1.6	0.33	12.25	2.30	5.6
119	0.393	0.5	7.43	0.48	1.5	0.37	18.72	2.26	4.7
121	0.393	0.5	7.42	0.48	1.9	0.24	18.66	2.25	3.6
123	0.393	0.5	8.67	0.41	1.7	0.85	25.05	2.24	15.0
148	0.427	0.6	8.74	0.41	2.0	0.26	25.64	2.28	5.4
130	0.427	0.6	5.97	0.60	2.1	0.16	12.60	2.34	1.8
181	0.407	0.6	10.31	0.33	2.0	0.36	34.94	2.15	7.1
186	0.407	0.6	10.32	0.33	2.0	0.23	34.99	2.15	4.5
192	0.407	0.5	11.21	0.31	1.8	0.29	40.98	2.14	5.5

Likewise, Table B.4 was used to obtain Fig. 3.10 of the variation of the observed maximum in initial amplitude against equilibrium depth to tube diameter ratio.

Table B.4

Variation of observed maximum in initial disturbance amplitude to equilibrium depth ratio with equilibrium depth to tube diameter ratio

Frame no.	depth/dia	error ± x10^{-1}	amp/depth	error ± x10^{-1}
63	0.45	0.8	0.30	0.20
68	0.38	0.5	0.40	0.19
92	0.35	0.6	0.70	0.18
121	0.36	0.5	0.17	0.16
123	0.27	0.9	0.62	0.41
130	0.41	0.3	0.29	0.16
148	0.38	0.5	0.32	0.13
187	0.30	0.8	0.51	0.30
192	0.35	0.7	0.70	0.19

In Tables B.3 and B.4 the quoted errors were calculated using standard normal distribution error analysis techniques. In the following errors analysis, all expressions such as $e(\mathcal{A})$ refer to the error in quantity $\mathcal{A}$ as measured experimentally, or as previously calculated.

If we define the following variables:

$$p = \left[1 + \frac{b_n + b_f}{d_m}\right]^2$$

$$q = \left[\frac{b_n - b_f}{d_m}\right]^2$$

then the following expression is used to determine the angle that the axis of the lens makes with the horizontal

$$\cos^2\theta = \frac{(p-q+1) \pm \sqrt{(p-q+1)^2 - 4p}}{2}$$

The error in b_i (i=n or f) is, from Table B.1, e(b) = 0.5 mm., thus:

$$[e(\Delta b)]^2 = [e(\Sigma b)]^2 = 2\,[e(b)]^2$$

and the error in the measured angles is obtained using the following expressions:

$$\left[\frac{e(p)}{p}\right]^2 = ((2)^2 + 1)\left[\left[\frac{e(\Sigma b)}{\Sigma b}\right]^2 + \left[\frac{e(d_m)}{d_m}\right]^2\right]$$

$$\left[\frac{e(q)}{q}\right]^2 = (2)^2\left[\left[\frac{e(\Delta b)}{\Delta b}\right]^2 + \left[\frac{e(d_m)}{d_m}\right]^2\right]$$

$$[e(p-q)]^2 = [e(p)]^2 + [e(q)]^2$$

and after all suitable manipulations we get, for the error in $\cos\theta$:

$$\left[\frac{e(\cos\theta)}{\cos\theta}\right]^2 = (\tfrac{1}{2})^2 \frac{[e(p-q)]^2 + (\tfrac{1}{2})^2 \dfrac{((2)^2+1)\left[\dfrac{e(p-q)}{(p-q)}\right]^2 (p-q+1)^4 + [e(p)]^2}{(p-q+1)^2 - 4p}}{\left[\,(p-q+1) + \sqrt{(p-q+1)^2 - 4p}\,\right]^2}$$

If we denote r as the actual radius of the tube, then the final error in the real depth of liquid in the tube is given by:

$$[e(\text{depth})]^2 = [e(r)]^2 + \left\{(\tfrac{1}{2})^2\left[\frac{e(p)}{p}\right]^2 + \left[\frac{e(\cos\theta)}{\cos\theta}\right]^2 + \left[\frac{e(r)}{r}\right]^2\right\} \frac{r^2 p}{\cos^2\theta}$$

In addition to calculating the error associated with calculating the real depth of the liquid in the tube, it is necessary to calculate the error in obtaining the mixture Froude number for the flow. First the error in calculating the mass fluxes for the various flows from the expressions in section 3 are used and we arrive at the following for the errors:

$$\left[\frac{e(Q_L)}{Q_L}\right]^2 = (\tfrac{1}{2})^2\left[\left[\frac{e(\Delta h)}{\Delta h}\right]^2 + \left[\frac{0.005}{15.8}\right]^2\right] + \left[\frac{0.00005}{k_L}\right]^2$$

$$\left[\frac{e(Q_G)}{Q_G}\right]^2 = (\tfrac{1}{2})^2\left[\left[\frac{e(\Sigma T)}{\Sigma T}\right]^2 + \left[\frac{e(\Delta h)}{\Delta h}\right]^2 + \left[\frac{0.005}{P}\right]^2 + \left[\frac{0.005}{273.15}\right]^2 + \left[\frac{0.05}{14.7}\right]^2\right] + \left[\frac{0.0000005}{k_G}\right]^2$$

(really small terms are included just for completeness) where Q_i (i=G or L) are the mass fluxes, Δh is the difference in the height of fluid in the limbs of the manometer tubes for the gas and liquid orifice plates which could be read accurate to 1 mm., ΣT is the absolute temperature in Kelvin, read accurate to 0.05 K, P is the absolute pressure of the gas flow to the orifice plate, and k_i (i=g or L) are the respective orifice plate constants. Hence we may obtain the error in the mixture Froude number. And so the data for the Figs. 3.9 and 3.10 in Tables B.3 and B.4 is arrived at.

Appendix C

Fast ciné film of several transitions was obtained and tracings of these appear in Chapter 3, the Experimental section. No "bridging" phenomenon was ever observed from these films, and so within the parameter space under consideration, it would seem reasonable to assume that the criterion for slug flow to occur is not dependent on this bridging taking place. The films obtained were carefully numbered, and the following tables show the data concerned with each film, and this data was used for Figs. 3.17 to 3.20.

Although there must have been some error in aligning the axis of the lens of the fast ciné camera with the horizontal, no analysis of this error could be made from the fast ciné film because the images of the flow were already somewhat unresolved due to the speed of the flow, and the already harsh lighting used could not be increased for fear of seriously damaging the tubes. Therefore, no such analysis is performed here, unlike that of Appendix B.

In the following tables, the values Δx_m and Δy_m are the measured horizontal and vertical displacements (with care these could be measured to $\frac{1}{4}$ mm), whether of droplets or of peaks of the wave or of the front surface of the wave, between two specified frames and using the scale factor of 1 cm. (real) ≡ 1.2 cm. (measured) on A4 paper. This was then reduced so that Figs. 3.13 to 3.16 are the true scale. The time between frames is always 4.0 ms. .

Table C.1

Data for Fig. 3.17 taken from Fig. 3.13 for slug flow with gas mass flux 8.724×10^{-3} kg s^{-1} and liquid mass flux 0.390 kg s^{-1}.

Frame no.	Time Interval (ms)	Δx_m (cm)	Δy_m (cm)	u (m s^{-1})	v (m s^{-1})
○ 1 - 2	4.0	0.85	0.00	1.8	0.0
○ 2 - 3	4.0	0.82	0.00	1.7	0.0
○ 3 - 4	4.0	0.62	0.00	1.3	0.0
○ 6 - 8	8.0	0.37	0.60	0.4	0.6
○ 10 - 12	8.0	1.65	0.30	1.7	0.3
○ 24 - 25	4.0	1.32	0.15	2.8	0.3
○ 32 - 34	8.0	3.05	0.00	3.2	0.0
• 6 - 8	8.0	1.50	0.00	1.6	0.0
• 8 - 10	8.0	1.30	0.00	1.4	0.0
• 10 - 12	8.0	3.05	0.22	1.7	0.3
• 12 - 15	12.0	1.50	0.80	1.0	0.6
• 24 - 25	4.0	1.00	0.00	2.1	0.0
peaks of waves					
10 - 12	8.0	1.57	0.00	1.6	0.0
12 - 13	4.0	0.70	0.60	1.5	1.3
13 - 14	4.0	0.70	0.15	1.5	0.3
14 - 15	4.0	0.45	0.25	0.9	0.7
15 - 16	4.0	0.77	-0.25	1.6	-0.5
16 - 17	4.0	0.95	0.00	2.0	0.0
17 - 18	4.0	0.45	0.00	0.9	0.0
18 - 20	8.0	1.40	0.30	1.5	0.3
20 - 21	4.0	0.52	0.00	1.1	0.0
21 - 22	4.0	0.52	0.00	1.1	0.0
22 - 24	8.0	1.75	0.00	1.8	0.0
24 - 25	4.0	1.10	-0.25	2.3	-0.5
25 - 32	28.0	4.20	0.60	1.3	0.2
32 - 34	8.0	1.67	0.00	1.7	0.0
34 - 36	8.0	1.37	-0.47	1.4	-0.5
36 - 38	8.0	1.50	0.25	1.6	0.3
38 - 44	24.0	4.42	0.20	1.5	0.1
44 - 47	12.0	1.27	-0.85	0.8	0.6
front of waves					
10 - 12	8.0	1.40	0.00	1.5	0.0
12 - 13	4.0	0.40	0.60	0.8	1.3
13 - 14	4.0	0.65	0.15	1.4	0.3
14 - 15	4.0	0.50	0.35	1.0	0.7
15 - 16	4.0	0.85	-0.35	1.8	-0.7
16 - 17	4.0	1.10	0.00	2.3	0.0
17 - 18	4.0	0.50	0.00	1.0	0.0
18 - 20	8.0	1.22	0.25	1.3	0.3
20 - 21	4.0	0.50	0.10	1.0	0.2
21 - 22	4.0	0.80	-0.10	1.7	0.2
22 - 24	8.0	2.77	-0.30	2.9	-0.3
24 - 25	4.0	0.70	0.00	1.5	0.0

Frame no.	Time Interval (ms)	Δx_m (cm)	Δy_m (cm)	u (m s^{-1})	v (m s^{-1})
25 - 32	28.0	4.50	0.00	1.3	0.0
32 - 34	8.0	1.25	0.45	1.3	0.5
34 - 36	8.0	1.45	-0.45	1.5	-0.5
36 - 38	8.0	1.20	0.00	1.3	0.0
38 - 44	24.0	4.70	0.45	1.6	0.2
44 - 47	12.0	1.60	-0.45	1.1	-0.3

Table C.2

Data for Fig. 3.18 taken from Fig. 3.14 for slug flow with gas mass flux 8.724×10^{-3} kg s^{-1} and liquid mass flux 0.390 kg s^{-1}.

Frame no.	Time Interval (ms)	Δx_m (cm)	Δy_m (cm)	u (m s^{-1})	v (m s^{-1})
• 5 - 6	4.0	2.00	0.15	4.2	0.3
• 6 - 7	4.0	1.90	-0.20	4.0	-0.4
○ 1 - 2	4.0	1.30	0.15	2.7	0.3
○ 2 - 3	4.0	1.80	-0.20	3.8	-0.4
○ 3 - 4	4.0	1.90	-0.15	4.1	-0.3
○ 4 - 5	4.0	1.90	-0.50	4.0	-0.3
peak of waves					
15 - 17	8.0	1.40	0.00	1.5	0.0
17 - 26	36.0	3.17	1.30	0.7	0.3
26 - 29	12.0	2.30	0.45	1.6	0.3
29 - 37	32.0	6.45	-0.35	1.7	-0.1
37 - 40	12.0	3.30	-0.30	2.3	-0.2
40 - 48	32.0	5.80	-0.32	1.5	-0.1
front of waves					
26 - 29	12.0	2.10	0.00	1.5	0.0
29 - 34	20.0	4.40	0.00	1.8	0.0
29 - 37	32.0	6.55	0.00	1.7	0.0
37 - 48	44.0	8.80	0.00	1.7	0.0

Table C.3

Data for Fig. 3.19 taken from Fig. 3.15 for slug flow with gas mass flux 8.724×10^{-3} kg s^{-1} and liquid mass flux 0.390 kg s^{-1}.

Frame no.	Time Interval (ms)	Δx_m (cm)	Δy_m (cm)	u (m s^{-1})	v (m s^{-1})
peak of waves					
12 - 16	16.0	1.45	0.00	0.7	0.0
16 - 18	8.0	2.00	0.62	2.1	0.7
18 - 20	8.0	2.62	0.32	2.7	0.3
20 - 23	12.0	0.62	0.35	1.8	0.2
23 - 26	12.0	1.90	-0.17	1.3	-0.1
26 - 28	8.0	1.95	0.50	2.0	0.5
28 - 30	8.0	1.90	0.22	2.0	0.2
30 - 34	16.0	3.30	-0.22	1.7	-0.1
34 - 37	12.0	2.55	0.00	1.7	0.0
front of waves					
12 - 16	16.0	1.70	0.00	0.9	0.0
16 - 18	8.0	2.02	0:60	2.1	0.6
18 - 20	8.0	2.65	0.15	2.8	0.2
20 - 23	12.0	2.25	0.47	1.6	0.3
23 - 26	12.0	1.87	0.10	1.3	0.1
26 - 28	8.0	1.92	0.00	2.0	0.0
28 - 30	8.0	1.67	0.37	1.7	0.4
30 - 34	16.0	3.77	-0.32	2.0	-0.2
34 - 37	12.0	2.32	0.17	1.6	0.1

Table C.4

Data for Fig. 3.20 taken from Fig. 3.16 for slug flow with gas mass flux 9.504×10^{-3} kg s^{-1} and liquid mass flux 0.375 kg s^{-1}.

Frame no.	Time Interval (ms)	Δx_m (cm)	Δy_m (cm)	u (m s^{-1})	v (m s^{-1})
peak of waves					
1 - 3	8.0	0.57	0.10	0.6	0.1
3 - 5	8.0	1.40	-0.10	1.5	-0.1
5 - 8	12.0	1.40	-0.05	1.0	0.0
12 - 15	12.0	1.55	0.20	1.1	0.2
15 - 18	12.0	1.50	0.25	1.0	0.2
18 - 20	12.0	1.90	0:60	2.0	0.6
20 - 21	4.0	0.95	0.20	2.0	0.4
21 - 24	12.0	1.50	-0.50	1.0	-0.3
24 - 27	12.0	2.00	0.10	1.4	0.1
27 - 32	20.0	3.80	-0.10	1.6	0.0
32 - 35	12.0	1.75	-0.40	1.2	0.3
front of waves					
18 - 20	8.0	1.25	0.00	1.3	0.0
20 - 21	4.0	0.80	0.00	1.7	0.0
21 - 24	12.0	1.85	0.00	1.3	0.0
24 - 27	12.0	2.40	0.00	1.7	0.0

APPENDIX D

In order to obtain the double coloured flash photographs shown in Chapter 3, the Experimental section, the following circuitry was designed to fire the two flash guns within an adjustable, short time interval. Any further data concerning the 74121 monostable multivibrator and the 74123 dual retriggerable monostable multivibrator can be found in Rony & Larsen (1979), "The Bugbook II".

The time interval between the triggering of the flash guns is controlled by the 121 monostable, and this was adjusted by means of the variable 50 kΩ resistor and the pulse width controlled by the choice of the 3.5 μF capacitor. Similarly, the pulse width of the 123 dual monostable is controlled by means of the 91 kΩ resistors and the 0.1 μF capacitors.

The circuit diagrams on the following pages show the arrangement of the TTL circuitry used for the purposes of triggering two flash guns, and for triggering two cameras. The latter arrangement was used in attempting to obtain data concerning the pressure transitions within the experimental apparatus from inclined manometer readings, although this proved futile because the manometer responded too slowly and was too damped to be of any real use. The circuitry for the twin camera operations makes use of a 555 monostable multivibrator which is an analog-digital hybrid chip.

Fig. D.1

Circuit diagram for the twin flash firing mechanism

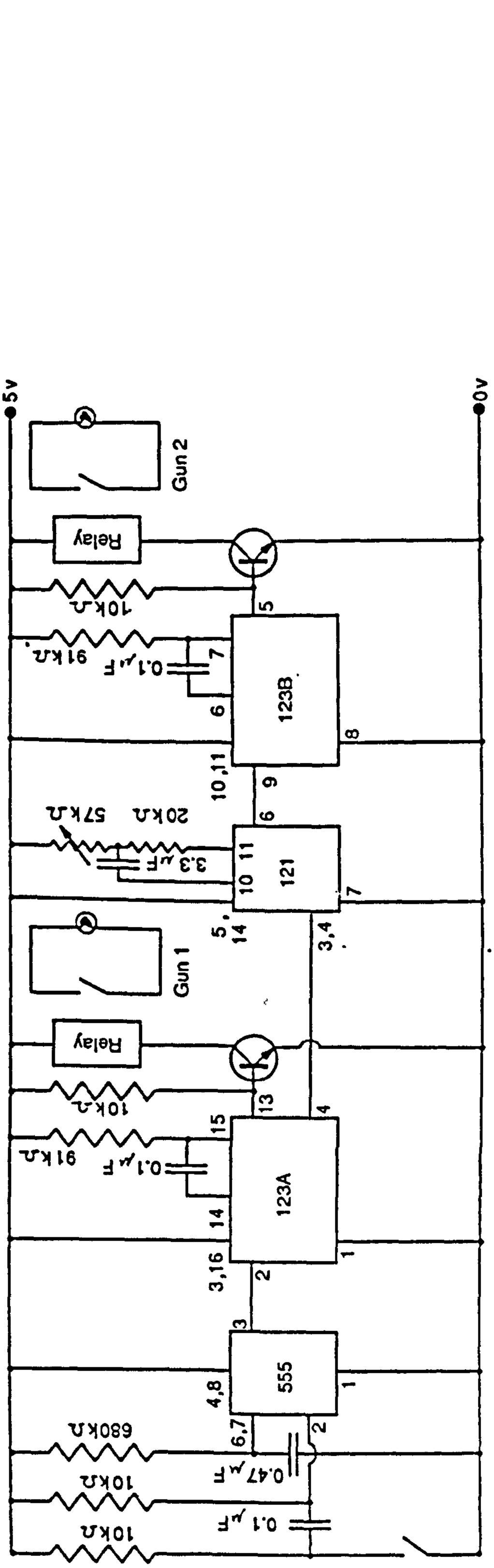

Fig. D.2

Circuit diagram for the twin camera firing mechanism

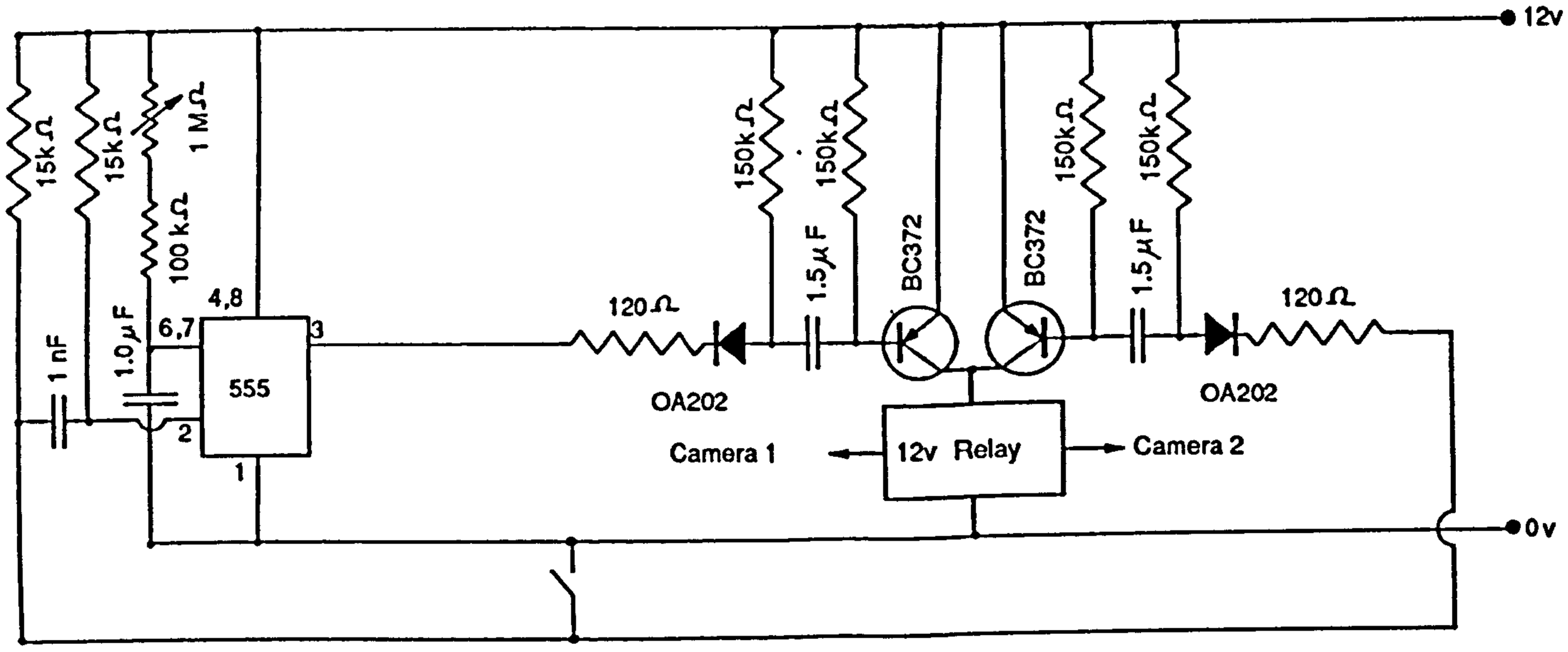

APPENDIX E

In Chapter 4 we considered a steam-water two-phase flow. In order to do this we required an equation of state for the steam so that the steady one-dimensional gas model could be used. In Keenan et al. (1978) we find such an equation of state in terms of the Helmholtz free energy. This Helmholtz free energy is expressed in terms of a series, the coefficients of which were determined from experimental data. Table E.1 (over) contains the coefficients A_{ij} that are used in this series.

Table E.1

The coefficients of $A_{i,j}$ used in the equation of state for steam.

j / i	1	2	3	4	5	6	7
1	29.492937	-5.1985860	6.8335354	-0.1564104	-6.3972405	-3.9661401	-0.69048554
2	-132.13917	7.7779182	-26.149751	-0.72546108	26.409282	15.453061	2.7407416
3	274.64632	-33.301902	65.326396	-9.2734289	-47.740374	-29.142470	-5.1028070
4	-360.93828	-16.254622	-26.181978	4.3125840	56.323130	29.568796	3.9636085
5	342.18431	-177.31074	0	0	0	0	0
6	-244.50042	127.48742	0	0	0	0	0
7	155.18535	137.46153	0	0	0	0	0
8	5.9728487	155.97836	0	0	0	0	0
9	-410.30848	337.31180	-137.46618	6.7874938	136.87317	79.847970	13.041253
10	-416.05860	-209.88866	-733.96848	10.401717	645.81880	399.17570	71.531353